Thermoelectric Energy Harvesting for Sensor Powering

Yongjia Wu

Dissertation submitted to the faculty of the Virginia Polytechnic Institute and State University in partial fulfillment of the requirements for the degree of

Doctor of Philosophy
In
Mechanical Engineering

Lei Zuo, Chair
Thomas E. Diller
Rui Qiao
Michael D. Heibel

05/09/2019
Blacksburg, Virginia
Keywords: Thermoelectric, energy harvesting, heat transfer, sensor powering

Thermoelectric Energy Harvesting for Sensor Powering

Yongjia Wu

ABSTRACT

The dissertation solved some critical issues in thermoelectric energy harvesting and tried to broaden the thermoelectric application for energy recovery and sensor powering. The scientific innovations of this dissertation were based on the new advance on thermoelectric material, device optimization, fabrication methods, and system integration to increase energy conversion efficiency and reliability of the thermoelectric energy harvester.

The dissertation reviewed the most promising materials that owned a high figure of merit (ZT) value or had the potential to increase ZT through compositional manipulation or nano-structuring. Some of the state-of-art methods to enhance the ZT value as well as the principles underneath were also reviewed. The nanostructured bulk thermoelectric materials were identified as the most promising candidate for future thermoelectric applications as they provided enormous opportunities for material manipulation.

The optimizations of the thermoelectric generator (TEG) depended on the accuracy of the mathematical model. In this dissertation, a general and comprehensive thermodynamic model for a commercial thermoelectric generator was established. Some of the unnecessary assumptions in the conventional models were removed to improve the accuracy of the model. This model can quantize the effects of the Thomson effect, contact thermal and electrical resistance, and heat leakage, on the performance of a thermoelectric generator. The heat sink can be another issue for the design of high-performance TEG. An innovative heat sink design integrated with self-oscillating impinging jet generated by the fluidic oscillator arrays were adopted to enhance the heat convection. The performance of the heat sink was characterized by large eddy simulation.

The compatibility mismatch had been a practical problem that hindered the further improvement of energy conversion efficiency of thermoelectrics. In this dissertation, a

novel method to optimize the geometry of the thermo-elements was developed. By varying the thickness and cross-sectional area of each thermoelectric segment along the length of the thermo-element, the compatibility mismatch problem in the segmented TEG construction was eliminated. The optimized segmented TEG can make the best of the existing thermoelectric materials and achieve the maximum energy conversion efficiency in a wide temperature range. A segmented TEG with an unprecedented efficiency of 23.72% was established using this method. The complex geometry structure of the established thermo-elements would introduce extra difficulty in fabrication. Thus selective laser melting, a high-temperature additive manufacture method, was proposed for the fabrication. A model was built based on the continuous equations to guide the selective-laser-melting manufacturing of thermoelectric material with other nanoparticles mixed for high thermoelectric performance.

Thermoelectric energy harvesting played a critical role in the self-powered wireless sensors, as it was compact and quiet. In this dissertation, various thermoelectric energy harvesters were established for self-powered sensors to in-situ monitor the working condition in the gas turbine and the interior conditions in nuclear canisters. The sensors, taking advantage of the thermal energy existing in the local environment, can work continuously and provide tremendous data for system monitor and diagnosis without external energy supply.

Thermoelectric Energy Harvesting for Sensor Powering

Yongjia Wu

GENERAL AUDIENCE ABSTRACT

The dissertation addressed some critical issues in thermoelectric energy harvesting and broadened its application for energy recovery and sensor powering. Some of the most advanced technologies were developed to improve the energy conversion efficiency and reliability of the thermoelectric energy harvesters.

In this dissertation, a general and comprehensive thermodynamic model for a commercial thermoelectric generator (TEG) was established. The model can be used to optimize the design of the existing commercial TEG modules. High performance heat sink design was critical to maximize the temperature drop in the TEG module, thus increase the power output and energy conversion efficiency of the TEG. An innovative heat sink design integrated with self-oscillating impinging jet generated by the fluidic oscillator arrays were designed to cool the cold end of the TEG, thus enhance the performance of the TEG. The performance of the heat sink was characterized by large eddy simulation.

A single thermoelectric material only had high thermoelectric performance in a narrow temperature range. A segmented TEG could achieve a high energy conversion efficiency over a wide temperature range by adopting different materials which had high thermoelectric performance at low, moderate, and hight temperature ranges. However, the material compatibility mismatch had been a practical problem that hindered the further improvement of energy conversion efficiency of the segmented TEG. In this dissertation, a novel method was developed to eliminate the compatibility mismatch problem via optimizing the geometry of the thermo-elements. A segmented TEG with an unprecedented efficiency of 23.72% was constructed using the method proposed in this dissertation. The complex geometry structure of the established thermo-elements would introduce extra difficulty in fabrication. Thus selective laser melting, a high-temperature additive manufacture method, was proposed for the fabrication. A physical model based on the conservation equations was built to guide the selective-laser-melting manufacturing of the optimized segmented TEG mentioned above.

In this dissertation, two thermoelectric energy harvesters were built for self-powered sensors to in-situ monitor the interior conditions in nuclear canisters. The sensors, taking advantage of the thermal energy existing in the local environment, can work continuously and provide tremendous data for system monitor and diagnosis without external energy supply. Also, a compact thermoelectric energy harvester was developed to power the gas sensor for combustion monitoring and control.

Acknowledgment

I am deeply grateful to everyone who helped and supported me during this endeavor. Without them, it would be impossible for me to complete this dissertation.

I am deeply grateful to Dr. Lei Zuo, my Ph.D. adviser, for the constant help and encouragement he provided in the past four years. His guidance is invaluable for my entire professional career. His enthusiasm and dedication to the research inspired me to work hard and finally decided to continue my career in academia. His vision and knowledge enhanced my capacity to formulate and solve the problem in my projects. He gave me the freedom to explore the areas I had interest in and never discouraged my "stupid" ideas. His attitude to work will also continue to affect my future life.

I am indebted to my families for their love and support in the past many years. Most of my thanks go to my parents, Mr. Zhenggen Wu and Mrs. Weining Lu. They had no chance to go to high school because of the Cultural Revolution that happened in their generation. They knew how valuable the knowledge was for my sister and me. They supported me to have my Ph.D. study in the USA though they had no idea what their son was doing. They had given sister and me all the riches that life could offer. I am also deeply grateful to my sister Jiamin Wu for her moral support. We grew up together and shared so many happy moments. I want to thank my grandparents for so much love they gave me when I was a small boy. I would never have made it here without them.

I want to thank my master adviser, Professor Tingzhen Ming, who led me to research thermal and fluid science and engineering. He encouraged me to continue my Ph.D. study in the USA after I got my master degree under his supervision. I also want to thank Professor Thomas E. Diller, Professor Rui Qiao, and Dr. Michael D. Heibel for serving my advisory committee. Their comments have been constructive for my research and significantly improved the quality of my dissertation. I would also acknowledge Dr. Michael D. Heibel for his help with the gamma radiation experiments done in Westinghouse Company at Pittsburgh.

I want to thank my colleagues at the energy harvesting center, including Jie Chen, Jackson Klein, Dr. Shifeng Yu, Dr. Shuyu Wang, Hanchen Zhou, and Kan Sun, for their generous help and technical discussions during my Ph.D. study. I would also want to think some of my friends, including Dr. Yilun Liu, Dr. Weiche Tai, Dr. Changwei Liang, Mingyi Liu, Yu Pan, Dr. Yan Ding, Xiaofan Li, Dr. Feng Qian, Dr. Sijing Guo, Hongjip Kim, Yinyin Fan, Yue Yuan, Qiumeng Xu, Qiuchi Xiong, Boxi Jiang, Jia Mi, Yuzhe Chen, Isil Anakok, Ahmed Sallam, and Chen Zhu. They made my life in Blacksburg to become more relaxed and full of good memories.

I want to thank all staff members in the Department of Mechanical Engineering. Special thanks go to Lauren Mills who helped me with most of the department documents.

I would also acknowledge the funding support from DOE via Grant #16-10884 and #13-5479, and NSF via Grant #1508862 and #1335384.

Contents

List of figures .... **xii**

List of tables .... **xx**

Nomenclature .... **xxi**

Chapter 1. Introduction and Background **1**

1.1 A brief history of thermoelectrics 1

1.2 The working principle of thermoelectric generators 3

1.3 Energy harvesting technologies 5

1.3.1 Thermoelectric energy harvesting 5

1.3.2 Other energy harvesting technologies 13

1.4 Advanced thermoelectric materials 15

1.5 The thermoelectric material fabrication method 23

1.5.1 Spark plasma sintering for bulk material fabrication 23

1.5.2 Molecular beam epitaxy and chemical vapor deposition for thin film thermoelectric material fabrication 24

1.5.3 Selective laser melting for the fabrication of nanostructured bulk thermoelectric materials 25

1.5.4 Thermal spay and cold spay for thermoelectric film fabrication 26

1.6 Thermoelectric material characterization 27

1.6.1 Microstructure characterization 27

1.6.2 Thermal conductivity characterization 29

1.6.3 Electrical conductivity characterization 31

1.6.4 Seebeck coefficient characterization 33

1.7 Thermoelectric properties and Onsager relations 34

1.7.1 Electrical conductivity and Seebeck coefficient 35

1.7.2 Thermal conductivity 36

1.7.3 Calculate the ZT using single-band theory 38

1.8 Strategies to enhance the ZT value of thermoelectric material 42

1.8.1 Traditional ways to increase $\boldsymbol{\beta}$ 42

1.8.2 Carriers concentration optimization to enhance ZT 43

1.8.3 Reduce the lattice thermal conductivity 44

1.8.4 Nanotechnologies to change the density of states of the electrons 45

1.8.5 Band engineering to enhance Seebeck coefficient 47

1.9 Objectives and contributions of the dissertation 48

1.10 Dissertation Organization 49

Chapter 2. Increase the Efficiency of TEG via Thermal Network Optimization .. 51
2.1 Chapter introduction ... 51
2.2 The limitation of the conventional model ... 51
2.3 Thermodynamic analysis of thermo-elements ... 53
2.4 TEG device-level performance ... 61
2.5 Summary for the chapter ... 68
Chapter 3. Heat Sink Design Integrating the Sweeping Impinging Jet ... 70
3.1 High-performance heat sink design for TEG ... 70
3.2 Introduction to the fluidic oscillators ... 71
3.3 The design of the fluidic oscillators ... 74
3.4 Numerical models ... 75
3.4.1 The $\boldsymbol{k-\omega}$ SST model ... 75
3.4.2 The ELES model ... 76
3.4.3 Numerical methodology ... 78
3.5 Simulation results and discussion ... 80
3.5.1 The flow field and oscillation frequencies ... 80
3.5.2 Heat transfer results ... 83
3.6 Validation of the modeling results ... 88
3.7 Summary for the chapter ... 89
Chapter 4. Increase the Efficiency of TEG via Thermo-element Geometry Optimization ... 91
4.1 Chapter introduction ... 91
4.2 Segmented TEG for high energy conversion efficiency ... 91
4.3 An optimization method based on the compatibility analysis ... 94
4.4 The conventional thermo-element ... 100
4.5 The optimized thermo-element ... 103
4.6 Summary for the chapter ... 107
Chapter 5. Selective Laser Melting for Thermoelectric Material Fabrication 109
5.1 Chapter introduction ... 109
5.2 Integrated design and manufacturing of the nanostructured TEG using SLM 109
5.2.1 SLM for TEG fabrication ... 109
5.2.2 The potential benefits using selective laser sintering for thermoelectric material fabrication ... 112
5.3 Introduction to SLM ... 114

5.4 The mathematical model to simulate SLM processing of multi-component thermoelectric powders 117

5.4.1 The physical model 117

5.4.2 Governing equations 118

5.4.3 Shrinkage tracking 122

5.4.4 The boundary conditions 123

5.4.5 Numerical procedures 125

5.4.6 Material properties and input parameters 126

5.4.7 Results and discussion 127

5.5 Summary for the chapter 135

Chapter 6. Thermoelectric Energy Harvesting for Through-Wall Wireless Communication in the Nuclear Environment 136

6.1 Chapter introduction 136

6.2 Energy harvesting for nuclear waste monitoring 137

6.3 Thermal and fluid dynamic analysis of the dry cask system 138

6.3.1 SCALE decay heat calculation 139

6.3.2 Conceptual principles 141

6.3.3 Mathematical model 143

6.3.4 Decay heat in the fuel assembly 146

6.3.5 Material Properties and Boundary Conditions 147

6.3.6 Discussion about the CFD simulation results 156

6.4 Energy harvester design to harvest gamma radiation energy 158

6.4.1 Problem formulation 158

6.4.2 Energy demand for sensing and communicating system powering 160

6.4.3 Energy sources available 161

6.4.4 Gamma heat deposited in the tungsten plate 163

6.4.5 The design of the gamma-heating energy harvester 165

6.5 Energy harvester design for harvesting existing temperature gradient 169

6.5.1 The design of the temperature-gradient energy harvester 169

6.5.2 Fin number optimization 171

6.5.3 Simulate the heat transfer performance of the high-pressure helium using hydraulic mineral oil 173

6.5.4 Simulation results 176

6.5.5 Experiment to test the energy harvester 178

6.6 The impacts of gamma radiation on the performance of the thermoelectric material ... 181
  6.6.1 Potential effects caused by the gamma radiation ... 181
  6.6.2 The radiation experiment setup ... 182
  6.6.3 The impacts of gamma radiation on the thermoelectric materials ... 183
  6.6.4 Uncertainty analysis of the measurements ... 185
6.7 Radiation and thermal shielding for the electronics and energy harvesters ... 188
  6.7.1 Radiation shielding material ... 188
  6.7.2 Gamma and neutron shielding in the canister ... 190
  6.7.3 The thermal and radiation block design for the electronics ... 192
  6.7.4 Summary for the chapter ... 194
Chapter 7. Thermoelectric Energy Harvesting for the Gas Turbine Sensing and Monitoring System ... 196
7.1 Chapter introduction ... 196
7.2 Sensors working in the gas turbine ... 197
7.3 Thermoelectric energy harvester design ... 198
  7.3.1 Experimental setup ... 198
  7.3.2 A numerical model for the energy harvester ... 199
7.4 The Performance of the thermoelectric energy harvester ... 204
7.5 Summary for the chapter ... 208
Chapter 8. Conclusion and Future work ... 209
8.1 Conclusions ... 209
8.2 Future work ... 211
References ... 216
Appendix A ... 226
Publications ... 235

List of figures

Figure 1.1. Carriers drift caused by temperature gradient 3

Figure 1.2. Heat transfer processes in the TEGs.. 5

Figure 1.3. The efficiency of some typical electricity generation technologies 6

Figure 1.4. (a) A MSL curiosity powered by the MMRTG. Photo courtesy of NASA/JPL-Caltech [8]. (b) A MMRTG designed by JPL-Caltech [8]. 7

Figure 1.5. (a) Vehicle exhaust energy harvesting system. (b) Rectangular shaped heat exchanger for thermoelectric energy harvesting [12]. 8

Figure 1.6. (a) Schematic diagram of the flow and flame stabilization in micro-combustor along with thermoelectric modules attached to heating cup [13]. (b) Integration of thermoelectric modules and heat sinks with the micro-combustor [13]. 8

Figure 1.7. A wristwatch powered by thermoelectrics [17]... 9

Figure 1.8. Flexible thermoelectric generator for wearable biometric sensors [18] 10

Figure 1.9. (a) Illustration of thermoelectric textiles utilizing a zigzag stitch. Red and blue yarns contained polymer nanofibers coated with n and p-type thermoelectric materials, respectively. (b) Photographs of realized thermoelectric textiles [19]..... 10

Figure 1.10. Thermoelectric energy harvesting to power the wireless communication system for the SMR reactor component [31] 11

Figure 1.11. Gamma radiation test of the thermoelectric energy harvester and electronics in Westinghouse [23]. 12

Figure 1.12. Thermoelectric energy harvester works in dual functions, both as an energy source and a flow meter sensor 13

Figure 1.13. The current-of-state thermoelectric materials and their figure-of-merit ZT as a function of temperature and year.[48].. 15

Figure 1.14. Atomic structures of (a) the unit-cell of Bi2Te3 [53] and (b) Bi2Te3 with a 60° twin boundary [54]. The dotted black line indicates the 60° twin boundary. 16

Figure 1.15. (a) Unit cell of skutterudites consisting of eight small cubes [64]; (b) unfilled skutterudites [65]; (c) filled skutterudites [66]. 18

Figure 1.16. (a) Atom structure of magnesium silicide [69]; (b) The comparison of reservation, cost, and toxicity between different elements [70]. 19

Figure 1.17. (a) The $Ba_8Ga_{16}Ge_{30}$ thermoelectric material with the Ba guest atoms inside Ga/Ge cages. (b) The vibration motion of the cage structure [71]. 19
Figure 1.18. The atomic structure of a typical Half-Heusler material 21
Figure 1.19. (a) Crystal structure along the a axis: grey, Sn atoms; red, Se atoms. (b) Highly distorted SnSe7 coordination polyhedron with three short and four long Sn–Se bonds. (c) Structure along the b axis. (d) Structure along the c axis. (e) ZT values along different axial directions [75]... 22
Figure 1.20. All-length-scale hierarchy in thermoelectric materials. (a) Maximum achievable ZT values for the respective length scales. (b) ZT as a function of temperature for an ingot of PbTe with different doping strategies [78]. 23
Figure 1.21. The conventional method to fabricate TEG module [79]............................ 24
Figure 1.22. Molecular beam epitaxy [84].. 25
Figure 1.23. The conventional method to fabricate the TEG module 26
Figure 1.24. Thermoelectric material fabrication using thermal spay [79]. 27
Figure 1.25. A X-ray Diffraction machine from Siemens 28
Figure 1.26. Thermal conductivity measurement using the laser flash method 30
Figure 1.27. 3ω-method for thermal conductivity measurement [89].............................. 31
Figure 1.28. Four-probe method for electrical conductivity measurement [79] 31
Figure 1.29. Van der Pauw method 32
Figure 1.30. Measure the Seebeck coefficient using ZEM-3 series [91]......................... 33
Figure 1.31. Seebeck measurement in the vacuum chamber [79] 34
Figure 1.32. The variations of electrical conductivity, electronic thermal conductivity, Seebeck coefficient, and ZT with carrier concentration 43
Figure 1.33. The accumulated lattice thermal conductivity of phonons [46]. 44
Figure 1.34. Phonon dispersion relation along and perpendicular to the super-lattice plane; Acoustic phonon in bulk Si [92]. 45
Figure 1.35. The energy density of states in (a) bulk, (b) quantum well, (c) quantum wire, and (d) quantum dot. 46
Figure 1.36. Scattering carriers with low energy to enhance Seebeck coefficient [46].... 47
Figure 2.1. Schematic diagram of (a) TEG model; (b) Thermal network in the TEG...... 53

Figure 2.2. The performance modeling of a couple of thermo-elements: (a) Power output of device vs load resistance; (b) Efficiency of device vs electrical current; (c) Power output vs electrical current for $Th = 150$ °C, $Tc = 50$ °C. 60

Figure 2.3. Modeling of TEG system based on commercial HZ-2 TEG module: (a) Effective temperature varied with load electrical resistance factor; (b) Current varied with load electrical resistance factor; (c) Power varied with load electrical resistance factor; (d) Efficiency varied with load electrical resistance factor. 66

Figure 3.1. Innovative heat exchanger design that could increase the heat transfer [110] 70

Figure 3.2. (a) The angled fluidic oscillator, (b) The curved fluidic oscillator, (c) The direct jet. 74

Figure 3.3. Different turbulence models used in different regions in the fluidic oscillators 77

Figure 3.4. The grid systems for (a) the angled design and (b) the curved design. 78

Figure 3.5. Boundary conditions for the modeling 79

Figure 3.6. (a)-(d) Instantaneous pressure contours and (e)-(h) flow patterns of the curved fluidic oscillator for one oscillation cycle when Re=5,000 (T is the period). 81

Figure 3.7. (a)-(d) Instantaneous pressure contours and (e)-(h) flow patterns of the angled fluidic oscillator for one oscillation cycle when Re=5,000 (T is the period). 81

Figure 3.8. The oscillatory frequency of the curved and angled designs at Re=3,000, 4,000, and 5,000. 82

Figure 3.9. (a)-(d) Instantaneous temperature contours of curved design using $k - \omega$ SST model. (e)-(h) Instantaneous temperature contours of curved design using ELES model. (i)-(l) Instantaneous temperature contours of angled design using ELES model. 84

Figure 3.10. (a)-(c) Time-averaged Nu number contours on the impingement surface for the three designs at Re=5000 using ELES model, (d)-(f) Time-averaged Nu number contours on the impingement surface for the three designs at Re=3000 using ELES model. 85

Figure 3.11. Time-averaged surface Nu distribution for the sweeping jet on the channel centerline at Re = 3000, 4000, and 5000 for the curved design 86

Figure 3.12. Time-averaged surface Nu distribution for the sweeping jet on the channel centerline at Re = 3000, 4000, and 5000 for the angled design 86

Figure 3.13. Time-averaged surface Nu distribution for the jet on the channel centerline at Re = 3000, 4000, and 5000 for the direct jet design 87

Figure 4.1. (a) Segmented TEG using different TE materials to achieve the highest averaged ZT value in a broad temperature range; (b) A segmented TEG design using these materials for high device efficiency. 92

Figure 4.2. Mathematical segments of a single thermo-element. The direction of positive variables was shown relative to the hot- and cold-ends... 95

Figure 4.3. The procedures of the TEG geometry optimization method 99

Figure 4.4. Variation of ZT values with temperature for (a) N- and (b) P-type thermoelectric materials... 101

Figure 4.5. Variation of u and s with temperature for the segmented TEG.................... 102

Figure 4.6. Variation of ηr_Max and ηr with temperature for the segmented TEG...... 102

Figure 4.7. Variations of (a) the cross-sectional areas, (b) accumulated lengths and (c) efficiencies (from the hot ends) with temperature for P- and N-type thermo-elements 105

Figure 4.8. (a-b) Variations of the cross-sectional areas with the accumulated lengths for P- and N-type thermo-elements 106

Figure 4.9. Depositing TEG device directly on industrial components using SLM....... 107

Figure 5.1. TEG for vehicle exhaust energy harvesting 110

Figure 5.2. (a) The SLM equipment and (b) fabrication process................................... 115

Figure 5.3. (a) SLM manufacturing of multi-component thermoelectric powders with nanoparticles embedded. (b) Four distinct regions in the powder bed for the first scanning trace... 118

Figure 5.4. The shrinkage phenomenon in the powder bed during the SLM process: (a) Stage One, (b) Stage Two, (c) Stage Three, (d) Stage Four. 122

Figure 5.5. The boundaries of the computation domain 124

Figure 5.6. The numerical scheme for SLM simulation 126

Figure 5.7. The comparison of the simulated and measured fusion boundaries for SLM of the 6063 aluminum sheet. 129

Figure 5.8. The shrinkages of the powder bed during the SLM process. P=18.75 W, R=0.3 mm, (a1) V= 0.02m/s; (b1) V= 0.04 m/s; (c1) V= 0.06 m/s; P=25 W, R=0.3 mm, (a2) V= 0.02 m/s; (b2) V= 0.04 m/s; (c2) V= 0.06 m/s. 130
Figure 5.9. The temperature profiles during the SLM process. P=18.75 W, R=0.3 mm, (a1) V= 0.02m/s; (b1) V= 0.04 m/s; (c1) V= 0.06 m/s; P=25 W, R=0.3 mm, (a2) V= 0.02 m/s; (b2) V= 0.04 m/s; (c2) V= 0.06 m/s. 131
Figure 5.10. The melting pool size during the SLM process. P=18.75 W, R=0.3 mm, (a1) V= 0.02m/s; (b1) V= 0.04 m/s; (c1) V= 0.06 m/s; P=25 W, R=0.3 mm, (a2) V= 0.02 m/s; (b2) V= 0.04 m/s; (c2) V= 0.06 m/s. 132
Figure 5.11. The velocity vector in the melting pool. P=18.75 W, R=0.3 mm, (a1) V= 0.02m/s; (b1) V= 0.04 m/s; (c1) V= 0.06 m/s; P=25 W, R=0.3 mm, (a2) V= 0.02 m/s; (b2) V= 0.04 m/s; (c2) V= 0.06 m/s. 133
Figure 5.12. The Si nanoparticles concentration ratio distribution near the melting pool. P=18.75 W, R=0.3 mm, (a1) V= 0.02m/s; (b1) V= 0.04 m/s; (c1) V= 0.06 m/s; P=25 W, R=0.3 mm, (a2) V= 0.02 m/s; (b2) V= 0.04 m/s; (c2) V= 0.06 m/s. 134
Figure 6.1. Depiction of dry cask storage where (a) nuclear waste storage at the at sites where it is generated [182] is shown along with (b) a cutaway of the dry storage canister [183]. 137
Figure 6.2. Model of the Holtec International dry cask canister. 142
Figure 6.3. Holtec International dry cask canister: (a) Internal structure of the dry cask system; (b) the grid system. 145
Figure 6.4. The load heat distribution in the fuel assembly: (a) Load heat profile in the radial direction; (b) Load heat profile in the axial direction of the fuel assembly [192]. 146
Figure 6.5. The in-plane thermal conductivity and the axial conductivity of the fuel region with a filling gas of helium. 147
Figure 6.6. The temperature profiles in the canister at years five after the fuel removed from the reactor using the transitional SST k-ω turbulence model. 150
Figure 6.7. The temperature profiles in the canister at years 55 after the fuel removed from the reactor using the transitional SST k-ω turbulence model. 151
Figure 6.8. The radial temperature profile at Z=3.19 m at the symmetry surface 152

Figure 6.9. The temperature profile along the outer surface of the canister. 152
Figure 6.10. The temperature profile along the outer surface of the canister. 153
Figure 6.11. The radial flow velocity profile at Z=3.19 m in the symmetry surface...... 154
Figure 6.12. (a) The flow temperature at the outlet of the air channel; (b) The flow rate at the outlet of the air channel.. 155
Figure 6.13. The temperature profile along the outer surface of the canister. 156
Figure 6.14. (a) The enclosed metal wall and thick concrete protection in nuclear reactors [199] and (b) spent fuel stored in the dry casks. 158
Figure 6.15. Energy harvesting for sensing and communicating system powering 159
Figure 6.16. (a) The temperature and flow velocity profiles near the canister wall for years 5 and 55 (50 years of storage in the canister) [207]; (b) The temperature and flow velocity (4 cm away from the canister wall) variations with time. 162
Figure 6.17. Gamma heating calculation: (a) gamma radiation deposited in tungsten; (b) a quarter model for gamma heating calculation using MNCP6. 164
Figure 6.18 Energy deposited in the tungsten plates at the top and side of the MPC canister for 50 years of dry cask storage... 165
Figure 6.19. Gamma heating energy harvester design... 166
Figure 6.20. The performance of the gamma heating energy harvester: (a) temperature contour of the energy harvester; (b) temperature profile of the TEGs; (c) electrical potential profile of the TEGs 168
Figure 6.21. The voltage and power output of the gamma heating energy harvester during 50-years operation.. 168
Figure 6.22. Thermal energy harvester design... 170
Figure 6.23. The geometry configuration of a heat sink.. 171
Figure 6.24. Optimization of fin number for a finned surface placed in the convective helium flow near the MPC wall. 172
Figure 6.25. Flow pattern in the fin channel.. 174
Figure 6.26. Heat transfer performance of different fluids: (a) local heat transfer coefficients when $u = 0.15\ m/s$ and (b) averaged heat transfer coefficients varying with the flow velocity. 176

Figure 6.27. Simulation of the performance of the thermal energy harvester in hydraulic mineral oil at $u = 0.0143\ m/s$ for year 55 case: (a) Fluid velocity contours; (b) Temperature profile in TEG; and (c) Electrical potential profile in TEG. 176
Figure 6.28. The performance test of the energy harvester: (a) The overall experimental setup in the lab, (b) The energy harvester, and (c) the oil channel to simulate the helium environment. 178
Figure 6.29. The experimental results for the thermal energy harvester in hydraulic mineral oil: (a) The hot- and cold- end temperatures of TEG, and flow temperature, (b) The open circuit voltage output. 180
Figure 6.30. Thermoelectric material radiation test setup 182
Figure 6.31. (a) Temperature profile of the source; (b) The open circuit voltage output of the TEG module. 183
Figure 6.32. The comparison of (a) Seebeck coefficient, (b) electrical resistivity, and (c) thermal diffusivity of the Bi_2Te_3 sample before and after gamma radiation 184
Figure 6.33. The temperature uniformity on each cross-section of the thermo-element when radiation emissivity is 0.8. 187
Figure 6.34. The penetration ability for different radiation particles [218]. 188
Figure 6.35. MNCP6 model to test the radiation shielding performance. 191
Figure 6.36. The accumulated gamma dose in the electronics vs time. 191
Figure 6.37. Radiation and thermal shielding block 192
Figure 6.38. Temperature contours in the thermal and radiation shielding block. 193
Figure 7.1. The concept of using TEG to power the sensing and monitoring system in the gas turbine: (a) a typical gas turbine used for power generation; (b) self-powered temperature, pressure, and gas sensors embedded in the gas turbine. 196
Figure 7.2 (a) TEG energy harvester prototype; (b) Experimental setup 198
Figure 7.3. (a) Thermal network in the energy harvester; (b) Segmented thermo-element. 199
Figure 7.4. Properties of the P, N-type thermoelectric materials varying with temperature [222]: (a)Thermal conductivity; (b) Electrical resistivity; (c) Seebeck coefficient; (d) ZT. 203
Figure 7.5. The iteration scheme for the TEG model 203

Figure 7.6. The comparison of the experimental and modeling results: (a) Voltage output and (b) Power output of the thermoelectric energy harvester prototype. 204

Figure 7.7. T_C and T_{sink} change versus the source temperature...................................... 205

Figure 7.8. The efficiency of the TEG module.. 206

Figure 7.9 (a) The calculated temperature profiles in the thermo-elements; (b) Heat fluxes through the thermo-elements with RL=1.5 Ω.. 207

Figure 8.1. (a) A high performance heat sink design; (b) membrane surface chemistry; (c) fluidic oscillator. 213

Figure 8.2. The atomic structure of Mg_2Si 214

Figure 8.3. Big data analysis to find a general turbulence model by related the Reynolds/SGS stress to multiple parameters of the mean/resolved flows............. 215

List of tables

Table 1.1. Phonon scattering factors in different situations 39

Table 2.1. Cases to exam the models 66

Table 3.1. The main geometry parameters of the fluid oscillators 75

Table 3.2 Boundary conditions 79

Table 3.3. The average temperature difference and Nu number on the impingement surface covered by the jet (6.5×1.5 mm^2) 85

Table 3.4. The stagnation Nu numbers for the direct jets with different Re numbers 88

Table 5.1. The physical properties of the mixed powders and SLM operation conditions 127

Table 5.2. The physical properties of nonporous 6063 aluminum powders and melted aluminum [175] 128

Table 6.1. Decay heat, gamma intensity, and neutron intensity from the 15 MTUs of spent fuel for 50 years of dry cask storage. 140

Table 6.2. The main dimensions of the Holtec HI-STORM 100 overpack and MPC-32 canister 141

Table 6.3. Thermal physical properties of the helium and air 148

Table 6.4. Boundary conditions for the CFD simulation 149

Table 6.5. The comparison between different through wall wireless communication technologies 160

Table 6.6. Material properties 167

Table 6.7. The thermal properties of different fluids 173

Table 6.8. The coefficients for Eq. (6-21) [215] 175

Table 6.9. The simulation results for different year cases 177

Table 6.10. Summary of the experimental results 180

Table 6.11. The electrical resistivity uncertainty sources 180

Table 6.12. The electrical resistivity uncertainty sources [217] 186

Table 6.13. The Seebeck coefficient measurement uncertainty sources [217] 186

Table 6.14. Constituent Element Weight Percentages and Theoretical Densities of the W-B_4C Composite Materials 190

Table 6.15. The thermal conductivity and thickness of each layer 192

Nomenclature

Symbols

$A_P, A_N, A_g, A_{CH}, A_{CC}$	Cross-section areas of P, N-type thermo-elements, filling gas, hot and cold end ceramic covers, m^2
A	Van Driest constant, in Chapter 3
$a_E, a_W, a_N, a_S, a_F, a_B, a_P$	TVD coefficients
B	Deformation parameter of the particle
c_p	Thermal capacity, $J \cdot kg^{-1} \cdot K^{-1}$
C_{SGS}	Factors in the LES model
C_s	Nano-particle concentration ratio in solid and liquid
C^+	Effective concentration ratio
d	Nozzle diameter, *mm*
$D,\ D_f$	Characteristic length, m
D	Specific diffusion coefficient, $kg/(m \cdot s)$, in chapter five
D^+	Effective diffusive coefficient, $kg/(m \cdot s)$
$D_e, D_w, D_n, D_s, D_f, D_b$	Diffusion conductance, $kg/(m^2 \cdot s)$
E	Electric field intensity, $V \cdot m^{-1}$
f_h, f_c	Hot and cold end TEG module thermal conductance factor
$F_e, F_w, F_n, F_s, F_f, F_b$	Convective mass flux, $kg/(m^2 \cdot s)$
f_s, f_l	Solid and liquid mass faction
g	Gravity acceleration, m/s^2
H, h	Enthalpy, J/kg
h_c	Convective heat transfer coefficient, $W/(m^2K)$
I	Electrical current, A
J	Current density, $A \cdot m^{-2}$
$K_P, K_N, K_g, K_{CH}, K_{CC}$	Thermal conductance of P, N-type thermo-elements, thermal conductance of a thermocouple, thermal conductance of hot and cold end ceramic covers, $W \cdot K^{-1}$
$K_P^*, K_N^*, R_P^*, R_N^*$	Reduced thermal conductance, reduced electrical resistance

K_H, K_C, K_{CH}, K_{CC}, K_{CCH}, K_{CCC}	Thermal conductance of the hot and cold end ceramic covers, hot end and cold end ceramic cover thermal conductance, hot and cold end contact layer thermal conductance, $W \cdot K^{-1}$
K_{SH}, K_{SC}	Hot and cold end heat sink/exchanger thermal conductance, $W \cdot K^{-1}$
k	Turbulence kinetic energy (J/kg) or equilibrium partition ratio in Chapter 5
k^+	Effective thermal conductivity, W/mK
K_0	Permeability coefficient
k_s, k_l	Solid and liquid thermal conductivity, $W/(m \cdot K)$
k_p, k_g	Powder and gas thermal conductivity, $W/(m \cdot K)$
k_R	Thermal conductivity part of the powder bed owing to radiation, $W/(m \cdot K)$
l	Nozzle height, mm
L_P, L_N	Leg length of P, N-type thermo-pellets, m
L_{ij}	Germano identity
L	Latent heat, J/kg, in Chapter 5
M_{ij}	Intermediate parameter
Nu	Nusselt number
P	Power output, W
p	Pressure, Pa
q, q_h, q_c	Total heat flow, hot end heat absorption and cold end heat absorption, W
q_0	Laser intensity, W/m^2, in Chapter 5
Q	Heat flow, $W \cdot m^{-2}$
q'	Heat flux, $W \cdot m^{-2}$
R_P, R_N, R_{PN}	Electrical resistance of P, N-type thermoelectric materials, electrical resistance of a thermocouple, Ω

R_{ch}, R_{cc}, R_c	Electrical contact resistance at the hot and cold ends of thermo-pellets, total electrical contact resistance, Ω
R_G, R_L	Internal resistance of TEG, load electrical resistance, Ω
r	Ratio of gradients, in Chapter 5
R	Laser diameter, m, in Chapter 5
s, r_c, r_{cc}, r_{ch}	Electrical load resistance factor, total contact layer electrical resistance factor, hot and cold end electrical contact resistance factors
s	Compatibility factor, V^{-1}, in Chapter 3
s	Shrinkage, m, in Chapter 5
S_i	Energy source terms, $W \cdot s^{-1}$
S_{ij}	Mean rate of deformation, s^{-1}
S_h	Energy source term, W/m^3
S_u^{DC}	The deferred correction source term
S_C	Nano-particle concentration source term, m^{-3}
$\Delta T, T_h, T_c$	Temperature difference, hot and cold end temperatures of thermo-pellets, K
T_H, T_C	Hot and cold temperatures of TEG module, K
T	Temperature, K
T^+	Dimensionless temperature
t	Time, s
T_f	Oscillating period, s
T_M	Melting temperature, K
ΔT	Temperature difference, K
T_0	Reference temperature, K
T_a	Ambient temperature, K
u, v, w, θ	Non-dimensional factors, in Chapter 2
u	Reduced current, V^{-1}, in Chapter 3
u_i	Velocity, $m \cdot s^{-1}$
U_0	Inlet velocity, $m \cdot s^{-1}$

u_b	Laser beaming moving speed, m/s
u, v, w	Velocity in x, y, and z directions, m/s, in Chapter 5
v_s, v_n	Velocity parallel and perpendicular to the surface, m/s
w	Turbulence frequency, s^{-1}
w_s	Velocity caused by powder shrinkage, m/s
x, y, z	Coordinates, m
x_R	Effective length for radiation between particles, *m*
y^+	Dimensionless wall distance
Z, Z_{PN}	Thermoelectric figure-of-merit of material
z	Distance between nozzle outlet and the heating surface, *mm*
Greek Symbols	
$\alpha, \alpha_P, \alpha_N, \alpha_{PN}$	Seebeck coefficient, Seebeck coefficients of P, N-type thermoelectric materials, Seebeck coefficient difference of P, N-type thermoelectric materials, V/K,
β_T	Thermal expansion coefficient, K^{-1}
β_s	Solid expansion coefficient, K^{-1}
δ_{ij}	Kronecker delta
ε_b	Emissivity
ε	Porosity, in Chapter 5
η, η_C, γ	Efficiency, Carnot efficiency, and reduced efficiency
θ	Energy absorption coefficient, in Chapter 5
κ	Thermal conductivity, $W \cdot K^{-1} \cdot m^{-1}$
κ	A constant, in Chapter 3
$\lambda_P, \lambda_N, \lambda_g, \lambda_{CH}, \lambda_{CC}$	Thermal conductivities of P, N-type thermoelectric materials, filling gas, hot end ceramic cover and cold end ceramic covers, $W \cdot K^{-1} \cdot m^{-1}$
λ	Thermal conductivity, $W \cdot K^{-1} \cdot m^{-2}$
μ	Dynamic viscosity, $kg \cdot m^{-1} \cdot s^{-1}$
μ^+	Effective viscosity, $kg/(m \cdot s)$
μ_l	Liquid viscosity, $kg/(m \cdot s)$

μ_s	Solid viscosity, $kg/(m \cdot s)$
μ_t	Eddy viscosity, $kg \cdot m^{-1} \cdot s^{-1}$
ρ_P, ρ_N	Electrical resistivity of P, N-type thermoelectric materials, $\Omega \cdot m$
ρ	Density, $kg \cdot m^{-3}$
σ, σ_b	Stefan-Boltzmann constant, $W \cdot m^{-2} \cdot K^{-4}$
σ_k, β^*, $\sigma_{\omega,2}$, γ_2, β_2	Factors in the k-w SST turbulence model
σ_T, σ_L	Turbulence Prandtl number, molecular Prandtl number
$\sigma_{\omega,1}$	Turbulence frequency Prandtl number
$\partial\sigma/\partial T$	Change rate of surface tension, $N/(m \cdot K)$
σ_s	Surface tension, N/m
τ_P, τ_N, τ_{PN}	Thomson coefficients of P, N-type thermoelectric materials, Thomson coefficient difference of P, N-type thermoelectric materials, V/K
τ_{ij} , T_{ij}	Reynolds stresses, $kg \cdot m^{-1} \cdot s^{-2}$
φ	The concentration radio
ψ	Limiter function
ϕ	Variable to be solved; flattened surface fraction of particle in contact with another particle, in chapter 5
Δ_1, Δ_2	Filtering length, m
Abbreviations	
AM	Additive manufacture
CFD	Computational fluid dynamics
CFL	Courant–Friedrichs–Lewy condition
ELES	Embedded large eddy simulation
FGTM	Functional graded thermoelectric material
LES	Large eddy simulation
RANS	Reynolds-averaged Navier-Stokes
RTG	Radioisotope thermoelectric generator
SGS	Sub-grid-scale stresses

SST	Shear stress transport
SIMPLE	Semi-implicit method for pressure linked equations
SPS	Spark plasma sintering
SLS/SLM	Selective laser sintering/melting
TEG	Thermoelectric generator

Chapter 1. Introduction and Background

1.1 A brief history of thermoelectrics

The thermoelectric generator (TEG) is a solid-state device which converts thermal energy into electricity based on Seebeck effect and Peltier effect without any moving parts. When there exists a temperature difference between the hot and cold ends of the thermoelectric materials, the charge carriers (electrons, e^-, in n-type materials and holes, h^+, in p-type materials) at the hot side moves to the cold side, building an electrostatic potential in the material. The Seebeck Effect was first discovered in metal in 1821, when Thomas Johann Seebeck, a German scientist, found that a compass needle defected when the joint of two conductors was heated. But the effect did not arouse much attention because the Seebeck coefficient of metal was very small (typically less than 10 μV/K). With the discovery of semiconductors and their alloys with high Seebeck in 1950s, the new potential of thermoelectric technology refocused people's attention. The classical thermoelectric materials, including Bi_2Te_3 and its alloys with Bi_2Se_3/Sb_2Te_3 working in low temperature ranges, PbTe and its alloys with PbSe/SnTe in medium temperature ranges, and SiGe alloys in high temperature ranges, all have Seebeck coefficients of more than 200 μV/K, making it possible to develop generators or coolers based on these thermoelectric materials. Thermoelectric energy conversion has many advantages over other conventional energy harvesting technologies due to quietness, small size, cleanliness, high energy density, long lifecycle, and simplicity. TEGs are currently widely used in applications ranging from power generators in space missions [1] to common thermocouple sensors, from small energy harvesters for self-powered sensors to large scale waste energy recovery [2]. The TEGs can be integrated directly onto many key industrial components, including pipes, pump housings, heat exchangers, reactor vessels, boiler bodies, distillation columns, shielding structures, and other components, acting as reliable energy sources to power sensors, actuators, energy management circuits, and communications equipment.

The thermoelectric energy harvesting technology has received intensive attention in the past two decades years as the efficiency of the devices has been greatly increased thanks to the impressive progress in the nanomaterials and thermal design technology since the 1990s [3]. According to newest research, a ZT of 3.5 was reported by Harman *et al.* [4] in

Bi-doped n-type PbSeTe/PbTe quantum-dot super-lattice, and the corresponding energy conversion efficiency was expected to reach 20%. Another work done by Venkatasubramania *et al*. [5] reported a thin-film Bi_2Te_3/Sb_2Te_3 super-lattice device with a ZT value as high as 2.4. All these progresses significantly extended the potential application range of the devices. There was no evidence showed that there were physical limitations for the ZT value. Mahan and Sofo [6] thought that ZT=14 were achievable in rare-earth compounds. However, an inconvenient truth about thermoelectric is that, until now, the conversion efficiency of TEG is still less than the mechanical thermal engines [7]. For the moment, the practical and economic applications of this technology are still limited in relatively small scale and decentralized energy harvesting.

Overall, the development of thermoelectrics can be divided into four stages. The important events in the development of thermoelectrics in history are listed as follows:

1. Discover of thermoelectric effects
    a. 1821, Thomas Johann Seebeck, Seebeck effect (S)
    b. 1833, Jean Charles Athanase Peltier, Peltier effect (Π)
    c. 1838, Heinrich Lenz, Lenz explains
2. Thermodynamics exploration
    a. 1850's, Lord Kelvin, the interrelation between $S\ and\ \Pi$
    b. 1885, Lord Rayleigh, power generation concept
    c. 1911, Edmund Altenkirch, Figure of Merit (ZT)
3. Modern period
    a. 1930's, the discovery of semiconductors
    b. 1947, Maria Telkes, a 5% TEG generator
    c. 1949, Abram Fedorovich Ioffe, theory of semiconductor thermoelectrics
    d. 1953, Julian Goldsmid, the first thermoelectric refrigerator
    e. 1956, Abram Fedorovich Ioffe, alloying
    f. 1970's, space application
4. Reassessment
    a. 1993, Mildred Dresselhaus, low dimensional thermoelectric materials
    b. Will the ZT>>1 in the future?

1.2 The working principle of thermoelectric generators

The term "thermoelectric effect" encompasses three separately identified effects: the Seebeck effect, Peltier effect, and Thomson effect. The three effects are interrelated as explained in the follows.

Seebeck effect

Figure 1.1 shows the schematic particles-transport picture in the thermoelectric materials. The carriers, including electrons and holes, are free to move and carry charge as well as energy. When there exists a temperature gradient in the materials, the carriers drift from the hot end to the cold end. The build-up of charge carriers results in a net charge, producing an electrostatic potential within the material. The equilibrium state is reached until a balance is achieved between the chemical potential for diffusion and the electrostatic repulsion due to the build-up of charge. This is the so-called Seebeck effect, the basis for thermoelectrics.

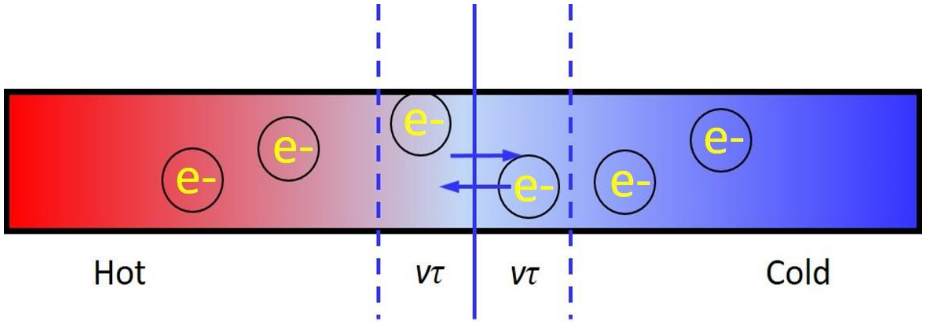

Figure 1.1. Carriers drift caused by temperature gradient

Assuming that the carrier velocity is v_x in the x-direction at a specific surface, a simple kinetic theory calculation gives the velocity driven by the chemical potential for diffusion as

$$v_\theta = \frac{1}{2}(v_x)|_{x-v_x\tau} - \frac{1}{2}(v_x)|_{x+v_x\tau} = -v_x\tau\frac{d(v_x)}{dx} = \tau\frac{d\left(v_x^2/2\right)}{dx} \tag{1.1}$$

On the other hand, the velocity driven by the electrostatic repulsion due to the build-up of charge is

$$v_E = -\frac{eV\tau}{m} \tag{1.2}$$

When these two effects achieve a balance,

$$v_\theta + v_E = 0 \tag{1.3}$$

Then the built electrical potential equals to

$$V = -\frac{C_v}{3ne}\nabla T \tag{1.4}$$

where $\alpha = -\frac{C_v}{3ne}$ is the Seebeck coefficient.

This kinetic model is not accurate, as it does not consider the quantum effect. However, the model is a good start to describe the motion of the carriers in the thermoelectric materials.

Peltier effect

The Peltier effect is the reverse effect of the Seebeck effect. When a current is made to flow through a junction between two conductors, heat may be generated or removed at the junction. The Peltier heat generated at the junction obeys this law

$$q = \pi I T \tag{1.5}$$

where π is the Peltier coefficient and I is the current. The Peltier coefficient represents how much heat is carried by per charge. Its value depends on the current direction. Thermoelectric cooling device exploits this effect to work as refrigerators.

Thomson effect

The Seebeck coefficients of the thermoelectric materials are temperature dependent, and so a spatial gradient in temperature can result in a gradient in the Seebeck coefficient. If a current is applied, then a continuous version of the Peltier effect will occur within the material. This is the so-called Thomson effect. The heat generation rate per volume due to Thomson effect can be described by

$$\dot{q} = \beta J \nabla T = T\frac{\partial \alpha}{\partial T} \cdot J \nabla T \tag{1.6}$$

where $\beta = T\frac{\partial \alpha}{\partial T}$ is the Thomson coefficient, J is the current density, and ∇T is the temperature gradient. The heat generation rate due to Thomson effect also depends on the current direction.

Figure 1.2 shows the heat transfer processes in a typical TEG. The thermal energy enters into the hot end of the TEG via conduction, convection, and radiation. A temperature difference is then built in the TEG module. Because of the thermoelectric effect, a portion of the thermal energy is converted into electricity, while the rest is dissipated into the cold source through the heat sink.

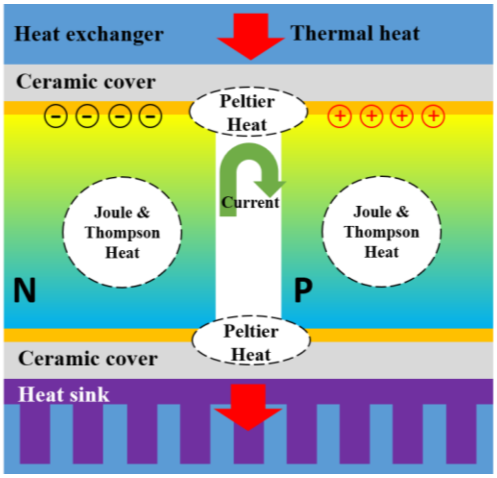

Figure 1.2. Heat transfer processes in the TEGs

1.3 Energy harvesting technologies

1.3.1 Thermoelectric energy harvesting

A typical TEG contains many thermoelectric couples consisting of n-type and p-type thermo-elements wired electrically in series and thermally in parallel. The performance of a thermoelectric material for both power generation and cooling is judged by its figure of merit (ZT):

$$ZT = \frac{\sigma\alpha^2}{k} T \tag{1.7}$$

where α is the Seebeck coefficient, σ is the electrical conductivity, T is the absolute temperature, and k is the thermal conductivity.

The efficiency of an ideal TEG is given by

$$\phi_{max} = \eta_c \gamma = \left(1 - \frac{T_c}{T_h}\right) \cdot \frac{\sqrt{1+ZT}-1}{\sqrt{1+ZT}+T_c/T_h} \tag{1.8}$$

where η_c is the Carnot efficiency, γ is the reduced efficiency, T_c and T_h are the cold and hot end temperatures, respectively. γ is always less than 1.0, which means the efficiency of TEG is less than Carnot efficiency. As shown in Figure 1.3, the efficiency of the TEG increases with the temperature difference and ZT value. To compete with other electricity generation technologies, the ZT value should be as high as 4.0. Currently, the ZT values of most bulk thermoelectric materials are around 1.0. The applications of thermoelectrics are still limited to small scale energy conversion where the cost is not the prime consideration.

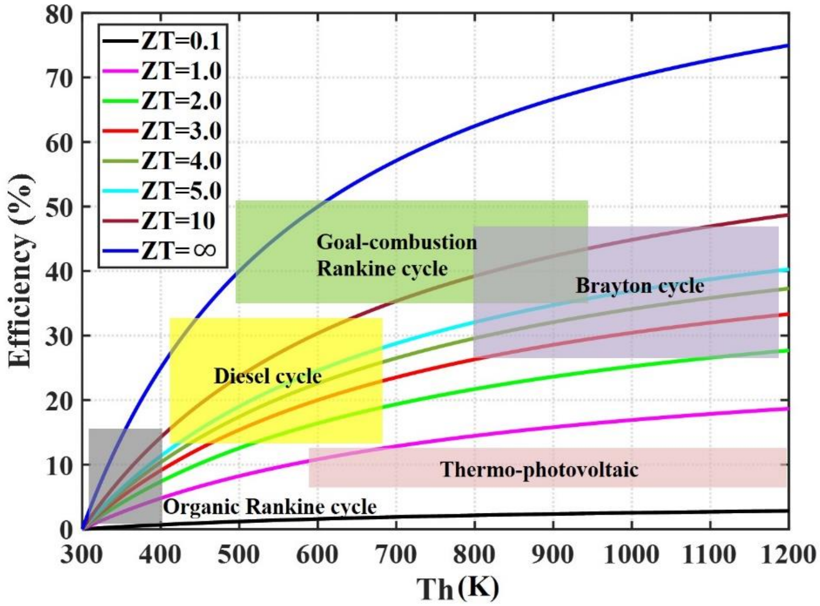

Figure 1.3. The efficiency of some typical electricity generation technologies

In the past 40 years, TEGs have been widely used to generate electrical power in various situations where the electrical grid system cannot reach. Driven by the United States' interest and involvement in the exploration of space, the radioisotope thermoelectric generators (RTGs) have been used in the deep space probes since the 1970s. These devices could supply continuous electrical energy for several years without significant decrease, particularly in cases at large distance from the Sun or beneath planetary surfaces, where low solar light intensity levels and extreme temperatures could preclude the use of solar power and chemical power generation systems. In recent years, to meet the energy demand of the National Aeronautics and Space Administration (NASA) for various space mission, for example powering the Mars Science Laboratory (MSL) Curiosity rover on Mars [8] (Figure 1.4 (a)), a multi-mission radioisotope thermoelectric generator (MMRTG) was developed and tested in Jet Propulsion Laboratory (JPL) at Caltech [9, 10], as shown in Figure 1.4(b). The general-purpose heat source (GPHS) was the package containing the plutonium dioxide fuel along the center axis of the generator. The heat source energy input can be easily scaled by adding more GPHS units. TAGS/PbSnTe was used for the P-type thermo-element and PbTe for the N-type thermo-element. A sealing and packaging system was well designed to make sure this MMRTG can supply hundreds of watts of electricity continuously for more than ten years.

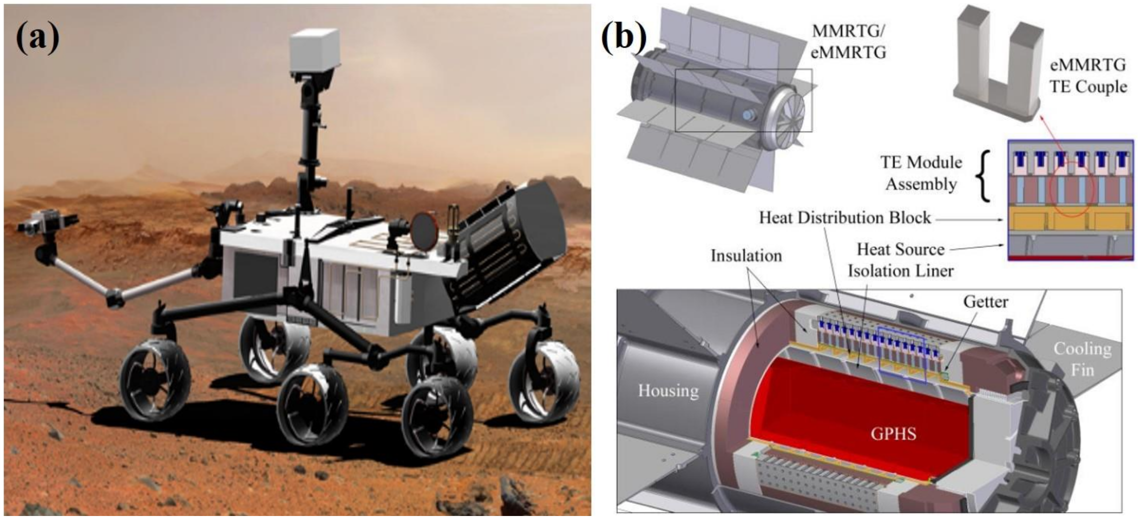

Figure 1.4. (a) A MSL curiosity powered by the MMRTG. Photo courtesy of NASA/JPL-Caltech [8]. (b) A MMRTG designed by JPL-Caltech [8].

Thermoelectric systems can harness waste heat and increase the overall energy conversion efficiency through co-generation. In a typical vehicle, about two-thirds of the fuel energy is lost as waste heat via engine exhaust gases and engine coolant. The energy recovery from the exhaust heat, typically at a temperature of 300-600 °C, has great potential to increase vehicle fuel economy, such as by reducing the load on the vehicle’s alternator or by supplying supplemental power to the electrical motor in a hybrid vehicle’s drivetrain. As a DOE report indicated, 350-390 watts of electricity recovery can provide 3 and 4% fuel efficiency improvement for a Chevy Suburban or a BMW sedan [11]. Developing high-efficiency, low-cost, reliable, workable solutions to integrate TEGs on the majority of new vehicles or retrofit into existing vehicles would represent significant fuel saving. Large multinational vehicle companies, including Ford, BMW, Renault, and Honda, had demonstrated their interests in exhaust energy recovery using TEGs [12]. A typical energy harvesting system consists of dozens of TEGs placed on the exhaust pipe surface, which was shaped as a rectangle, hexagon, etc. The cold ends of the TEGs were cooled with heat exchangers using engine coolant. An example of a rectangular shaped heat exchanger can be seen in Figure 1.5(b). An energy harvesting system built by Ford reported a maximum of approximately 400 W electricity generation with 4.6 kg of thermoelectric material [12].

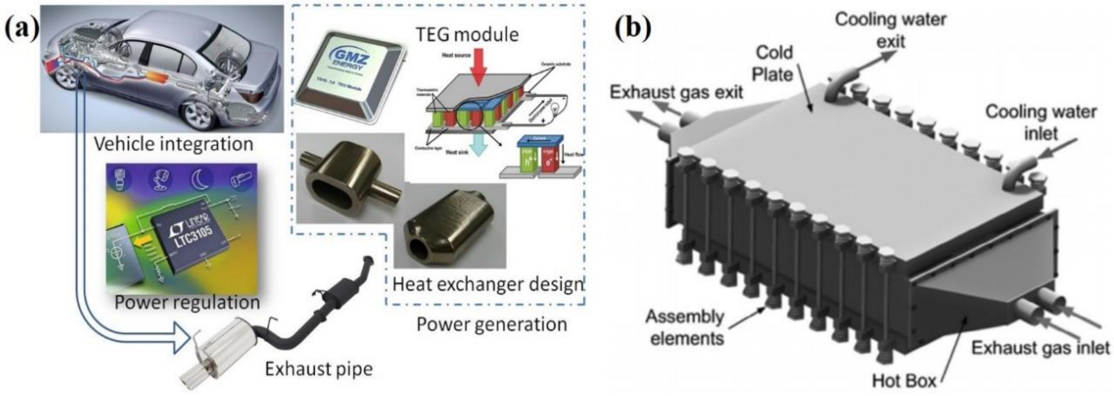

Figure 1.5. (a) Vehicle exhaust energy harvesting system. (b) Rectangular shaped heat exchanger for thermoelectric energy harvesting [12].

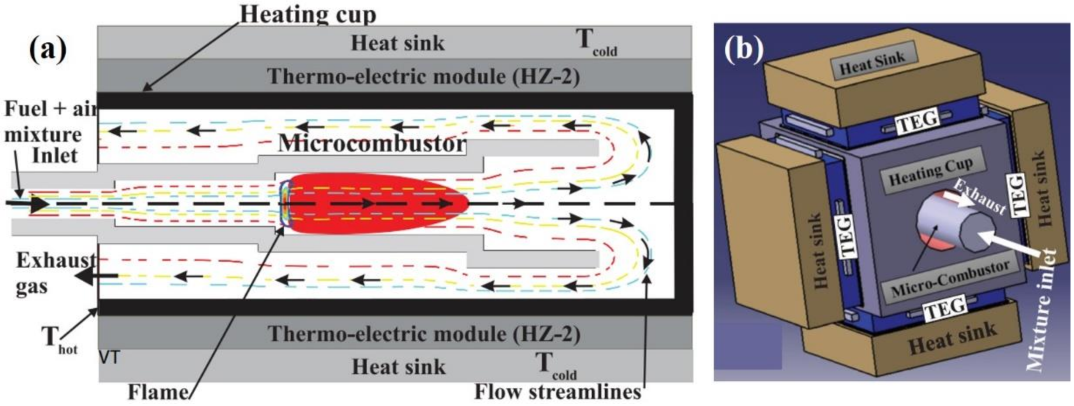

Figure 1.6. (a) Schematic diagram of the flow and flame stabilization in micro-combustor along with thermoelectric modules attached to heating cup [13]. (b) Integration of thermoelectric modules and heat sinks with the micro-combustor [13].

TEGs can be easily integrated into the existing energy system because of its scalability [14]. The microcomputers, micro-airplanes, micro-robotics, and micro-pumps can be of special interests for particular situations. To power these systems can be challengeable because of the weight and volume limit. Yadav et al. [13] established a prototype micro-TEG system based on the micro-combustion concept. The system consisted of four Bi_2Te_3 based thermoelectric modules mounted on a 0.5 cm^3 volume micro-combustor. The system delivers a maximum power of 2.35 W with a fuel (propane) flow rate of 3.98 g/h. A maximum conversion efficiency of 4.58% was achieved at a voltage of 4.34 V and a current of 0.54 A. With some small adaption, this system can work in a two-functional mode, with micro-combustor working as the propeller and micro-TEG as the electricity generator. The compact energy system using fuel with high energy density might be able to power the miniaturized airplanes.

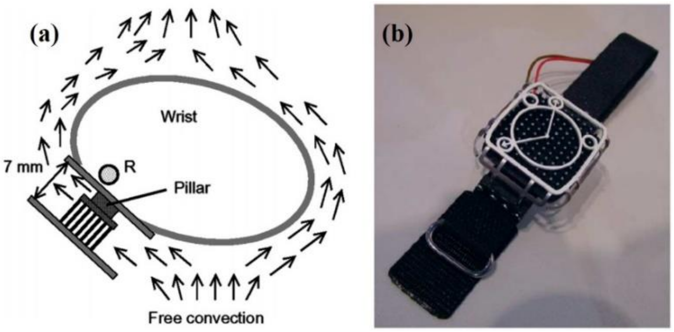

Figure 1.7. A wristwatch powered by thermoelectrics [17]

Using small TEGs to harvest mWatts energy for wearable electronics was another novel application. The first commercial wristwatch powered by the thermoelectrics was made by Seiko Instruments Inc. in 1998 [15]. However, this wristwatch was not sold well as it was too expensive and it might stop to work in hot weather. Despite this, it was still an attractive topic developing small and cost-effective thermoelectric generators scavenging energy from the environment to provide power autonomy to miniaturized and wearable electronic products operating at very low power [16]. Shown in Figure 1.7 was a thermoelectric converter developed by Leonov et al. [17], which took advantage of human warmth for energy harvesting. To solve the fitting problem, the substrate of the TEG should be flexible. The straightforward solution was to fabricate thin film TEGs using MEMS fabrication technologies [18]. By depositing a well-aligned thin thermoelectric film on a flexible substrate, the device was able to harvest nWs to mWs energy at a temperature difference of 10-40 K. Integrate the TEGs into the textile structures was another way to solving the fitting problem. Lee et al. [19] designed the woven-yarn thermoelectric textiles for electronic devices powering. By weaving yarns containing alternating n- and p-type thermoelectric segments, the thermo-elements were incorporated into textiles in a zigzag way. These textile structures acted as the electrical pathways between the n- and p-type yarns, while the wavy shape of the textile structure helped to build a temperature difference within the thermo-elements. Depending on the textile patterns, the energy output for this device varied from 0.02-0.05 W/m^2 at a temperature difference of 20 K.

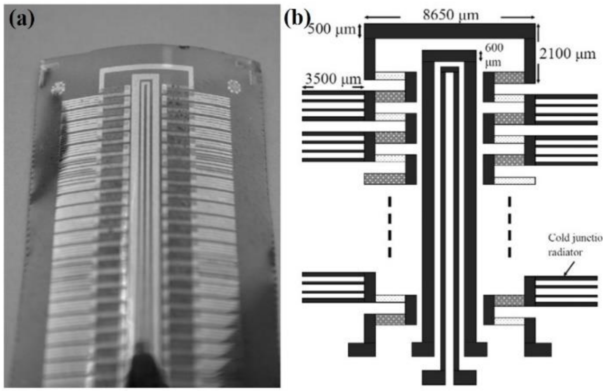

Figure 1.8. Flexible thermoelectric generator for wearable biometric sensors [18]

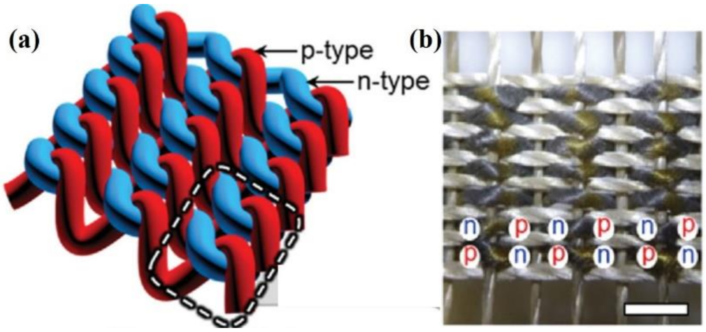

Figure 1.9. (a) Illustration of thermoelectric textiles utilizing a zigzag stitch. Red and blue yarns contained polymer nanofibers coated with n and p-type thermoelectric materials, respectively. (b) Photographs of realized thermoelectric textiles [19].

Wireless sensors are used in a wide range of civilian and defense applications to provide real-time information of critical parameters, such as temperature, position, pressure, speed, and many others [20-23]. To supply energy to large numbers of sensor nodes was a great challenge for the traditional cable system due to the high wiring cost and the battery-powered system due to the logistics and environment challenge of replacing batteries. Harvesting energy from the sensors' environment is a promising method, and sometimes is the only way to operate the sensor [24-27]. The energy sources in the sensor environment include solar light, mechanical vibration or motion, fluid flow, electromagnetic wave, pressure fluctuation, thermal variation or gradient, radiation energies, etc. [28-30]. In many cases, the energy densities of these sources are very small. Designing a compact and high-efficiency energy harvester to collect adequate energy to power the sensor nodes is not a trivial task.

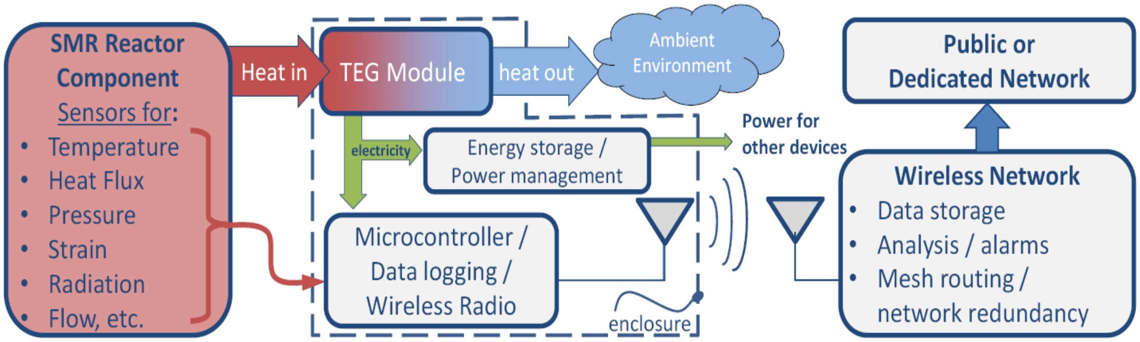

Figure 1.10. Thermoelectric energy harvesting to power the wireless communication system for the SMR reactor component [31]

In nuclear application, energy harvesting and wireless communication provide a promising opportunity to revolutionize nuclear sensors and instrumentations and to benefit reactor design and fuel cycle facilities by reducing the cost of power, wiring, and signal transmission or eliminating battery replacement. More importantly, when a severe accident or massive loss of grid power happens, the energy harvester can still provide self-sustainable power to monitor the critical parameters of the nuclear power plant or fuel cycle facilities. Back to 1960s, Corelli and Frost [32] reported that the radiation from the spent fuel could affect the physical properties of the thermoelectric materials. At 1961, Kilp and Mitchell [33] found that the gamma radiation might help to increase the electrical resistivity and Seebeck coefficient but reduce the overall power factor. Several recent studies reported on the radiation effect on thermoelectric material, heat pipes, and related power electronics [23]. Chen et al. [23] designed a thermoelectric energy harvester (Figure 1.11), together with the corresponding energy management circuit and wireless communication system. Both the energy harvester and the electronics were tested in a Co-60 gamma radiation chamber provided by Westinghouse Electric Company in Pittsburgh. It was found that the thermoelectric modules' Seebeck coefficients were not affected by gamma radiation up to 200 kGy. However, the energy management circuit (A DC-DC converter) should be properly shielded to reduce total radiation exposure to less than 380 Gy. And the wireless transmitter lost function after a gamma radiation dose of 944 Gy.

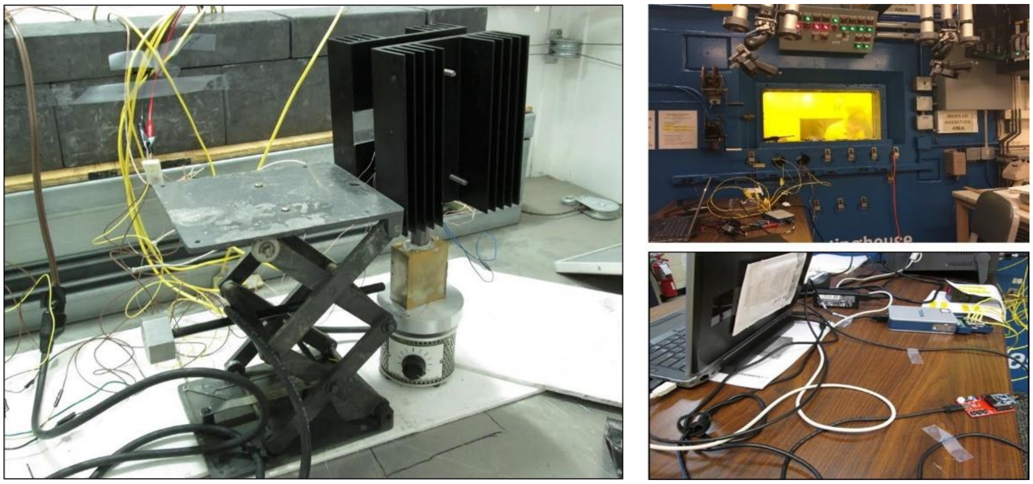

Figure 1.11. Gamma radiation test of the thermoelectric energy harvester and electronics in Westinghouse [23].

Accurate measurement of coolant flow rate (mass flow rates or volume flow rate) is essential for determining the maximum power required by the nuclear plant operation and critical for monitoring its operation safety. Most of the flowmeters available in the market are intrusive flowmeters. Due to the material degradation caused by corrosion/erosion, large measurement errors, or even a total failure of the sensor, are inevitable during a long term operation in the nuclear plant. Non-intrusive technologies, such as electromagnetic flowmeter, laser Doppler anemometry, and ultrasonic flowmeter, have been considered to replace intrusive flow meters to overcome the corrosion/erosion problem at high temperature. However, many of the existing technologies have fundamental limits. For example, laser Doppler anemometry has been recognized as a leading non-intrusive velocity measurement technology. However, this technology cannot be used in fluids where no light can pass through as is the case of the metal wall. Another problem is that this technology requires the inclusion of tracking particles to reflect the optical Doppler signal. But it is impractical to introduce those small tracking particles into an enclosed system or pipes with large flow rates. Alothman et al. [34] suggested that it was possible to develop a flow meter using TEGs. Since the voltage output of the TEG itself is a function of the flow rate when there is temperature difference existing between the fluid and environment, through careful calibration, it is possible to develop an integrated self-powered wireless sensing and communication system with TEG energy harvester itself working as an energy source as well as a non-intrusive flowmeter.

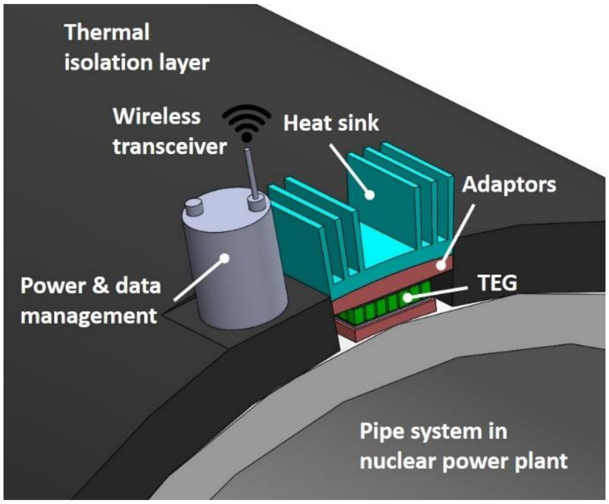

Figure 1.12. Thermoelectric energy harvester works in dual functions, both as an energy source and a flow meter sensor

1.3.2 Other energy harvesting technologies

Solar cell power is an excellent energy resource where direct sunlight is available. During daylight hours, outdoor solar energy is abundant and has a power density of 100 mW/cm^2. When put into indoor environments, the power density drops down to 10–20 µW/cm^2. For solar energy harvesting, the most commonly used technology is photovoltaic cell [35], while other technologies convert solar energy into thermal energy first and thermal engines are used to generate electricity. The efficiencies of the solar cell range from a low of approximately 10-15% for commercial products to state-of-art values of 30% [36], with some experimental results reaching as high as 40% [37]. This offers a huge potential for self-powered wireless sensor node. A solar collector with of an efficiency of 15% and an area of 20 cm^2 would generate over 300 mW peak of electrical energy in the direct outdoor sunlight, which is more than enough to power most wireless sensor nodes. Since the intensity of sunshine varies according to the season, time of day, and weather conditions, an electrical power management circuit is often necessary for a practical solar energy harvester for wireless sensors.

Vibration and acoustic phenomenon are characterized by amplitude and frequency. The frequency of individual energy harvesting transducers operating over narrow ranges must match the characteristics of the energy sources. Piezoelectric and electromagnetic generator combined with the mechanical motion rectifier [38, 39] is widely used to convert the vibration energy to electricity. Piezoelectric stacks are compact and easy to scale. Energy harvesters based on piezoelectric materials are a very effective way to provide limited power for self-powered wireless sensors and low-power electronics working in vibration environments [40]. Electromagnetic energy harvesting is an attractive technology for small and medium scale energy harvesting [38]. Typically, when compared with piezoelectrics, electromagnetic generators have higher efficiency and power output. However, the size is a little bit larger. With the development in the design of compact and high-efficiency energy harvesters over the last decade, devices can provide useable amounts of electrical energy derived from mechanical vibrations. Systems for harvesting energy from traffic-induced bridge vibrations, for example, have been used to modest power data acquisition devices for bridge health monitoring purposes [41].

Thermal energy is abundant in the environment and, in most cases, has a higher energy density than other energies. The thermal energy can be harvested when the temperature varies in the spatial or time domain. For thermal energy harvesting, there are a number of existing and emerging energy conversion technologies available, including the thermoelectric generator, organic Rankine cycle, the Kalina cycle, phase-changing-material engine generator, thermo-photovoltaic generator, the magneto-caloric generator, the thermo-acoustic-piezoelectric generator, etc. Thermoelectric energy conversion is especially interesting among all these technologies because it is a solid state energy conversion technology. The efficiencies of commercial TEG modules heavily rely on the temperature difference and ZT value of the materials, which can be as high as 10.0% [42], while some literature pronounced an efficiency as high as 20% [43]. Since the thermoelectric energy harvester can be scaled down to μm-scale, it can be easily integrated into a sensing system.

In the situation where a cable system is prohibited by the infrastructure and no energy resources are available, energy transport technologies combined with energy harvesting technologies can be used to power sensors. The most commonly used energy transport technologies include acoustic energy transfer [44] and radio frequency (RF) radiation energy transfer [45]. Though the efficiencies of the energy transfer are low for these two technologies, using artificial RF or acoustic energy sources with reasonable energy input and receivers of high energy conversion efficiency, people can still build an energy supply system to power the wireless sensor nodes.

1.4 Advanced thermoelectric materials

The modern thermoelectric research began in the 1940s with the discovery of semiconductors. The classical thermoelectric materials include Bi_2Te_3, PbTe, and SiGe working in different temperature regions. All of them have Seebeck coefficients of more than 200 µV/K and ZT values about 1.0 in the corresponding working temperature range. Generators or coolers based on these materials and their alloys are still the most commonly used today. Since these three materials were heavily studied for decades, many good review papers and books were available in the open literature [46, 47]. However, for a long period after their discovery, the progress in achieving higher ZT value was very slow.

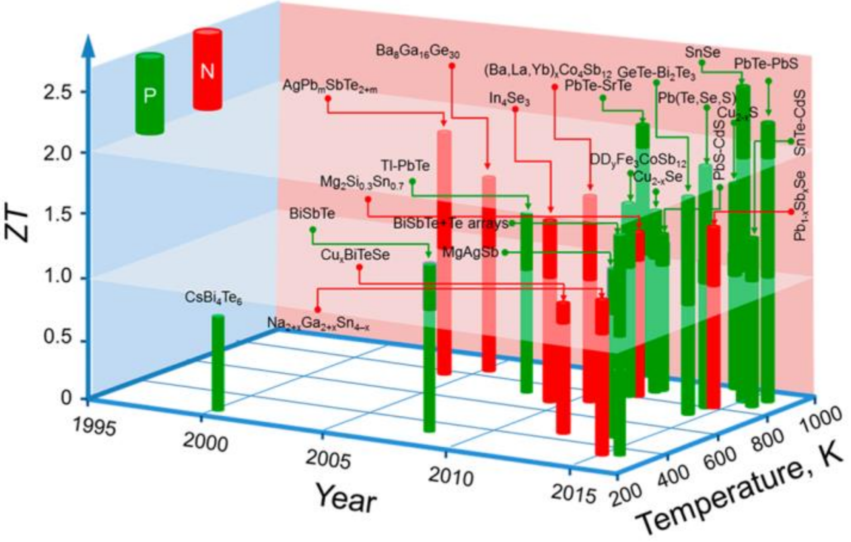

Figure 1.13. The current-of-state thermoelectric materials and their figure-of-merit ZT as a function of temperature and year.[48]

A resurgence of interest in thermoelectrics began in the early 1990s when Dresselhaus predicted [49, 50] that thermoelectric efficiency could be greatly enhanced using nano-technologies, which led to experimental efforts to demonstrate the proof-of-principle in the next decades. A lot of progress was made in this field, with the recent achievements documented in some good review papers [51, 52], with some of the main achievements in the last two decades explicated in Figure 1.13.

The search for high-ZT materials is the primary task in thermoelectric society. The bulk material research was of special interests because they were thought to be more stable and cost-effective than low-dimensional materials. Though high *ZT*s were reported in nanomaterials, many of these materials were not practical for large-scale commercial use because they were fabricated by atomic layer deposition processes, such as molecular beam epitaxy, which was accused of being expensive, time-consuming, and easily damaged [46]. Bulk material can be the only choice to achieve meaningful power output. In the last two decades, several classes of bulk materials were discovered to have the potential for future thermoelectric applications.

Bismuth Telluride

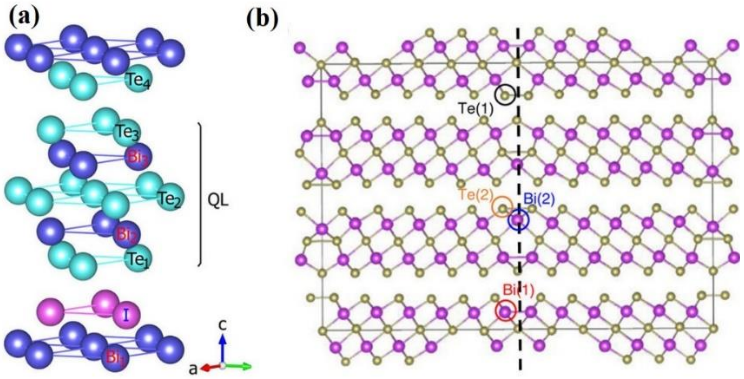

Figure 1.14. Atomic structures of (a) the unit-cell of Bi2Te3 [53] and (b) Bi2Te3 with a 60° twin boundary [54]. The dotted black line indicates the 60° twin boundary.

Bi_2Te_3 was the first thermoelectric materials reported to have high ZT value at room temperature. The density of this material is 7.74 g/cm^3, with a melting temperature of 853 K. As shown in Figure 1.14 is the atomic structure of the Bi_2Te_3. In the [001] direction, a clear layered structure is observed. The binding between the two near Te atoms can be relatively weak. The electrical and thermal conductivities of bismuth telluride are highly anisotropic. The lattice conductivity is about twice as large along the cleavage planes as it is in the perpendicular direction. The electron mobilities that parallels and perpendicular to the cleavage planes differ a lot.

Since Goldsmid andDouglas [55] first proposed to use Bi_2Te_3 based thermoelectric material for refrigeration in 1954, this compound has been extensively used in the construction of thermoelectric modules. The performance of materials based on Bi_2Te_3 has been steadily improved since the original observations. Most of the early improvements came about through a reduction in the lattice thermal conductivity. This was achieved through the use of solid solutions of bismuth telluride with the isomorphs compounds, including antimony telluride and bismuth selenide [56]. In recent years, further reductions in the lattice conductivity have been obtained by the adoption of nanostructures [5].

TAGS

The so-called TAGS materials, $(GeTe)_x(AgSbTe_2)_{100-x}$ (x=0.70-0.95), which crystallize in the α-GeTe structure type at ambient conditions and exhibit rock-salt type at high-temperature, represent some of the best characterized thermoelectric materials with ZT values above 1.0 [57]. Experiments showed that they could reach ZT values of up to 1.7 at 500 °C [58]. In order to optimize the thermoelectric properties of TAGS, many different substitution variants were investigated, such as $(GeTe)_{85}(Ag_ySbTe_{y/2+1.5})_{15}$, where the thermal conductivity was reduced without significantly affecting the electrical conductivity, and the power factor increased due to an optimized charge carrier concentration without significantly decreasing the carrier mobility [59]. It was also found that quenched and nanostructured Te/Sb/Ge/Ag (TAGS) compounds with rather high concentrations of cation vacancies exhibited improved thermoelectric properties as compared to corresponding conventional TAGS (with constant Ag/Sb ratio of 1.0) due to a significant reduction of the lattice thermal conductivity [57].

Skutterudites

Skutterudites were attractive semiconducting materials discovered in the 1990s. These materials were well known for their phonon-glass-electron-crystal (PGEC) characteristics, a concept proposed by Slack [60]. The skutterudite family has many different solid solutions. These materials cover a large range of band gaps, which provide a lot of possibilities to adjust the composition and doping level to achieve the desired properties. The unit cell of the skutterudite structure (cubic, space group Im3) is shown in Figure 1.15. The unit cell consists of eight small cubes, two of them empty, and six of them containing the anions As^{4-} in the center. This arrangement is necessary to maintain the stoichiometric ratio Co^{3+}:As^{4-}=4:3. Ternary skutterudite compositions are derived from binary compounds by keeping a total valence electron count (VEC) of 72, such as $Co_4Sn_6Te_6$, and $FeCo_3Sb_{12}$. The existence of the two voids creates an opportunity to fill foreign atoms into the skutterudite lattice without changing its basic structure. They can take the form $R(M_4X_{12})$ where R is a filling atom, M is Fe, Ru, Os, or Co, and X is P, As, or Sb. The first filled skutterudite ($LaFe_4P_{12}$) was synthesized in 1977 by Jeitschko and Brown [61]. The various atomic composition choices provide researchers many opportunities to manipulate the properties of the material. Appropriate filling atoms result in “rattling” within the unit cell cage [62], which significantly depresses the lattice thermal conductivity, while having a small effect on the electrical conductivity and the Seebeck coefficient. An excellent in-depth review of skutterudites can be found in reference [63].

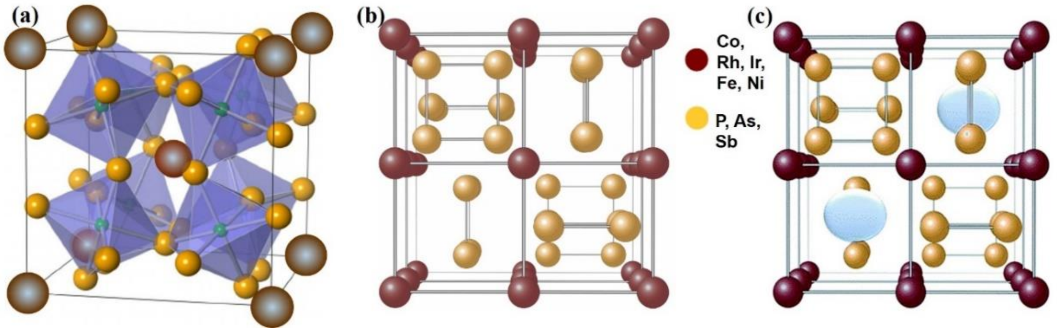

Figure 1.15. (a) Unit cell of skutterudites consisting of eight small cubes [64]; (b) unfilled skutterudites [65]; (c) filled skutterudites [66].

Magnesium silicide

Magnesium silicide (Mg_2Si) is an inorganic compound having a face-centered cubic lattice structure. In its unit cell, it possesses the anti-fluorite structure with Si^{4-} ions occupying the corners and face-centered positions and Mg^{2+} ions occupying eight tetrahedral sites in the interior (Figure 1.16). The density of pure Mg_2Si is 1.98 g/cm^3, relatively small compared with other thermoelectric materials. Though the ZT value of

$MgSi_2$ is slightly lower than Bi_2Te_3, this material has many advantages over other materials because it is abundant, inexpensive, light-weighted, and non-toxic. A ZT value of ~1.4 is reported in Bi-doped $Mg_2Si_{1-x}Sn_x$ at 773 K with an average ZT of 0.9 between 400 and 773 K [67], which is reasonably high for most thermoelectric applications. Furthermore, the mechanical properties of Mg_2Si are superior to those of PbTe for medium temperature energy harvesting. Li et al. [68] demonstrated that thermoelectric and mechanical performance of Mg_2Si could be significantly enhanced by nano-structuring via non-equilibrium syntheses, such as melt-spinning followed by spark plasma synthesis (SPS) or hot pressing. Thus, Mg_2Si-based compounds are promising alternatives to Te-based compounds for large scale energy harvesting.

	Mg	Si	Bi	Te	Pb	Co	Sb
Reserves (ppm)	32,000	267,700	0.06	~5 (ppb)	8	29	0.2
Cost (K¥/MT)	200	90	849	9000	98	3500000	430
Toxicity	NO	NO	YES	YES	YES	YES	YES

Figure 1.16. (a) Atom structure of magnesium silicide [69]; (b) The comparison of reservation, cost, and toxicity between different elements [70].

Clathrates

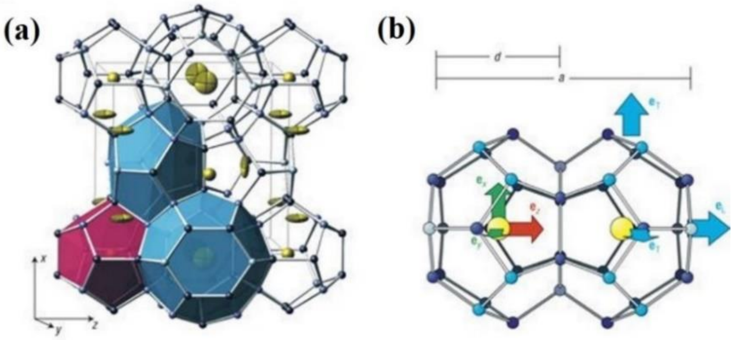

Figure 1.17. (a) The $Ba_8Ga_{16}Ge_{30}$ thermoelectric material with the Ba guest atoms inside Ga/Ge cages. (b) The vibration motion of the cage structure [71].

Clathrates are inclusion compounds in which the guest molecule is in a cage formed by the host molecule [54]. The clathrates can be divided into two major groups: type I and type II. Both types have a cubic unit cell but differ according to the number and size of the voids presented in the structure. There are numerous possible compositional filling variations for those materials, resulting in vastly different electronic properties ranging from semi-metallic to semiconducting [72]. Clathrates has great potential for thermoelectric application because numerous options are available for thermoelectric-property optimization. Nolas et al. [73] reported the transport properties of polycrystalline Ge clathrates with general composition $Sr_8Ga_{16}Ge_{30}$ (Figure 1.17) in the temperature range of 5-300 K. They estimated that ZT>1 was achievable at T>700 K, thus promising for high-temperature thermoelectric application. The authors claimed that the $Sr_8Ga_{16}Ge_{30}$ compound was a true PGEC material system where the thermal conductivity was drastically reduced by compositional filling, while good electrical properties were maintained. Similar to skutterudites, the extremely low thermal conductivity in the clathrates was attributed to the "rattling" phenomenon caused by the Sr element filling the voids. However, it was found that the coupling between the lattice thermal conductivity and electrical properties were much weaker in the clathrates, which was especially desired for the thermoelectric application.

Half-Heusler materials

Heusler compounds (Figure 1.18) are magnetic inter-metallics with face-centered cubic crystal structure and composition of XYZ (half-Heuslers) or X_2YZ (full-Heuslers), where X and Y are transition metals. Heusler compounds have low electrical resistivity combined with large Seebeck coefficient values. Large power factors on the order of 25–30 $\mu W \cdot cm^{-1} \cdot K^{-2}$ had been experimentally obtained for several of these materials, e.g. ZrNiSn [74]. Research found that the electrical properties of these materials could be easily manipulated through doping, compositional variations and/or atomic substitutions. While the power factors were promising, the thermal conductivities of ternary compounds, such as ZrNiSn and HfNiSn, were rather high. The lattice thermal conductivity ranged from 5.9 to 17 $Wm^{-1}K^{-1}$ for ZrNiSn. Efforts should therefore focus on further reducing the lattice thermal conductivities of these materials.

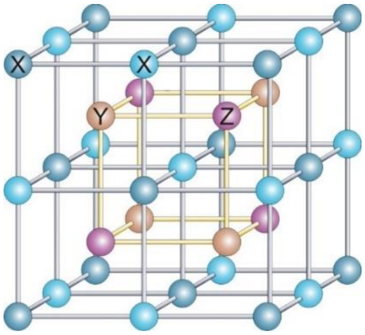

Figure 1.18. The atomic structure of a typical Half-Heusler material

Tin selenide

SnSe has stiff bonds and distorted lattice, crystallizing in the orthorhombic structure at room temperature. The perspective views of the room-temperature SnSe crystal structure along the *a*, *b*, and *c* axial directions are shown in Figure 1.19. The Sn–Se bonding within the plane of the slabs is strong, while the Sn–Se bonding along the *a* direction is weaker. According to reference [75], SnSe has exhibited the unprecedented ZT values, with ~2.62 at 923 K along the *b* axis and ~2.3 along the *c* axis. When coupled with the Carnot efficiency for heat conversion, an overall energy conversion efficiency of approximately 25% was expected at a temperature difference of 500 K. The crystal structure of SnSe undergoes a phase transition at ~750 K, where it changes from Pnma to a higher symmetry Cmcm structure. This phase transition preserves many good transport properties of SnSe. The Cmcm phase exhibits a substantially reduced energy gap and enhanced carrier mobility while maintaining the ultra-low thermal conductivity thus yielding the record ZT [75]. The ultra-low thermal conductivity of SnSe is attributed to the highly un-harmonic and anisotropic bonding and layered structure (as low as 0.23 $Wm^{-1}K^{-1}$). In particular, the SnSe crystal avoids toxic lead and rare-earth tellurium elements that are prevalently used in current commercial products. When integrated with nanotechnology, it is promising that its ZT value can be further enhanced. It is highly expected that SnSe will be soon used in thermoelectric energy harvesting.

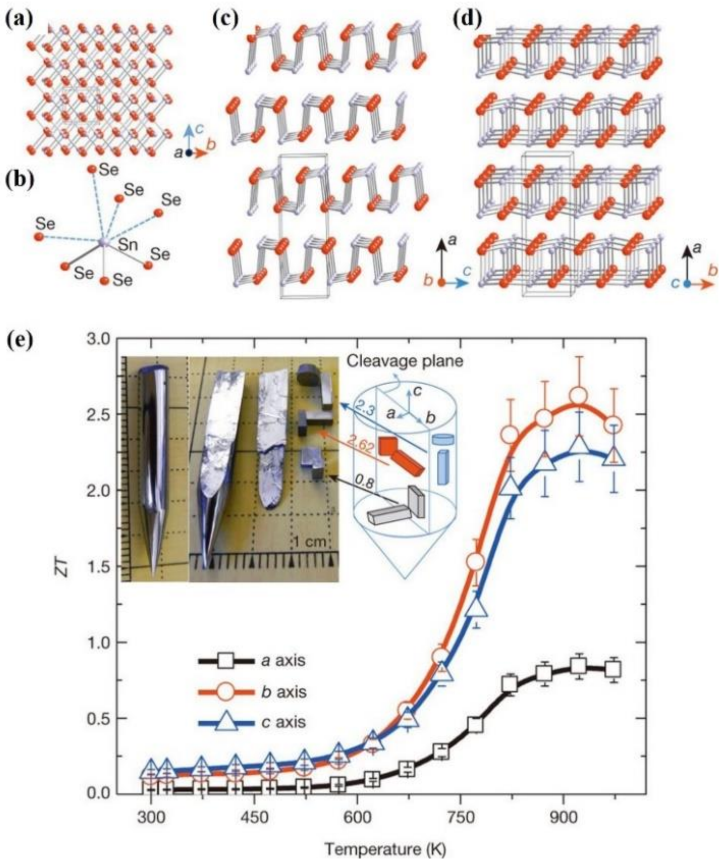

Figure 1.19. (a) Crystal structure along the a axis: grey, Sn atoms; red, Se atoms. (b) Highly distorted SnSe7 coordination polyhedron with three short and four long Sn–Se bonds. (c) Structure along the b axis. (d) Structure along the c axis. (e) ZT values along different axial directions [75].

Lead telluride

Lead telluride (Figure 1.20) crystallizes in the NaCl crystal structure with Pb atoms occupying the cation and Te forming the anionic lattice. PbTe is a traditional thermoelectric material and owns a decent ZT in the medium temperature range. In recent years, people found that the ZT value of PbTe could be greatly enhanced through several innovative strategies. Nanostructuring, in particular, has been proven an effective approach to enhance ZT by reducing the lattice thermal conductivity. Recent research found that p-type $PbTe_{1-x}Se_x$ had excellent thermoelectric properties (ZT~1.8) arising from multiple valence bands [76]. PbTe doped by Tl was reported to have enhanced ZT through the introduction of a density-of-states distortion in the valence band [77]. Biswas et al.[78] used the all-scale hierarchical architectures strategy to increase the ZT of nanostructured PbTe–SrTe (0–

4mol%) doped with 2mol% Na, with a ZT~2.2 reported at 915 K. The technologies mentioned above did not conflict with each other. Thus it is possible to combine these technologies to enhance the ZT value of PbTe further.

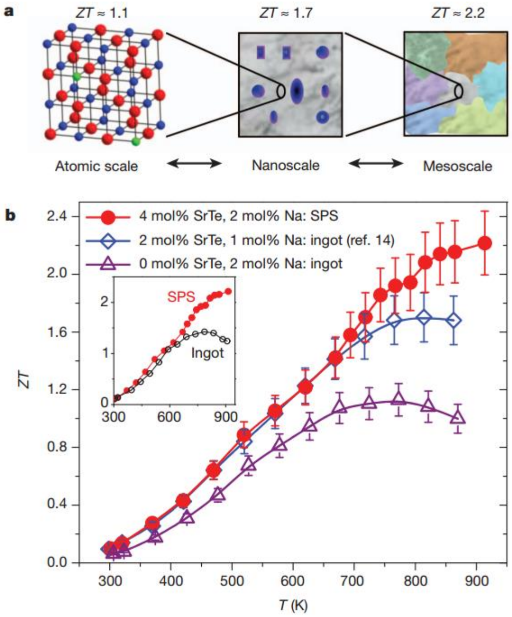

Figure 1.20. All-length-scale hierarchy in thermoelectric materials. (a) Maximum achievable ZT values for the respective length scales. (b) ZT as a function of temperature for an ingot of PbTe with different doping strategies [78].

1.5 The thermoelectric material fabrication method

1.5.1 Spark plasma sintering for bulk material fabrication

Conventionally, TEGs are fabricated following the steps in Figure 1.21. First, the rare materials are mixed in the right ratio and melted at a high temperature to achieve uniform properties. Second, the synthetic ingots are annealed at an appropriate temperature to obtain the right phase. Third, the ingots are grounded into powders for hot pressing or spark plasma sintering (SPS). Finally, the sintered material is cut into thermoelectric elements. The elements are aligned thermally in parallel and electrically in series to form a TEG module. The hot pressing and SPS are superior to the Bridgman method because they can preserve the abundant grain boundaries in the sintered materials, thus resulted in higher ZT. This method can fabricate most of the commonly seen TE materials, such as PbTe, Mg_2Si, filled skutterudite, and Bi_2Te_3 with peak ZT values higher than 1.0.

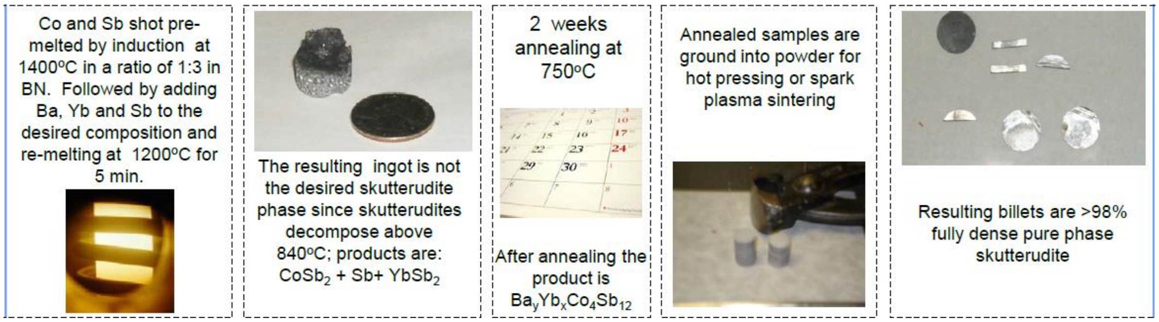

Figure 1.21. The conventional method to fabricate TEG module [79].

1.5.2 Molecular beam epitaxy and chemical vapor deposition for thin film thermoelectric material fabrication

The molecular beam epitaxy (MBE) process was developed in the late 1960s at Bell Telephone Laboratories by Arthur and Cho [80]. Since it was born, MBE played a key role in the growth and development of nanoscience and was considered one of the fundamental tools for the development of the nanotechnology [81]. MBE takes place in ultra-high vacuum ($10^{-8} - 10^{-12}$ Torr), where the pure sources of material are vaporized in separate ovens. The atoms or molecules released by the sources are transported like a 'beam' to a substrate, where they are deposited. During operation, reflection high-energy electron diffraction is often used for monitoring the growth of the crystal layers. The deposition rate of the MBE is relatively low when compared with other technologies. A computer-controlled shutter in front of each furnace allows the precise control of the thickness of each layer down to a single layer of atoms. In this way, the researchers can build nanostructures with precisely controlled compositions. The absence of carrier gases results in the highest achievable purity of the grown films. Using MBE to fabricate thin film and super-lattice thermoelectric materials can be found in the open literature [82, 83].

Chemical vapor deposition (CVD) is another frequently used technology for thin film thermoelectric material fabrication. In a typical CVD, the substrate is exposed to volatile precursors, which react and decompose on the substrate surface to produce the desired deposit. By-products produced during the reactions are removed by gas flow through the reaction chamber. Lithography and etching are often used to pattern thin-film thermoelectric.

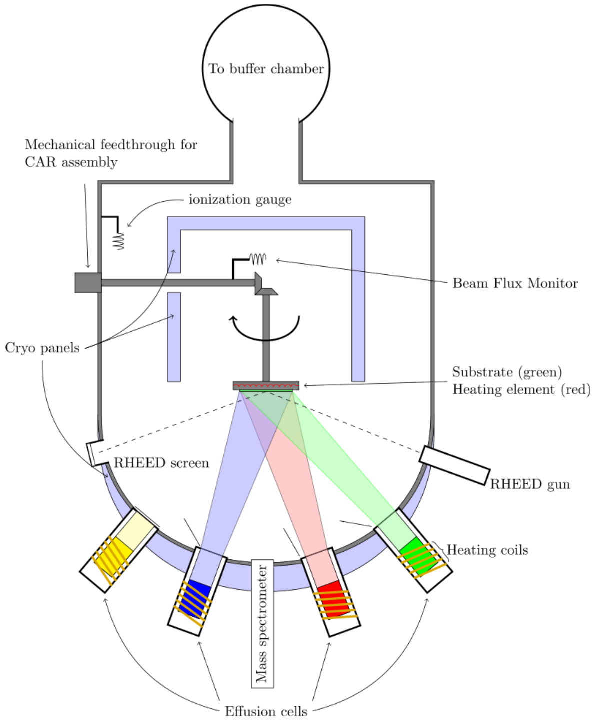

Figure 1.22. Molecular beam epitaxy [84].

1.5.3 Selective laser melting for the fabrication of nanostructured bulk thermoelectric materials

Selective laser melting (SLM), shown in Figure 1.23, is a high-temperature additive manufacturing technology. Recently, SLM was employed to prepare Bi_2Te_3-based thermoelectric materials [85-87]. A maximum ZT value of 0.84 was reported at 400 K [86], which is comparable to ZT values of samples prepared by the commonly used hot pressing or SPS. These preliminary efforts demonstrated the promise of using SLM as an advanced additive manufacturing tool for thermoelectric materials preparation and devices/modules manufacturing. However, fundamental challenges, such as ZT enhancement and thermomechanical reliability of TEGs, still exist in this multidisciplinary area. Unlike 3D printing of metal components, in TEG manufacturing, high electrical conductivity, low thermal conductivity, high Seebeck coefficient, and good mechanical properties should be considered comprehensively.

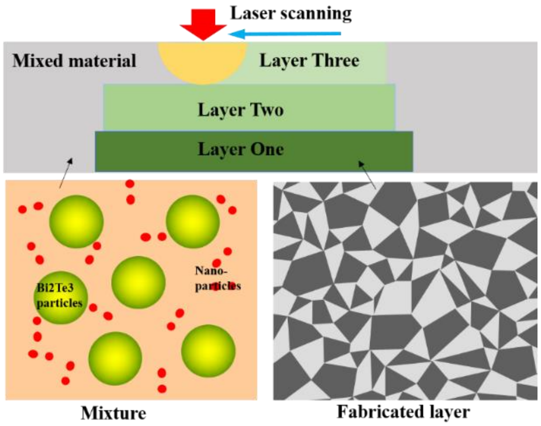

Figure 1.23. The conventional method to fabricate the TEG module

1.5.4 Thermal spray and cold spray for thermoelectric film fabrication

The thermal spray had long been recognized as one of the techniques to fast produce high-quality surface coatings. As shown in Figure 1.24, during the spraying, feedstock materials are heated to molten or semi-molten state. These particles are then transported by operating media before they are deposited on the substrate at high speed, accumulating vertically to form the laminated coating. Pretreatment of substrates is very important for thermal spay, as the primary adhesion mechanism is mechanical bonding, rather metallurgical bonding. For those particles that are not melted during the spray, they are buried inside the coating. After deposition, the hot particles will shrink, solidify, and form a mechanical bond dominated structure. Longtin et al. [2] proposed using thermal spay for large scale thermoelectric material fabrication for its desired characteristics, such as high throughput, rapid quenching rate (10^6 –10^8 K/s.), and good surface geometry adaptability. A careful test of the deposited material found that the ZT value of the deposited material was about 30% of the material fabricated by the conventional method. This can be attributed to the oxidation, and porous structure happened during the processing.

The cold spraying (often called gas dynamic cold spray) [88] was originally developed in Russia in the 1990s when people accidentally observed the rapid formation of coatings when experimenting with the particle erosion of the target exposed to a high-velocity flow loaded with fine powders. In cold spraying, particles are accelerated to ultrasonic speeds by the carrier gas through a de Laval type nozzle. Upon impact, solid particles with extremely high kinetic energy deform plastically and bond metallurgically to the substrate and form a coating. The critical velocity needed to form bonding depends on the materials properties, powder size, and temperature. Soft metals, such as Cu and Al, are best suitable for cold spraying. The deposition rate is typically low for alloy powders, and the window of suitable process parameters and right powder sizes is narrow. Generally, to accelerate powders to high velocity, fine powders (<20 micrometers) are required. It is possible to accelerate powder particles to much higher velocity to fabricate hard materials using helium as the carrier gas. However, helium is costly, and its flow rate is much higher than nitrogen.

Figure 1.24. Thermoelectric material fabrication using thermal spay [79].

1.6 Thermoelectric material characterization

The thermoelectric performance of the material is judged by ZT, which is a function of thermal conductivity, electrical conductivity, and Seebeck coefficient. The characterization methods for the material microstructure and the three parameters were summarized as follows.

1.6.1 Microstructure characterization

X-ray diffraction (XRD) analysis, scanning electron microscopy (SEM), energy-dispersive X-ray spectroscopy (EDS), and transmission electron microscopy (TEM) are the four main tools that used to characterize the microstructure of the thermoelectric materials.

XRD, as shown in figure 1.25, is the most common method used for characterizing the atomic and molecular structure of a crystal, in which the crystalline atoms cause a beam of X-rays to diffract into many specific directions. By measuring the angles and intensities of these diffracted beams, a crystallographer can produce a three-dimensional picture of the density of electrons within the crystal. From this electron density, the mean positions of the atoms in the crystal can be determined, as well as their chemical bonds, their disorder, and various other information. The Bragg's law specifies the relationship between the lattice length and the wavelength of the X-ray as

$$2d\sin\theta = n\lambda \tag{1-1}$$

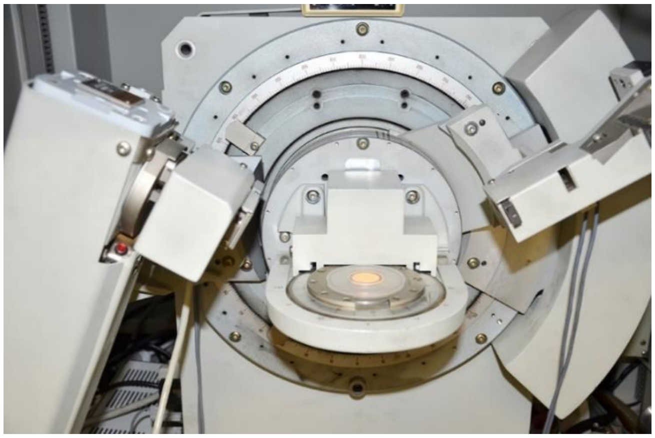

Figure 1.25. A X-ray Diffraction machine from Siemens

SEM is a type of electron microscope that produces images of a sample by scanning it with a focused beam of electrons. The electrons interact with atoms in the sample, producing signals that can be detected and that contain information about the sample's surface topography. SEM can achieve resolution better than 1.0 nanometer.

EDS is an analytical technique used for the chemical characterization of a sample. It works based on the fundamental principle that each element has a unique atomic structure allowing a unique set of peaks on its X-ray spectrum. To stimulate the emission of characteristic X-rays from a specimen, a high-energy beam of charged particles such as electrons or protons or a beam of X-rays is focused on the sample being studied. Consequently, ground state electrons in discrete energy levels may be excited to a higher energy level. The electrons in high energy level are not stable and will emit photons which contains the information of the shell structure of the elements. By measuring the number and energy of the photons, the elemental composition of the specimen is revealed.

TEM is a microscopy technique in which a beam of electrons is transmitted through an ultra-thin specimen, interacting with the specimen as it passes through. An image is formed from the interaction of the electrons and the specimen. Then the image is magnified and focused onto an imaging device, such as a fluorescent screen. TEM is capable of imaging at a significantly higher resolution than light microscopes, owing to the small de Broglie wavelength of electrons. This enables the examination of the fine detail (even as small as a single column of atoms), which is thousands of times smaller than the smallest resolvable object in a light microscope. This super capacity allows it to form a major analysis method in a wide range of scientific fields.

1.6.2 Thermal conductivity characterization

Laser flash method for bulk materials

Thermal conductivity of the bulk samples can be measured using a laser flash method. The laser flash analysis (Figure 1.26) measures the thermal conductivity based on the temperature change with time of the backside of a sample after heating the front side with a laser beam instantaneously. The higher the thermal diffusivity of the sample, the faster the energy reaches the backside. The thermal diffusivity can be calculated by

$$\alpha = 1.37 \cdot \frac{L^2}{\pi^2 t_{1/2}} \tag{1-2}$$

where, $t_{1/2}$ represents half of the time required for the temperature on the back side to reach the maximum value after the sample surface is irradiated with an instantaneous heat source, L is the thickness of the sample.

To measure the specific heat of the sample, a standard sample with known thermal conductivity is used as the reference. Then the specific heat of the unknown sample is found at a target temperature by comparing the temperature changes of the sample at room temperature and target temperature, assuming that the unknown sample absorbed the same heat. The following equation is used to calculate the thermal capacity of the unknown sample,

$$Cp_u^{T_i} = \frac{\Delta T_u^{Tr}}{\Delta T_u^{Ti}} Cp_u^{T_r} \tag{1-3}$$

where $\Delta T_u^{Tr}$and $\Delta T_u^{Ti}$is measured by the system, and $Cp_u^{T_r}$ is calculated by

$$Cp_u^{T_r} = \frac{Q}{m_u \Delta T_u^{Tr}} \tag{1-4}$$

m and Cp^{Tr} represent the weight and specific heat at room temperature (Tr), the subscript u represent the unknown sample. The thermal conductivity of the unknown sample is obtained from thermal diffusivity, specific heat, and density using the following equation.

$$\lambda = \alpha \cdot Cp \cdot \rho \tag{1-5}$$

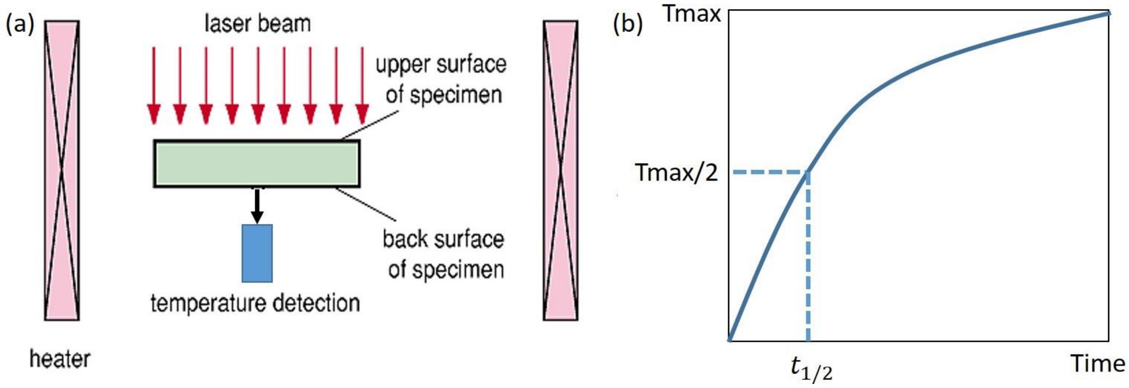

Figure 1.26. Thermal conductivity measurement using the laser flash method

3ω-method for thin film materials

The 3ω technique [89] is the most widely used and an effective technique for measuring the thermal conductivity of dielectric thin films. There are four electrical pads shown in Figure 1.27: the outer two pads are used for providing the modulated heating, while the inner two pads are used for measuring the voltage drop across the micro-bridge. The heater is driven by AC at frequency ω. The periodic temperature oscillation follows the periodic heating and occurs at a frequency 2ω but delayed in phase ϕ. This temperature oscillation then causes the resistance of the heater to oscillate at a frequency 2ω. Because the current is driven at a frequency ω and the resistance changes at a frequency 2ω, an RMS voltage at frequency 3ω results. The 3ω voltage amplitude is directly measurable and contains information about the amplitude of the temperature fluctuations of the micro-bridge. The amplitude of the temperature oscillation is then compared to a thermal model as a function of the heating frequency to determine the effective thermal diffusivity of the underlying material.

$$V_{mb} = IR_{mb} = I_0 \cdot cos\omega t[R_0 + R_1(T_s + T_m cos2\omega t)] \tag{1-6}$$

Thermal conductivity is determined by the linear slope of the ΔT vs. log(ω) curve. The main advantages of the 3ω-method are the minimization of radiation effects and easier acquisition of the temperature dependence of the thermal conductivity than in the steady-state techniques. Although some expertise in thin film patterning and microlithography is required, this technique is considered as the best pseudo-contact method available. Other techniques for measuring the thermal conductivity of low dimensional materials include transient thermo-reflectance technique (TTR) and scanning thermal microscopy (SThM).

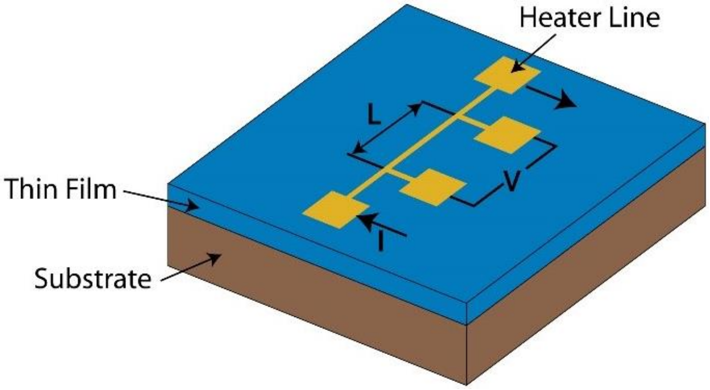

Figure 1.27. 3ω-method for thermal conductivity measurement [89]

1.6.3 Electrical conductivity characterization

Four-probe method

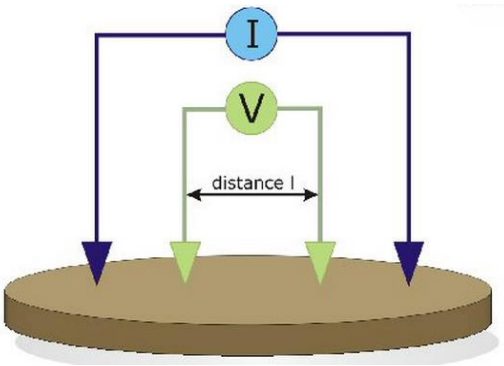

Figure 1.28. Four-probe method for electrical conductivity measurement [79]

The four-probe method was widely used to measure the electrical conductivity of materials with various shapes. The typical set up of this method is the equal-distance placement of four in-line probes or points. The spacing of between every two probes is usually 1 mm (Figure 1.28). Current is applied through the outer two probes and is measured. At the same time, the inner two probes measure the electrical voltage between these two points. The electrical resistivity of the sample can be calculated using

$$\rho = \frac{V \cdot A}{I \cdot l} \tag{1-7}$$

It should be noted that the surface condition is very sensitive to the measurement because of contaminations, such the oxidation of the surface can contribute the increase of resistivity or, affect the contact between the probes and sample.

Van der Pauw method

The van der Pauw Method [90] (Figure 1.29) is a technique widely used to measure the electrical resistivity and the Hall coefficient of a sample. It can accurately measure the properties of a sample of any arbitrary shape, as long as the sample is approximately two-dimensional and the electrodes are placed on its perimeter.

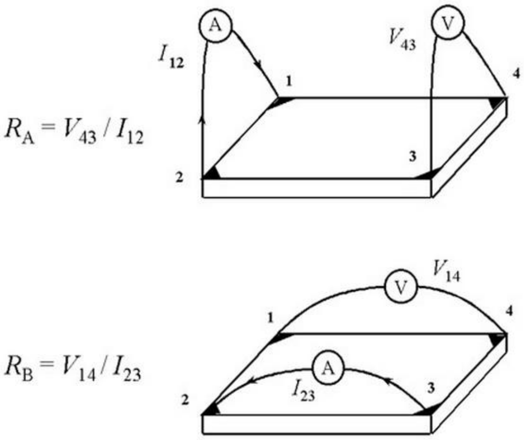

Figure 1.29. Van der Pauw method

To reduce errors, the sample should be symmetrical and no isolated holes on the sample. Four electrical point contacts are required to conduct the measurement. The contacts must be on the boundary of the sample and be infinitely small. In addition to this, any leads from the contacts should be constructed from the same batch of wire to minimize thermoelectric effects. For the same reason, the four contacts should be made of the same material. By measuring from the different directions, see R_A and R_B in the figure below, the correct resistance value can be obtained.

1.6.4 Seebeck coefficient characterization

Direct measurement for bulk material

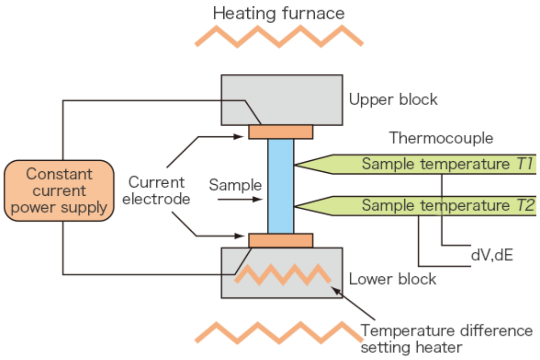

Figure 1.30. Measure the Seebeck coefficient using ZEM-3 series [91].

A prism or cylindrical sample is set in a vertical position between the upper and lower blocks in the heating furnace. While the sample is heated and held at a specified temperature, it is heated by the heater in the lower block to provide a temperature gradient. Seebeck coefficient is measured by measuring the upper and lower temperatures T_1 and T_2 with the thermocouples pressed against the side of the sample, followed by measurement of thermal electromotive force ΔV between the same wires. The Seebeck coefficient can be calculated using

$$\alpha = -\frac{\Delta V}{\Delta T} \tag{1-8}$$

MMR method for thin film material

The measurement of Seebeck Coefficient is always difficult to achieve as the unit of electrical voltage is microvolt which is on the noise level. A method developed by MMR Technologies was widely used to measure the Seebeck coefficients of thin film samples. During the measurement, the voltage generated in the sample was compared with that of the reference sample.

$$V_1 = \alpha_1 \Delta T \tag{1-9}$$

$$V_2 = \alpha_2 \Delta T \tag{1-10}$$

Then

$$\alpha_1 = \alpha_2 \frac{V_1}{V_2} \tag{1-11}$$

Note that the temperature difference is small, so is the thermoelectric voltage. Any noise could affect the result of the measurement, and such noise can hardly be removed. The accuracy can be improved by taking two different measurements, using different sets of power inputs.

$$V_{1,P_1} = \alpha_1 \Delta T_{P_1} + \Delta V_1 \tag{1-12}$$

$$V_{2,P_1} = \alpha_2 \Delta T_{P_1} + \Delta V_2 \tag{1-13}$$

$$V_{1,P_2} = \alpha_1 \Delta T_{P_2} + \Delta V_1 \tag{1-14}$$

$$V_{2,P_2} = \alpha_2 \Delta T_{P_2} + \Delta V_2 \tag{1-15}$$

The offset voltages can be assumed to be the same because these offset voltages come from the joints of the wires which does not vary much around a certain temperature. The overall value of the Seebeck coefficient can be obtained using

$$\alpha_1 = \alpha_2 \frac{(V_{1,P_1} - V_{1,P_2})}{(V_{2,P_1} - V_{1,P_2})} \tag{1-16}$$

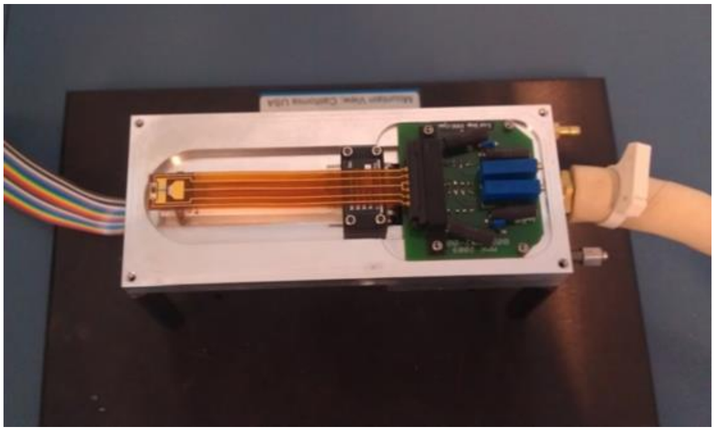

Figure 1.31. Seebeck measurement in the vacuum chamber [79]

1.7 Thermoelectric properties and Onsager relations

In this section, some of the state-of-art strategies for the ZT enhancement were reviewed. The thermal and electrical properties of the thermoelectric material, as well as the thermodynamic governing equation, were derived starting from the Boltzmann transport equations based on the single band assumption.

The most important parameters that used to evaluate the performance of the thermoelectric material is the ZT value,

$$ZT = \frac{\sigma \alpha^2}{k_e + k_l + k_b} T \tag{1-17}$$

where k_e is the electron thermal conductivity, k_l is the lattice thermal conductivity, k_b is the bipolar heat transfer, σ is the electrical conductivity, and α is the Seebeck coefficient. To achieve high ZT, the electrical conductivity and Seebeck coefficient should be as high as possible, while thermal conductivity should be suppressed to the minimum value. However, a modification to any one of these parameters adversely affects the other transport coefficients. Therefore, increasing ZT is a challenging work, and should be considered in a comprehensive way.

The ZT values of the thermoelectric materials were associated with several parameters mentioned above, which can be derived out using the Boltzmann transport equation. The time evolution of the N-carriers in the material is governed by the Liouville's equation as follows [92],

$$\frac{\partial f^{(N)}}{\partial t} + \sum_{i=1}^{n} \dot{r}^{(i)} \cdot \frac{\partial f^{(N)}}{\partial r^{(i)}} + \sum_{i=1}^{n} \dot{p}^{(i)} \cdot \frac{\partial f^{(N)}}{\partial p^{(i)}} = 0 \tag{1-18}$$

The behavior of the N-particles can be simplified by a particle distribution function, the famous Boltzmann transport equation, using the molecular chaos assumption.

$$\frac{\partial f}{\partial t} + \frac{d\boldsymbol{r}}{dt} \cdot \nabla_r f + \frac{d\boldsymbol{p}}{dt} \cdot \nabla_{\boldsymbol{p}} f = \left(\frac{\partial f}{\partial t}\right)_c \tag{1-19}$$

The distribution function is rewritten by introducing the relax time approximation,

$$f = f_0 - \tau \left(\boldsymbol{v} \cdot \nabla_{\boldsymbol{r}} f_0 + \frac{\boldsymbol{F}}{m} \cdot \nabla_{\boldsymbol{v}} f_0 \right) \tag{1-20}$$

where $f_0 = f(E) = \frac{1}{e^{\left(\frac{E-E_f}{k_B T}\right)}+1}$ (Fermi-Dirac distribution) for electrons, and $f_0 = f(v) = \frac{1}{e^{\left(\frac{hv}{k_B T}\right)}-1}$ (Bose-Einstein distribution) for phonons and photons.

1.7.1 Electrical conductivity and Seebeck coefficient

For electrons moving in the *x*-direction, the distribution of the electrons is governed by $f = f_0 - \tau \left(\boldsymbol{v_x} \cdot \nabla_{\boldsymbol{x}} f_0 + \frac{eE_x}{m} \cdot \nabla_{\boldsymbol{v_x}} f_0 \right)$, where f is the Fermi-Dirac distribution.

The current in the *x*-direction is summed by the electrons moving in the *x*-direction in the k space.

$$J_{ex} = \frac{1}{V} \left[\sum_{k_x=-\infty}^{\infty} \sum_{k_y=-\infty}^{\infty} \sum_{k_z=-\infty}^{\infty} v_x (-e) f \right]$$

$$= -\frac{2}{(2\pi)^3}\int_{-\infty}^{\infty}\int_{-\infty}^{\infty}\int_{-\infty}^{\infty}(ev_x f)dk_x dk_y dk_z$$

$$= -\frac{e}{3}\left(\frac{dE_f}{dx} + eE_x\right)\int_0^{\infty}\tau v^2 \cdot D(E)\frac{\partial f_0}{\partial x}dE = \sigma E_x \tag{1-21}$$

Substituting $\frac{\partial f_0}{\partial x} = -\frac{\partial f_0}{\partial E}\cdot\frac{dE_f}{dx} - \frac{E-E_f}{T}\frac{\partial f_0}{\partial E}\frac{dT}{dx}$ into the equation above,

$$J_{ex} = the\ -\frac{e}{3}\int_0^{\infty}\tau v^2 \cdot \left(\frac{dE_f}{dx} + \frac{E-E_f}{T}\frac{dT}{dx} + eE_x\right)\cdot D(E)\frac{\partial f_0}{\partial E}dE$$

$$= -\frac{e^2}{3}\int \tau v^2\, D(E)\frac{\partial f_0}{\partial E}dE \cdot \left(-\frac{d\Phi}{dx}\right) + \frac{e}{3T}\int \tau v^2 \left(E - E_f\right)D(E)\frac{\partial f_0}{\partial E}dE \cdot \left(-\frac{dT}{dx}\right)$$

$$= L_{11}\left(-\frac{d\Phi}{dx}\right) + L_{12}\left(-\frac{dT}{dx}\right) \tag{1-22}$$

The electrical conductivity and Seebeck coefficients can be expressed as

$$\sigma = L_{11} = -\frac{e^2}{3}\int \tau v^2\, D(E)\frac{\partial f_0}{\partial E}dE = en\mu_e \tag{1-23}$$

$$L_{12} = \frac{e}{3T}\int \tau v^2 \left(E - E_f\right)D(E)\frac{\partial f_0}{\partial E}dE \tag{1-24}$$

$$\alpha = -\frac{(d\Phi/dx)}{(dT/dx)} = \frac{L_{12}}{L_{11}} = -\frac{1}{eT}\frac{\int \tau v^2 D(E)\frac{\partial f_0}{\partial E}\cdot\left(E-E_f\right)dE}{\int \tau v^2 D(E)\frac{\partial f_0}{\partial E}dE} \tag{1-25}$$

The expression indicates that the Seebeck coefficient is a measure of the average energy of an electron above the Fermi level weighted by the differential electrical conductivity at each energy level under the open circuit condition. That explains why energy filtering might enhance average Seebeck coefficient.

1.7.2 Thermal conductivity

Lattice thermal conductivity

The heat flux along the *x*-direction can be calculated by summing the phonons moving in the *x*-direction in the k space.

$$J_{qx} = \sum_s \frac{1}{V}\left[\sum_{k_x=-\infty}^{\infty}\sum_{k_y=-\infty}^{\infty}\sum_{k_z=-\infty}^{\infty} v_x \hbar\omega f\right] \tag{1-26}$$

where s represents the summation over all polarization, and f is the Bose-Einstein distribution. Transfer the Eq. (1-26) first into an integration over all wave-vectors and then into an integration over energy and solid angle.

$$J_{qx}(x) = \int_0^{\omega_{max}} d\omega\left\{\int_0^{2\pi}\left[\int_0^{\pi} v\cdot cos\theta\cdot h\omega\left(f_0 - \tau\frac{df_0}{dT}\frac{dT}{dx}v\cdot cos\theta\right)\frac{D(\omega)}{4\pi}\cdot sin\theta\cdot d\,\theta\right]d\varphi\right\}$$

$$= -\frac{1}{2}\frac{dT}{dx}\int_0^{\omega_{max}} d\omega\left\{\int_0^{\pi}\tau v^2\cdot sin\theta\cdot cos^2\theta\cdot\hbar\omega D(\omega)\frac{df_0}{dT}d\theta\right\} = -k_l\frac{dT}{dx} \tag{1-27}$$

Thus the thermal conductivity can be expressed as

$$k_l = \frac{1}{3}\int_0^{\omega_{max}} \tau v^2 C_\omega d\omega = Cv\Lambda/3 \tag{1-28}$$

where $\Lambda = \tau v$, and $C_\omega = \hbar\omega D(\omega)\, df_0/dT$, and the relax time ($\tau$) is highly frequency dependent.

At the low-temperature range (less than Debye temperature), the specific heat of the phonons can be estimated using the Debye model,

$$C(T) = \int_0^{\omega_{max}} C_\omega d\omega = \frac{36\pi^4 k_B}{15}\left(\frac{N}{V}\right)\left(\frac{T}{\theta_D}\right)^3 \propto T^3 \tag{1-29}$$

At the high-temperature range, the phonon specific heat calculated using the Einstein model is

$$C(T) = N_p k_B \left(\frac{N'}{V}\right)\frac{\left(\frac{\hbar\omega_E}{k_B T}\right)^2 \exp\left(\frac{\hbar\omega_E}{k_B T}\right)}{\left[\exp\left(\frac{\hbar\omega_E}{k_B T}\right)-1\right]^2} = constant \tag{1-30}$$

The thermal capacity of the electrons can be calculated using

$$C_e(T) = \int_0^\infty \left(E - E_f\right)\frac{df}{dT}D(E)dE \approx \frac{1}{2}\pi^2 n_e k_B T/T_f \propto T \tag{1-31}$$

Generally, the electronic thermal capacity is much smaller than the phonon specific heat in the semiconductors. Most of the thermoelectric materials work in the high-temperature range. Thus the thermal capacity can be assumed to be constant.

Bipolar thermal conductivity

Electrons and holes, respectively contribute the current in the thermoelectric material,

$$i_1 = \sigma_1\left(E - \alpha_1\frac{\partial T}{\partial x}\right), i_2 = \sigma_2\left(E - \alpha_2\frac{\partial T}{\partial x}\right) \tag{1-32}$$

The heat flux densities due to the two carrier types are

$$q_1 = \alpha_1 T i_1 - k_{e,1}\frac{\partial T}{\partial x}, q_2 = \alpha_2 T i_2 - k_{e,2}\frac{\partial T}{\partial x} \tag{1-33}$$

When examining the thermal resistance, the electrical current is set to be 0.

$$i_1 = -i_2 = \frac{\sigma_1\sigma_2}{\sigma_1+\sigma_2}(\alpha_1 - \alpha_2)\frac{\partial T}{\partial x} \tag{1-34}$$

The total heat flux contributed by the electrons and holes is

$$q = q_1 + q_2 = -\left(k_{e,1} + k_{e,2} + \frac{\sigma_1\sigma_2}{\sigma_1+\sigma_2}(\alpha_1 - \alpha_2)^2 T\right)\frac{dT}{dx} \tag{1-35}$$

For thermoelectric materials, it is expected that the first two terms are relatively small when compared with lattice heat transfer. The third term, known as the bipolar thermodiffusion effect, is observed most easily in semiconductors that have a small energy gap, where the density of minor carriers is significant.

$$k_b = \frac{\sigma_1\sigma_2}{\sigma_1+\sigma_2}(\alpha_1 - \alpha_2)^2 T \tag{1-36}$$

To suppress the bipolar thermal conductivity, the thermoelectric materials should be heavily doped to reduce the density of the minor carriers.

Electronic thermal conductivity

Similar to the treatment of the phonons, the electronic heat flux can be calculated using

$$J_q = \int (E - E_f) v_x f dv_x dv_y dv_z = L_{21}\left(E_x + \frac{1}{e}\frac{dE_f}{dx}\right) + L_{22}\left(-\frac{dT}{dx}\right) \tag{1-37}$$

where

$$L_{21} = \frac{e}{3}\int \tau v^2 \left(E - E_f\right) D(E) \frac{\partial f_0}{\partial E} dE = T L_{12} \tag{1-38}$$

$$L_{22} = -\frac{1}{3T}\int \tau v^2 \left(E - E_f\right)^2 D(E) \frac{\partial f_0}{\partial E} dE \tag{1-39}$$

The relation between the electronic current and the electronic thermal flux is given by

$$J_q = \frac{L_{21}}{L_{11}} J_e + \left(L_{22} - \frac{L_{12}L_{21}}{L_{11}}\right)\left(-\frac{dT}{dx}\right) = \Pi J_e - k_e \frac{dT}{dx} \tag{1-40}$$

where $\Pi = \frac{L_{21}}{L_{11}} = T\alpha$ is the Peltier coefficient and $k_e = L_{22} - \frac{L_{12}L_{21}}{L_{11}}$ is the electronic thermal conductivity.

As we know, the energy deposited inside a differential volume in the thermoelectric material includes heat fluxes variation and the electrochemical potential drop (Joule heat).

$$\dot{Q} = -\frac{dJ_q}{dx} + J_e\left(-\frac{d\Phi}{dx}\right) = -\left(T\frac{dS}{dT}\right) J_e \frac{dT}{dx} + \frac{d}{dx}\left(k\frac{dT}{dx}\right) + \frac{J_e^2}{\sigma} \tag{1-41}$$

which is the exact thermo-dynamic governing equations widely used in the multi-physics simulations of thermoelectrics.

1.7.3 Calculate the ZT using single-band theory

To better understand the interrelations between the thermal and electrical properties and find ways to enhance the performance of thermoelectric materials, in this section, the

ZT values of metals and semiconductors are calculated based on the classical one band theory.

Known from the section above, the expression of the coupling coefficients can be rewritten neatly as

$$L_{11} = -e^2K_0,\ L_{12} = -eK_1,\ L_{21} = -\frac{e}{T}K_1, \text{ and } L_{22} = -\frac{1}{T}K_2 \tag{1-42}$$

where $K_s = -\frac{1}{3}\int \tau v^2\, D(E)\,\frac{\partial f_0}{\partial E}E^s dE \quad (s = 1\sim3)$. Assuming that the relax time is related to energy via $\tau = \tau_0 E^r$ and the Fermi surface is spherical ($v^2 = \frac{2E}{3m^*}$),

$$K_s = -\frac{8}{3}\left(\frac{2}{h^2}\right)^{\frac{3}{2}}(m^*)^{\frac{1}{2}}T\tau_0\int \frac{\partial f_0}{\partial E}E^{r+\frac{3}{2}+s}\,dE \tag{1-43}$$

where $F_n(E) = \int \frac{\partial f_0}{\partial E}E^{r+\frac{3}{2}+s}\,dE$ is the Fermi-Dirac integral. The scatter factor (r) can vary in different situations, which are given as below.

Table 1.1. Phonon scattering factors in different situations

Dominate scattering mechanism	Scattering factor (r)
Acoustic phonon scattering	-1/2
Optical phonon scattering	1/2
Ironic scattering	3/2
Alloying scattering	-1/2
Neutral scattering	0

In non-degeneration case ($\eta = \frac{E-E_f}{k_BT} \ll 0$):

The Fermi-Dirac integral can be simplified as

$$F_n(\eta) = \exp(\eta)\int \xi^n exp(-\xi)\,d\xi = exp(\eta)\Gamma(n+1) \tag{1-44}$$

Eq. (1-43) is simplified to $K_s = -\frac{8\pi}{3}\left(\frac{2}{h^2}\right)^{\frac{3}{2}}(m^*)^{\frac{1}{2}}T\tau_0(k_BT)^{r+\frac{3}{2}+s}exp(\eta)\Gamma\left(r+\frac{5}{2}+s\right)$. Substituting K_s into the coupling coefficients, the Seebeck coefficient is read as

$$\alpha = \pm\frac{1}{T}\frac{L_{21}}{L_{11}} = \pm\frac{k_B}{e}\left[\eta-\left(r+\frac{5}{2}\right)\right] \tag{1-45}$$

The electrical conductivity is given by

$$\sigma = -e^2 K_0 = -\frac{8\pi e^2}{3}\left(\frac{2}{h^2}\right)^{\frac{3}{2}}(m^*)^{\frac{1}{2}} T\tau_0 (k_B T)^{r+\frac{3}{2}} exp(\eta)\Gamma\left(r+\frac{5}{2}\right) \tag{1-46}$$

The Lorenz number relates the electrical conductivity with the electrical conductivity

$$L = \frac{\lambda T}{\sigma} = \frac{1}{e^2 T^2}\left(\frac{K_2}{K_0} - \frac{K_1^2}{K_0^2}\right) = \left(\frac{k_B}{e}\right)^2\left(r+\frac{5}{2}\right) \tag{1-47}$$

And the electron density can be calculated using

$$n = \int f(E)g(E)dE = 2\left(\frac{2\pi m^* k_B T}{h^2}\right)^{3/2} exp(\eta) \tag{1-48}$$

In this case, substituting the equations above into the definition equation of ZT

$$ZT = \frac{\alpha^2 \sigma T}{k_l + k_e} = \frac{\alpha^2}{\frac{k_l}{\sigma T} + L} = \frac{\left[\left(r+\frac{5}{2}\right) - \eta_f\right]^2}{\left[\beta exp(\eta_f)\right]^{-1} + L} \tag{1-49}$$

where $\beta = \left(\frac{k_B}{e}\right)^2 \frac{\sigma_0}{k_l} T$, and $\sigma_0 = 2e\mu\left(\frac{2\pi m^* k_B T}{h^2}\right)^{3/2}$. It can be seen that the ZT value is only determined by β and η_f. To achieve the best doping level, $\frac{\partial(ZT)}{\partial \eta_f} = 0$,

$$\eta_{opt} + 2\left(r+\frac{5}{2}\right)\beta \cdot exp(\eta_{opt}) = r + \frac{1}{2} \tag{1-50}$$

In this equation, only r and β are variable. For the materials available now, $0 < \beta < 0.5$. To bound the best doping level, the r can vary between $\left[-\frac{3}{2}, \frac{3}{2}\right]$.

When $0 < \beta < 0.5$, since $r > -3/2$, $\eta_{opt} > -1.3$.

When $\beta \ll 1$, since $r < 3/2$, $\eta_{opt} < 2$.

To achieve the best doping level, the dimensionless Fermi level should be $-1.3 < \eta_{opt} < 2$. The doping level relates with the dimensionless Fermi level by

$$n = \frac{(m^*)^{1/2}}{2\pi^2}\frac{(2k_B T)^{3/2}}{\hbar^3} F_{r+\frac{1}{2}}(\eta_{opt}) \tag{1-51}$$

It is observed that the best doping level is only determined by Fermi-integration F and scattering factor r. Substituting η_{opt} and r into Eq. (1-51) above, the best doping level is $n = 10^{25\sim 26}\ m^{-3}$. It should be note that $-1.3 < \eta_{opt} < 2$ has already violated the pre-condition for non-degeneration ($\eta \ll 0$), but the principle still works in most situation.

To find the best Seebeck coefficient, $\frac{\partial(ZT)}{\partial \alpha} = 0$,

$$\alpha\left(\frac{d}{d\alpha}\log\alpha\right) = -2\left[1 + \frac{k_e}{k_l}\left(1 - \frac{1}{2}\cdot\frac{d(\log L)}{d(\log\alpha)}\right)\right] \tag{1-52}$$

$$\alpha_{opt} = -172\left(1 + \frac{k_e}{k_l}\right) \tag{1-53}$$

For most thermoelectric material, $\frac{k_e}{k_l} = 0.15 \sim 0.5$. Thus the optimum Seebeck coefficient should be $\alpha_{opt} = 200 \sim 250\ \mu V/K$. It should be noted that, in this estimation, the non-degeneration condition might be violated, so the conclusion here might not be exactly correct. But the real situation should not derivate much from the result here.

Assuming $\beta = 0.5$ and ironic scattering mechanism ($r = 3/2$) is dominated, a maximum *ZT* of 3.0 is achievable at an optimum doping level of $\eta_{opt} \approx 0.8$. So $ZT = 4.0$ is a safe margin for bulk semi-conductor based thermoelectric material.

In degeneration case ($\eta = \frac{E-E_f}{k_B T} \gg 0$), e.g., metals:

In this case, the Fermi-Dirac integral can be approximated by

$$F_n(\eta) = \exp(\eta) \int \xi^n exp(-\xi)\, d\xi = \frac{\eta^{n+1}}{n+1} + \frac{\pi^2}{6} n\eta^{n-1} + \cdots \qquad (1\text{-}54)$$

Then the equation to calculate the Seebeck coefficient can be simplified as

$$\alpha = \pm \frac{\pi^2}{3} \frac{k_B}{e} \frac{\left(r+\frac{3}{2}\right)}{\eta} \qquad (1\text{-}55)$$

And the electrical conductivity is given by

$$\sigma = -\frac{8\pi e^2}{3} \left(\frac{2}{h^2}\right)^{\frac{3}{2}} (m^*)^{\frac{1}{2}} \tau_0 (k_B T)^{r+\frac{3}{2}} \eta^{3/2} \qquad (1\text{-}56)$$

The Lorenz number in this situation is given by

$$L = \frac{\lambda T}{\sigma} = \frac{1}{e^2 T^2} \left(\frac{K_2}{K_0} - \frac{K_1^2}{K_0^2}\right) = \frac{\pi^2}{3} \left(\frac{k_B}{e}\right)^2 = constant \qquad (1\text{-}57)$$

This is the so-called Wiedemann-Franz law. This law is widely used to estimate the thermal conductivity contributed by electrons. In this case, the ZT is bounded by

$$ZT \leq \frac{3\pi^2}{64} = 0.46, \text{ if } \xi > 4. \qquad (1\text{-}58)$$

This bound is valid for all the metals.

In the section, a single-band model is used to estimate the upper limit of the *ZT* value. When the Fermi level is far away from the conducting band, the Seebeck coefficient approaches to infinite. This is not true in the real case. To solve this problem, the two band model was introduced in references [93-95]. Using this model [95], it was predicted that the ZT was less than 4.0 at room temperature in acoustic phonons scattering dominating situation. If acoustic and optical phonons both matter, the ZT<2.0 at room temperature and

ZT<4.0 at T=1200 K was predicted using the optimum material properties available at that time. This conclusion is still valid today, even for nanomaterials.

1.8 Strategies to enhance the ZT value of thermoelectric material

There are many ways to enhance the performance of thermoelectric materials. In the following section, some of the state-of-the-art approaches to design high-performance bulk thermoelectric materials are summarized. The discussion in this section is based on the theories built in Section 2.3. This summary tries to cover all aspects in the recent development in thermoelectric materials, from band engineering to microstructure manipulations, and from matrix/precipitates band alignment to compositionally alloyed nanostructures. This discussion can be a comprehensive guide to design and explore advanced thermoelectric materials.

1.8.1 Traditional ways to increase $\boldsymbol{\beta}$

As can be seen in Eq. (1-49), $ZT \propto \beta$, a larger β is desired to achieve higher ZT. β can be seen as a property of the thermoelectric material since all the parameters in the definition function are material properties. The concept to increase β to enhance ZT was first proposed by Ioffe [96].

$$\beta = \left(\frac{k_B}{e}\right)^2 \frac{\sigma_0}{k_l} T \propto \frac{\mu (m^*)^{3/2}}{k_l} \tag{1-59}$$

where k_l, μ and m^* are inter-related. Generally, the mobility (μ) will decrease with the increase of effective mass (m^*). To obtain the larger β, $\frac{\mu (m^*)^{3/2}}{k_l}$ shoud considered as a whole. It was found that, increasing the number of band extrema (N_V) might help to increase carrier effective mass m^* and thus the β. Good thermoelectric materials, such as Bi_2Te_3, PbTe, SiGe, $CoSb_3$, Mg_2Si, and half-Heusler alloy were observed to have multiple valleys. Currently, one of the frequently-used strategies to find material with high β is to examine materials with the asymmetry related N_V [97]. Another way to increase N_V is to converge different bands [98] in the Brillouin zone within a few k_BT variation. This phenomenon was observed in n-type $Mg_2Si_{1-x}Sn_x$ solid solutions, $PbTe_{1-x}Se_x$, and many others. Physically, the effective mass m^* relates directly to the curvature of the bands. Distorting the band [77] via doping might help to increase m^*.

To measure the β is more complicate than the electrical conductivity and Seebeck coefficient, as the carrier mobility and effective mass are involved. Some researchers observed an empirical law that might help to estimate the β in an easy way. There is a nearly linear relationship between α and $\ln\sigma$ for most heavily doped materials. The intercept that the line intersects with axis-$\ln\sigma$ is proportional to $\mu(m^*)^{3/2}$. This is an alternative way to measure the β.

1.8.2 Carriers concentration optimization to enhance ZT

As we have proved in Section 1.8.3, the optimum carrier concentration is about $n = 10^{25\sim26}\, m^{-3}$ to achieve the maximum ZT value. Figure 1.32 shows the how some parameters vary with carrier concentration in the thermoelectric material. Generally, the electrical conductivity and electronic thermal conductivity increase with the carrier concentration. The Seebeck coefficient, however, decreases with carrier concentration. As a result, the ZT value increases and then decreases with the carrier concentration. For simplification, in most case, the lattice thermal conductivity is thought can be manipulated independent from the electrical properties, though doping can reduce the lattice thermal conductivity by introducing lattice defects.

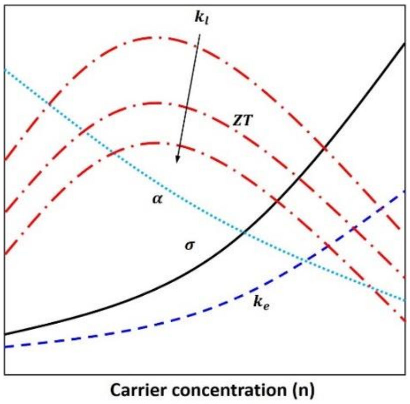

Figure 1.32. The variations of electrical conductivity, electronic thermal conductivity, Seebeck coefficient, and ZT with carrier concentration

1.8.3 Reduce the lattice thermal conductivity

Alloying and grain size manipulation to scattering phonons

The most straightforward idea to increase the figure of merit is to reduce the lattice thermal conductivity without significantly altering the electronic properties of the material (so-called phonon glass electron crystal concept). The phonon mean free path varies from 1-1000 nm, as shown in Figure 1.33. For different materials, the mean free path of phonons and their contribution to the thermal conductivity can be very different. For Si, over half of the thermal conductivity is contributed by phonons with a mean free path longer than 400 nm even at room temperature. However, for PbTe, about 10% of its thermal conductivity is contributed by phonons with mean free path larger than 10nm. Since most of the thermoelectric materials work in the high-temperature range (higher than their Debye temperatures), the phonons with high frequency can be effectively scattered via alloying. Thus the low-frequency phonons can play an important role in the alloying materials. All-scale hierarchical phonon [78] scattering concept was proposed in recent years to reduce the thermal conductivity of thermoelectric material to the low limit. It is expected that if the particle sizes are carefully manipulated, the introduced boundaries have a small effect on the electrons because de Broglie wavelength of electrons is larger than the dominant phonons. However, the experimental results could not support this hypothesis. This is most likely to be due to difficulties in nanoscale manufacturing and not an error in theory.

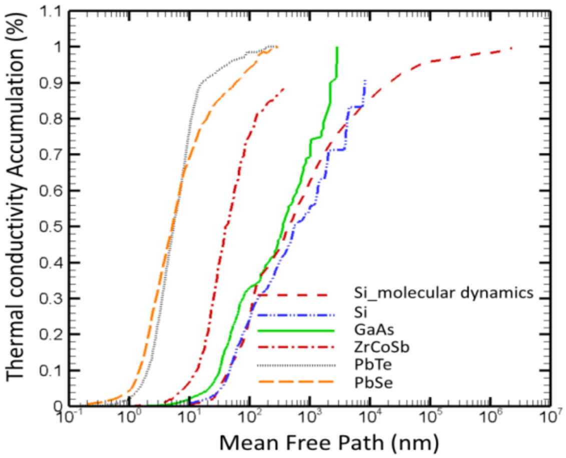

Figure 1.33. The accumulated lattice thermal conductivity of phonons [46].

Nanostructured material to suppress phonon transport

Another method to reduce the thermal conductivity is to introduce nanotechnology. The phonon dispersion in the low dimensional materials (Figure 1.34), including super-lattice, nanowire, and nanoparticle, are different from the corresponding bulk materials. Taking super-lattice for example, because of the acoustic mismatch at the grain boundary between two materials, the phonon transport perpendicular to the super-lattice plane can be effectively suppressed. However, the lattice thermal conductivity cannot be reduced to zero, since the mean free path of the phonon is always larger than the interatomic distance.

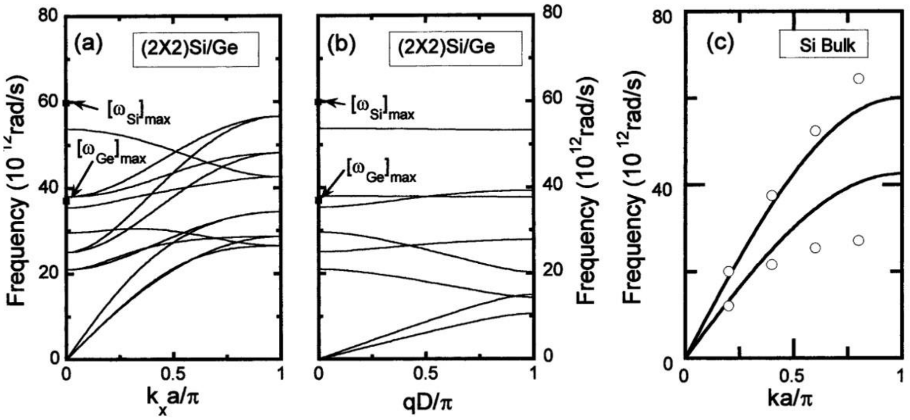

Figure 1.34. Phonon dispersion relation along and perpendicular to the super-lattice plane; Acoustic phonon in bulk Si [92].

1.8.4 Nanotechnologies to change the density of states of the electrons

Using nanotechnology to enhance the performance of thermoelectric material was first proposed by Hicks and Dresselhaus in their famous papers [49, 50] published in 1993. Taking a 2D material for example, the energy-wave-vector relationship can be described by

$$E(k_x, k_y, n) = \frac{\hbar^2}{2m^*}\left(k_x^2 + k_y^2\right) + n^2\frac{\hbar^2\pi^2}{2m^*d^2}\,(n = 1, 2, 3, \ldots\ldots, N) \quad (1\text{-}60)$$

where d is the width of the quantum well and m^* is the effective mass of the electron. In the *x* and *y* directions, the dispersion relationships are the same to the bulk material. While in the *z* direction, the energy becomes discrete. The density of states in the low dimensional materials are different from the corresponding bulk material, as shown in Figure 1.35.

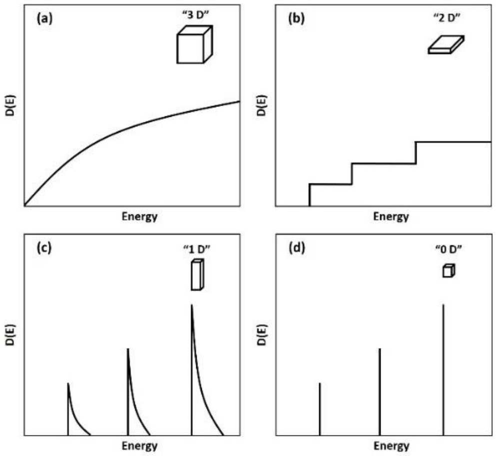

Figure 1.35. The energy density of states in (a) bulk, (b) quantum well, (c) quantum wire, and (d) quantum dot.

Substituting the energy dispersion relationship into Eqs. (1-23), (1-25), and (1-40), the electronic thermal conductivity, electronic conductivity, and Seebeck coefficient are given by

$$k_e = \frac{\tau\hbar^2}{4\pi a}\left(\frac{2k_BT}{\hbar^2}\right)\left(\frac{m_y}{m_x}\right)^{1/2} k_B\left(3F_2 - \frac{4F_1^2}{F_0}\right) \tag{1-61}$$

$$\alpha = -\frac{k_B}{e}\left(\frac{2F_1}{F_0} - \eta^*\right) \tag{1-62}$$

$$\sigma = \frac{e}{2\pi a}\left(\frac{2k_BT}{\hbar^2}\right)\left(m_xm_y\right)^{\frac{1}{2}}F_0\mu_x \tag{1-63}$$

where F_n is the Fermi-Dirac integration and $\eta^* = \left(E - E_f - \frac{\hbar^2\pi^2}{2m_zd^2}\right)/(k_BT)$.

The ZT for a 2D quantum well becomes

$$Z_{2D}T = \frac{\left(\frac{2F_1}{F_0}-\eta^*\right)^2 F_0}{\frac{1}{B'}+3F_2-\frac{4F_1^2}{F_0}}, \tag{1-64}$$

where $B' = \frac{1}{2\pi a}\left(\frac{2k_BT}{\hbar^2}\right)\left(m_xm_y\right)^{\frac{1}{2}}\frac{k_B^2T}{ek_l}\mu_x$.

Using this model, Hicks and Dresselhaus [49] predicted a dramatic increase of ZT with a decrease of the layer thickness (d). When $d = 3.8\ A$, it was theoretical predicted that $ZT = 6.0$ was achievable in the $a_0 - b_0$ plane orientation in the Bi_2Te_3 material. It was also claimed that an even higher ZT can be achieved for "1D" and "2D" materials. This was a remarkable achievement if this theory worked.

A lot of efforts was put into the study of nanostructured thermoelectric materials since this theory was proposed. People highly expected that the nanotechnology would greatly increase the ZT value. If a ZT of 4.0 was fulfilled, the TEG was able to compete with the combustion based thermal engines widely used in the industry, which would have a deep influence on the life of human beings. Until now, the highest ZT value reported was 3.5 in Bi-doped n-type PbSeTe/PbTe quantum-dot super-lattice by Harman et al. [4]. In 2019, Byeon et al. [99] reported a peak ZT>400 in Cu_2Se in a narrow temperature range.

1.8.5 Band engineering to enhance Seebeck coefficient

As we know from Section 1.7.1, the electrical conductivity can be expressed as

$$\sigma = ne\mu \tag{1-65}$$

The Seebeck coefficient can be rewritten as

$$\alpha = \frac{\pi^2}{3}\frac{k_B^2 T}{e}\left\{\frac{d[\ln\sigma(E)]}{dE}\right\}\bigg|_{E=E_F} = \frac{\pi^2}{3}\frac{k_B^2 T}{e}\left\{\frac{1}{n}\frac{dn}{dE}+\frac{1}{\mu}\frac{d\mu}{dE}\right\}\bigg|_{E=E_F} \tag{1-66}$$

It can be seen that, the Seebeck coefficient can be enhanced through (1) an increased energy dependence of $\mu(E)$, for instance by a scattering mechanism that strongly depends on the energy of the charge carriers (Figure 1.36), or (2) an increased energy-dependence of $n(E)$, for instance by a local increase in $g(E)$. According to Mahan-Sofo theory, systems in which there is a local increase in the density of states (DOS, $g(E)$) over a narrow energy range might help to increase Seebeck coefficient. Such a situation can occur when the valence or conduction band of the host semiconductor resonates with one energy level of a localized atom in a semiconductor matrix.

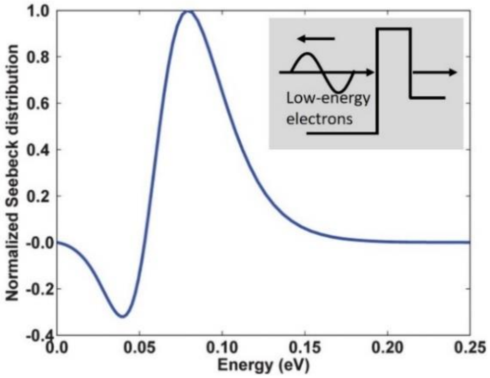

Figure 1.36. Scattering carriers with low energy to enhance Seebeck coefficient [46].

1.9 Objectives and contributions of the dissertation

The objective of this dissertation was to explore the thermoelectric application for energy recovery and sensor powering through innovations in material selection, device design optimization, and material fabrication. The contributions of the dissertation were broad, as explained as follows:

Contribution 1: In this dissertation, some of the most promising strategies for ZT enhancement were summarized together with the principles underneath. There were hundreds of papers published in thermoelectrics every year. The strategies to achieve high ZT were so divergent. This thesis tried to present a brief but clear picture of the recent advance in thermoelectrics and make the suggestions for the development of the next-generation high-performance thermoelectric materials.

Contribution 2: In this dissertation, a general model with reduced assumptions were made to analyze the impacts of the Thomson effect, contact resistance, and heat leakage on the performance of a TEG module. The model can be easily adapted for other thermoelectric energy harvesting systems.

Contribution 3: To enhance the temperature drop in the thermoelectric material, a high-performance microchannel heat sink with a large specific surface area was designed. The convective heat transfer performance of the self-oscillating jet generated by the fluidic oscillator was studied using large eddy simulation.

Contribution 4: In this dissertation, a novel method to optimize the geometry of a segmented TEG was first proposed based on the compatibility analysis. Theoretically, this method can make the most of the existing thermoelectric materials with high ZT values. The optimized module achieved an unprecedented efficiency of 23.72% at a temperature difference of 800 K. Selective laser melting was proposed for this module fabrication as the complicated shape can be easily realized via additive manufacturing.

Contribution 5: A novel integrated design and manufacturing of the nanostructured TEG by the one-step strategy using selective laser melting based additive manufacturing with graded doping was proposed. A comprehensive model to simulate the SLM processing of multi-component thermoelectric powders was established based on the conservation equations.

Contribution 6: Monitoring the temperature and pressure within the dry cask system was very important to ensure the safe storage of the nuclear-spent fuel. Two energy harvesters were built to harvest the gamma-radiation energy and thermal energy, respectively, within the canister for the self-powered sensors. The first energy harvester design utilized the gamma heating effect in the tungsten to create a hot spot for thermoelectric energy harvesting. The second design took advantage of the existing temperature gradient near the canister wall for thermoelectric energy harvesting. Radiation shielding design for the energy harvester and energy management circuit was demonstrated. The potential impacts of the gamma radiation on the thermoelectric materials were examined.

Contribution 7: In this dissertation, a thermoelectric energy harvester was designed to harvest the thermal energy from the gas turbine surface for the autonomous sensor nodes in the gas turbine, providing continuous, real-time, and reliable operation parameter sensing and monitoring. The energy output of this harvester was about 0.92 W with a source temperature of 325 °C, which met the energy demands of dozens of sensors nodes.

1.10 Dissertation Organization

The dissertation was divided into seven sections. In the first chapter, the recent progress in thermoelectrics was reviewed. Some of the most important techniques for thermoelectric material fabrication and characterization were summarized. The emerging technologies to enhance the performance of the thermoelectric materials, as well as the principle underneath, were summarized. The information in chapter one was broad, which acted as the basis for the following chapters. In the second chapter, a general thermodynamic model to analyze the performance of the thermoelectric generator was presented. This model was general and can be easily adapted to analyze the performance of any thermoelectric energy harvester. In the third chapter, a novel micro-channel heat sink was designed to enlarge the temperature drop within the energy harvester. Its heat transfer performance was characterized by the large eddy simulation. In the fourth chapter, a novel method based on the compatibility analysis was demonstrated to optimize the geometry shape of the thermo-element. This shape was complicated and could only be manufactured by additive manufacturing, for example, selective laser melting. In chapter five, a model developed based on the conservative equations was developed to simulate the heat and mass transfer processes during the selective laser melting of multi-component thermoelectric powders. In chapter six, two thermoelectric energy harvesters, one for gamma radiation energy harvesting and another for the temperature gradient energy harvesting, were demonstrated. These energy harvesters were developed to power the sensors enclosed in the canisters for nuclear spent fuel storage. In chapter seven, a compact thermoelectric energy harvester was designed to harvest thermal energy from the hot surface of the gas turbine for the sensor powering. In chapter eight, some of the key conclusions were summarized together with future work to further improve the performance of the thermoelectric energy harvesters. Besides these, some ideas coming into my mind during the Ph.D. study were shared at the end of the dissertation.

The chapter was adapted from a paper, "Yongjia Wu, Lei Zuo, Jie Chen, Jackson Klein. A model to analyze the device level performance of the thermoelectric generator, Energy, 115 (2016): 591-603."

Chapter 2. Increase the Efficiency of TEG via Thermal Network Optimization

2.1 Chapter introduction

The thermoelectric generator (TEG) was a distinctive solid-state heat engine with great potential in various scale energy harvesting. Device-level heat transfer coupled with energy conversion made the accurate analysis of the system very complicated. In this chapter, the thermodynamic analysis of a TEG module was carried out to study the influence of the contact layer resistance, Thomson Effect, Joule heat, and heat leakage on the performance of the TEG. All expressions of power output, current, and efficiency of the device were derived and compared with the experimental result of a commercial module. The equations for the simplified model were also given concisely to give a full picture of TEG modeling. The model could evaluate the influence of all the factors and redress some derivations in the existing models.

2.2 The limitation of the conventional model

The device level efficiency of the TEG was always much lower than the ideal situation because the temperature drop in the heat sink and encapsulation was significant. There were many mathematical models built to analyze the performance of TEG models [100-103]. In most cases, people neglected the contact layer thermal and electrical resistance, Thomson Effect, and heat leakage to simplify the models. However, with the development of MEMS, more subtle TEGs/TECs were required due to the significant influence from the factors mentioned above [5]. Thus, more accurate, resilient device level analysis was required to evaluate their performance. The conceptual design and optimization of TEG were still the main concerns in TEG research. An accurate analysis depended on a more sophisticated mathematical model. The performance of the TEG affected by the Fourier's heat conductivity, Peltier Effect, and Joule heat generation rate had been analyzed by many research works [104]. The influence of the Thomson effect on the performance of a thermoelectric generator was also studied by some articles [104], though in most cases, the Thomson Effect had a relatively small impact on the performance of TEG. In a real situation, heat sink and heat exchanger were fixed on the cold and hot end of TEG to maximize its efficiency and power output. Application of thermoelectric energy conversion from thermal to the electricity required careful device level analysis [103]. Besides, in the actual TEG module, there were many layers, such as a diffusion barrier between thermos-elements and interconnectors, air or thermal insulation materials filling the gap between P, N-type thermo-elements, and thermal grease layer between different components. Only when all these factors were taken into consideration, could we give a precise evaluation of the performance of a TEG module.

The most widely used thermodynamic model to evaluate the performance of the TEG module was the ideal one-dimensional TEG model given in many books [105]. This model assumed that the contact layer was ideal with no resistance and no heat leakage and no material properties changed with temperature. The model was coarse and, in most cases, would overestimate the performance of the device. Subsequently, researchers developed more accurate models to make a more precise description of the thermoelectric device. Min and Rowe[106] investigated the effect of thermo-element length on the module's coefficient of performance (COP) and heat pumping capacity. The results showed that the performance of TEG was largely deteriorated by the thermal/electrical contact resistances, particularly when the thermo-element length was small. As the Thomson Effect was secondary in thermoelectric modules, it could be neglected in most cases. However, the more accurate analysis found that Thomson Effect can significantly change the temperature profile in the thermos-elements and consequently influence their performance. Freunek et al.[104] put forward a model including the Thomson Effect, the Peltier heat, a parameterization of the Joule heat, as well as all thermal and electrical resistance. The model calculated the efficiency utilizing the temperature difference between the hot and cold ends of the thermos-elements by subtracting the temperature difference lost in the covering material and contact layers. However, the mathematical expressions were too complicated. They only gave power output and efficiency expressions with Thomson coefficients neglected. Huang et al.[107] analyzed the influence of the Thomson Effect on the maximum attainable temperature difference in the thermoelectric cooler (TEC). They suggested that COP could be improved by taking advantage of the Thomson effect in some cases. Chen et al.[102] conducted a non-equilibrium thermodynamic study on a couple of thermos-elements to assess the influence of Thomson Effect. In their research, a constant Thomson coefficient was introduced to avoid nonlinear thermodynamic equations. However, the model did not give the maximum efficiency and power output of the device. And, the research was also limited to the thermos-element level.

2.3 Thermodynamic analysis of thermo-elements

A thermoelectric generator was constructed by p, n-type elements connected electrically in series and thermally in parallel (Figure 2.1(a)). The thermal-electrical conversion efficiency of an ideal one-dimensional TEG could be described as

$$\phi_{max} = \eta_c \gamma = \frac{T_h - T_c}{T_h} \cdot \frac{\sqrt{1+ZT}-1}{\sqrt{1+ZT}+T_c/T_h} \tag{2-1}$$

The performance of TEG was dependent upon the thermoelectric properties of the material, and the hot and cold junction temperatures. In a real situation (Figure 2.1(b)), the performance of a TEG could be much more complicated when the electrical and thermal resistance, Thomson effect, heat leakage, and temperature drop in the heat sinks at the hot and cold end were taken into consideration.

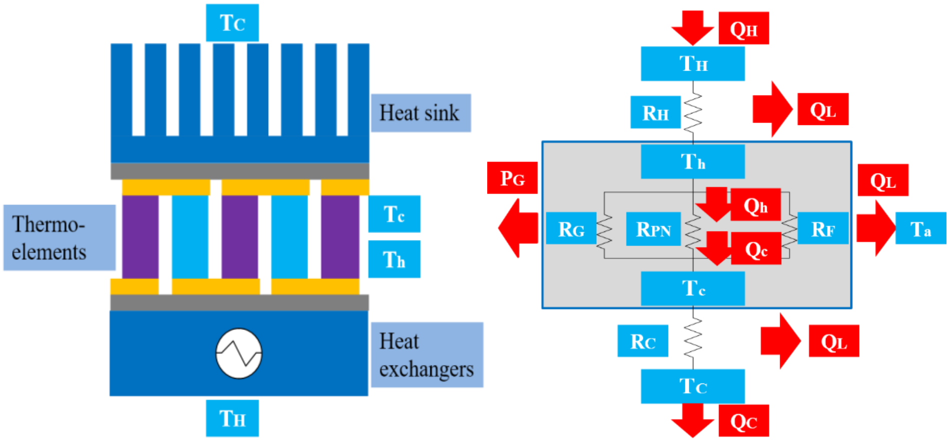

Figure 2.1. Schematic diagram of (a) TEG model; (b) Thermal network in the TEG

In the conventional method, the heat term was simplified by assuming that all the contact regions were ideal and the properties of the TE materials temperature were independent. The contribution of the Thomson effect was also neglected in many research papers, on the assumption that it was relatively small, which was true only when the device was operated at the relatively low-temperature difference and the Seebeck coefficients of TE materials showed little variations. Here we established our mathematical model based on the thermodynamic analysis. Some dimensionless parameters were introduced to make the model adaptable for different TEG device modeling.

The cross-section areas of P, N-type thermos-elements were A_P and A_N. The lengths of P, N-type thermos-elements were L_P and L_P, respectively. Assuming the average thermal conductivity of P, N-type TE materials were $\bar{\lambda}_P$and $\bar{\lambda}_N$, the thermal conductance of P, N-type thermo-pins were given by

$$K_P = \frac{\bar{\lambda}_P A_P}{L_P}, K_N = \frac{\bar{\lambda}_N A_N}{L_N}. \tag{2-2}$$

Similarly, the thermal conductance of ceramic cover in the hot and cold end was

$$K_{CH} = \frac{\bar{\lambda}_{CH} A_{CH}}{L_{CH}}, K_{CC} = \frac{\bar{\lambda}_{CC} A_{CC}}{L_{CC}}. \tag{2-3}$$

The P, N-type thermo-elements gap cross-section area was set as A_G. Then the cross-section area of a TEG could be described as

$$A_{CH} = A_{CC} = A_P + A_N + A_G. \tag{2-4}$$

Assuming the average electrical resistivity of P, N-type TE materials were $\overline{\rho_P}$ and $\overline{\rho_N}$, the electrical resistance of P, N-type thermo-elements were

$$R_P = \frac{\bar{\rho}_P L_P}{A_P}, R_N = \frac{\bar{\rho}_N L_N}{A_N}. \tag{2-5}$$

The Thomson Effect was a function of temperature and had the Kelvin relationship with Seebeck coefficient. In some studies, the Thomson coefficient was approximated as a polynomial function of temperature. Here we assume it was a constant to simplify the calculation. The assumption was of good precision when the temperature drop in the material was not large, and the Seebeck coefficient of the thermoelectric material varied monotonically with temperature ($\tau = T\, \partial\alpha / \partial T$).

The thermodynamic control equations in one-dimensional thermo-elements were

$$\text{N:} \frac{d^2 T}{dx^2} + \frac{I^2}{\bar{\lambda}_N} \frac{\bar{\rho}_N}{A_N^2} - \frac{I}{\bar{\lambda}_N} \frac{\bar{\tau}_N}{A_N} \frac{dT}{dx} = 0. \tag{2-6}$$

$$\text{P: } \frac{d^2T}{dx^2} + \frac{I^2}{\bar{\lambda}_P}\frac{\overline{\rho_P}}{A_P^2} + \frac{I}{\bar{\lambda}_P}\frac{\bar{\tau}_P}{A_P}\frac{dT}{dx} = 0. \tag{2-7}$$

Solving the equations above, the temperature profiles in the P, N-type thermos-elements were described as follows

$$\text{N: } T(x) = \frac{T_h - T_c - \frac{I\bar{\rho}_N}{\bar{\tau}_N A_N}L_N}{e^{\frac{\bar{\tau}_N I L_N}{\bar{\lambda}_N A_N}} - 1}\left(e^{\frac{\bar{\tau}_N I}{\bar{\lambda}_N A_N}x} - 1\right) + \left(\frac{I\bar{\rho}_N}{\bar{\tau}_N A_N}\right)x + T_c. \tag{2-8}$$

$$\text{P: } T(x) = \frac{T_h - T_c + \frac{I\bar{\rho}_P}{\bar{\tau}_P A_P}L_P}{e^{\frac{\bar{\tau}_P I L_P}{\bar{\lambda}_P A_P}} - 1}\left(e^{\frac{\bar{\tau}_P I}{\bar{\lambda}_P A_P}x} - 1\right) - \left(\frac{I\bar{\rho}_P}{\bar{\tau}_P A_P}\right)x + T_c. \tag{2-9}$$

where τ $(T\,\partial\alpha/\partial T)$ was the Thomson coefficient, I was the electrical current, T_h and T_c were the hot and cold end temperatures of the thermos-elements, respectively.

Heat flux in the cross-section could be calculated by

$$q = I\alpha T + \lambda A\frac{dT}{dx}. \tag{2-10}$$

Energy balances were maintained at the hot and cold ends of the devices. The heat fluxes through the hot/cold-end respectively were given by

$$q_h = q_{Nh} + q_{Ph} = \left(\alpha_P^h - \alpha_N^h\right)T_h I + \bar{\lambda}_N A_N \left.\frac{dT}{dx}\right|_{x=L_N} + \bar{\lambda}_P A_P \left.\frac{dT}{dx}\right|_{x=L_P}. \tag{2-11}$$

$$q_c = q_{Nc} + q_{Pc} = (\alpha_P^c - \alpha_N^c)T_c I + \bar{\lambda}_N A_N \left.\frac{dT}{dx}\right|_{x=0} + \bar{\lambda}_P A_P \left.\frac{dT}{dx}\right|_{x=0}. \tag{2-12}$$

where the Seebeck coefficients of P, N-type TE materials at the hot and cold end were α_P^h, α_P^c, α_N^h, α_N^c, respectively. Substituting Eqs. (2-8) and (2-9) into Eqs. (2-11) and (2-12) yielded

$$\begin{aligned} q_h = {} & \left(\alpha_P^h - \alpha_N^h\right)T_h I + (K_P^* + K_N^*)(T_h - T_c) + I^2[R_P^* + R_N^* - (R_P + R_N)] - \\ & (\tau_P - \tau_N)(T_h - T_c)I - I^2\left(R_{ch,P} + R_{ch,N}\right). \end{aligned} \tag{2-13}$$

$$q_c = (\alpha_P^c - \alpha_N^c)T_c I + (K_P^* + K_N^*)(T_h - T_c) + I^2(R_P^* + R_N^*) + I^2\left(R_{ch,P} + R_{ch,N}\right). \tag{2-14}$$

where

$$K_P^* = \frac{\tau_P I}{e^{\frac{\tau_P I L_P}{\lambda_P A_P}} - 1}, \quad K_N^* = \frac{\tau_N I}{e^{\frac{\tau_N I L_N}{\lambda_N A_N}} - 1}.$$

$$R_P^* = R_P\left[\frac{\lambda_P A_P}{\tau_P I L_P} - \frac{1}{e^{\frac{\tau_P I L_P}{\lambda_P A_P}} - 1}\right], \quad R_N^* = R_N\left[\frac{\lambda_N A_N}{\tau_N I L_N} - \frac{1}{1 - e^{\frac{\tau_N I L_N}{\lambda_N A_N}}}\right].$$

In Eqs. (2-13) and (2-14), the first term described heat absorbed by Peltier Effect, the second term specified the Fourier conductivity, the third term explained the Joule heat, the fourth term showed the Thomson heat and the last term was the contact layer Joule heat.

The electrical current passing the thermocouple could be expressed as

$$I = \frac{T_h(\alpha_P^h - \alpha_N^h) - T_c(\alpha_P^c - \alpha_N^c) - (\tau_P - \tau_N)(T_h - T_c)}{R_P + R_N + R_{ch,P} + R_{ch,N} + R_{cc,P} + R_{cc,N} + R_L} \tag{2-15}$$

Defining parameters as follows

$\alpha_{PN}^h = \alpha_P^h - \alpha_N^h,$

$\alpha_{PN}^c = \alpha_P^c - \alpha_N^c,$

$R_{PN} = R_P + R_N,$

$R_{ch} = R_{ch,P} + R_{ch,N} = \left(r_{ch,P} + r_{ch,N}\right)R_{PN},$

$R_{cc} = R_{cc} + R_{cc} = \left(r_{cc} + r_{cc,N}\right)R_{PN},$

$R_c = R_{cc} + R_{ch} = (r_{cc} + r_{ch})R_{PN},$

$R_G = R_{PN} + R_c = (1 + r_c)R_{PN},$

$R_L = sR_{PN},$

$\Delta T = T_h - T_c,$

$K_{PN} = K_P + K_N,$

$\tau_{PN} = \tau_P - \tau_N.$

The expressions for I and q_h could be simplified to

$$I = \frac{T_h\alpha_{PN}^h - T_c\alpha_{PN}^c - \tau_{PN}\Delta T}{R_G + R_L}, \tag{2-16}$$

$$q_h = \alpha_{PN}^h T_h I + (K_P^* + K_N^*)\Delta T + I^2(R_P^* + R_N^* - R_{PN}) - \tau_{PN}\Delta T I - I^2 R_{ch}. \tag{2-17}$$

The power output of the model was given by

$$P = q_h - q_c = I^2 R_L = \left(\alpha_{PN}^h T_h - \alpha_{PN}^c T_c\right)I - (\tau_P - \tau_N)\Delta T I - I^2 R_{PN} - I^2 R_c. \tag{2-18}$$

The efficiency of only one couple of P, N-type thermos-elements was as follows,

$$\eta = \frac{P}{q_h} = \frac{\left(T_h\alpha_{PN}^h - T_c\alpha_{PN}^c\right)I - (\tau_P - \tau_N)\Delta T I - I^2 R_{PN} - I^2 R_c}{\alpha_{PN}^h T_h I + \left(K_P^* + K_N^*\right)\Delta T + I^2\left(R_P^* + R_N^* - R_{PN}\right) - \tau_{PN}\Delta T I - I^2 R_{ch}}. \tag{2-19}$$

Substituting the dimensionless parameters into Eq. (2-19) yielded,

$$\eta = \frac{\left(T_h\alpha_{PN}^h - T_c\alpha_{PN}^c - \tau_{PN}\Delta T\right)^2 \frac{s}{1 + r_c + s}}{\left(\alpha_{PN}^h T_h - \tau_{PN}\Delta T\right)\left(\alpha_{PN}^h T_h - \alpha_{PN}^c T_c - \tau_{PN}\Delta T\right) + \left(K_P^* + K_N^*\right)\Delta T(1 + r_c + s)R_{PN} + \frac{\left(T_h\alpha_{PN}^h - T_c\alpha_{PN}^c - \tau_{PN}\Delta T\right)^2}{(1 + r_c + s)}\left(\frac{R_P^* + R_N^*}{R_{PN}} - 1 - r_{ch}\right)} \tag{2-20}$$

Defining the dimensionless parameters to simplify the above equations,

$$\frac{\alpha_{PN}^h}{\alpha_{PN}^c} = \mu, \frac{\tau_{PN}}{\alpha_{PN}^c} = \nu, \frac{K_P^* + K_N^*}{K_P + K_N} = \omega, \frac{R_P^* + R_N^*}{R_{PN}} = \theta. \tag{2-21}$$

Then Eq. (2-19) can be rewritten as

$$\eta = \frac{(T_h\mu - T_c - \Delta T\nu)^2 \frac{s}{1+r_c+s}}{(T_h\mu - \Delta T\nu)(T_h\mu - \Delta T\nu - T_c) + \frac{1}{Z_{PN}^c}\omega\Delta T(1+r_c+s) + \frac{(T_h\mu - \Delta T\nu - T_c)^2}{1+r_c+s}(\theta - 1 - r_{ch})}. \tag{2-22}$$

It was obvious that the efficiency of the TEG was determined by many factors. For the given TE materials, the Z value of the device could be optimized by changing the cross-section area ratio. The larger the Z is, the higher the efficiency would be. The maximum Z of the module was given by

$$Z_{PN}^c = \frac{(\alpha_{PN}^c)^2}{K_{PN}R_{PN}} \le Z_{max}^c = \frac{(\alpha_{PN}^c)^2}{\left(\sqrt{\lambda_N\rho_N} + \sqrt{\lambda_P\rho_P}\right)^2}, when\ A_P = A_N\frac{L_P}{L_N}\sqrt{\frac{\rho_P\lambda_N}{\rho_N\lambda_P}}. \tag{2-23}$$

The efficiency of the module could be rearranged as follows

$$\eta = \frac{(T_h\mu - T_c - \Delta T\nu)^2}{\frac{(T_h\mu - \Delta T\nu - T_c)[(T_h\mu - \Delta T\nu)(\theta + r_{cc}) + T_c(1 + r_{ch} - \theta)] + \frac{1}{Z_{PN}^c}\omega\Delta T(1+r_c)^2}{s} + \frac{1}{Z_{PN}^c}\omega\Delta T s + \left[\frac{2}{Z_{PN}^c}\omega\Delta T(1+r_c) + (T_h\mu - \Delta T\nu)(T_h\mu - \Delta T\nu - T_c)\right]} \tag{2-24}$$

Known from Eq. (2-14), the maximum efficiency of the module could be achieved when the denominator reached the peak value,

$$\eta \le \eta_{max} = \frac{(T_h\mu - T_c - \Delta T\nu)^2}{2\sqrt{\frac{1}{Z_{PN}^c}\omega\Delta T\left\{(T_h\mu - \Delta T\nu - T_c)[(T_h\mu - \Delta T\nu)(\theta + r_{cc}) + T_c(1 + r_{ch} - \theta)] + \frac{1}{Z_{PN}^c}\omega\Delta T(1+r_c)^2\right\}} + \left[\frac{2}{Z_{PN}^c}\omega\Delta T(1+r_c) + (T_h\mu - \Delta T\nu)(T_h\mu - \Delta T\nu - T_c)\right]} \tag{2-25}$$

When

$$s = \sqrt{\frac{(T_h\mu - \Delta T\nu - T_c)[(T_h\mu - \Delta T\nu)(\theta + r_{cc}) + T_c(1 + r_{ch} - \theta)] + \frac{1}{Z_{PN}^c}\omega\Delta T(1+r_c)^2}{\frac{1}{Z_{PN}^c}\omega\Delta T}}. \tag{2-26}$$

The power output of the module could be further simplified to

$$P = \left(T_h\alpha_{PN}^h - T_c\alpha_{PN}^c - \tau_{PN}\Delta T\right)^2 \frac{s}{(1+r_c+s)^2 R_{PN}}. \tag{2-27}$$

Taking typical Bi_2Te_3-based P, N-type thermos-elements (HZ-2 module, Technology, Inc.) for example, when $\lambda_P = 1.4\ \mathrm{W/K}$, $\lambda_N = 1.1\ \mathrm{W/K}$, $L_P = L_N = 0.298\ \mathrm{cm}$, $A_P = A_N = 0.0225\ cm^2$, $\tau_P = 9.33 \times 10^{-5}\ \mathrm{V/K}$, $\tau_N = 1.86 \times 10^{-5}\ \mathrm{V/K}$, $I = 0.5\ A$, $\left|\frac{\tau_P I L_P}{\lambda_P A_P}\right| = 0.0441 \ll 1$, $\left|\frac{\tau_N I L_N}{\lambda_N A_N}\right| = 0.0112 \ll 1$. Then the $K_P^*, K_N^*, R_P^*, R_N^*$ could be approximated as

$$K_P^* \cong K_P\left(1-\frac{\tau_P I L_P}{2\lambda_P A_P}\right),\ K_N^* \cong K_N\left(1+\frac{\tau_N I L_N}{2\lambda_N A_N}\right), \tag{2-28}$$

$$R_P^* \cong \frac{R_P}{2}\left(1+\frac{\tau_P I L_P}{6\lambda_P A_P}\right),\ R_N^* \cong \frac{R_N}{2}\left(1-\frac{\tau_P I L_N}{6\lambda_N A_N}\right). \tag{2-29}$$

Substitution of Eqs. (2-28) and (2-29) into Eqs. (2-13) and (2-14) yielded,

$$q_h = \alpha_{PN}^h T_h I + \left(K_{PN}-\frac{1}{2}\tau_{PN} I\right)\Delta T - \frac{1}{2}I^2 R_{PN} + \frac{I^3}{12}\left(\tau_P\frac{R_P}{K_P}-\tau_N\frac{R_N}{K_N}\right) - \tau_{PN}\Delta T I - I^2 R_{ch} \tag{2-30}$$

$$q_c = \alpha_{PN}^c T_c I + \left(K_{PN}-\frac{1}{2}\tau_{PN} I\right)\Delta T + \frac{1}{2}I^2 R_{PN} + \frac{I^3}{12}\left(\tau_P\frac{R_P}{K_P}-\tau_N\frac{R_N}{K_N}\right) + I^2 R_{cc} \tag{2-31}$$

Then the efficiency of the module could be simplified as follows

$$\eta = \frac{P}{q_h} = \frac{(\alpha_{PN}^h T_h - \alpha_{PN}^c T_c)I - \tau_{PN}\Delta T I - I^2 R_{PN} - I^2 R_c}{\alpha_{PN}^h T_h I + \left(K_{PN}-\frac{1}{2}\tau_{PN} I\right)\Delta T - \frac{1}{2}I^2 R_{PN} + \frac{I^3}{12}\left(\tau_P\frac{R_P}{K_P}-\tau_N\frac{R_N}{K_N}\right) - \tau_{PN}\Delta T I - I^2 R_{ch}} \tag{2-32}$$

In some simplified models, the Seebeck coefficients of the P, N-type thermos-elements were set to be constants. On doing this, the electrical current and efficiency of the module could be further simplified as follows

$$I = \frac{\Delta T \alpha_{PN}}{R_G + R_L} \tag{2-33}$$

$$q_h = \alpha_{PN}^h T_h I + K_{PN}\Delta T - \frac{1}{2}I^2 R_{PN} - I^2 R_{ch} \tag{2-34}$$

$$\eta = \frac{P}{q_h} = \frac{s\Delta T}{T_h(1+r_c+s) + \frac{1}{Z_{PN}}(1+r_c+s)^2 - \left(\frac{1}{2}+r_{ch}\right)\Delta T} \tag{2-35}$$

where $Z_{PN} = \frac{\alpha_{PN}^2}{K_{PN}R_{PN}} \leq Z_{max} = \frac{\alpha_{PN}^2}{\left(\sqrt{\lambda_N\rho_N}+\sqrt{\lambda_P\rho_P}\right)^2}, when\ A_P = A_N\frac{L_P}{L_N}\sqrt{\frac{\rho_P\lambda_N}{\rho_N\lambda_P}}$

When $\frac{\partial\eta}{\partial s} = 0,\ s = \sqrt{(1+r_c)^2 + \left[\left(\frac{1}{2}+r_{cc}\right)T_h + \left(\frac{1}{2}+r_{ch}\right)T_c\right]Z_{PN}},$

$$\eta_{max} = \frac{\Delta T}{2\sqrt{\frac{1}{Z_{PN}}\left[\left(\frac{1}{2}+r_{cc}\right)T_h + \left(\frac{1}{2}+r_{ch}\right)T_c + \frac{1}{Z_{PN}}(1+r_c)^2\right] + \frac{1}{Z_{PN}}(1+r_c) + T_h}} \tag{2-36}$$

If the heat loss and thermal resistance on the cold and hot end were not considered, the maximum efficiency of the model could be further simplified to Eq. (2-1). It is obvious that the maximum efficiency of the model was determined by the temperature at the cold and hot ends, and the ZT value of thermoelectric materials. This was exactly the one-dimensional ideal TEG model [108]. Though the one-dimensional model was simple and straightforward, there were some flaws. When the length of the TEG approached zero, the model predicted infinite power output of the system. However, it would never happen in real circumstance. Fortunately, the more accurate model we developed above can eliminate the flaw.

To evaluate how much the electrical resistance and the Thomson Effect could influence the performance of commercial modules [109], we used three mathematical models to analyze the commercial HZ-2 module. Here the value of electrical contact resistance was estimated from the device dimension level, and the Thomson coefficient was calculated from the property data sheet in the company website [109].

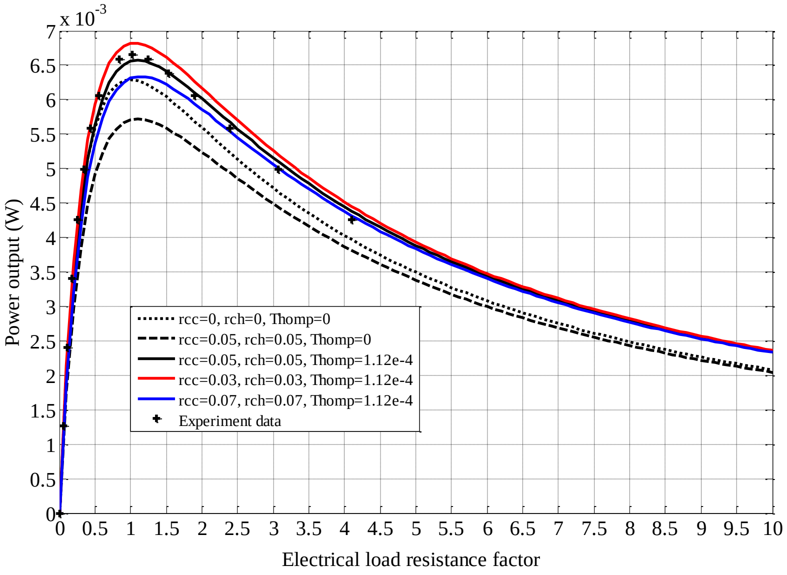

(a)

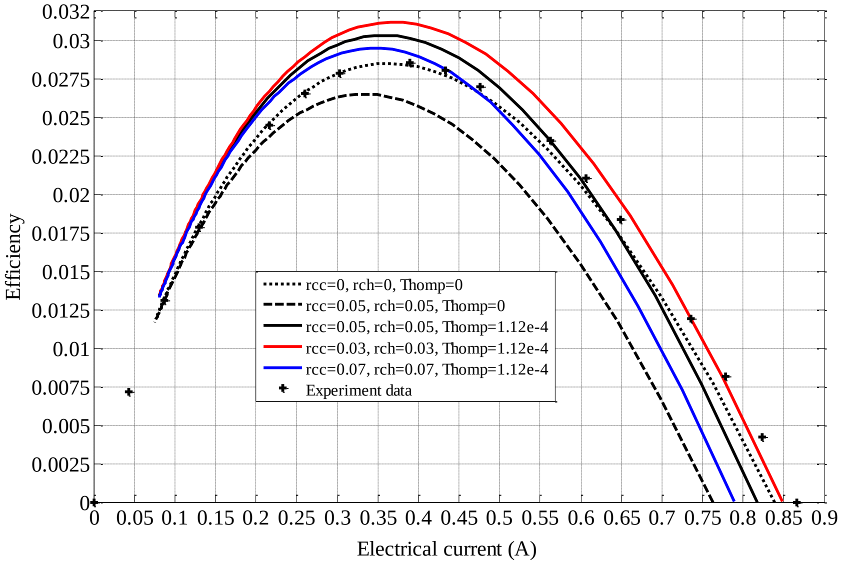

(b)

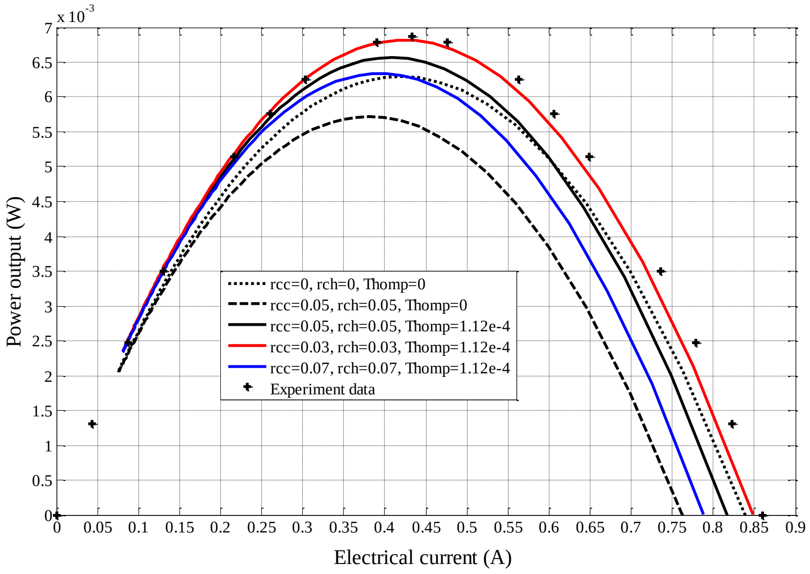

(c)

Figure 2.2. The performance modeling of a couple of thermo-elements: (a) Power output of device vs load resistance; (b) Efficiency of device vs electrical current; (c) Power output vs electrical current for $T_h = 150\ °\text{C}$, $T_c = 50\ °\text{C}$. Model I: $r_{cc} = r_{ch} = 0$, $\tau_P = \tau_N = 0$. Model II: $r_{cc} = r_{ch} = 0.05$ and $\tau_P = \tau_N = 0$. Model III: $r_{cc} = r_{ch} = 0.05, 0.03,$ or 0.07 and $\tau_P = 9.33 \times 10^{-5}\ \text{V/K}$, $\tau_N = -1.86 \times 10^{-5}\ \text{V/K}$.

As shown in Figure 2.2(a), all the three models could predict the performance of the device with reasonable accuracy. However, the improved model (model III) had the best accuracy. The maximum power output of a couple of thermo-elements was about 6.5×10^{-3} W, and the peak power output of the module was about 0.65 W. It should be noted that the coarsest model (Model I) matched the experiment data even better than the improved Model II. This happened not because Model I was better, but rather because the deviations introduced by electrical resistance and Thomson Effect counteract with each other. In Figure 2.2(b), Model I best matched with the experiment data, while Model III slightly overestimated the efficiency and model two underestimated the performance. The coarse model had a good performance here, because the Thomson heat here was coincidently in the same direction with Fourier heat flow, counteracting the contact layer Joule heat. Here, the performance of Model III could be further improved by introducing more accurate thermoelectric material property expressions. As shown in Figure 2.2(c), Model III could estimate the power output vs. electrical current best. However, in the high current range, the model underestimated the performance of the module. If we want to achieve better accuracy, more precise Thomson coefficient consideration should be adopted in the calculation.

2.4 TEG device-level performance

In a real TEG system (Figure 2.1), heat sinks/exchangers were often fixed at the hot and cold ends to maximum the highest temperature difference between the thermo-elements. To protect the thermoelectric materials from cracks and evaporation, some thermal and electrical insulation materials were introduced to fill the gaps between P, N-type thermo-elements. In the following section, we would present a model to predict the device level thermal performance of TEG.

Supposing the thermal conductances in the hot and cold end were K_H and K_C, respectively, the total thermal conductance in the hot and cold end were given by

$$\frac{1}{K_H} = \frac{1}{K_{CH}} + \frac{1}{K_{CCH}} + \frac{1}{K_{SH}} = \frac{1}{f_h}\frac{1}{K_{PN}} \tag{2-37}$$

$$\frac{1}{K_C} = \frac{1}{K_{CC}} + \frac{1}{K_{CCC}} + \frac{1}{K_{SC}} = \frac{1}{f_c}\frac{1}{K_{PN}} \tag{2-38}$$

where K_{CH}, K_{CCH} and K_{SH} were thermal conductance of hot end ceramic cover, contact layer and heat sink, respectively. K_{CC}, K_{CCC} and K_{SC} were thermal conductance of cold end ceramic cover, contact layer and heat sink, respectively.

To accurately calculate the performance of the whole device, the thermal conductance through the gas-filled space was given by

$$K_g = \frac{\lambda_g A_g}{L_g} + \varepsilon\sigma A_g (T_h^2 + T_c^2)(T_h + T_c) = f_g K_{PN} \tag{2-39}$$

where λ_g, A_g, L_g, ε were thermal conductivity of air, the cross-section area of the gas passage, gas passage length and emissivity of the ceramic plate surface. Since T_h and T_c were functions of hot and cold source temperature, f_g would slightly fluctuate during the calculation. We assumed it was constant. Here, $\sigma = 5.67 \times 10^{-8}\ W \cdot m^{-2} K^{-2}$ was the Stefan-Boltzmann constant. In order to reduce the thermal stress and heat leakage in the modules, thermal isolation material was often employed filling the air gap. For this situation, only the first term should be kept in Eq. (2-39).

Heat flow through the gas-filled space could be expressed as

$$q_g = K_g(T_h - T_c) \tag{2-40}$$

The energy conservation equation in the hot and cold end could be described as following

$$q_g = q_c = K_H(T_H - T_h) \tag{2-41}$$

$$P = q_h - q_c \tag{2-42}$$

Substituting Eqs. (2-63), (2-64) and (2-77) into Eqs. (2-91) and (2-92), the above equations could be rewritten as

$$\begin{cases} K_H(T_H - T_h) = \alpha_{PN}^h T_h I + (K_{PN} + K_g)\Delta T - \frac{1}{2} I^2 R_{PN} + \frac{I^3}{12}\left(\tau_P \frac{R_P}{K_P} - \tau_N \frac{R_N}{K_N}\right) - \frac{3}{2}\tau_{PN}\Delta T I - I^2 R_{ch} \\ K_H(T_H - T_h) - K_C[(T_h - \Delta T) - T_c] = I^2 R_L \end{cases} \tag{2-43}$$

The electrical current flowing through the thermoelectric material was given by

$$I = \frac{(\alpha_{PN}^c T_h - \tau_{PN})\Delta T + (\alpha_{PN}^h - \alpha_{PN}^c)T_h}{R_G + R_L} \tag{2-44}$$

Eq. (2-44) could be rearranged as

$$I = \frac{(\alpha_{PN}^h T_h - \tau_{PN})\Delta T + (\alpha_{PN}^h - \alpha_{PN}^c)T_c}{R_G + R_L} \tag{2-45}$$

Adding Eq. (2-45) into Eq. (2-46),

$$I = \frac{\left(\frac{\alpha_{PN}^h - \alpha_{PN}^c}{2} - \tau_{PN}\right)\Delta T + (\alpha_{PN}^h - \alpha_{PN}^c)\frac{T_h + T_c}{2}}{R_G + R_L} \tag{2-46}$$

The Thomson coefficient was constant for our model, then

$$\left(\alpha_{PN}^h - \alpha_{PN}^c\right)\frac{T_h + T_c}{2} \cong \tau_{PN}\Delta T \tag{2-47}$$

Eq. (2-46) was further simplified to

$$I = \frac{\alpha_{PN}^h + \alpha_{PN}^c}{2(R_G + R_L)}\Delta T \tag{2-48}$$

Substituting Eq. (2-48) into the Eq. (2-43), we obtain

$$C_1 \cdot \Delta T^3 + C_2 \cdot \Delta T^2 + C_3 \cdot \Delta T + C_4 = 0 \tag{2-49}$$

where

$$C_1 = \frac{s\alpha_{PN}^h\left(\alpha_{PN}^h + \alpha_{PN}^c\right)^3}{8(K_H + K_C)(1 + r_{cc} + r_{ch} + s)^3 R_{PN}^2} + \frac{1}{96}\frac{\left(\alpha_{PN}^h + \alpha_{PN}^c\right)^3}{(1 + r_{cc} + r_{ch} + s)^3 R_{PN}^3}\left(\tau_P \frac{R_P}{K_P} - \tau_N \frac{R_N}{K_N}\right)$$

$$C_2 = \frac{K_C\alpha_{PN}^h\left(\alpha_{PN}^h + \alpha_{PN}^c\right)}{2(K_H + K_C)(1 + r_{cc} + r_{ch} + s)R_{PN}} - \frac{1}{4}\frac{K_H\left(\alpha_{PN}^h + \alpha_{PN}^c\right)^2 s}{(K_H + K_C)(1 + r_{cc} + r_{ch} + s)^2 R_{PN}} - \frac{\left(\alpha_{PN}^h + \alpha_{PN}^c\right)^2(1 + 2r_{ch})}{8(1 + r_{cc} + r_{ch} + s)^2 R_{PN}} - \frac{3\tau_{PN}\left(\alpha_{PN}^h + \alpha_{PN}^c\right)}{4(1 + r_{cc} + r_{ch} + s)R_{PN}}$$

$$C_3 = \frac{(K_H T_H + K_C T_C)\cdot\alpha_{PN}^h\cdot\left(\alpha_{PN}^h + \alpha_{PN}^c\right)}{2(K_H + K_C)(1 + r_{cc} + r_{ch} + s)R_{PN}} + K_{PN} + K_g + \frac{K_C K_H}{K_H + K_C}$$

$C_4 = \frac{(K_H T_H + K_C T_C) K_H}{K_H + K_C} - K_H T_H$

This was a cubic equation that can be solved by the Cartan formula. The commercial HZ-2 TEG module fabricated by Hi-Z Technology, Inc., was employed to validate the model's accuracy. In the module, $\lambda_P = 1.4\, W/K$, $\lambda_P = 1.1\, W/K$, $L_P = L_N = 2.98$ mm, $A_P = A_N = 1.5 \times 1.5\, mm^2$, $\rho_P = 1.3 \times 10^{-5}\, \Omega \bullet m$, $\rho_N = 1.4 \times 10^{-5}\, \Omega \bullet m$, $\alpha_P^h = 2.1 \times 10^{-4}\, V/K$, $\alpha_P^c = 1.85 \times 10^{-4}\, V/K$, $\alpha_N^h = -1.80 \times 10^{-4}\, V/K$, $\alpha_N^c = -1.75 \times 10^{-4}\, V/K$, $\tau_P = 9.33 \times 10^{-5}\, V/K$, $\tau_N = 1.86 \times 10^{-5}\, V/K$, $I = 0.5\, A$, $K_P = 1.06 \times 10^{-3}\, Wm/K$, $K_N = 0.83 \times 10^{-3}\, Wm/K$, $R_P = 1.72 \times 10^{-3}\, \Omega$, $R_N = 1.85 \times 10^{-3}\, \Omega$, $f_g = f_c = 1.0$, $r_{cc} = r_{ch} = 0$. Substituting these values into the first and second terms of C_1,

$$\begin{cases} \frac{s\alpha_{PN}^h \left(\alpha_{PN}^h + \alpha_{PN}^c\right)^3}{8(K_H+K_C)(1+r_{cc}+r_{ch}+s)^3 R_{PN}^2} < \frac{\alpha_{PN}^h \left(\alpha_{PN}^h + \alpha_{PN}^c\right)^3}{8(K_H+K_C)(1+r_{cc}+r_{ch}+s)^2 R_{PN}^2} \sim 10^{-10} \\ \frac{\left(\alpha_{PN}^h + \alpha_{PN}^c\right)^3}{96(1+r_{cc}+r_{ch}+s)^3 R_{PN}^3} \left(\tau_P \frac{R_P}{K_P} - \tau_N \frac{R_N}{K_N}\right) < \frac{\left(\alpha_{PN}^h + \alpha_{PN}^c\right)^3}{96(1+r_{cc}+r_{ch}+s)^3 R_{PN}^3} \left(\tau_P \frac{R_P}{K_P} - \tau_N \frac{R_N}{K_N}\right) \sim 10^{-11} \end{cases} \tag{2-50}$$

For the HZ-2 TEG module, ΔT was less than 200 K for most situations, so the value of the first term of the equation was in the order of 10^{-3}. The values of other terms were of magnitude 10. When solving the equation, the first term could be neglected with little derivation, reducing the equation to a quadratic. Solving the coupled equations above, then we obtained

$$\begin{cases} T_h = f(T_H, T_C) \\ I = g(T_H, T_C) \\ T_h = h(T_H, T_C) \end{cases} \tag{2-51}$$

In the case when $\alpha_{PN}^h = \alpha_{PN}^c = \alpha$ and $\tau_{PN} = 0$, the above equations was furtherly simplified as follows

$$\begin{cases} K_H(T_H - T_h) = \frac{\alpha^2 \cdot \Delta T \cdot T_h}{R_G + R_L} + K_{PN}\Delta T - \frac{1}{2}\left(\frac{\alpha \Delta T}{R_G + R_L}\right)^2 (R_{PN} + 2R_{ch}) \\ K_H(T_H - T_h) - K_C[(T_h - \Delta T) - T_c] = \left(\frac{\alpha \Delta T}{R_G + R_L}\right)^2 R_L \end{cases} \tag{2-52}$$

The factors in the cubic equation reduced to

$C_1 = \frac{-s\alpha_{PN}^4}{(K_H+K_C)(1+r_{cc}+r_{ch}+s)^3 R_{PN}^2} \sim -10^{-10}$

$C_2 = \frac{K_C \alpha_{PN}^2}{(K_H+K_C)(1+r_{cc}+r_{ch}+s) R_{PN}} - \frac{K_H \alpha_{PN}^2 s}{(K_H+K_C)(1+r_{cc}+r_{ch}+s)^2 R_{PN}} - \frac{\alpha_{PN}^2 (1+2r_{ch})}{2(1+r_{cc}+r_{ch}+s)^2 R_{PN}}$

$C_3 = \frac{(K_H T_H + K_C T_C) \cdot \alpha_{PN}^2}{(K_H+K_C)(1+r_{cc}+r_{ch}+s) R_{PN}} + K_{PN} + K_g + \frac{K_C K_H}{K_H + K_C}$

$C_4 = \frac{(K_H T_H + K_C T_C)K_H}{K_H + K_C} - K_H T_H$

The value of the first term of the equation was of magnitude 10^{-3}. The values of other terms were of magnitude 10, so the first term can be neglected with little derivation when solving the equation. Eq. (2-52) was widely used to obtain the effective temperature drop in the thermo-elements.

Comparing the calculation results of the three models for the commercial HZ-2 TEG module, we were able to evaluate the sensitivity of the TEG module to electrical resistance at the contact layer, filled gap heat flow leakage, and Thomson coefficients. In the coarsest model, the Thomson effect and contact layer electrical resistance were unaccounted. The constant Thomson coefficient, the filled gap heat flow, and various contact layer electrical resistance were then added into the consideration for the improved models. The situations we employed were list in Table 2.1.

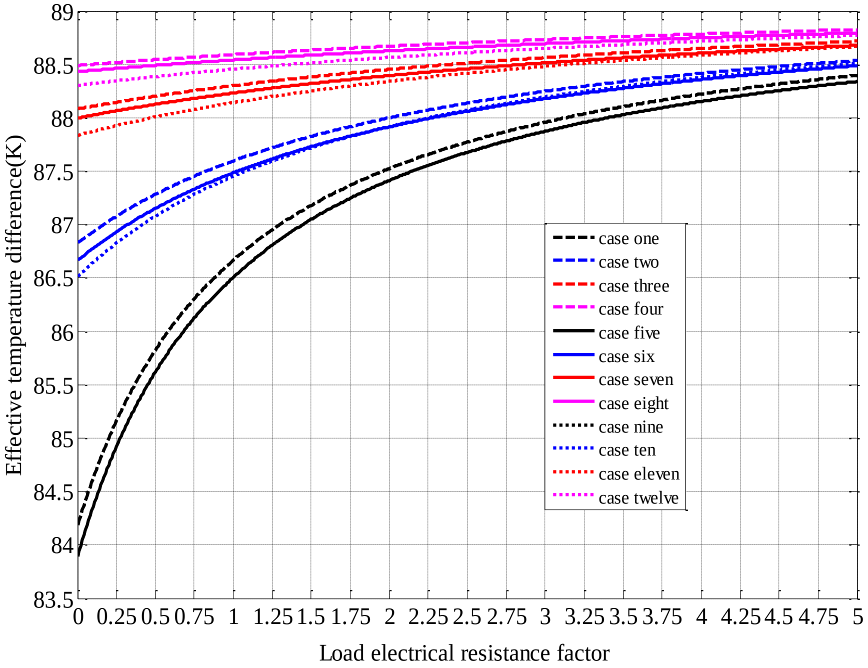

(a)

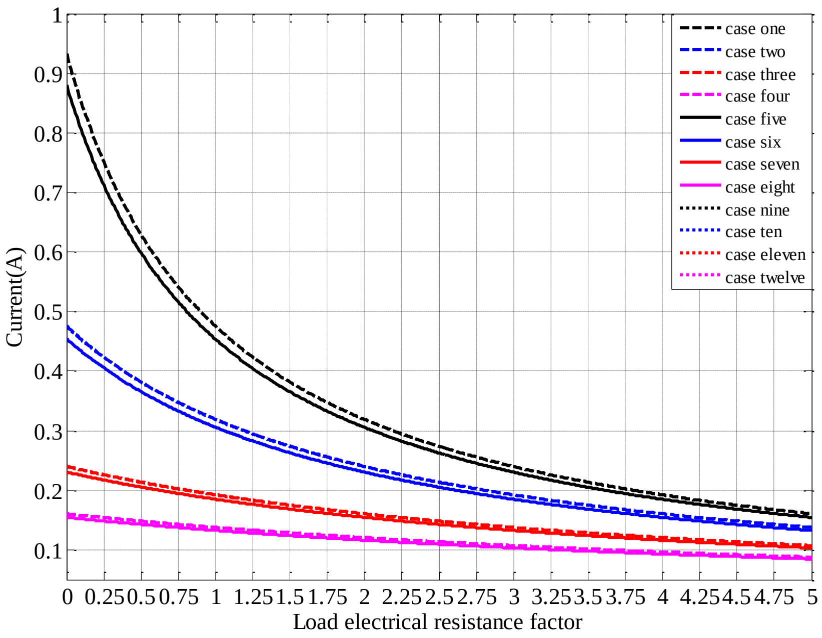

Current(A)
Load electrical resistance factor
0
0.1
0.2
0.3
0.4
0.5
0.6
0.7
0.8
0.9
1
0.25
0.5
0.75
1.25
1.5
1.75
2
2.25
2.5
2.75
3
3.25
3.5
3.75
4
4.25
4.5
4.75
5
case one
case two
case three
case four
case five
case six
case seven
case eight
case nine
case ten
case eleven
case twelve

(b)

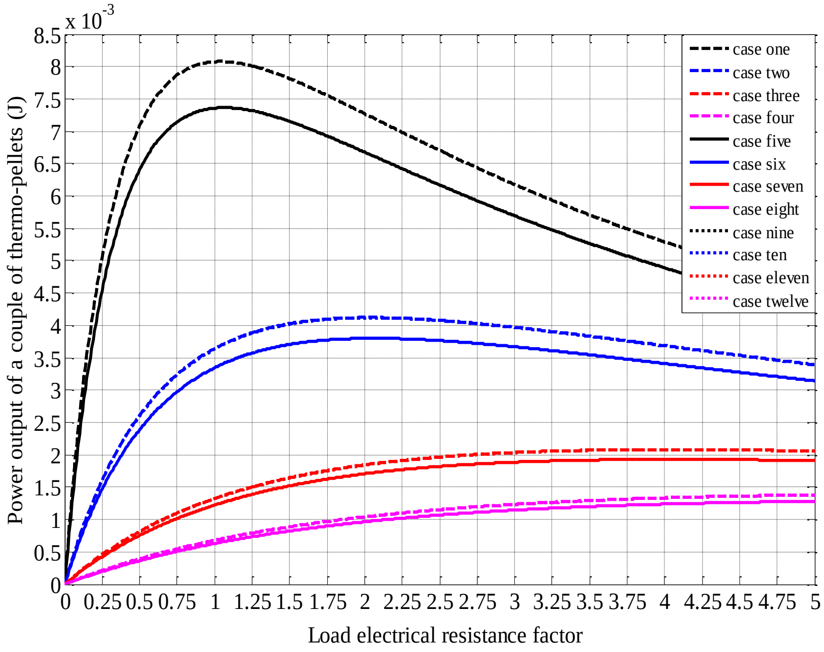

x 10^-3
Power output of a couple of thermo-pellets (J)
Load electrical resistance factor
0
0.5
1
1.5
2
2.5
3
3.5
4
4.5
5
5.5
6
6.5
7
7.5
8
8.5
0.25
0.75
1.25
1.75
2.25
2.75
3.25
3.75
4.25
4.75
case one
case two
case three
case four
case five
case six
case seven
case eight
case nine
case ten
case eleven
case twelve

(c)

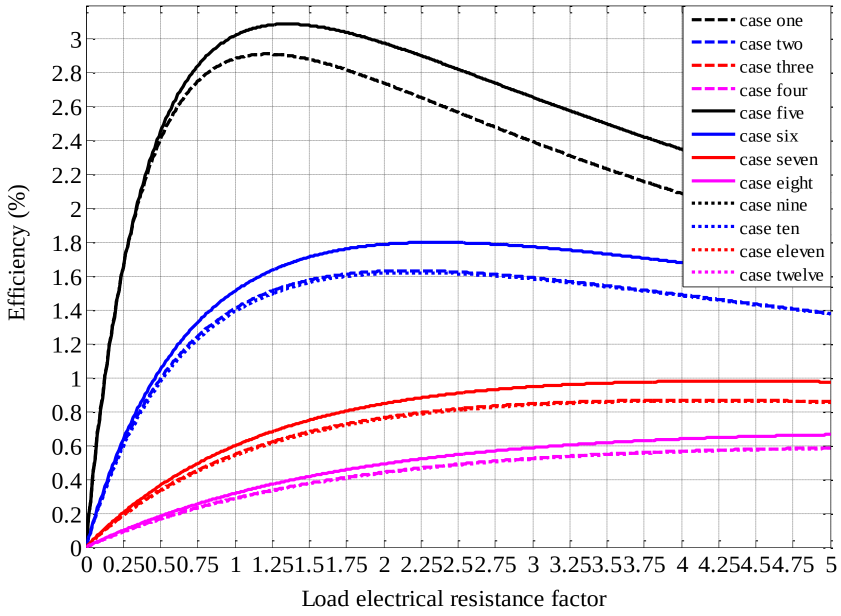

(d)

Figure 2.3. Modeling of TEG system based on commercial HZ-2 TEG module: (a) Effective temperature varied with load electrical resistance factor; (b) Current varied with load electrical resistance factor; (c) Power varied with load electrical resistance factor; (d) Efficiency varied with load electrical resistance factor.

Table 2.1. Cases to exam the models

Cases	r_{ch}	r_{cc}	τ_{PN}
Case one	0	0	1.12×10^{-4}
Case two	1	0	1.12×10^{-4}
Case three	3	0	1.12×10^{-4}
Case four	5	0	1.12×10^{-4}
Case five	0	0	0
Case six	1	0	0
Case seven	3	0	0
Case eight	5	0	0
Case nine	0	0	1.12×10^{-4}
Case ten	0	1	1.12×10^{-4}
Case eleven	0	3	1.12×10^{-4}
Case twelve	0	5	1.12×10^{-4}

*Parameter values adopted in the modeling: T_H=423 K, T_C=323 K, f_H=f_C=10, f_g=0.1.

As Figure 2.3(a) illustrated, the temperature difference between the hot and cold ends increased with the load resistance because larger load resistance led to less Peltier heat absorption at the ends. When the Thomson Effect was accounted for, for the same contact layer electrical resistance, the temperature difference was slightly lower than the coarse model (model one). Also, the contact layer electrical resistance would significantly change the temperature difference. It could be reasons as the larger contact electrical resistance resulted in smaller electrical current, consequently less Peltier heat absorption at the two ends.

Figure 2.3(b) showed the electrical current output of the TEG device. It was obvious that the larger contact layer electrical resistance, the lower current output was. However, when the contact resistance had the same value, loading it on the hot or cold end caused some variation in the temperature distribution, but it had little impact on the current output of the system. Also, the Thomson coefficient in the HZ-2 model slightly increased the current output. Figure 2.3(c) showed the power output of a couple of thermo-elements in the device. It was found that larger electrical resistance in the hot/cold end contact layer lowered the power output of the system. When the electrical contact layer was as large as the internal electrical resistance, the power output could be only half of that when no contact layer electrical resistance was considered. The Thomson effect did affect the power output of the system, with about 10% percent increase for the same electrical load resistance factor. Also, the optimized electrical load resistance for the peak power output shifted to a higher value. It was reasonable since the peak power output was achieved when electrical load resistance equaled to the internal resistance. It was safe to conclude that Thomson Effect cannot be neglected for accurate modeling analysis when temperature gradient was large (~5.0×10^4 K/m) in the thermo-elements, and that contact layer electrical resistance could largely reduce the maximum power output of the system.

As seen in Figure 2.3(d), the efficiency of the device increased quickly and then decreased gradually as the electrical load resistance increased. Here the efficiency of the improved model was slightly lower than the coarse one. It could be reasoned as a combined result of two phenomena: on the one hand, heat leakage through the thermal isolation material is taken into consideration in the improved model reduced the module efficiency; on the other hand, Thomson Effect slightly increased the conversion efficiency. It reminded us that, through careful thermoelectric material doping, making the Seebeck coefficients gradient matched with the temperature gradient, we could maximize the current, power output, and efficiency of the device by taking advantage of Thomson Effect. Moreover, the electrical resistance at the contact layer significantly lowered the efficiency of the whole system. Perfect contact layer was of vital importance for the device fabrication, especially when the device was micrometers thick. When contact layer electrical resistance increased, the electrical load resistance corresponding to peak efficiency shifted from low value to high value, and the efficiency of the device became un-sensitive to the load resistance. In MEMS fabrication, the device might have larger individual differences because the contact layer resistance was difficult to control.

2.5 Summary for the chapter

In section 2.4, we developed a more accurate model to evaluate the performance of a TEG module with the contact layer resistance, Thomson Effect, Joule heat, and thermo-element gap heat leakage all taken account. The sensitivity of the factors, including hot and cold end electrical resistance, and Thomson Effect, which might affect the module's performance, were analyzed. Through modeling and analysis, we could draw the following conclusions:

1) The thermoelectric effect of Seebeck, Peltier, and Thomson effects was integrated with Fourier heat and Joule source terms to analyze the performance of the TEG modules. A constant Thomson coefficient was accounted, and both full and simplified expressions of the voltage, current, power output, and efficiency were given by introducing some dimensionless parameters. Comparisons between the three models and experimental results validated the accuracy of the improved model. The results indicated that the Thomson Effect could become significant when the temperature gradient was relatively large in the module. Neglecting the effect could lead to as more as 10% derivation from the actual efficiency in some cases. Careful material doping could help to increase the efficiency of the device by taking advantage of the Thomson Effect.
2) Thermal and electrical resistance at the contact layers no doubts deteriorated the performance of the TEG module. The contact layer thermal resistance reduced the effective temperature drop in the thermo-elements, while the electrical resistance significantly reduced the peak efficiency and power output of the device. The effect could be more notable for MEMS TEG because the internal resistance of such TEGs

were small and tiny flaws in the contact layer would markedly deteriorate its performance.

3) The thermal resistance of the ceramic covers and heat sinks/exchangers fixed at the two ends of the TEG system had a negative influence on the system performance. Heat leakage via the gap between the thermo-elements was another factor reducing its efficiency. The narrower gap and filling materials with higher thermal resistivity were required for high-performance TEG system design.

In Section 2.5, the Thomson Effect was set to be a constant to linear the heat transfer governing equation in the model. The improved model was more accurate, and it was adaptable to analyze various TEG systems by specifying the geometry sizes and material properties of a given system. A further study using numerical tool to simulate the coupled effects of thermal-electric in the TEG system would be conducted in the later chapters, in which more sophisticated material properties expressions and better boundary control could be used to reduce the derivations further.

The chapter was adapted from a paper, "Yongjia Wu, Shifeng Yu, Lei Zuo. Large eddy simulation analysis of the heat transfer enhancement using self-oscillating fluidic oscillators. International Journal of Heat and Mass Transfer, 131 (2019): 463-471."

Chapter 3. Heat Sink Design Integrating the Sweeping Impinging Jet

3.1 High-performance heat sink design for TEG

Conventional heat sinks took advantage of pin-fin to improve the hot side temperature and sweeping-impingement cooling to reduce the cold side temperature, providing the maximum temperature difference between the hot and cold sides of the TEG. This, in turn, provided higher efficiency and power output from the TEG. In this chapter, we developed an advanced heat exchanger based on heat exchangers that were examined by Dr. Ekkad. [110] (see Figure 3.1(a)-(b)) and fluidic oscillators designed in our group. The addition of pin fins in the hot gas path of the tailpipe provided increased heat transfer coefficients as well as increased surface and residence time for heat transfer. The cold side junction of the TEG element was cooled by enhanced sweeping-impingement cooling to provide near coolant temperatures. The temperature difference could be maximized in this way to enhance the energy conversion efficiency of the thermoelectric energy harvester for vehicle exhaust energy harvesting.

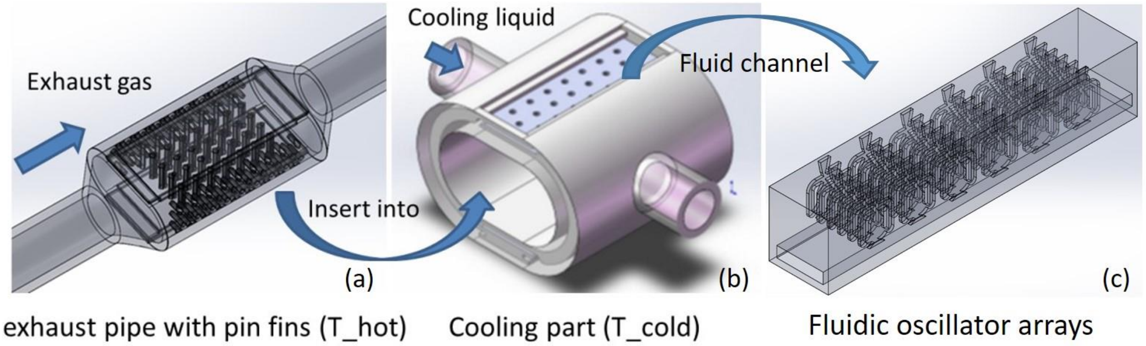

Figure 3.1. Innovative heat exchanger design that could increase the heat transfer [110]

3.2 Introduction to the fluidic oscillators

The fluidic oscillator was a unique device that can convert a steady state jet into an oscillatory one based on the intrinsic flow instability mechanisms. The attractive features of the fluidic oscillator for flow control was its characteristics of unsteady blowing, which could be used to manipulate the flow field without any moving parts actively. The fluidic oscillator was widely used in flow separation control, jet thrust vectoring, cavity tone suppression, drag reduction, combustion control, and heat transfer enhancement [111-114]. Numerous design had been proposed since it originated from the 1960s. Generally, the fluidic oscillators can be categorized into two types, wall-attachment and jet-interaction oscillators [115], regarding the driven mechanisms of the oscillations. The wall-attachment type with two feedback channels, as shown in Figure 3.1, was the most often studied one and would be adopted for the analysis in this thesis.

A typical wall-attachment fluidic oscillator included a power nozzle, the main mixing chamber, two feedback channels, and an exit throat. Though the general working principles of the fluidic oscillators were well documented in various literature [113, 116], the detailed flow physics of these devices was not. The jet coming out from the power nozzle would attach to one of the two side walls of the mixing chamber due to the Coanda effect. As the flow field was not symmetric, the fluid mass rates entering into the two feedback loops were different. This transverse disturbance led to a change in the pressure through the control nozzles, which drove the power jet to detach from the original sidewall and attach to the opposite sidewall. Due to the symmetry of the device, the same process repeated, resulting in an oscillatory fluid motion at the exit throat. Previous research found that fluidic oscillators were robust in a wide range of operating conditions.

The fluid dynamic characteristics of the fluidic oscillators, such as the oscillation frequency, pressure variation, and oscillating amplitude, were intensively studied in many open kinds of literature. Seo et al. [117] used a 2-D dimensional model to investigate the internal fluid dynamics of a fluidic oscillator by solving the incompressible Navier–Stokes equations. They analyzed the influence of geometric variations, including changes in the feedback channel length and the mixing chamber length on the oscillation frequency and amplitude. Woszidlo and Wygnanski [118] experimentally and numerically investigated the parameters governing separation control using an array of sweeping jet actuators distributed evenly along the span of a generic airfoil. They found that by controlling separation, actuation still yielded almost twice the range of lift coefficients accompanied by almost twice the maximum lift-to-drag ratio. Metka and Gregory [119] experimentally studied drag reduction on the 25-deg Ahmed generic vehicle model with quasi-steady blowing at the roof–slant interface using a span-wise array of fluidic oscillators. A drag reduction up to 7.5% was observed on the model with the actuation. The reduction was due to separation control on the slant surface. Jeong and Kim [120] optimized the 3-D geometry shape of a fluidic oscillator by solving the transient Reynolds-averaged Navier-Stokes (RANS) equations to enhance peak jet velocity at the exit throat and simultaneously reduce pressure drop. Bobusch et al. [121] did experiments to investigate the internal flow characteristics of a fluidic oscillator. Geometrical features, in particular at the inlet and outlet of the mixing chamber, were found to have crucial impacts on oscillation frequency and jet deflection. Choephel et al. [122] conducted experiments to explore the use of fluidic oscillators for improving the aerodynamic performance of the S903 airfoil. The improvements in lift coefficient ranged from 10% to 20% depending on the Reynolds number. The actuation level was studied in the experiments. The same phenomenon was observed in work done by DeSalvo et al. [123]. Cattafesta and Sheplak [124] gave a detailed review of using fluidic oscillators for active flow control.

Most of the research on fluidic oscillators focused on their fluid dynamic performance. Using sweeping jet impingement caused by the fluidic oscillator for heat transfer enhancement application was still relatively new. Jet impingement was an effective way to cool device working in a high-temperature environment, such as vane leading edge cooling in gas turbine [114]. However, steady jet impingent could only effectively cool a hot spot, as the Nusselt number decreased drastically from the stagnation point to the sides. The sweeping jet had great potential enhancing impingement heat transfer through its larger spreading angle and regions of high turbulent mixing due to the sweeping nature of the flow at the exit throat. There was a great potential to implement the present self-oscillating-impinging-jet concept in future gas turbine cooling systems, electronics cooling, multi-phase cooling, micro-fluid cooling, and thin film cooling. Camci and Herr [112] first used a self-oscillating-impinging-jet configuration to enhance the heat removal performance of the impinging jets. The new design significantly enhanced the heat transfer coefficient ranging from 20 percent to 70 percent over the stationary jet values because of the oscillation motion of the impinging jet together with the larger impingement zone. Hossain et al. [114] developed a sweeping jet film cooling technology based on conventional curved fluidic oscillators to improve the cooling effectiveness of gas turbine engines. Both experimental and numerical studies were conducted to test the performance of a row of five sweeping jet film cooling holes. They found that the unsteady sweeping action of the jet augmented the heat transfer near the hole exit. In their other work [113], they used unsteady RANS simulations to analyze the effects of surface curvature on the performance of sweeping jet impingement heat transfer. Agricola et al. [111] compared the heat transfer coefficient of a sweeping impinging jet to a steady circular orifice jet. They found that impingement heat transfer using a sweeping jet was improved at high Reynolds numbers. Park et al. [125] experimentally examined the heat transfer of a sweeping jet impinging on a flat wall for several Reynolds number and nozzle-to-plate spacings. Compared to a steady round jet, the sweeping jet showed the superior capability of heat transfer.

The self-oscillating impinging jet had great potential to be implemented in future high-performance multi-phase cooling, modern electronic cooling, and compact heat exchangers. Though a lot of progress was made in recent years, using fluidic oscillators for heat removal was still not fully explored. For example, in refs. [125] and [111], the conclusions on the heat transfer enhanced using self-oscillating impinging jet for low Re numbers (Re<10000) were not consistent. These can be reasoned as follows. On the one hand, to accurately measure the convective heat coefficients was by no means an easy task. On the other hand, the two-equations RANS turbulence model, for example, the commonly used $k-\omega$ SST model, might overestimate the heat convective coefficients for direct jets [126]. In this dissertation, the heat removal performance of two commonly used 3D fluidic oscillators [127], a curved one and a angled one, were compared using two turbulence models. The curved oscillator design was used in a number of refs [128-130] and the angled oscillator design was used in some others [131, 132]. The transient RANS $k-\omega$ SST turbulence model and the embedded large eddy simulation (ELES) turbulence model [133] were both used to investigate the heat removal performance of the two sweeping jets. The ELES model used the RANS model to simulate the regions that were less important and large eddy simulation (LES) model for the regions of interest. In this way, the ELES model preserved the turbulence resolution of LES model without introducing much additional computation cost. The water rather than air was selected as the working fluid here, since water had higher heat removal performance though it was harder to manipulate the range of its Re numbers in real experiments.

3.3 The design of the fluidic oscillators

In this study, the geometry of the angled fluidic oscillator (Table 3.1) was scaled from the computational model used in ref. [131], and the geometry of the curved one was adjusted from ref. [127]. The 3-D geometry information of the fluidic oscillators was shown in Figure 3.2. The overall size (25 mm × 11.25 mm × 1.5 mm) of the two devices were the same. The width of the inlets was 2D (where D=1.0 mm in both designs). The thickness of the fluidic oscillator was 0.5D, and the thickness of the fluid channel was 1.5D. The outlet of the channel was 12.5D away from the center of the throat to make sure the outlet boundary condition would not significantly affect the fluid dynamics of the sweeping jet. The angle and width of the outlet throat were the same for the two models. Besides, a direct jet model was also established (by removing the feedback loops of the fluidic oscillator) to act as a reference. The simulation was performed using water with Re=3,000, 4,000, and 5,000, respectively.

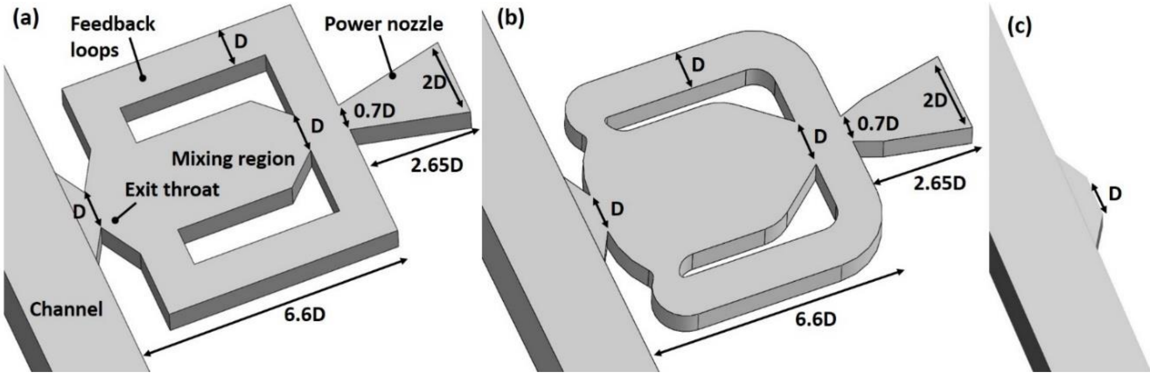

Figure 3.2. (a) The angled fluidic oscillator, (b) The curved fluidic oscillator, (c) The direct jet.

Table 3.1. The main geometry parameters of the fluid oscillators

Parameters	size	Parameters	size
The throat width	1.0 mm	Outlet distance	12.5 mm
Fluid oscillator thickness	0.5 mm	Feedback loop width	1.0 mm
Inlet width	2.0 mm	Feedback loop length	5.6 mm
Fluid channel thickness	1.5 mm	Mixing chamber width	3.0 mm
Fluid channel height	2.0 mm	The heat flux surface	1.5 × 12.5 mm^2

3.4 Numerical models

3.4.1 The $k-\omega$ SST model

The flows through the fluidic oscillators were simulated by solving the incompressible Navier–Stokes equations. The $k-\omega$ SST model and the ELES model were used to simulate the turbulence separately. The $k-\omega$ SST model developed by Menter et al. [134] was thought to be robust to fit turbulence for a wide Re number range. By introducing the blending functions, this model combines the good near-wall behavior of the $k-\omega$ model with the robustness of the $k-\varepsilon$ model in the far field in a numerically stable way. However, previous studies showed that the $k-\omega$ SST model tended to over predict the Nu number near the impingement zone [126]. The governing equations of the transitional $k-\omega$ SST model were prescribed by:

Continuity equation

$$\frac{\partial(\rho)}{\partial t}+\frac{\partial(\rho u_j)}{\partial x_j}=0 \tag{3-1}$$

Momentum equations

$$\frac{\partial(\rho u_i)}{\partial t}+\frac{\partial(\rho u_i u_j)}{\partial x_j}=-\frac{\partial p}{\partial x_i}+\frac{\partial \tau_{ij}}{\partial x_j}+\frac{\partial}{\partial x_j}\left(\mu\frac{\partial u_i}{\partial x_j}\right) \tag{3-2}$$

where $\tau_{ij}=-\rho\overline{u_i'u_j'}=2\mu_t S_{ij}$, S_{ij} was the mean rate of the strain tensor.

Energy equation

$$\frac{\partial(\rho c_p T)}{\partial t}+\frac{\partial(\rho c_p u_j T)}{\partial x_j}=\frac{\partial}{\partial x_j}\left(\lambda\frac{\partial T}{\partial x_j}\right)-\tau_{ij}\frac{\partial u_i}{\partial x_j}+S_i \tag{3-3}$$

The k equation

$$\frac{\partial(\rho k)}{\partial t}+\frac{\partial(\rho k u_j)}{\partial x_j}=\frac{\partial\left(\left(\mu+\frac{\mu_t}{\sigma_k}\right)\frac{\partial k}{\partial x_i}\right)}{\partial x_j}+\left(\tau_{ij}\cdot S_{ij}-\frac{2}{3}\rho k\frac{\partial u_i}{\partial x_j}\delta_{ij}\right)-\beta^*\rho k\omega \tag{3-4}$$

The ω equation

$$\frac{\partial(\rho\omega)}{\partial t} + \frac{\partial(\rho\omega u_j)}{\partial x_j} = \frac{\partial\left(\left(\mu + \frac{\mu_t}{\sigma_{\omega,1}}\right)\frac{\partial\omega}{\partial x_i}\right)}{\partial x_j} + \gamma_2\left(2\rho S_{ij}\cdot S_{ij} - \frac{2}{3}\rho\omega\frac{\partial u_i}{\partial x_j}\delta_{ij}\right) - \beta_2\rho\omega^2 + 2\frac{\rho}{\sigma_{\omega,2}\omega}\frac{\partial k}{\partial x_k}\frac{\partial\omega}{\partial x_k} \tag{3-5}$$

where the σ_k, β^*, $\sigma_{\omega,2}$, γ_2 and β_2 were revised constants, with the corresponding values 2.0, 0.009, 1.17, 0.44, and 0.083, respectively. μ_t and $\sigma_{\omega,1}$ were related to the blending functions [133] to make the equations suitable for both the near wall and far field region.

3.4.2 The ELES model

Large eddy simulation was thought to be more accurate than transient RANS models, as it only modeled the sub-grid-scale turbulence. However, LES had very limited impact on industrial CFD simulations, mainly due to its high computational cost. To preserve the resolution of large turbulent structures in industrial flow simulations, zonal models were desirable in many cases, where LES model was applied in the regions with high turbulence intensity, and RANS model was used for regions of fewer interests. The information in the RANS and LES regions was exchanged at the interfaces using suitable methods. In this way, the combination of RANS and LES obviated the need to specify the inlet boundary condition for the LES simulation. ELES model was adopted to simulate the fluid dynamics of the sweeping jet in this study. In the power nozzle, two feedback loops, and channel far away from the sweeping jet, the $k - \omega$ SST model was used to save the computational cost. In the exit throat and the regions of the sweeping jet, the dynamic Smagorinsky model was used to obtain more accurate fluid dynamics and heat transfer results. At the LES-RANS interfaces, vortex method was used to generate a time-dependent inlet condition for the LES region. The combination of these two models was depicted in Figure 3.3.

The dynamic Smagorinsky model was developed based on the standard Smagorinsky model by Germano et al. [126] and Lilly et al.[135]. The local values of C_{SGS}, a coefficient in the eddy-viscosity model equation, was dynamically computed based on the information provided by the resolved scales of fluid motion. Taking the SGS stresses to be proportional to the stresses due to eddies at the smallest resolved scale, the SGS stress tensors using two different filtering length, Δ_1 and Δ_2 ($\Delta_2 > \Delta_1$), were modeled in the same way with the standard Smagorinsky-Lilly model,

$$\tau_{ij} = -2C_{SGS}^2\rho{\Delta_1}^2|\bar{S}|\left(\overline{S_{ij}} - \frac{1}{3}\overline{S_{kk}}\delta_{ij}\right) \tag{3-6}$$

$$T_{ij} = -2C_{SGS}^2\rho{\Delta_2}^2|\tilde{\bar{S}}|\left(\widetilde{\bar{S}_{ij}} - \frac{1}{3}\widetilde{\bar{S}_{kk}}\delta_{ij}\right) \quad (3\text{-}7)$$

where $\bar{S} = \sqrt{2S_{ij}S_{ij}}$. In Eqs. (6) and (7), the bar overhead represented for the first filtering operation with Δ_1 (the grid filter). And the tilde overhead represents for the filtering operation with Δ_2 (the test filter).

The grid filtered SGS and the test-filtered SGS were related by the Germano identity [126],

$$L_{ij} = T_{ij} - \tilde{\tau}_{ij} \quad (3\text{-}8)$$

L_{ij} in Eq. (3-8) could be computed from the resolved large eddy field using

$$L_{ij} = \tilde{\bar{u}}_i\tilde{\bar{u}}_j - \widetilde{\bar{u}_i\bar{u}_j} \quad (3\text{-}9)$$

Substituting Eq. (3-9) and grid-filter Eqs. (3-6) and (3-7) into Eq. (3-8), the constant C_{SGS}^2 could be calculated by

$$C_{SGS}^2 = \frac{\langle L_{ij} - L_{kk}\delta_{ij}/3\rangle}{\langle M_{ij}M_{ij}\rangle} \quad (3\text{-}10)$$

where $M_{ij} = -2\left(\Delta_2^2|\tilde{\bar{S}}|\widetilde{\bar{S}_{ij}} - \Delta_1^2\widetilde{|\bar{S}|\bar{S}_{ij}}\right)$. During the simulation, C_{SGS}^2 might become negative. To avoid numerical instability, both the numerator and the denominator in Eq. (3-10) were locally averaged using the test-filter. The dynamic Smagorinsky model was proved to be a robust eddy-viscosity model which was able to predict the turbulence near the wall and far field with good accuracy [134].

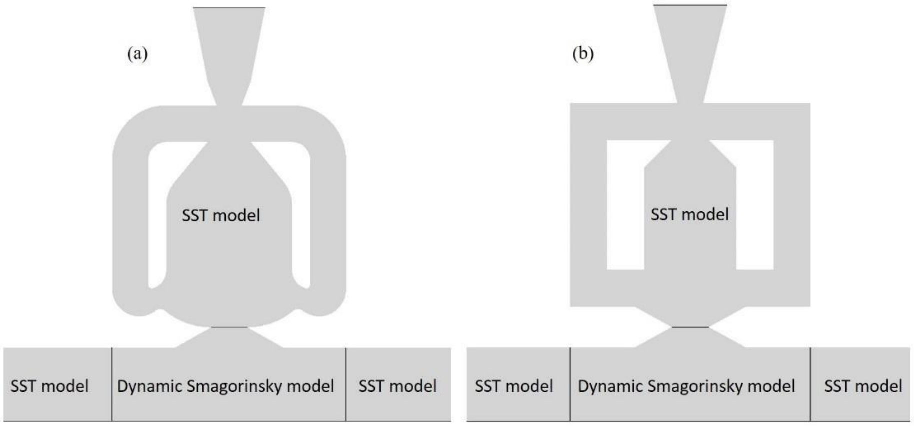

Figure 3.3. Different turbulence models used in different regions in the fluidic oscillators

3.4.3 Numerical methodology

The fluid dynamic analysis of the fluidic oscillator was carried out using the ANSYS/FLUENT 14.0 package. The grid numbers for the curved fluidic oscillator, the angled fluidic oscillator, and direct fluidic oscillators were 8.80, 8.18, and 5.5 million, respectively. The grids on the boundaries were adjusted to ensure that the dimensionless distance (y+) between the wall and the cell center of the near-wall first grids were around 1.0. The grid quality was well checked to ensure better convergence. The SIMPLE algorithm was used to solve the unsteady Navier-Stokes equations in a segregated manner. The Gauss-Green method was used for pressure discretization. The discretization method used for all the other parameters was the second-order upwind method to ensure numerical stability. A second order implicit method was used in the time domain with a time step of 10^{-6} s to obtain time-resolved flow fields and heat transfer results. The time step was estimated by the averaged velocity at the throat of the nozzle, where the flow mean velocity was high, to ensure the CFL number less than 1.0 in the computational domain. In each time step, the iteration continues until the residuals were less than 10^{-6} for the mass and momentum equations, 10^{-8} for the k and ω equations, and 10^{-10} for energy equations. At the interfaces between the unsteady RANS model and the LES model, the vortex method was used to generate velocity fluctuation.

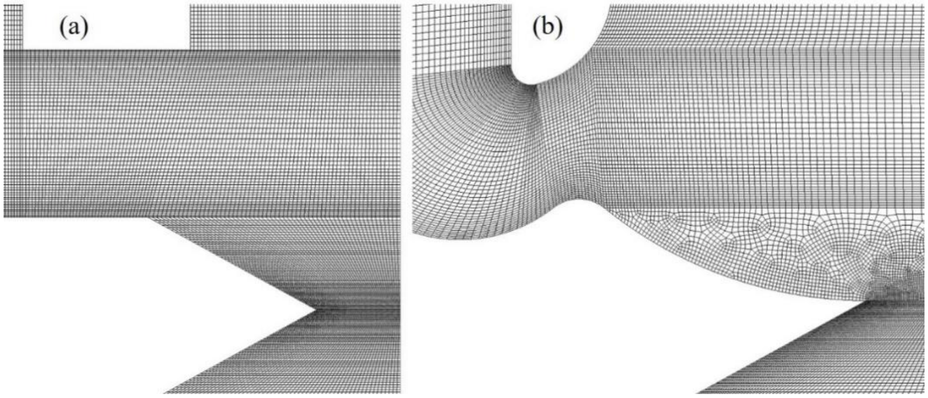

Figure 3.4. The grid systems for (a) the angled design and (b) the curved design.

A velocity inlet boundary condition was used with the velocity was estimated for $Re = 3{,}000, 4{,}000$ and, $5{,}000$ based on the throat hydraulic diameter (Figure 3.5 and Table 3.2). The inlet turbulence intensities were set 3%, 4%, and 5% for Re=3,000, 4,000, and 5,000, respectively. Though the heat transfer analysis of fluidic oscillators using air as the working fluid was seen in many open literatures, the experimental results using water were absent. To validate the results of the simulations, the grid independences were checked for all the three designs. For the angled design, three grid systems with 6.08, 8.80, and 10.85 million grids were built. When Re=5,000, the oscillation frequencies of the device were 164, 167, and 166, respectively. For the curved design, three grid systems with grid number 5.80, 8.18, and 10.34 millions were built. When Re=5,000, the oscillation frequencies were 165, 162, and 162, respectively. The simulation results were thought to be grid independent as the derivations of the oscillation frequency were less than 2.0% for all the simulation cases. The grid system using for the direct jet was the same to the angled design but with the two feedback channels removed, thus the simulation results of the direct jet were assumed grid independent. The simulation was performed for 100 non-dimensional time units (D/U_0) for each case. And the heat transfer data from the last three oscillation cycles was averaged as the final results.

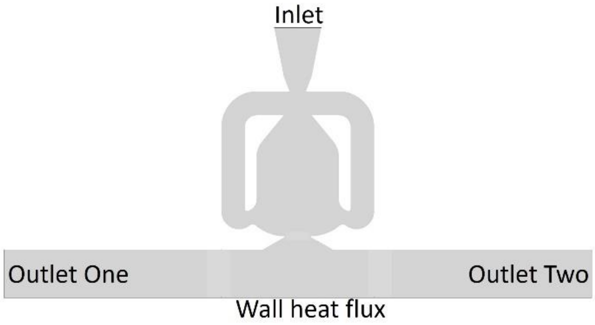

Figure 3.5. Boundary conditions for the modeling

Table 3.2 Boundary conditions

Inlet	Velocity outlet: Velocity=1.5072 for Re=3000, 2.0096 for Re=4000, and 2.512 for Re=5000 m/s, respectively. Temperature=300.0 K
Outlet One and Two	Pressure outlet: Relative pressure=0 Pa, Backflow temperature=300.0 K.
Wall heat flux	Non-slip standard wall condition, $q' = 1{,}000{,}000\ W/m^2$.
Other walls	Non-slip standard wall condition, Thermal isolated.

3.5 Simulation results and discussion

3.5.1 The flow field and oscillation frequencies

As depicted in Figure 3.6 and 3.7, a quasi-steady oscillatory flow pattern was observed for both two fluidic oscillator designs. The internal flow dynamics of the two fluidic oscillator designs had been intensively discussed in the previous experimental and numerical studies. The observed fluidic patterns in this study were nearly identical to those found in the open literature. Figure 3.6 and 3.7 showed the instantaneous pressure and flow fields of the curved and the angled fluidic oscillators for half of the sweeping period with Re=5000. The pressure and flow fields of the other half period were symmetric to this half period. Particularly, Figure 3.6 and 3.7 clearly showed that the interaction between the flows from the two feedback channels and the main jet in the inlet junction region initiated the switching of jet direction. At 0.0 T, the fluid jet was attached to the right side of the nozzle exit wall. This generated a pressure unbalance in the flow through the two feedback channels. As the flow in the right feedback channel was blocked, the pressure in the left feedback channel was much higher than that in the right channel. The relatively high pressure in the left feedback channel pushed the jet from the right side to the left side of the nozzle wall. However, because of the inertia, the jet in the mixing channel continued to sweep to the right side wall, as shown at 1/6 T. At 2/6 T, as the jet moved to the left side of the nozzle exit wall, the high-pressure region expanded into the right side of the mixing chamber and pushed the sweeping jet to the left side of the mixing chamber. At 1/2 T, the fluid jet was attached to the left side of the nozzle wall. As these processes repeated, the jet within the mixing chamber executed an oscillatory motion, thus generated a sweeping jet through the outlet throat. Careful observations on the pressure distributions of the two fluidic oscillators found that the curved design had a larger pressure fluctuation during an oscillation period. The larger pressure difference between the two feedback channels helped to enlarge the sweeping angle of the flow jet. As shown in Figure 3.6(e)-(h) and 3.7(e)-(h), the curved design had a slightly larger sweeping angle than the angled design.

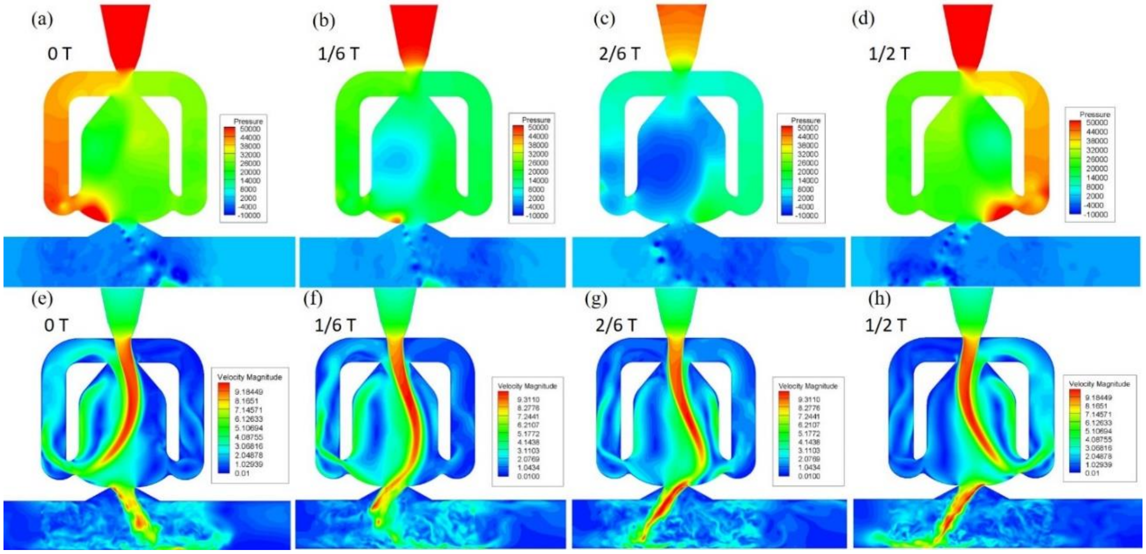

Figure 3.6. (a)-(d) Instantaneous pressure contours and (e)-(h) flow patterns of the curved fluidic oscillator for one oscillation cycle when Re=5,000 (T is the period).

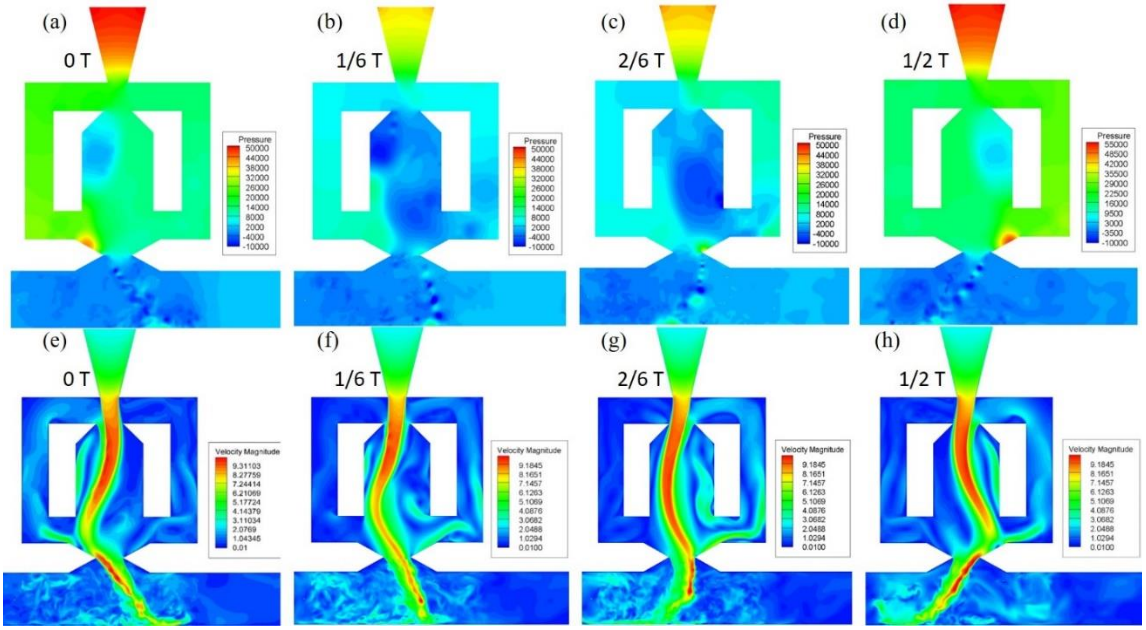

Figure 3.7. (a)-(d) Instantaneous pressure contours and (e)-(h) flow patterns of the angled fluidic oscillator for one oscillation cycle when Re=5,000 (T is the period).

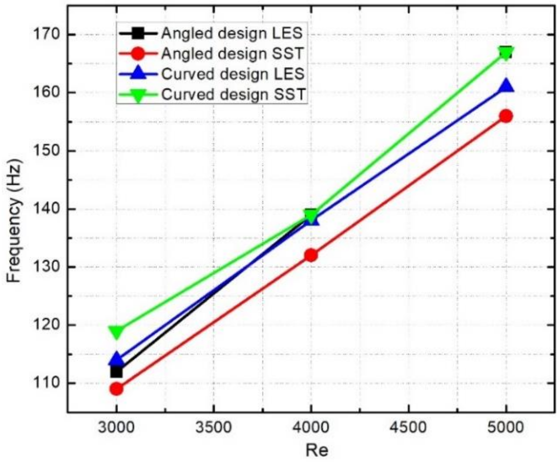

Figure 3.8. The oscillatory frequency of the curved and angled designs at Re=3,000, 4,000, and 5,000.

The oscillation frequency of the fluidic oscillator could be affected by many factors, such as the flow rate, feedback channel length, and working fluid. The oscillatory frequencies of the curved and the angled fluidic oscillators with Re=3,000, 4,000, and 5,000 were shown in Figure 3.8. Though the difference in design, the oscillatory frequencies of the curved and angled designs were quite close to each other with the same Re number. The frequencies of the oscillatory jets nearly linearly increased with the Re numbers for both designs. For the curved design, the oscillatory frequencies predicted by the ELES model and the $k-\omega$ SST model matched each other very well, with a difference less than 4%. For the angled design, the ELES model predicted the oscillation frequencies slightly higher than the SST model for all the Re numbers. However, the difference became larger for the cases with the higher Re numbers. In the main channel, the dynamic Smagorinsky model and *k-w* SST models were used to simulate the turbulence near and far away from the impingement zone, respectively. The LES model can provide more turbulence details. As observed in Figure 3.6 and 3.7, the turbulence structures including the large scale and small scale eddies were clearly shown in the impingement zone. However, in the regions using the $k-\omega$ SST model, the small scale eddies were filtered out. The turbulence eddies can play an important role in the mass and energy transport due to the additional inertia stress and thermal fluxes. Oscillation of the jet flow created strong turbulence fluctuations and vortexes in the impingement zone. It was highly expected that the strong flow convection due to the turbulence fluctuations was able to enhance the convective heat transfer.

3.5.2 Heat transfer results

It was well known that the turbulence introduced strong flow fluctuations and helped to destroy the boundary layers. It was reported in refs. [112, 125] that the intrinsic oscillation of the fluidic oscillator helped to enhance the overall convective heat transfer performance at the impingement zone. However, in some other literature [113], the sweeping jet did not show many advantages over the steady jet impingement in convective heat transfer, particularly near the impingement zone. The conclusion in the literature diverged. In this section, the problem was revisited and further clarified.

In this thesis, a constant heat flux boundary condition, $q' = 1{,}000{,}000\ W/m^2$, was set on the impingement wall. The time averaged Nu number was compared for the three designs to see if oscillation of the jet can enhance the heat transfer performance. The temperature distribution near the wall was known from the standard wall functions,

$$T^+ = \frac{\sigma_T}{\kappa} In(Ey^+) + \sigma_T \left(\frac{\pi/4}{sin(\pi/4)}\right)\left(\frac{A}{\kappa}\right)^{1/2}\left(\frac{\sigma_L}{\sigma_T} - 1\right)\left(\frac{\sigma_L}{\sigma_T}\right)^{-1/4} \tag{3-11}$$

where σ_T and σ_L are the turbulence Prandtl number and the molecular Prandtl number, respectively, A is the van Driest constant, and κ and E are constants for the velocity distribution near a solid wall.

The convective heat transfer coefficient related to Nu number via $h = \frac{Nu \cdot \lambda}{D_f}$. An energy balance was achieved on the impingement surface ($q' = k\nabla T = h\left(T - T_f\right)$), thus the Nu number could be calculated by

$$Nu = \frac{q' D_f}{\lambda\left(T - T_f\right)} \tag{3-12}$$

where the reference temperature was set to be 300 K and the hydraulic reference diameter was set to be 1.5 mm, the width of the fluid channel.

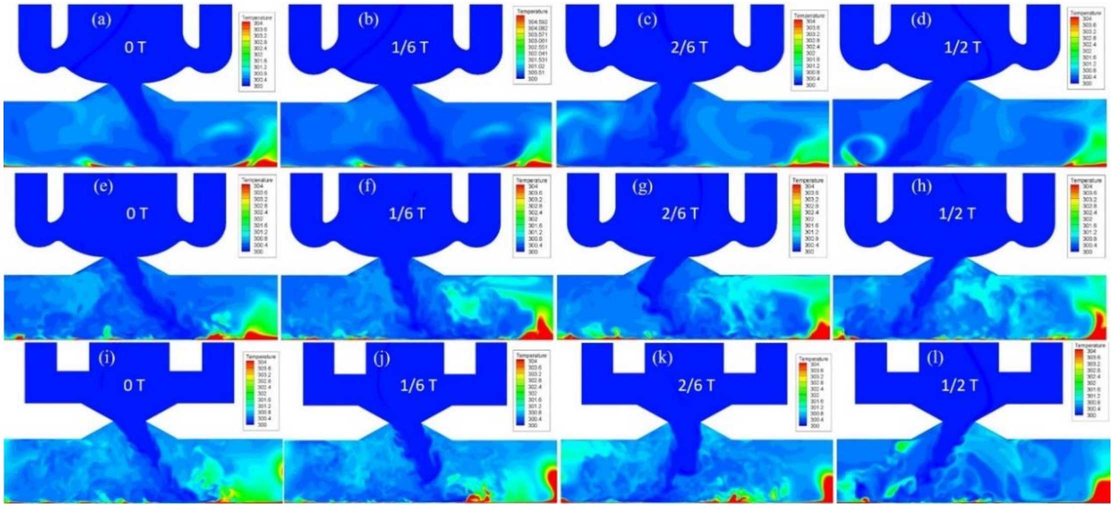

Figure 3.9. (a)-(d) Instantaneous temperature contours of curved design using $k-\omega$ SST model. (e)-(h) Instantaneous temperature contours of curved design using ELES model. (i)-(l) Instantaneous temperature contours of angled design using ELES model.

Figure 3.9(a)-(d) and (e)-(h) compared the instantaneous temperature contours of curved design using two different turbulence models. Strong turbulence fluctuations were observed in the impingement zones, particular for the LES model. As the turbulence indicated the contributions of additional fluid stresses and energy transfer due to oscillatory motion, the accuracy of the heat transfer simulation of the fluidic oscillators heavily relied on the accuracy of the turbulence modeling. Turbulent flows were characterized by eddies with a wide range of length and time scales. The LES model was believed to be able to capture the details of the eddies within a wider length and time scales. As shown in Figure 3.9, the temperature fluctuation was more clearly observed in simulation results using the ELES models. The strong turbulence fluctuation would increase convection and diffusion significantly, thus enhance the heat transfer process in the impingement zone. Figure 3.9(i)-(l) showed the instantaneous temperature contours of curved design simulated using the ELES model. The flow patterns of the curved design were quite similar to the angled design, but with smaller sweeping angles.

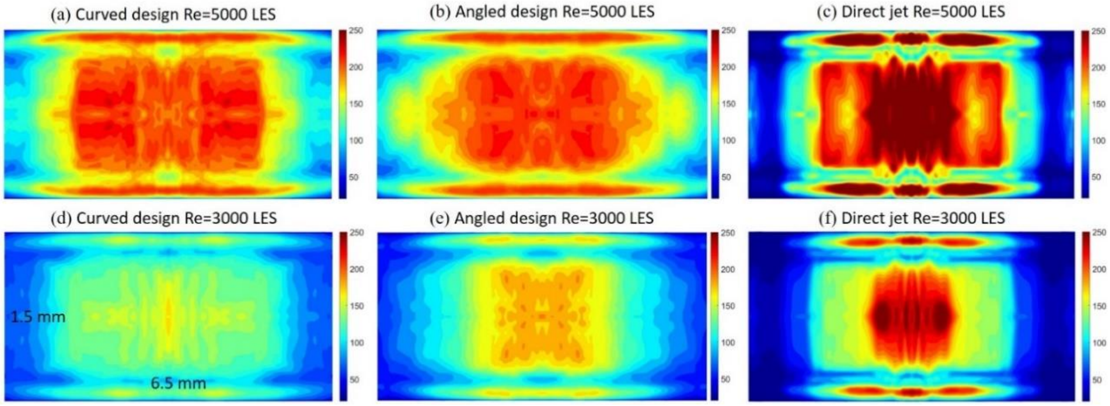

Figure 3.10. (a)-(c) Time-averaged Nu number contours on the impingement surface for the three designs at Re=5000 using ELES model, (d)-(f) Time-averaged Nu number contours on the impingement surface for the three designs at Re=3000 using ELES model.

Table 3.3. The average temperature difference and Nu number on the impingement surface covered by the jet (6.5 × 1.5 mm^2)

Re	Curved design		Angled design		Direct jet	
	ΔT	Nu_{avg}	ΔT	Nu_{avg}	ΔT	Nu_{avg}
3,000	22.27 K	105.24	21.12 K	110.97	22.94 K	102.17
4,000	17.51 K	133.85	17.08 K	137.22	19.07 K	122.90
5,000	14.98 K	156.46	15.11 K	155.11	16.23 K	144.41

Figure 3.10 showed the time-averaged surface Nu number contours on the jet impingement wall (6.5 × 1.5 mm^2) for the two sweeping and one direct jet at Re=3000 and 5000. Data were averaged over three full-time periods for each case. Some distinct features were observed for the different fluidic designs. Different from the direct jet, two distinct peaks were observed for the sweeping jets due to the bi-stable nature of the fluidic oscillators. The region of the high Nu numbers shifted from the center of the impingement zone as the sweeping jet spent most of the time attached to one of the mixing chamber walls. As shown in Figure 3.10, the distance between the high-Nu-number spots became further to each other with the higher Re number. Meanwhile, the coverage area of the impinging jet increased with Re number, as a larger high-Nu-number zone illustrated in Figure 3.10 for Re=5000. For Re=3,000 or 5,000, the curved design, the angled design, and the direct design owned a relatively wide, medium, and narrow high-Nu-number zone on the impingement wall. Near the vertical wall of the channel, two long and narrow high Nu zones were observed because of the interaction between the turbulence flow and the

walls. Though the direct jet owned a relatively narrow high-Nu-number zone, the maximum Nu number of the direct jet was larger than the sweeping jets. Overall, the heat transfer performance of the fluidic oscillators increased with the Re number. Also, this was reflected in lower surface temperature, as shown in Table 3.3. When compared with the direct jet, the curved design demonstrated 3.0-9.0% decrease in the average Nu number, while the angled design represented 7.0-9.0% decrease in the average Nu number. Impinging self-oscillating fluidic oscillators showed a small heat transfer enhancement for Re numbers ranging between 3,000-5,000.

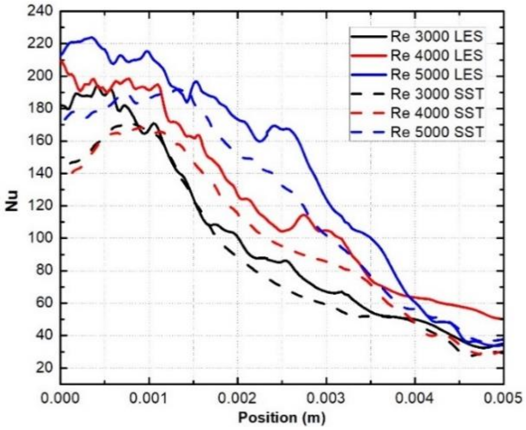

Figure 3.11. Time-averaged surface Nu distribution for the sweeping jet on the channel centerline at Re = 3000, 4000, and 5000 for the curved design

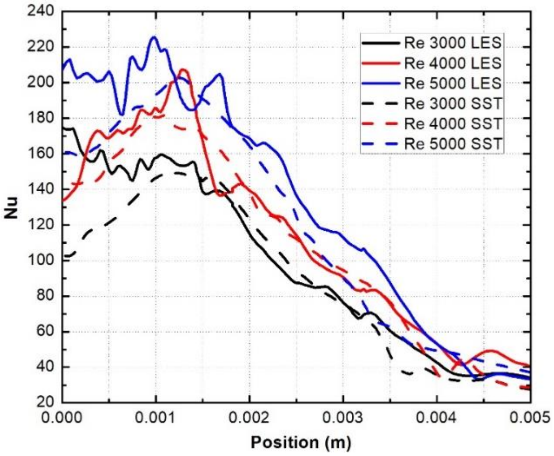

Figure 3.12. Time-averaged surface Nu distribution for the sweeping jet on the channel centerline at Re = 3000, 4000, and 5000 for the angled design

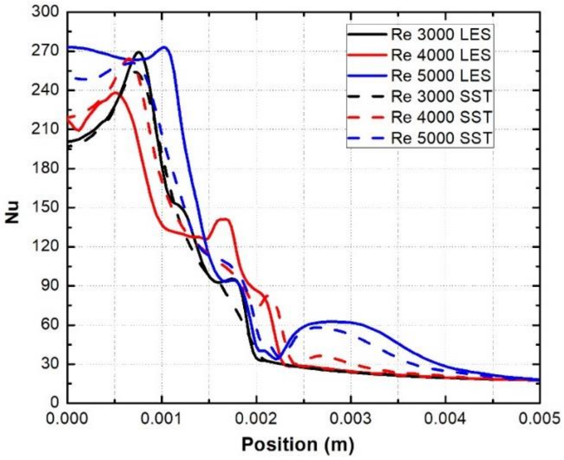

Figure 3.13. Time-averaged surface Nu distribution for the jet on the channel centerline at Re = 3000, 4000, and 5000 for the direct jet design

As shown in Figure 3.11, 3.12, and 3.13, overall, the Nu number distribution on the centerline of the channel predicted by the ELES model and the SST model matched each other very well for different Re numbers. Both turbulence models predicted higher Nu numbers with larger Re numbers. The $k-\omega$ SST model predicted two distinct Nu number peaks for the sweeping jets, while the peaks were not clear for the cases simulated using LES model. The Nu number distributions simulated using $k-\omega$ SST model were smoother than the LES model, as the turbulence fluctuations introduced extra energy fluxes thus effected the heat transfer process. As observed in Figure 3.11, 3.12, and 3.13, the Nu number distributions on the centerline of the impingement surface decreased from the center to the side. For the direct jet, the Nu number decreased shapely along the centerline of the impingement surface, while the decreasing tend was smoother for the sweeping jets. In the position between x=0 and 0.002 m, the Nu number varied by a factor of 2 for the curved design. For the angled design, the Nu number varied by a factor of 1.8 in the position between x=0 and 0.002 m along the centerline. For the direct jet, the Nu number varied by a factor of 9.0 for the same position. It should be noted that the simulation result for the direct jet was different from that reported in the open literature where the maximum heat transfer coefficient happened at the center of the impingement zone. As shown in Figure 3.13, the maximum heat transfer point slightly offset the center of the impingement zone. This can be reasoned by the unique divergent shape of the outlet throat.

3.6 Validation of the modeling results

In the literature, confined and submerged liquid jet impingements [136-139] were widely used for the enhanced heat transfer applications. In ref. [136], Garimella and Rice did experiments to measure the local heat transfer coefficient distribution and Nu numbers with various nozzle diameters, Reynolds numbers, nozzle-to-heat source spacings, and nozzle lengths. They proposed a correlation for the stagnation Nusselt number based on the experimental results:

$$\overline{Nu_0} = 0.492Re^{0.585}Pr^{0.4}\left(\frac{Z}{d}\right)^{0.024}\left(\frac{l}{d}\right)^{-0.09}, \quad 4000 \le Re \le 23000 \tag{3-13}$$

where Z is the distance between the confining plates, d is the nozzle diameter, l is the nozzle plate thickness.

Equation (3-13) was valid for the cases when the nozzle diameter ($1.59 < d < 6.35$ mm), Reynolds number (4,000 to 23,000), nozzle-to-heat source spacing ($1 \le Z/d \le 5$), and nozzle length ($0.25 \le l/d \le 12$). The composite correlations collect most of the data to within ±10% for the stagnation Nusselt number.

For the direct jet in this chapter, $d=0.8$ *mm* (hydraulic diameter), $Z=2.0$ *mm*, $l=0.5$ *mm*, $Pr=7.56$ (at T=300 K), *and* $Re=3000\sim5000$. The stagnation Nu numbers calculated for these cases were compared with the simulation data, as presented in Table 3.4.

Table 3.4. The stagnation Nu numbers for the direct jets with different Re numbers

Direct jet			
Re	LES	SST	Experimental result
4,000	212.20	214.31	150.83
5,000	271.35	250.67	171.87

As observed in Table 3.4, the difference between the LES model and the experimental results were about 29.2% and 36.9% for Re=4000 and 5000, respectively. Similarly, the difference between the SST model and the experimental results were about 29.9% and 33.6% for Re=4000 and 5000, respectively. The difference was acceptable as the nozzle geometry and the fluid channel design were different from the configuration in the literature.

3.7 Summary for the chapter

Unsteady RANS and ELES simulations were performed to evaluate the impinging heat transfer performance of two self-oscillating fluidic oscillators and one direct jet. Their performance with different Re numbers (3,000-5,000) was compared. The time-resolved pressure and flow fields were examined to understand the unsteady flow structure. To evaluate the heat transfer performance, the time-resolved temperature fields obtained by different turbulence models were compared. The time-averaged Nu numbers on the impingement surface were studied. Some key findings were listed below:

1) The numerical analysis of the fluid dynamics in the fluidic oscillators suggested that the jet deflection was initiated by the pressure difference within the two feedback channels. Then the jet deflection propagated downstream and formed the sweeping behavior in the mixing chamber and the outlet throat. The curved fluidic oscillator owned a larger pressure fluctuation than the angled design. Thus sweeping jet in the curved fluidic oscillator covered a larger impingement zone.
2) Both the $k-\omega$ SST model and the ELES model were used to conduct the turbulence simulations. Overall, the fluid dynamics, frequencies, and Nu numbers predicted by the two models matched each other reasonably well for different Re numbers.
3) The averaged heat transfer performance of the jets for all these three designs increased slightly with Re numbers. The direct impinging jet had better heat transfer performance at the center of the impingement zone. But its performance deteriorated sharply side from the center. The sweeping jets aroused by the fluidic oscillators increased the averaged Nu number on the impingement surface by 3.0-9.0% with Re ranging from 3,000 to 5,000. Overall, the enhancement of the average Nu number was not significant for the sweeping jet.
4) Two Nu number peaks were clearly observed in the results obtained using the $k-\omega$ SST turbulence model. The Nu numbers calculated by the ELES model fluctuated more significantly near the impingement zone due to the extra energy flux transport by the small eddies. Because of the strong turbulence, the two Nu-numbers peaks tended to expand and formed a larger high-Nu-number zone on the impingement surface. The Nu numbers varied by a factor of 2.0 from x=0 to 0002 m along the centerline of the

impingment surface. However, for the direct jet, the Nu number varied by a factor of 9.0. The sweeping jet could cool the impingement surface more uniformly.

The conclusions on the heat transfer enhancement using self-oscillating impinging jet were not consistent in the literature [110-112]. The conclusions diverged because the Re number, the geometry shape of the fluidic oscillator design, the distance to the impingement surface, and working fluids varied in the references. It should be noted that in the ref. [111], the forced convection heat transfer enhancement using a self-oscillating impinging jet increased 20-70% when compared with stationary jets for Re number ranging from 7,500 to 14,000. The authors claimed that the improvement was more significant for jets with high Re numbers. Also, they found that the distance from the jetting throat to the impingement plate had significant influence over the heat removal performance, which was not discussed in this dissertation. This research work was the one of the few research work characterizing the heat transfer enhancement using water as the working fluid. For the same speed, the Re number for the water was much smaller than the air, thus why we only characterize the performance of fluidic oscillators for Re=3,000, 4,000, and 5,000. In this dissertation, the simulation tool was used to characterize the heat transfer performance of the fluidic oscillators. It was desired to conduct experiments to further validate the simulation results reported in the dissertation.

The unsteady characteristics of fluidic oscillators were very attractive for the development of the next-generation heat exchangers with extremely high heat flux removal capacity. For example, as reported in ref. [140], multi-phase heat exchangers made by synthetic diamond integrated with a phase separation concept was used to design high-performance heat sinks with thermal conductivity exceeding 1000 $W/(m \cdot K)$. It was observed that the venting rate was critical for the phase separation thus effected the heat transfer performance. Also, the dry-out phenomenon was reported as a main obstacle for the further heat transfer improvement. It was highly expected that the fluidic oscillators could help to improve the gas venting and alleviating the dry-out phenomenon by separating the bubbles attached to the heating surface. It was also promising to significantly enhance the heat removal capacity of the heat exchangers by adjusting the inlet configurations of the heat exchangers using the fluidic oscillator arrays.

The chapter was adapted from a paper, "Yongjia Wu, Jihui Yang, Shikui Chen, Lei Zuo. Thermo-element geometry optimization for high thermoelectric efficiency. Energy, 147 (2018): 672-680."

Chapter 4. Increase the Efficiency of TEG via Thermo-element Geometry Optimization

4.1 Chapter introduction

The figure of merit (ZT) of thermoelectric materials is temperature dependent, thus the local compatibility factor changes significantly along the thermo-element length. A local optimization method to maximize the efficiency of a function graded thermoelectric generator was proposed and discussed in this chapter. By adjusting the cross-sectional area and segment's thickness, the reduced current equaled the compatibility factor of the material at every local thermo-element layer. This method can use the full potential of existing materials by maximizing the efficiency at every local thermo-element segment. For such a TEG working in a temperature range of 300-1100 K, the efficiencies of P-type segmented $Bi_{0.5}Sb_{1.5}Te_3$/BiSbTe/PbTe/FeNbSb thermoelement and a N-type segmented $Bi_2Te_{2.79}Se_{0.21}$/$Bi_2Te_{2.9}Se_{1.1}$/SnSe/SiGe thermo-element were 25.70% and 21.73%, respectively, much higher than the conventional segmented thermoelements. The overall efficiency of the device was more than 23.72%, making it a promising technology to harvest energy from medium and high-temperature industrial components. The optimized TEG can be fabricated by selective laser melting based additive manufacturing technology.

4.2 Segmented TEG for high energy conversion efficiency

Waste heat recovery from industrial process presented tremendous opportunities for energy savings across the industrial sectors, such as vehicle exhaust, power station, iron, and steel manufacturing. Generally, the efficiency of a TEG made by homogeneous materials was less than 10%, since no single material could achieve high efficiency in a wide temperature range. It was believed that one of the most promising ways to increase the efficiency of the TEG was to fabricate inhomogeneous materials and structures, such as segmented/cascaded TEGs [1, 43] and FGTM [141]. Currently, the best single-material-based TEG had an energy conversion efficiency of 16.4%, using skutterudites at a temperature difference of 500 K [142]. And the use of three-stage cascade-type TE modules could yield an overall energy conversion efficiency of 19.6% with the hot end temperature of 1200 K [43].

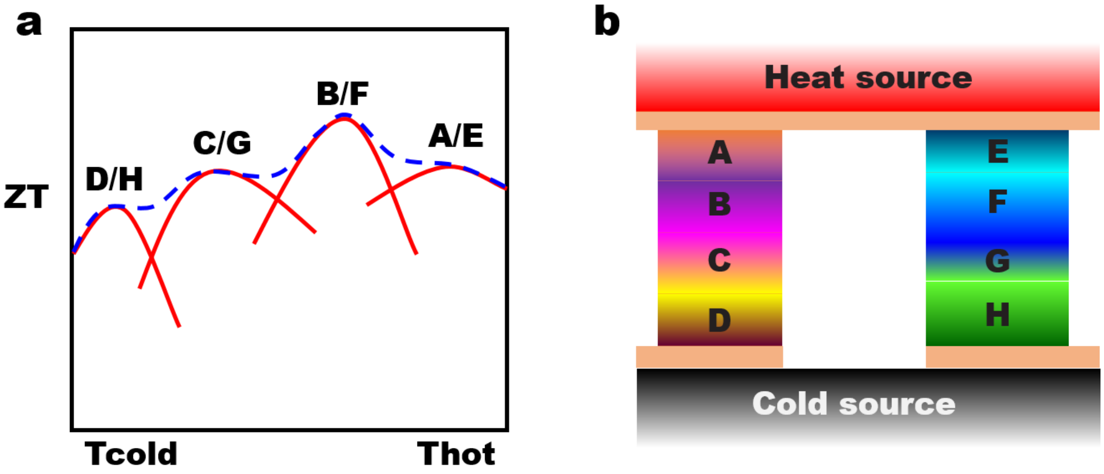

Figure 4.1. (a) Segmented TEG using different TE materials to achieve the highest averaged ZT value in a broad temperature range; (b) A segmented TEG design using these materials for high device efficiency.

A typical segmented TEG (Figure 4.1) consisting of low-, medium-, and high-temperature thermoelectric materials could take full advantage of the characteristics of different thermoelectric materials, thus achieving high overall efficiency in a broad temperature range [1]. Ioffe first proposed the concept to use the segmented design or FGTM to increase the overall efficiency of the device in the 1940s. Since the 1970s, segmented RTGs, based on PbTe and SiGe, with efficiencies ranging from 3.0% to 7.0%, have been successfully applied in spacecraft as energy sources, providing heat and 2.7-290 W of electricity for the spacecraft during 5-10 year space missions [1]. The success of segmented TEGs in deep space application proved the potential they had in medium and high-temperature energy harvesting. The very essence of a segmented TEG design was to maximize local segment operating efficiency according to the local temperature [143]. In a broad sense, a FGTM could be regarded as a segmented TEG with infinite segments. In FGTM, by changing the composite ingredients or the doping concentration along the thermo-element length gradually, the thermoelectric properties of the materials varied continuously. The local carrier concentration of the thermoelectric material could be adjusted to obtain the desired transport properties, thus achieving high efficiency in a wide temperature range. In recent years, the academic field witnessed inspiring progress in FGTM for power generation applications [144]. However, the implementation of FGTM was still impeded by some practical difficulties associated with material fabrication, characterization, and modeling.

In homogenous thermoelectric materials, the properties of the materials did not change much in a relatively narrow temperature range, thus the Thomson Effect can be neglected. However, the properties of segmented TEGs varied significantly with temperature, and the Thomson Effect had a significant influence on the system. Also, the fabrication of segmented TEG required more than simply piling up thermoelectric segments for different temperature intervals. The performance of segmented TEGs and FGTMs was closely related to the compatibility factor ($s = \left(\sqrt{1+ZT}-1\right)/(\alpha T)$), which varied with temperature appreciably. When the compatibility factors differed by a factor of 2 or more, the maximum efficiency could in fact decrease by segmentation [145]. Only when the reduced current ($u = J\nabla T$) equaled to s, did the local thermoelectric material achieve the maximum efficiency [143]. However, since the electric current on the thermo-element was constrained by the cross-sectional area of the TEG, the change in u was limited. The difference between u and s for the local thermoelectric segment made the actual efficiency of a TEG less than the theoretical peak value.

Conventionally, attempts to improve the economic viability of TEGs concentrated primarily on increasing their figure of merit (ZT). Though considerable effort had been put into this area since the 1990s when Hicks and Dresselhaus proposed that low dimensional thermoelectric materials might enhance the ZT value by several times [49, 50], materials with good and stable performance were still in exploration. Another attempt to improve their economic competitiveness was to make the best of materials commercially available [146]. Thermo-elements, limited by the manufacturing processes available now, were rectangular or cylindrical. As the cross-section of the thermo-elements was constant, the reduced current density cannot change with the compatibility accordingly, thus the efficiencies of the thermoelectric materials were not fully explored. The compatibility mismatch had been a practical problem that hinders the further improvement of efficiency of TEG device. To conduct an efficiency analysis of the segmented TEG relied on an accurate thermal model. Snyder [143] proposed a novel spreadsheet method to optimize the performance of a segmented TEG with rectangle geometry shape. This method, separating the internal variables and properties from the external ones, allowed one to compare the exact local efficiency with the ideal efficiency. In this thesis, a similar spreadsheet method was adopted to analyze the optimal geometry shape of each local thermoelectric segment.

Three thermoelectric material segments were selected for each of the thermoelectric legs in the device to balance the performance gains and system complications. The materials we chose for the N-type leg were $Bi_2(TeSe)_3$-based for the low-temperature range [147, 148], SnSe for the intermediate temperature range [149], and SiGe for the high-temperature range [150]. On the P-type side, the material choice for the low, intermediate, and high temperature range were $(BiSb)_2Se_3$-based [151, 152], PbTe [153], and FeNbSB [154], respectively. These materials were chosen for their high ZT values and similar compatibility factors at the interfaces. Besides, to realize the maximum average ZT, the low-temperature ends of both elements had two compositions, but within the same family of materials, hence we considered these single segments. By changing the thickness and cross-sectional area of each local thermoelectric segment, the compatibility mismatch problem in the segmented TEG construction was eliminated. This optimized segmented TEG could make the best of the existing thermoelectric materials. The relatively complex geometry structure of the thermo-elements would introduce extra difficulty in fabrication. It was not practical to use the conventional methods, such as hot pressing, SPS, and Bridgeman method to fabricate this kind of TEG module. SLM, a higher temperature AM method, was proposed to be a good choice for the manufacturer.

4.3 An optimization method based on the compatibility analysis

In a thermoelectric material, thermal energy was converted to electricity based on the Seebeck, Peltier, and Thomson effects. The efficiency of a general TEG device was traditionally described in terms of system parameters such as hot- and cold-side temperature, length and area of thermo-element, and load resistance. Because of the nonlinearity introduced by the Thomson heat term, in only the most simplified cases (e.g., temperature-independent thermoelectric properties), could the efficiency of the TEG device be computed analytically. In a function-graded and segmented TEG, all the properties (e.g., Seebeck coefficient, electrical resistivity, thermal resistivity) were highly temperature dependent. In most case, it was impossible to obtain analytical solutions. In this section, a spreadsheet method proposed by Snyder was used to optimize the geometry shape of the thermo-element. By taking Fourier's heat conductivity, Peltier Effect, Thomson Effect, and Joule heat into account, the analysis aimed at accurately predicting the possible highest efficiency of the TEG through geometry optimization using the most advanced materials. The thermo-element was divided into many segments mathematically. For each segment, the cross-sectional area and the length were optimized, thus achieving the peak efficiency at every temperature interval.

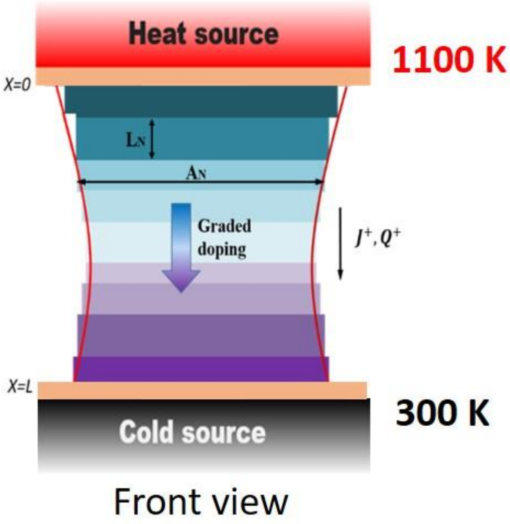

Figure 4.2. Mathematical segments of a single thermo-element. The direction of positive variables was shown relative to the hot- and cold-ends.

The electric current density through the thermo-element was

$$J = \frac{I}{A} \tag{4-1}$$

The generated electrical field in thermoelectric material was caused by Seebeck Effect ($E_1 = \alpha \nabla T$) and counteracted by Ohm's law ($E_2 = -\rho J$). The electrical field in the thermo-element at a given position was described as

$$E = \alpha \nabla T - \rho J \tag{4-2}$$

At the cross-section, the heat transported was given by

$$Q = \alpha TJ + \kappa \nabla T \tag{4-3}$$

where the first term was the heat absorbed by the Peltier Effect and the second term was the heat transferred according to the Fourier's law.

The electric power density (power generated per volume) was expressed as

$$P = EJ \tag{4-4}$$

According to the energy conservation law, the divergence of heat flux should be compensated by the source term from Joule heat. Then the electrical power density could be rewritten as

$$P = \nabla Q \tag{4-5}$$

Substituting Eq. (4-5) into Eq. (4-3) yielded

$$P = \nabla(\alpha TJ + \kappa \nabla T) = \nabla T\left(\frac{d\alpha}{dT} \cdot TJ + J\alpha\right) + \nabla J \cdot T\alpha + \nabla(\kappa \nabla T) \tag{4-6}$$

In Eq. (4-6), Effect ($\frac{d\alpha}{dT} \cdot T$) was the Thomson coefficient. Using the sign presented in Figure 4.2, a sign computation found that the power density ($P = -\rho J^2$) was negative. Here the electric current flux ($\nabla J \neq 0$) was a function of position. Plugging Eq. (4-4) into Eq. (4-6), yielded the steady state thermodynamic governing equation

$$\nabla(\kappa \nabla T) = -\nabla T \frac{d\alpha}{dT} \cdot TJ - \nabla J \cdot T\alpha - \rho J^2 \tag{4-7}$$

The relative current density (u), which was the ratio of the electric current density (J) to the heat flux by conduction $\kappa \nabla T$, was introduced to simplify the calculation, which was described as

$$u = \frac{J}{\kappa \nabla T} \tag{4-8}$$

Then the heat flux through the cross-section of the thermo-element and electric power density in term of u could be rewritten as

$$Q = (1 + \alpha u T)\kappa \nabla T \tag{4-9}$$

$$P = (\alpha - \rho u \kappa)\kappa \nabla T^2 \tag{4-10}$$

The variation of u was governed by Eq. (4-8), which was a function of temperature. For the one-dimensional problem, the variation of u in term of temperature could be expressed in term of the position.

$$\frac{du}{dT} = \frac{du}{dx} \cdot \frac{1}{\nabla T} \tag{4-11}$$

Differentiating Eq. (4-8) over x on both sides yielded variation of u in term of the position.

$$\frac{du}{dx} = \frac{dJ}{dx} \cdot \frac{1}{\kappa \nabla T} - \frac{J}{(\kappa \nabla T)^2}\left(\nabla(\kappa \nabla T)\right) \tag{4-12}$$

Plugging Eqs. (4-7) and (4-11) into Eq. (4-12), u value was constrained by the updated thermodynamic governing equation.

$$\frac{du}{dT} = u^2 T \cdot \frac{d\alpha}{dT} + \rho u^3 \kappa - \frac{dA}{dT} \cdot \frac{(1+uT\alpha)u}{A} \tag{4-13}$$

The local segment efficiency was defined as the power produced divided by the heat flux going through the local segment. For a small segment, the power generated per area was given by Pdx, and the efficiency of the local thermoelectric segments was neatly given by

$$\eta_{local} = \frac{Pdx}{Q} \tag{4-14}$$

Plugging Eqs. (4-9) and (4-10) into Eq. (4-14) yielded

$$\eta_{local} = \left(\frac{dT}{T}\right) \cdot \left(\frac{u(\alpha - u\rho\kappa)T}{u\alpha T + 1}\right) = \eta_C \cdot \eta_r \tag{4-15}$$

where the η_C was the Carnot efficiency, and η_r was the reduced efficiency. To achieve the highest efficiency, $\partial \eta_r / \partial u = 0$, the reduced current should equal to

$$u_{MAX} = s = \frac{\sqrt{1+ZT} - 1}{\alpha T} \tag{4-16}$$

The s in Eq. (4-16) was the so-called compatibility factor of the local thermoelectric segment, which was derived from the temperature-dependent material properties, such as α, ρ, κ. Thus s, like ZT, was independent from device geometry or the alteration of electric or thermal currents. The largest η_r was given by

$$\eta_{r\_MAX} = \frac{\sqrt{1+ZT} - 1}{\sqrt{1+ZT} + 1} \tag{4-17}$$

Only when u=s, would each TEG segments achieve the peak efficiency in the local position. For conventional TEG, the cross-section was constant, Eq. (4-13) could be simplified as

$$\frac{du}{dT} = u^2 T \cdot \frac{d\alpha}{dT} + \rho u^3 \kappa \tag{4-18}$$

Once u was selected at one point, it cannot be adjusted in a thermo-element to follow the temperature variation of s, because the variation of u was fixed by the thermodynamic governing equation (Eq. (4-12)). Conveniently, the variation of u ($u = \frac{J}{\kappa \nabla T}$) within a conventional thermoelectric leg was typically small, since all segments in a thermoelectric element were electrically and thermally in series, current J was the same and the thermal conductivity *k* varied little along the thermo-element with the same material. However, the material property s could vary significantly along the thermos-element, even in a same material working at a large temperature difference. So *u* and *s* cannot be equal at more than a few isolated points. The difference between u and s let the efficiency of the thermos-electric device deviate from the maximum efficiency that the device could achieve. The strategy to maximize the efficiency of the TEG device was to make the *u* close to the *s* at every thermoelectric segment.

Known from Eq. (4-13), if the cross-section was not a constant, the reduced current could be adjusted by tuning the shape of the thermo-element. Rearranging Eq. (4-13) varied the cross-sectional area in temperature.

$$dA = \frac{\left(u^2 T \cdot \frac{d\alpha}{dT} + \rho u^3 \kappa - \frac{du}{dT}\right) A dT}{(1 + uT\alpha)u} \tag{4-19}$$

After the cross-sectional area was obtained, plugging Eq. (4-19) into Eq. (2-13), the cross-sectional area was related to the temperature gradient by

$$A = \frac{\alpha I T}{\kappa \nabla T\left(\sqrt{1+ZT} - 1\right)} \tag{4-20}$$

Rearranging Eq. (4-20), the length of each segment was given by

$$dx = \frac{\kappa A dT\left(\sqrt{1+ZT} - 1\right)}{\alpha I T} \tag{4-21}$$

By tuning the length of each TEG segment, the value of *u* could be calibrated to the desired value. Once the geometry of each segment was obtained, the length, electrical resistance, and voltage output of the thermos-element could be obtained by integrations

$$L = \int dx \tag{4-22}$$

$$R = \int \rho A dx \tag{4-23}$$

$$V = \int \alpha dT \tag{4-24}$$

Dividing the thermo-element into numerous segments, according to refs. [155], the overall efficiency of the single thermo-element (P or N-type) could be expressed as

$$\eta_{series} = 1 - exp\left(-\int \frac{\eta_{local}}{T} dT\right) \tag{4-25}$$

The cross-sectional areas at the hot and cold ends of the P- and N-type thermo-elements were selected as the reference areas for the two thermo-elements respectively.

The ratio of the reference areas of the P-type thermo-element to the N-type thermo-element could be adjusted to make sure that the length of the P, N-type thermo-elements were the same.

$$L_P = L_N \tag{4-26}$$

For two thermoelectric elements thermally in parallel, the combined efficiency was an average of the efficiency of both generators weighted by the heat flow through each thermo-element. The efficiency of the TEG device finally arrived as

$$\eta_{TEG} = \frac{\eta_N Q_N + \eta_P Q_P}{Q_N + Q_P} \tag{4-27}$$

To implement the optimization approach, the temperature operation range (300-1100 K) was divided into temperature intervals at steps of 5K and 10 K, respectively. It was found that the relative difference between results for the two temperature step was less than 1.0%. Here result for a temperature step of 10 K was presented. The geometries of the local thermos-element segments were then optimized according to the local temperature. In each small temperature interval, the material properties were assumed to be the average values of properties at *Th* and *Tc*. The spreadsheet method was presented in Figure 4.2.

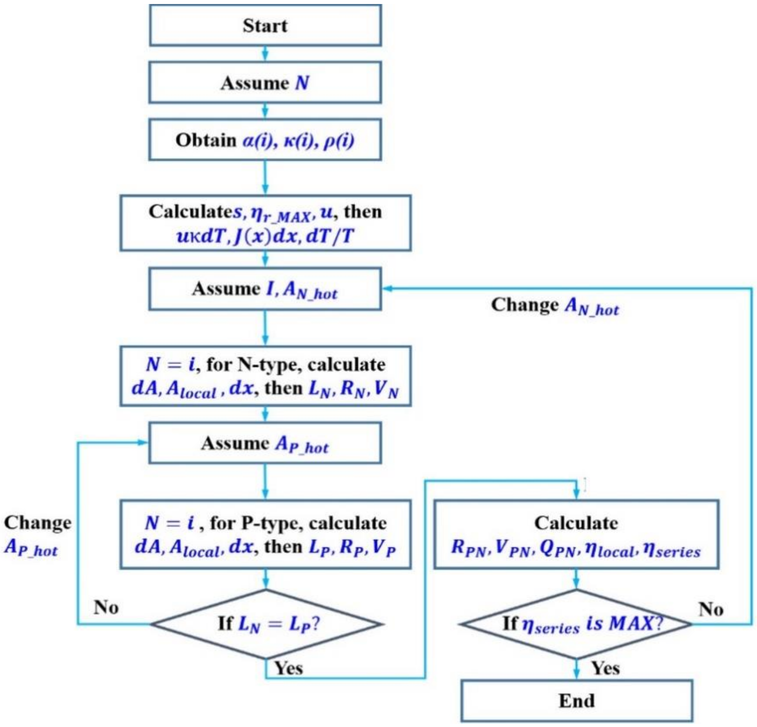

Figure 4.3. The procedures of the TEG geometry optimization method

4.4 The conventional thermo-element

The materials we selected were $Bi_2Te_{2.79}Se_{0.21}$/$Bi_2Te_{2.9}Se_{1.1}$/SnSe/SiGe for N-type thermo-element and $Bi_{0.5}Sb_{1.5}Te_3$/BiSbTe/PbTe/FeNbSb for P-type segmented. The thermoelectric properties (α, ρ, κ) were functions of temperature. At the interface between two different materials, the thermo-electric properties (e.g., ZT) were discontinuous (Figure 4.4).

In the computation, by combining the zero Thomson effect solution ($d\alpha/dT = 0$) with the zero resistance solution ($\rho k = 0$) [155, 156], the differential Eq. (4-28) could be approximated as follows

$$\frac{1}{u_n} = \frac{1}{u_{n-1}}\sqrt{1 - 2u_{n-1}^2\overline{\rho k}\Delta T} - \bar{T}\Delta\alpha \tag{4-28}$$

where operator $\Delta T = T_n - T_{n-1}$, $\Delta\alpha = \alpha(T_n) - \alpha(T_{n-1})$, and $\overline{\rho k}$ and $\bar{T}$ were the average of ρk and T between T_n and T_{n-1}. At the interface between two materials, the discontinuous change in u could be correctly calculated using $\Delta u = u^2 T\Delta\alpha$ that was simplified from Eq. (4-28). Using an initial, the reduced current (u) could be calculated using Eq. (4-18). By varying the initial u condition, the maximum efficiency could be calculated from Eq. (4-11) and (4-18). In this design, the optimal initial u for the P- and N-type thermo-elements were 3.65 and -1.16 V^{-1}.

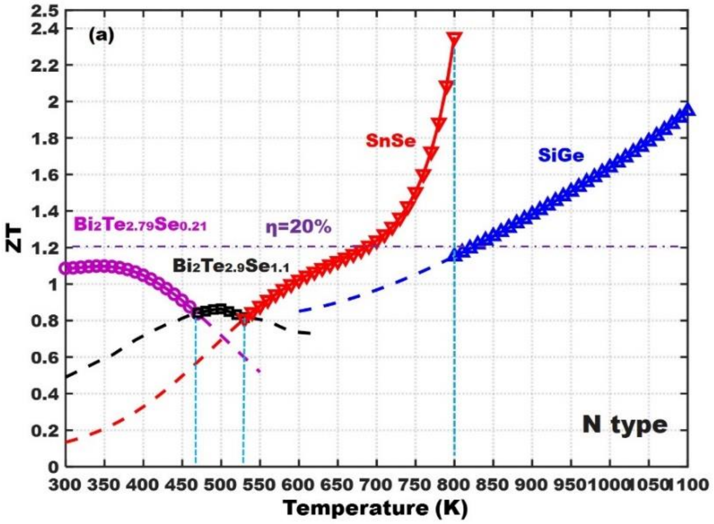

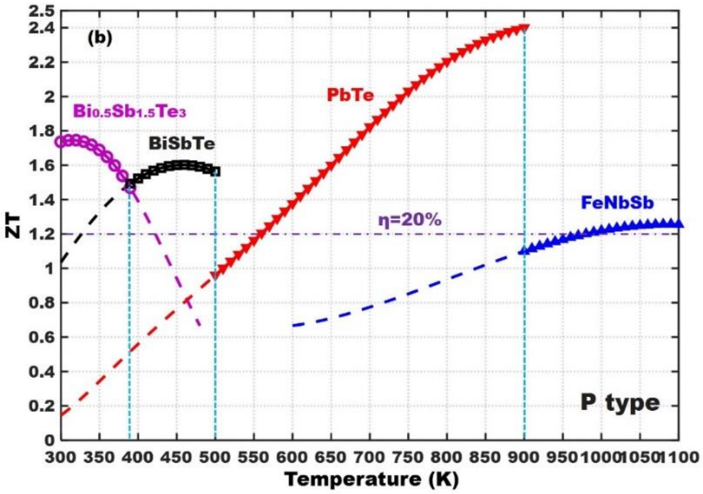

Figure 4.4. Variation of ZT values with temperature for (a) N- and (b) P-type thermoelectric materials

The reduced currents (u) and compatibility factors (s) of P- and N-type thermo-elements changed drastically with temperature, as shown in Figure 4.4. For the traditional thermo-element with the constant cross-section design, the reduced current didn't change much within this temperature range. However, the compatibility factor differed more significantly. Because the reduced current differed with the compatibility factor, as shown in Figure 4.5, the reduced efficiency of the thermo-element was lower than the maximum reduced efficiency (Figure 4.6).

The desired thermo-element length could be calculated by $l = \int_{T_c}^{T_h} ukdT/J$. If the electric current density was 5.0 A/mm^2 and the cross-sectional area of the N-type thermo-element was 100 mm^2, the corresponding thermo-element length of the N-type thermo-element was 14.3 mm. The length of the P-type thermo-element should equal to that of the N-type one, thus the cross-sectional area of the N type thermo-element should be adjusted accordingly. For this case, the cross-sectional area and the electric current density of the P-type thermo-element were 13.4 mm^2 and 37.3 A/mm^2, respectively. For the P- and N-type thermo-elements, the energy conversion efficiencies were 22.9% and 12.2%, respectively. Known from Figure 4.4, the average ZT for the P- and N-type thermo-elements were about 1.2, the expected efficiency should be about 20.0%. For P type thermo-element, the actual efficiency did not differ too much with the expected value. However, for the N type thermo-element, the actual efficiency (12.2%) was far below the desired value (20%). As explained in [145], if the compatibility factor differed by a factor of 2 or more, the maximum efficiency could be decreased by segmentation. The heat fluxes, calculated using equation (2-111), entered the hot ends of the P- and N-type thermo-element were 2.56 and 5.78 W, respectively. Substituting the heat fluxes into Eq. (2-129), the overall efficiency of the conventional thermoelectric device was 15.48%.

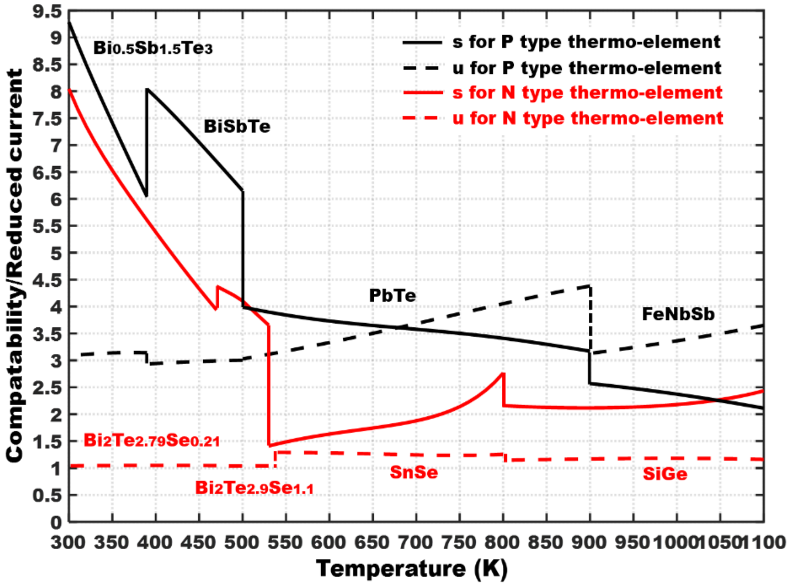

Figure 4.5. Variation of u and s with temperature for the segmented TEG

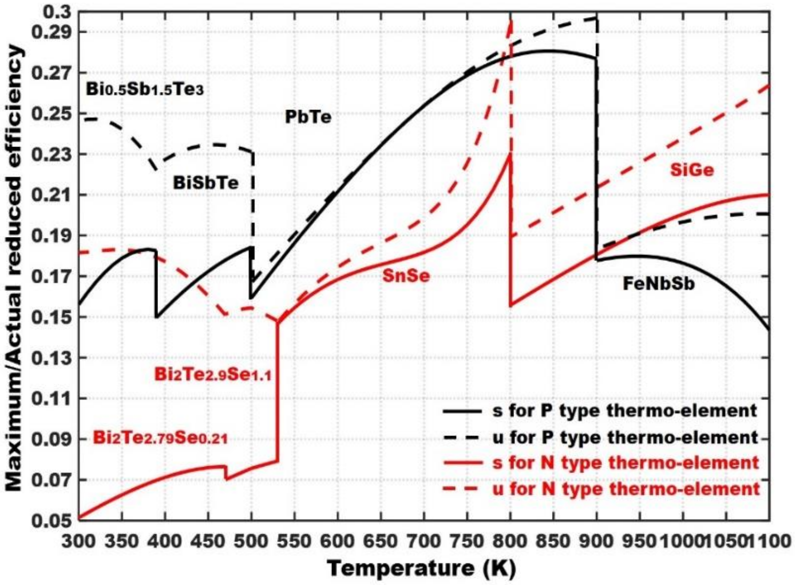

Figure 4.6. Variation of η_{r_Max} and η_r with temperature for the segmented TEG

4.5 The optimized thermo-element

As mentioned above, to achieve the maximum reduced efficiency, *u* should be as close to *s* as possible. For traditional thermo-element, restricted by the constant cross-section, *u* cannot change accordingly with the *s*. The substantial difference between *u* and s made the actual efficiency deviate far less than the maximum value. If the cross-section and segment length could vary according to the local temperature, the TEG could achieve the theoretical maximum efficiency. The mismatch problem of compatibility factor that restricted the combinations of different thermoelectric materials, in turn, could be solved.

The detailed procedures of the optimization method were described in Figure 4.3. The key idea underneath this scheme was to let the reduced current equal to the compatibility factor at every local segment. To achieve this, the cross-sectional area and the length of thermoelectric segments should be adjustable. The cross-sectional reference area of the N-type thermo-element used for this calculation was 100 mm^2, and the electric current density was 5.0 A/mm^2. Figure 4.7 showed the results calculated by the optimization method, including the cross-sectional areas, accumulated length, and efficiency (from the hot ends) for P- and N-type thermo-elements. To alleviate the possible difficulty in fabrication, the cross-sectional area between two different materials was continuous. As we can see from Figure 4.7(a), even in the same material, the cross-sectional area varied significantly with the temperature. As for the accumulated length, it did not increase strictly linearly with the temperature (Figure 4.7(b)). The variations of the cross-sectional area respect to the length of the thermo-elements were depicted in Figure 4.8. For the optimized P-type thermo-element, the cross-section area decreased with length gradually. The cross-sectional area at the hot end was about three times that at the cold end. For the N-type thermo-element, near the cold end, the cross-sectional area varied significantly along the thermo-element length. However, near the hot end, the cross-sectional area was nearly uniform. The variations of the cross-sectional area introduced extra difficult in the manufacture, which required the fabrication method with excellent material and geometry flexibility.

Using the efficiency optimization method, the maximum efficiencies achievable for the P- and N-type thermo-elements were 25.70% and 21.73% (Figure 4.8(c)), respectively. Computed using Eq. (4-9), the heat fluxes entering the hot ends of the P- and N-type thermo-elements were 3.55 and 3.52 W, respectively. And the overall efficiency of the

TEG device constructed by these two thermo-elements was 23.72%. When compared with the efficiencies obtained using the traditional thermo-elements, both the efficiencies of the optimized P- and N-type thermo-elements increased significantly, especially for the N-type one. The efficiency of the N-type thermo-element increased from 12.2% to 21.73%, while the efficiency of the P-type thermo-element increased from 22.9% to 25.70%. In a scenario where *s* varied smoothly, the conventional TEG worked well (like the P-type thermo-element). However, in other cases, the averaging method would lead to a large difference (like the N-type thermo-element) [108]. Snyder also mentioned this phenomenon in [108], where he explained why segmentation of $(AgSbTe_2)_{0.15}$ $(GeTe)_{0.85}$ (TAGS) with SnTe or PbTe had produced little extra power, but using filled skutterudite would increase the efficiency from 10.5% to 13.6% [143]. For segmented TEG or FGTM working in significant temperature difference, the combination of different thermoelectric materials to construct a high-performance TEG, constrained by the compatibility factor mismatch, were limited. However, for the design with variable thermo-element cross-section, the reduced current could be adjusted to match the compatibility factor conveniently. Thus there was no requirement on the material's compatibility factor. The only criterion that matters in constructing a high-performance TEG was *ZT* value.

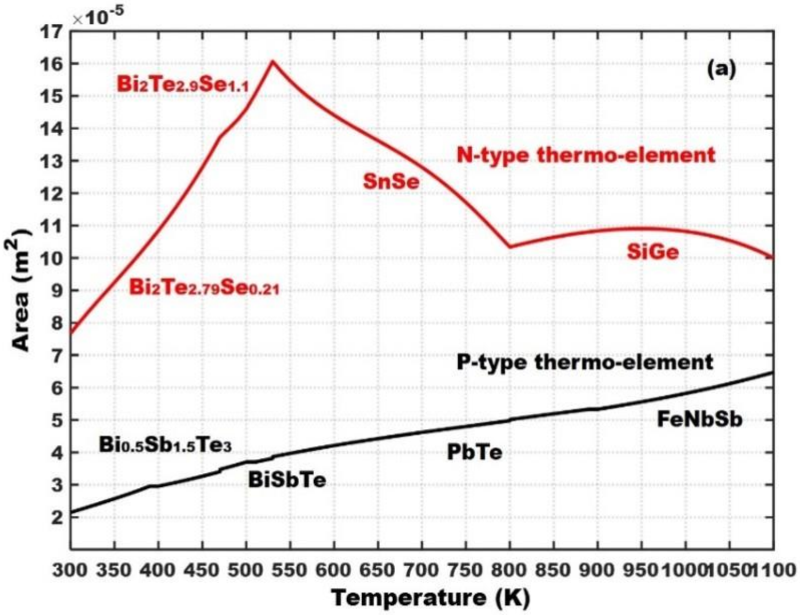

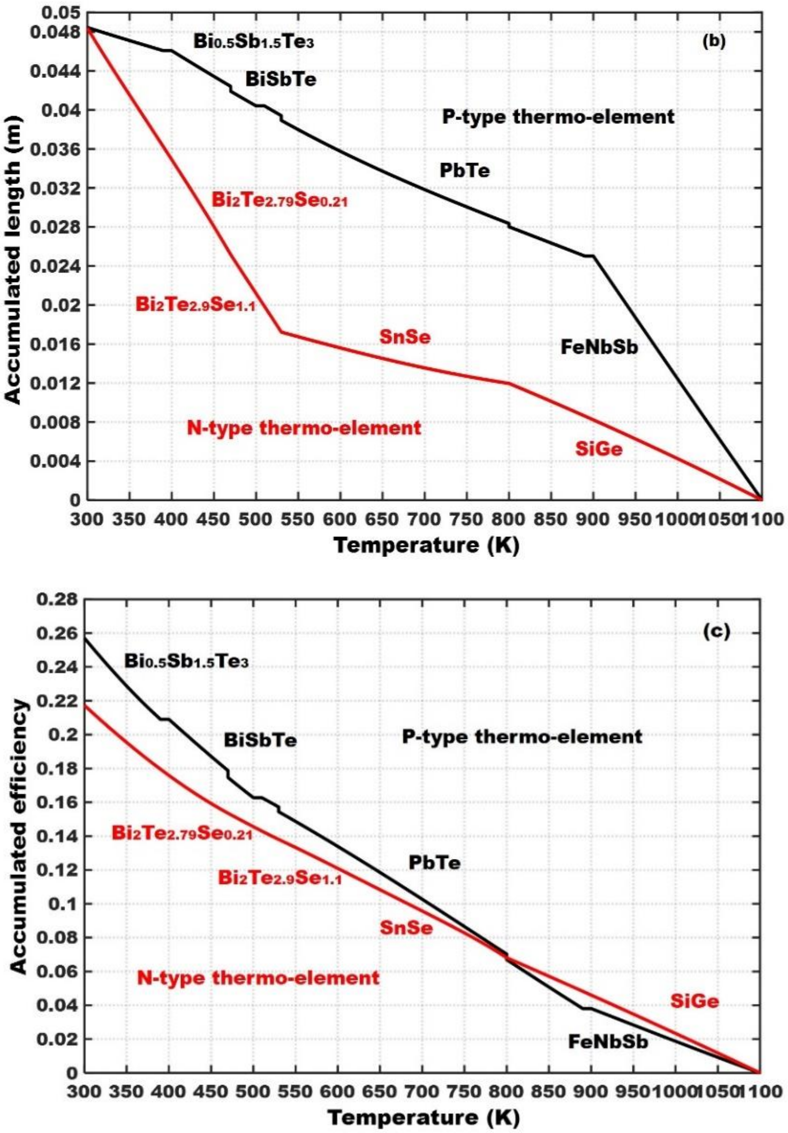

Figure 4.7. Variations of (a) the cross-sectional areas, (b) accumulated lengths and (c) efficiencies (from the hot ends) with temperature for P- and N-type thermo-elements

Conventionally, a TEG is fabricated by traditional methods, such as Bridgman, SPS, hot press, and thermal spray methods. Because of the complex geometry of segmented thermo-element, it was not convenient to implement this optimization method using conventional fabrication methods. Recently, several groups [85, 86] around the world did some preliminary work to test the possibility of sintering semiconductor thermoelectric material using selective laser sintering/melting (SLS/SLM). The thermoelectric properties varied according to the composition as expected, demonstrating the feasibility of laser melting as a rapid synthesis tool for thermoelectric compounds. As 3D AM methods (e.g., fabricated devices layer by layer with a thickness of 1-200 μm, it was convenient to change the stoichiometric proportions and geometry structures during processing. 3D printed TEG removed the need to assemble this fairly complex device piece by piece, instead of allowing it to be efficiently printed using a single machine (Figure 4.8).

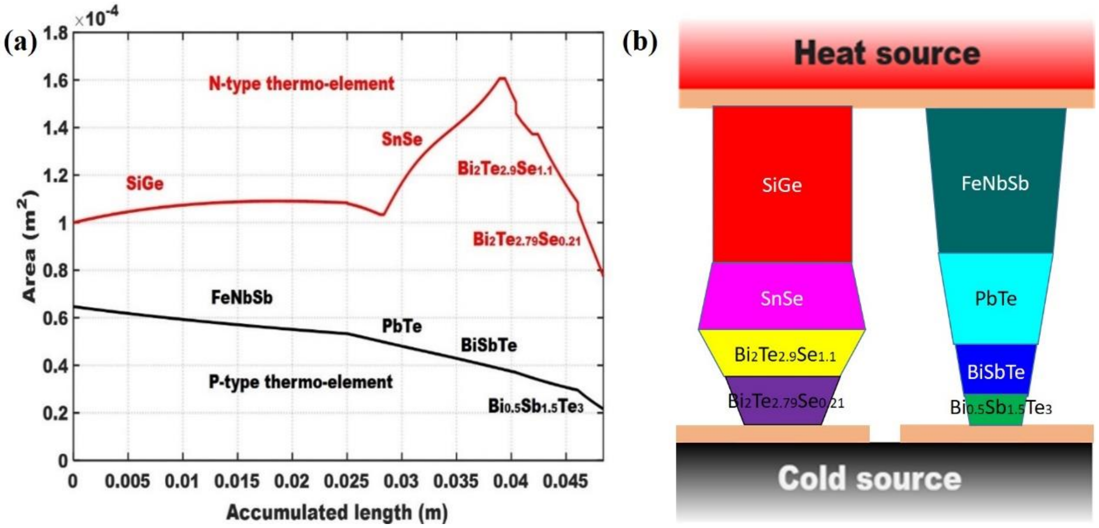

Figure 4.8. (a-b) Variations of the cross-sectional areas with the accumulated lengths for P- and N-type thermo-elements

The performance of the TEG was determined mainly by the ZT value of the thermoelectric material. There were many reasons to believe that the ZT value fabricated by SLM (Figure 4.9), though it might be a bit smaller than corresponding super lattice well synthesized [157] (which has very high cost and low throughput), would be competitive to that fabricated by a conventional method or even higher. The SLM method removed the energy and time-consuming melting and quenching processes in conventional fabrication, giving it a tremendous economic advantage over conventional methods. According to the recent research done by Tang et al. [86], the n-type $Bi_2Te_{2.7}Se_{0.3}$ fabricated by SLM manufacturing achieved an averaged ZT of ~0.7 in the temperature range of 300-550 K, which was comparable to that of the corresponding material commercially available. When integrated with technologies such as hyper-scale phonon scattering [78], graded doping [158], geometry optimization (described in the section above), and nano-structuring [159], the performance of the thermoelectric materials fabricated by SLM can be even enhanced. The wavelengths of the current carriers were much smaller than the phonons, the wavelength mismatch between the phonons and electrons made it was possible to maintain the electrical conductivity with carefully selected size and concentration of nanoparticles. Other potential nanoparticles after band alignment checking could be added into the matrix material acting as a carrier filtering layer [160]. Thus the Seebeck coefficient of the resulted deposited materials would be increased, and the bipolar thermal conductivity could be restricted [161]. The ZT of the final nanocomposites could be maximized by maintaining or even enhancing the electrical transport properties but also further decreasing the thermal conductivity [162]. Meanwhile, by removing the time-consuming melting and cutting processing in the conventional methods, the time and energy to produce a TEG module using 3D printing could be greatly reduced, resulting in a significant cut in the cost. Using SLM and integrating with this optimization strategy, we might develop a game-changing fabrication method for cheap and high-performance TEGs.

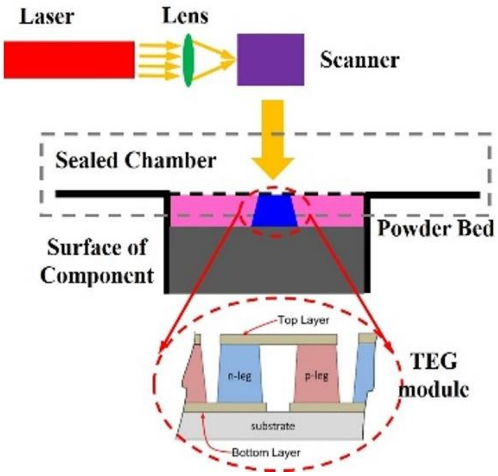

Figure 4.9. Depositing TEG device directly on industrial components using SLM

4.6 Summary for the chapter

In this chapter, a local optimization scheme based on a reduced current analysis was introduced to increase the efficiency of segmented TEG device. By calibrating the cross-sectional area and thickness of each segment, the reduced current matched to the compatibility factor of the thermoelectric materials at every point along the thermo-element, thus achieving the highest overall efficiency of TEG device.

1) A conventional N-type segmented $Bi_2Te_{2.79}Se_{0.21}$/ $Bi_2Te_{2.9}Se_{1.1}$/SnSe/SiGe thermo-element and a P-type $Bi_{0.5}Sb_{1.5}Te_3$/BiSbTe/PbTe/FeNbSb thermo-element working a temperature range of 300-1100 K were established. The efficiency of the P- and N-type thermo-elements were 22.9% and 12.2%, where the efficiency of N-type thermo-element was far less than the expected value predicted by the averaging method.
2) An optimization method was used to construct the P- and N-type thermo-elements by adjusting the geometry shape of each segment. The efficiency of the N-type thermo-element increased from 12.2% to 21.73%, while the efficiency of the P-type thermo-element increased from 22.9% to 25.70%. The optimized thermo-elements had significantly higher efficiency than the traditional ones because of removing the constraints in the compatibility factor.
3) The cross-sectional area varied along the thermo-element length, making it impossible to be fabricated by the conventional processes. SLM was proposed to be a workable and economical way to fabricate this TEG device. Further work could be done to try this idea using SLM.

Using the segmented TEG design to improve the energy conversion efficiency had been fully explored and verified in the literature [1, 138-140]. There was an urgent need to validate the concept developed in this chapter. This concept could be examined by comparing the energy conversion efficiencies of a simplified geometry optimized TEG design, for example, a two-layer optimized TEG, with a conventional TEG design.

Parts of the chapter were adapted from a paper, "Yongjia Wu, Lei Zuo, Kan Sun. Modeling the selective laser melting of multi-component thermoelectric powders. 2018 IDETC/CIE. Quebec. Canada."

Chapter 5. Selective Laser Melting for Thermoelectric Material Fabrication

5.1 Chapter introduction

More than two-thirds of the thermal energy was wasted as exhaust. To harvest energy from the vehicle exhaust represented a lot of opportunities alleviating air pollution and energy saving. Using thermoelectric for vehicle exhaust energy harvesting had been a hot research topic in the last two decades. However, there was still some problem that should be solved before this technology could be adopted for large scale energy harvesting. The interdisciplinary knowledge of material, fabrication, and system integration was required for the design of a high efficient energy harvester. In this chapter, we focused on the fabrication of high-performance TEGs exhaust energy recovery. A novel idea using selective laser melting method for high-performance thermoelectric material fabrication was proposed. This method was particularly suitable for the manufacturing of thermoelectrics with complex geometry shape, as illustrated in chapter 4. An in-house code based on the continuous equations was developed to simulate selective laser melting of the multi-component thermoelectric powders.

5.2 Integrated design and manufacturing of the nanostructured TEG using SLM

5.2.1 SLM for TEG fabrication

In a typical vehicle, about two-thirds of the fuel energy was lost as waste heat in engine exhaust gases and engine coolant. The energy recovery from the exhaust heat (Figure 5.1), typically in temperature 300-600°C, had great potential to increase vehicle fuel economy, such as by reducing the load on the vehicle's alternator or by supplying supplemental power to the electric motor in a hybrid vehicle's drivetrain. As a DOE report indicated, 5-10% fuel efficiency improvement was possible. 350-390 watts of electricity recovery already showed 3 and 4% fuel efficiency improvement for a truck Chevy Suburban and a BMW sedan [11]. Creating high-efficiency, low-cost, and industry-scalable solutions to integrate TEGs onto new or existing vehicles would represent significant fuel savings and pollution reduction. Considering the 253 million vehicles in the USA that consumed 170 billion gallons of fuel per year, the waste heat from the vehicle was over 50 billions of dollars lost each year, let alone other waste energies from the power stations, steel plants, and many others.

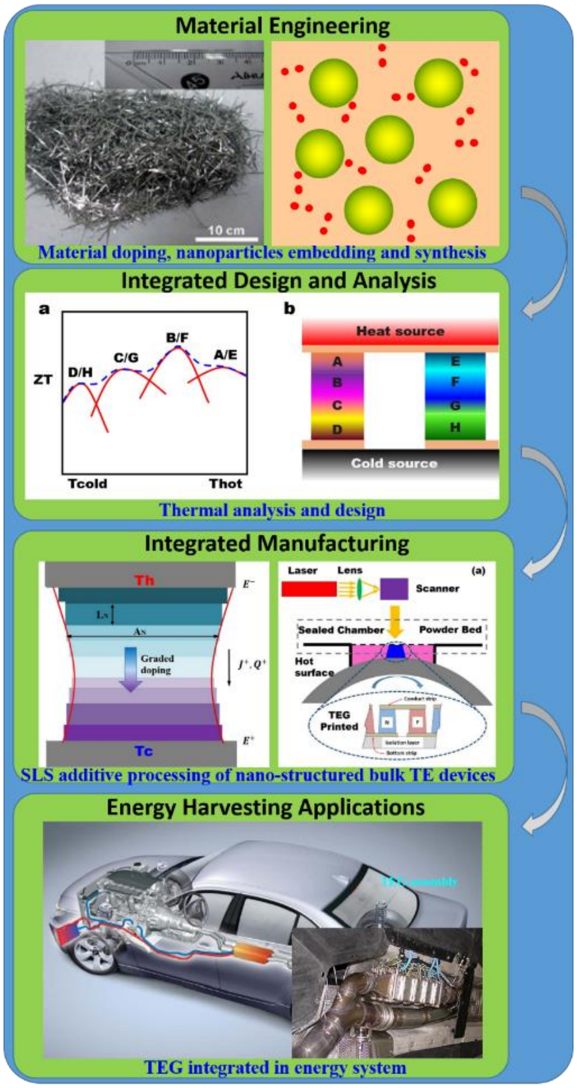

Figure 5.1. TEG for vehicle exhaust energy harvesting

Developing high-productive, compact, low-cost, reliable, workable solutions to integrate TEGs to the existing industrial components was the key for the large scale TEG application. In this chapter, a novel integrated design and manufacturing of the nanostructured TEG by the one-step strategy using selective laser melting based additive manufacturing (AM) with graded doping and nanoparticle embedding was proposed. By combining the nano-engineering of thermoelectric materials (nanocomposites or nano-alloys) with SLM, we could develop a one-step integrated nano-manufacturing of the whole TEG system through the fundamental research in nanomaterials, nanoscale heat transfer, manufacturing processing, and experimental validation. As the first step, multiple materials at different features would be fabricated, including the bottom and top ceramic electrical isolation, copper conductors, p and n-type of thermo-element, and diffusion barriers would be sintered on the exhaust pipe or other surfaces. Second, during the manufacturing, the doping stoichiometric proportions along the thermo-element varied according to the local temperature. By graded doping along the thermo-elements, the carrier concentration along the thermo-element could be optimized to the desired value (~10^{19}-10^{21} cm^3 [14]) at different temperature. Meanwhile, transient energy input, melting and solidification rate, temperature profile, and temperature gradient were carefully sensed, monitored, and controlled to get a consistent and desirable microstructure. Further, to enhance the adhesion and ZT of the resulted deposited material, an appropriate amount of Si or other potential nano-particles could be introduced into the raw thermo-element material powders. Additional benefits included better carrier mobility resulted from higher density and higher Seebeck coefficient resulted by the carrier energy filtering at the grain boundaries. Third, after the benchmark test of the SLM based thermo-element material processing method, a theatrical analysis would be carried out to optimize the geometry shape of the thermo-elements. SLM based AM method was an emerging technology to fabricate this kind of thermoelectric module. By fabricating the thermo-elements layer by layer, the cross-section area of the TEG could be easily adjusted. The reduced current could be adjusted to the desired value (compatibility factor). Thus the TEG module could make the most of the ZT value of the existing materials. Finally, through the integrated printing of thermo-elements, electrodes, and ceramic coverings, the thermal shocks, mechanical residue stress, and delamination at the contact interface could be greatly alleviated. Also, by removing the need for melting, cutting, and aligning the small thermo-elements in the conventional methods, the integrated TEG manufacturing method was readily scalable for low-cost and industrial-volumes production.

As envisaged above, the integrated nano-manufacture method, addressing some key challenges existing in the current fabrication of nanostructured thermoelectric materials and devices, provided a promising solution for the large-scale TEG energy harvesting for the industrial applications. This potentially game-changing approach in terms of design, materials, and manufacturing strategy would enable maximizing the electrical energy power output while enhancing durability and minimizing cost.

5.2.2 The potential benefits using selective laser sintering for thermoelectric material fabrication

Using solid-state thermoelectric generator (TEG) to harvest energy from the exhaust heat released by vehicle engines, fossil-fuel or nuclear power stations, or metal manufacturing plants, as well as low grade new and clean energy (like geothermal), was a very promising strategy to save energy and alleviate the air pollution problem. However, the TEG energy harvesting was still restricted by the relatively low energy conversion efficiency (typically 2-5%) and poor reliability, in both the material and the device level. The SLM proposed here would enable a compositional gradient along the length of the thermoelectric piles, providing an additional device optimization through controlling the carrier concentration gradient along the same direction. Developing highly productive, compact, low-cost, reliable, workable solutions to integrate TEGs to the existing industrial components was the key for large scale TEG applications. The previous research of thermal spray in our group found that high quench rate helped to increase the ZT value of thermoelectric materials. SLM based AM shared several merits with the thermal spray method, such as powder feeding, high quench rate, and high automation, but had important advantages over thermal spray by providing better process control for nanoparticle embedding, much higher density, milder environment, and less oxidation, and better bonding strength. SLM might provide a game-changing fabrication technology for a novel integrated design and manufacturing of the nanostructured TEG by the one-step strategy using SLM based AM with graded doping and nanoparticle embedding. Instead of a thin film for in-plane thermoelectrics, SLM could directly fabricate a thick layer of TEG (out of plane) on a non-flat surface without the use of ink solvent.

The proposed SLM based nanomanufacturing method had great advantages over the traditional methods, such as Bridgman method, Spark Plasma Sintering (SPS), and hot press by several key features, such as higher ZT induced by lower thermal conductivity, and more reliable contact layers. Also, the proposed SLM printed TEG removed the burdensome melting, cutting, aligning, and assembling processes in the conventional TEG manufacturing methods. The thermo-elements, ceramic coverings, and the electrical conductors could be printed by a single SLM machine. SLM manufacturing involved device integration of TEG directly onto exhaust components enabling robust, durable performance, creating an interdisciplinary solution to addressing the most fundamental challenges of scalable manufacturing of nanostructured TEGs. There were many reasons to believe that additive manufacturing can improve the performance of the TEG.

1) The non-equilibrium conditions produced during the laser-based AM process could introduce numerous nano-defects, nanoscale particles, and abundant multi-scale grain boundaries, reducing the thermal conductivity dramatically by hyper-scale phonon scattering.
2) Si or other nano-particles after band alignment checking can be used as additive materials in the proposed nano-manufacturing process, because of the following benefits: First, the nanoparticles can increase the adhesion of the deposited materials, improving the mechanical properties of the resulting deposited materials. Second, the nano-particles can fill the small gaps between the larger grains in TE materials, sustaining the electrical conductivity by increasing the carrier mobility. Third, the nano-particles concentrated at the boundary can act as a carrier filtering layer. Thus the resulting Seebeck coefficient can be increased, while the bipolar thermal conductivity can be restricted.
3) The laser-based AM can readily realize the graded doping and variable cross-section areas along the length of the thermo-elements for enhancing the ZT, which are the two key features making best use of the existing TE materials.
4) Using the laser-based AM, the direct manufacturing of the TE materials, thermal insulation layers, electrical conductor layers, and heat exchangers on the vehicle

exhaust components as a functional and integrated system can result in higher mechanical stability and thermal reliability as compared with existing manufacturing approaches.

5.3 Introduction to SLM

The SLM process [163] involved utilizing a high power laser, for example, a carbon dioxide laser, to fuse specific material powders into a mass that had the desired shape and physical properties. The laser selectively fused the powders by scanning the cross-sections generated from a 3-D digital description of the part, such as a CAD file or scan data, on the surface of a powder bed. After each cross-section scanning, the powder bed was lowered by one layer thickness (typically 1-200 μm), a new layer of material was applied on the top. The scanning process was repeated until the part was completed. The SLM fabrication could make the individual component to whatever shape and size. Particularly, SLM had a high energy input, thus could fabricate high melting-temperature material with high density (up to 99% full density) without adhesives for binding purpose.

In the SLM process, powders changed from solid phase to liquid phase and then back to solid phase rapidly and repeatedly because of the moving laser. A moving boundary separated the phases in the powder bed. Though an inert gas environment was sustained during the SLM fabrication, oxidation might happen even if a small amount of oxygen existed in the environment. Since the evaporation caused by the peak operation temperature was as high as 1500 °C, the control of the properties in the high-temperature environment was a practical problem. The superheat in the melting powders and the latent heat liberated or absorbed at the solid/liquid boundary made the control and monitoring process complicated. On the boundary of the melting pool, the powder was partly solid and partly liquid and resembled a porous medium that was referred to as a “mushy zone”. Thus, the properties of the material depended on the temperature evolution. Varying the SLM process parameters, including the laser wavelength and energy power, laser scan speed and spacing, and powder characteristics, dramatically influenced the resulting part properties, such as surface quality and part density. If the parameters were not well selected, the powders were either not sintered or completely melted. Also, the presence of porous in the powders can lead to the shrinkage of the powder bed during the SLM process.

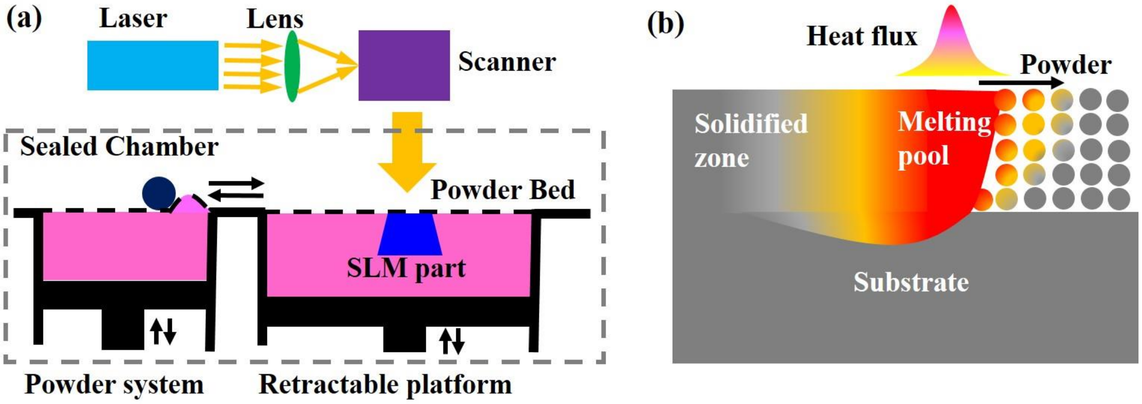

Figure 5.2. (a) The SLM equipment and (b) fabrication process

In the SLM process, a laser beam with adjustable power input and diameter was used to heat and melt the powder bed (Figure 5.2). The laser beam penetrated the powder bed to a certain depth, in which the beam was reflected and absorbed by the powders. The Gaussian beam distribution was the most widely adopted in the literature [164]. The absorption of the laser beam in the material was known to depend on several factors such as the material absorption coefficient, the nature of the surface, the wavelength of the incident laser beam, and surface temperature. For simplicity, a surface heat flux was assumed in many modeling works. The more sophisticated model took the penetration depth and material absorption coefficient into consideration [165].

The SLM was a complex melting and re-solidification process, in which fluid behavior had a great influence on the physical properties of the deposited materials. The binding mechanism invoked in full melting was primarily driven by the fluid phenomenon, such as viscosity, surface tension (or Raleigh instabilities), thermo-capillary (or Marangoni convection), wetting, evaporation, and oxidation. Therefore, it was necessary to develop a sound physical model which incorporates the functions to analyze the impacts of the processing parameters on the properties of sintered materials. To address this issue, researchers developed some sophisticated models with expanded capacity to quantify specific effects. There were mainly two tools, including conventional heat and mass transfer analysis and the lattice Boltzmann method, available to do the thermal and fluid analysis of the SLM process.

Since the laser sintering shared many similar characteristics with the welding process, the first SLM model was adapted from a model for the welding simulation [166]. Voller and Brent [166] classified the one-phase modeling of binary alloy solidification systems as three general models according to the problem domain. Validated by the experimental results for many metallurgical systems, these models could predict the macro-aggregation patterns during the solidification process. To better understand how the convective-diffusion process influenced the temperature and shape evolutions of the melting pool, Li et al. [167] established a three-dimensional numerical model to study the laser melting of ceramic materials. The binary phase diagram of the sintered ceramic material was integrated into the model to track phase change and flow motion in the melting pool. In a more comprehensive physical model developed by Xiao and Zhang [168], functions were added to analyze the shrinkage phenomena in the powder bed and the fluid flow driven by buoyancy force and surface tension gradient. The liquid velocities caused by capillary and gravity forces caused by shrinkage were considered as well.

Lattice Boltzmann method was a mesoscale economic tool for the modeling of the melting and re-solidification process during the SLM process [169, 170]. These models can provide the details of the time evolution of the microscopic particles which cannot be experimentally realized [171]. For example, the lattice Boltzmann method could simulate the Balling effect, an unfavorable effect caused by the surface tension force during SLM manufacturing. In ref. [169], a 2D lattice Boltzmann model was developed to investigate melting and re-solidification of a randomly packed powder bed under the irradiation of a Gaussian beam. This approach made many physical phenomena, for example, wetting phenomena and balling effect, which cannot be described in a standard continuum picture, accessible. Khairallah and Anderson [170] presented a 3D lattice Boltzmann model to investigate the SLM of the stainless powders utilizing the ALE3D multi-physics code, which incorporated the function to predict the Plateau-Rayleigh instability during the laser scanning. The simulations revealed some new physical insights that could be used for the development of physical models based on conservation equations.

In this thesis, a 3D model was developed to simulate the SLM manufacturing of thermoelectric material (Mg_2Si powder) with nanoparticles (Si nanoparticles) embedded for high thermoelectric performance. This physical model, cooperating the ability to analyze the fluid flow driven by buoyancy force and surface tension, can be utilized to analyze the influence of the process parameters on the pool size, particle aggregation, and temperature profile within the powder bed. The governing equations, including the continuity, momentum, energy, and nanoparticles transport equations, were discrete using the finite volume method (FVM), and then solved in a pressure-based manner. The total variation diminishing (TVD) discretization scheme was used for all the governing equations to preserve second order accuracy and unconditional stability. The SIMPLER algorithm integrated with the alternating direction implicit (ADI) method and block correction method was used to accelerate the convergence. An adaptive grid method was used for modeling the shrinkage phenomena within the powder bed.

5.4 The mathematical model to simulate SLM processing of multi-component thermoelectric powders

5.4.1 The physical model

SLM is a non-equilibrium manufacturing method, which can produce tremendous grain defects within the sintered material (Figure 5.3(a)). Shown in Figure 5.3(b) was the physical model used for the simulation. A Gaussian laser beam was moving over the powder bed with a velocity of U_b. The powder absorbed partition of the laser energy and formed a liquid pool in which the un-melted nanoparticles might be aggregated. After the laser beam moving away from the sintered zone, the melting pool cooled down quickly and re-solidified into a densified part. As shown in Figure 5.3(b), four distinct regions, which were a un-sintered region, a sintered region, a mushy region consisting of liquid dispersal within the solid dendrites, and a fluid region with dispersed nanoparticles, were identified in the powder bed. This system can be described by the equations governing the conservations of mass, momentum, energy, and the transport of the nanoparticles. The computational domain used for the modeling was 3.6 mm× 1.2 mm× 1.2 mm, which was much larger than the melting pool. The temperature on the boundaries far away from the melting pool were assumed constant. In this model, only half of the powder bed was simulated to save half of the computational resource.

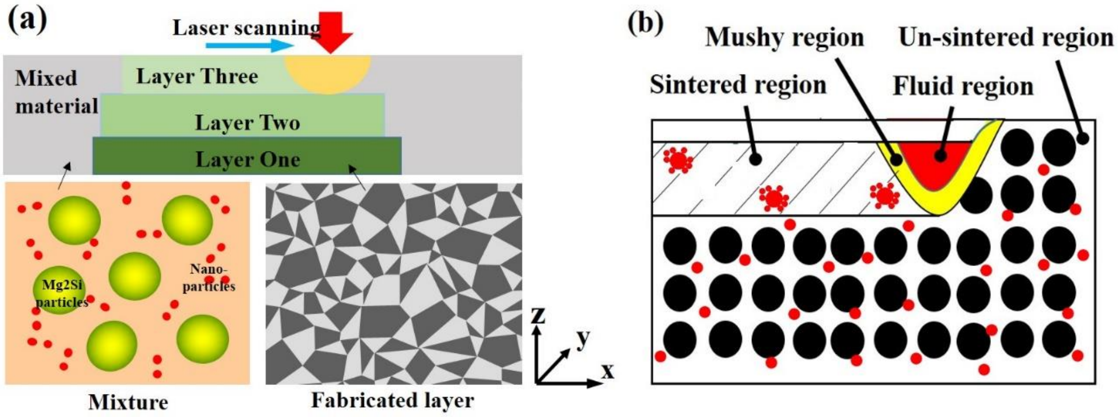

Figure 5.3. (a) SLM manufacturing of multi-component thermoelectric powders with nanoparticles embedded. (b) Four distinct regions in the powder bed for the first scanning trace.

5.4.2 Governing equations

The governing equations in this model were adapted from the one-phase model described in refs. [166, 168], but with some modification made to let it fit the current problem for multi-component thermoelectric material fabrication. To simplify the problem, some reasonable assumptions were made as follows:

a. The density of the powder bed was uniform. During the laser sintering, the gas in the porous was squeezed out gradually. In the fluid region and the sintered region, the gas was assumed completely drain out.

b. The buoyancy force caused by the density change was evaluated by the Boussinesq approximation because the thermal expansion coefficients were small.

c. The thermo-physical properties, including the thermal conductivity, specific heat, viscosity, and diffusion coefficient, were constant. But their values were different in the solid, mushy, and liquid regions because of the phase change.

d. The velocity induced by the shrinkage in the powder bed was in the *z*-direction. It only had impacts on the regions near the powder bed surface.

e. The code here focused on the simulation of the first trail on the powder bed. However, it could be easily adapted to simulate other cases in the SLM process.

Similar to the cases in refs. [168, 172], the laser beam was moving on the powder bed with a constant speed (u_b). The governing equations were accommodated to a one-phase model for all the four distinct regions in a moving coordinate system as follows.

The continuity equation

$$\frac{\partial \rho}{\partial t} + \frac{\partial\big(\rho(u-u_b)\big)}{\partial x} + \frac{\partial(\rho v)}{\partial y} + \frac{\partial(\rho w)}{\partial z} = 0 \tag{5-1}$$

The momentum equation

$$\frac{\partial\big(\rho(u-u_b)\big)}{\partial t} + \frac{\partial[\rho(u-u_b)^2]}{\partial x} + \frac{\partial(\rho(u-u_b)v)}{\partial y} + \frac{\partial(\rho(u-u_b)w)}{\partial z} = -\frac{\partial p}{\partial x} + \frac{\partial}{\partial x}\left(\mu^+ \frac{\partial u}{\partial x}\right) + \frac{\partial}{\partial y}\left(\mu^+ \frac{\partial u}{\partial y}\right) + \frac{\partial}{\partial z}\left(\mu^+ \frac{\partial u}{\partial z}\right) \tag{5-2}$$

$$\frac{\partial(\rho v)}{\partial t} + \frac{\partial[\rho v(u-u_b)]}{\partial x} + \frac{\partial(\rho v v)}{\partial y} + \frac{\partial(\rho v \mathrm{w})}{\partial z} = -\frac{\partial p}{\partial y} + \frac{\partial}{\partial x}\left(\mu^+ \frac{\partial v}{\partial x}\right) + \frac{\partial}{\partial y}\left(\mu^+ \frac{\partial v}{\partial y}\right) + \frac{\partial}{\partial z}\left(\mu^+ \frac{\partial v}{\partial z}\right) \tag{5-3}$$

$$\frac{\partial(\rho w)}{\partial t} + \frac{\partial[\rho w(u-u_b)]}{\partial x} + \frac{\partial(\rho w v)}{\partial y} + \frac{\partial(\rho w w)}{\partial z} = -\frac{\partial p}{\partial z} + \frac{\partial}{\partial x}\left(\mu^+ \frac{\partial w}{\partial x}\right) + \frac{\partial}{\partial y}\left(\mu^+ \frac{\partial w}{\partial y}\right) + \frac{\partial}{\partial z}\left(\mu^+ \frac{\partial w}{\partial z}\right) +$$

$$\rho_{ref}\, g_r (T - T_e)(\beta_T + \beta_s C_s) \tag{5-4}$$

The energy equation

$$\frac{\partial(\rho h)}{\partial t} + \frac{\partial\big(\rho h(u-u_b)\big)}{\partial x} + \frac{\partial(\rho h v)}{\partial y} + \frac{\partial(\rho h w)}{\partial z} = \frac{\partial}{\partial x}\left(k^+ \frac{\partial T}{\partial x}\right) + \frac{\partial}{\partial y}\left(k^+ \frac{\partial T}{\partial y}\right) + \frac{\partial}{\partial z}\left(k^+ \frac{\partial T}{\partial z}\right) + S_h \tag{5-5}$$

The nanoparticle transport equation

$$\frac{\partial(\rho C^+)}{\partial t} + \frac{\partial\big(\rho C^+(u-u_b)\big)}{\partial x} + \frac{\partial(\rho C^+ v)}{\partial y} + \frac{\partial(\rho C^+ w)}{\partial z} = \frac{\partial}{\partial x}\left(D^+ \frac{\partial C^+}{\partial x}\right) + \frac{\partial}{\partial y}\left(D^+ \frac{\partial C^+}{\partial y}\right) + \frac{\partial}{\partial z}\left(D^+ \frac{\partial C^+}{\partial z}\right) + S_C \tag{5-6}$$

where u, v, and w were the velocities in x, y, and z directions respectively, ρ was the density, p was the pressure, h was the enthalpy, μ^+ was the effective viscosity, k^+ was the effective thermal conductivity, C^+ was the effective particle concentration, D^+ was the effective diffusion coefficient, S_C and S_h were source terms for the energy equation and nanoparticle equation respectively, β_T was the liquid thermal expansion coefficient, β_s was the solid particle expansion coefficient, and C_s was the solid mass concentration.

Because the thermal expansion coefficient and mass concentration of Si nanoparticle were relatively small, Si nanoparticles played a minor role in the Buoyance force. Thus the solid expansion term in Eq. (5-4) was neglected in the calculation. Like the treatment in ref. [168], the relative velocity (w_s) to the coordinate system caused by the shrinkage of the porous powder bed was given by

$$w_s = \begin{cases} 0, & z \geq s \\ \varepsilon\left(\frac{\partial s}{\partial t} - u_b \frac{\partial s}{\partial x}\right), & z < s \end{cases} \tag{5-7}$$

It was assumed that the powders started to melt at $T_M - \Delta T$, and became fully melted at a temperature of T_M. The mass fraction of the liquid was assumed linearly correlated to the temperature in this temperature interval (ΔT). To simplify the model, the porosity of the fully melted material was assumed 0.0. Also, no density changed during the phase change process.

$$f_l = \begin{cases} 1, & T \geq T_M \\ \frac{T_M - T}{\Delta T}, & T_M - \Delta T < T < T_M \\ 0, & T < T_M - \Delta T \end{cases} \tag{5-8}$$

The physical properties of the partially melted material in the mush region were simplified as the summation of that of the powder and liquid weighted by their corresponding mass fractions. The effective diffusion coefficient and the effective thermal conductivity were given by

$$\mu^+ = \mu_s f_s + \mu_l f_l \tag{5-9}$$

$$k^+ = f_s k_s + f_l k_l \tag{5-10}$$

The powders used for the laser sintering was not pure materials. For example, doping elements and additive nanoparticles were mixed with the thermoelectric powders to enhance the ZT value. The thermal conductivity of the final powders was assumed to be the summation of the thermal conductivity (k_{pi}) of the different powder components weighted by their corresponding mass fractions (g_{pi}).

$$k_p = \sum_{i=1}^{n} g_{pi} k_{pi} \tag{5-11}$$

For a randomly packed powder bed with large thermal conductivity ratio (k_p/k_g, k_p and k_g were the thermal conductivities of the particle and gas, respectively), an empirical equations built by Hadley [173] and further outlined in ref. [168] was employed to estimate the effective thermal conductivity of the mixed powders. For the angular brass particles, the parameter α_0 varied significantly with the particle contact, in this modeling work, $\alpha_0 = 0.005$ was used [173].

$$\frac{k_{eff}}{k_g} = (1 - \alpha_0) \frac{\varepsilon f_0 + (k_p/k_g)(1 - \varepsilon f_0)}{1 - \varepsilon(1 - f_0) + \varepsilon(k_p/k_g)(1 - f_0)} + \alpha_0 \frac{2(k_p/k_g)^2(1 - \varepsilon) + (1 + 2\varepsilon)(k_p/k_g)}{(2 + \varepsilon)(k_p/k_g) + 1 - \varepsilon} \tag{5-12}$$

where

$$f_0 = 0.8 + 0.1\varepsilon, \tag{5-13}$$

Sih and Barlow [174] described another model to calculate the emissivity and thermal conductivity of the powder bed. This model predicted a thermal conductivity smaller than the model developed by Hadley [173]. This model was more suitable for non-packed powder beds. In the model proposed by Sih and Barlow, the emissivity of the powder bed was given by

$$\varepsilon_H = \frac{\varepsilon_S\left[2+3.082\left(\frac{1-\varepsilon}{\varepsilon}\right)^2\right]}{\varepsilon_S\left[1+3.082\left(\frac{1-\varepsilon}{\varepsilon}\right)^2\right]+1} \tag{5-14}$$

The thermal conductivity of the powder bed could be estimated by

$$\frac{k_{eff}}{k_g} = (1-\alpha_0)\left(1+\frac{\varphi k_R}{k_g}\right) + \alpha_0\left\{(1+\phi)\left[\frac{2}{1-\frac{Bk_g}{k_s}}\left(\frac{B}{\left(1-\frac{Bk_g}{k_s}\right)^2}\left(1-\frac{k_g}{k_s}\right)\ln\frac{k_s}{Bk_g} - \frac{B+1}{2} - \frac{B-1}{1-\frac{Bk_g}{k_s}}\right) + \frac{k_R}{k_g}\right] + \phi\,\frac{k_{contact}}{k_g}\right\} \tag{5-15}$$

where

$$\alpha_0 = \sqrt{1-\varepsilon} \tag{5-16}$$

$$\mathrm{B} = 1.25\left(\frac{1-\varepsilon}{\varepsilon}\right)^{10/9} \tag{5-17}$$

$$k_R = \frac{4\varepsilon\sigma_b T^3 x_R}{1-0.132\varepsilon} \tag{5-18}$$

In Eq. (5-15), ϕ was the flattened surface fraction of particle in contact with another particle, which was equal to the flattened surface area divided by the cross-sectional area of the particle. k_R was thermal conductivity of the powder bed owing to radiation denoted by Damköhler's equation (Eq. (5-18)). x_R was the effective length for radiation, which was the particle diameter of the powder. B was the deformation parameter of the particle.

The concentration of the additive particles in the original powder was C_s. The nanoparticle concentration ratio between the solid and the liquid was assumed to be a constant ($C_s = \varphi C_l$). Similar to the treatment in ref. [10], the effective nanoparticle diffusive coefficient of the powder was estimated by

$$D^+ = f_s D_s + f_l D_l/\varphi \tag{5-19}$$

The thermal capacity of the powders was temperature dependent. The integration of thermal capacity gave the enthalpy of the powders.

$$h = \int_0^T c_{ps}\,dT \tag{5-20}$$

The melting and solidification processes accompanied latent heat absorption and release. The latent heat was proportional to the liquid mass fraction. The enthalpy change during the phase transition could be divided into two parts, including the thermal capacity change and the latent heat.

$$\delta H = \left[\int_0^T \left(c_{pl} - c_{ps}\right) dT + L\right] f_l \tag{5-21}$$

As the thermal capacity of the liquid and the solid was assumed the same in this study, Eq. (5-22) was simplified as

$$\delta H = \begin{cases} 0, & T < T_M - \Delta T \\ L f_l, & T_M - \Delta T < T < T_M \\ L, & T > T_M - \Delta T \end{cases} \tag{5-22}$$

The source term for the energy equation was adapted from ref. [166]. While the first term was the transient term caused by the latent heat absorption and release, the others were the source terms introduced by the mass convection in the melting pool.

$$S_h = \frac{-\partial}{\partial t}(\rho \delta H) - \frac{\partial}{\partial x}(\rho (u - u_b)\delta H) - \frac{\partial}{\partial y}(\rho v \delta H) - \frac{\partial}{\partial z}(\rho w \delta H) \tag{5-23}$$

The source terms for nanoparticle transport equation was presented in Eq. (5-24), where the first term on the right of the equation was the transient term caused by the melting and solidification of the powders, and the other terms were introduced by the mass convection

$$S_C = \frac{-\partial}{\partial t}\left[\left(\frac{1}{k} - 1\right)\rho f_1 C_s\right] - \frac{\partial}{\partial x}\left[\left(\frac{1}{k} - 1\right)\rho f_1 C_s (u - u_b)\right] - \frac{\partial}{\partial y}\left[\left(\frac{1}{k} - 1\right)\rho f_1 C_s v\right] - \frac{\partial}{\partial z}\left[\left(\frac{1}{k} - 1\right)\rho f_1 C_s w\right] \tag{5-24}$$

5.4.3 Shrinkage tracking

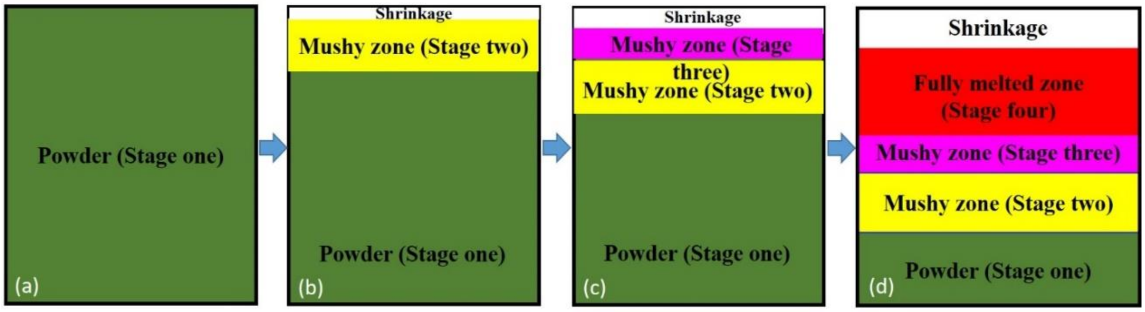

Figure 5.4. The shrinkage phenomenon in the powder bed during the SLM process: (a) Stage One, (b) Stage Two, (c) Stage Three, (d) Stage Four.

Because of the capillary effect and gravity force, when the powder was melted, the liquid would take the place of the gas gap, forming a liquid pool of full density. The shrinkage in the powder bed introduced extra difficulty to the thermal and fluid analysis for the SLM process. In this thesis, the heating process was divided into four sub-stages (Figure 5.4).

Stage One: Pre-heating ($T < T_M - \Delta T$)

At this stage, the temperature of the heated powder was lower than the melting point. No melting and shrinkage happened in the powder bed.

Stage Two: Preliminary melting ($T_M - \Delta T \leq T \leq T_M - \Delta T \frac{\varepsilon}{1-\varepsilon}$)

At this stage, only a small proportion of the powders was melted. A partition of the gas gap within the powder was occupied by the liquid. The volume of the powder melted in a local grid can be expressed as $f_l(1 - \varepsilon)dxdydz$. Since the gas gap volume in the powder bed was not completely filled at this stage, the shrinkage volume in the powder equaled to the melted powder volume, which was given by

$$\Delta S_2 = f_l(1 - \varepsilon)dxdydz \tag{5-25}$$

Stage Three: Partially melting ($T_M - \Delta T \frac{\varepsilon}{1-\varepsilon} < T < T_M$)

At this stage, as the gas within the powder bed was completely driven out, further powder melting would not lead to further shrinkage. The shrinkage at the local position equaled to the volume of the powder porosity.

$$\Delta S_3 = \varepsilon dxdydz \tag{5-26}$$

Stage Four: Fully melting ($T \geq T_M$)

At this stage, the powders were fully melted, and no gas was left in the powder bed. As the density change was not considered during the phase change process, no further shrinkage happened in this stage.

$$\Delta S_4 = \varepsilon dxdydz \tag{5-27}$$

Accumulated shrinkage

The accumulated shrinkage in the powder bed was calculated by integrating the shrinkage of each cell along the *z*-direction.

$$s = \left(\sum_{T_M - \Delta T}^{T_M - \Delta T * \frac{1-\varepsilon}{\varepsilon}} \Delta S_2 + \sum_{Tf}^{T_M} \Delta S_3 + \sum_{T_M}^{T_{MAX}} \Delta S_4 \right) / (dxdy) \tag{5-28}$$

5.4.4 The boundary conditions

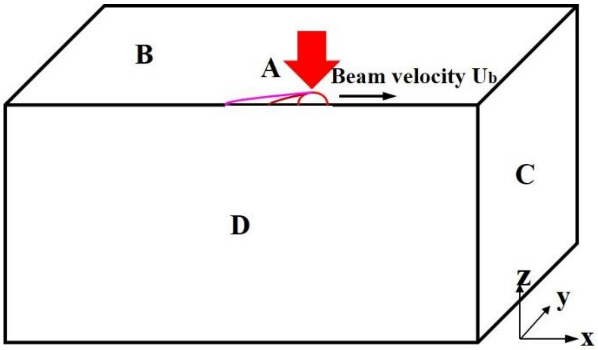

Figure 5.5. The boundaries of the computation domain

Boundary A (The heating spot in Figure 5.5): A Gaussian heat flux entered into the powder bed through boundary A. A part of the energy was lost through convection and radiation.

$$-k_{eff}\partial T/\partial z|_{z=s} = \theta q_{laser} + h_c(T - T_a) + \varepsilon_b\sigma_b(T^4 - T_a^4) \tag{5-29}$$

where the Gaussian heat flux was given by

$$q_{laser} = -\frac{q_0}{\pi R^2} exp\left(-\frac{r^2}{R^2}\right) \tag{5-30}$$

The thermo-capillary effect was caused by the temperature gradients near the powder bed surface. The shear force and surface tension at the free surface were assumed to achieve a balance during the SLM process.

$$\mu^+\left(\partial v_{s_1}/\partial n_1 + \partial v_{n1}/\partial s_1\right) = \sigma_{s_1}\frac{\partial T}{\partial s_1}\ (xz\ plane) \tag{5-31}$$

$$\mu^+\left(\partial v_{s_2}/\partial n_2 + \partial v_{n2}/\partial s_2\right) = \sigma_{s_2}\frac{\partial T}{\partial s_2}\ (yz\ plane) \tag{5-32}$$

The nanoparticle concentration gradient was zero at this boundary.

$$\partial C^+/\partial z|_{z=s} = 0 \tag{5-33}$$

Boundary B (The top surface except for A in Figure 5.5): All the conditions were the same to boundary A but the temperature. An energy balance was achieved at this boundary.

$$-k_{eff}\partial T/\partial z|_{z=s} = h_c(T - T_a) + \varepsilon_b\sigma_b(T^4 - T_a^4) \tag{5-34}$$

Boundary C (The right, left, and bottom surfaces in Figure 5.5): The side and bottom surfaces were far away from the heat source. As the thermal conductivity of the powder was relatively small, the temperature fluctuations on these boundaries were minimal. Thus constant temperatures were assumed on these surfaces.

$$T = T_a \tag{5-35}$$

No particle motion was assumed on the boundary. The nanoparticle concentration gradient was zero.

$$u = v = w = 0 \tag{5-36}$$

$$\partial C^{+}/\partial x|_{z=0,L} = 0 \tag{5-37}$$

Boundary D (The front surface in Figure 5.5): It is a symmetric surface.

$$\partial T/\partial y|_{y=0} = 0 \tag{5-38}$$

$$v = 0, \frac{\partial u}{\partial y} = \frac{\partial w}{\partial y} = 0 \tag{5-39}$$

$$\partial C^{+}/\partial y|_{y=0} = 0 \tag{5-40}$$

5.4.5 Numerical procedures

The SLM process was a three-dimensional quasi-steady state heat and mass transfer problem in a moving coordinate system. The mathematical model, specified by the continuity, momentum, energy, and nano-particle transport equations (Eq. (5-1)-(5-6)), as well as the constitute equations (Eqs. (5-7)-(5-24)), was solved numerically using the SIMPLER algorithm. The properties of the material were updated according to the temperature updated from the last iteration. Because the shrinkage of the powder surface was unknown beforehand, a false transient method was employed for surface tracking. The solution was assumed converged when the velocity and temperature distributions did not change with the false time. The convection and diffusion terms were discretized utilizing a total variation diminishing (TVD) scheme proposed by Van Leer [175] with the limiter function given by Eq. (5-41). The TVD scheme was utilized here because it was of second order accuracy and unconditionally stable without overshoot.

$$\psi(r) = \frac{r+|r|}{1+r} \tag{5-41}$$

The discretized equations in a three-dimensional Cartesian grid system was extended from that in a two-dimensional system documented in ref. [176],

$$a_P\phi_P = a_W\phi_W + a_E\phi_E + a_S\phi_S + a_N\phi_N + a_F\phi_F + a_B\phi_B + S_u^{DC} + S_\phi \tag{5-42}$$

where the central coefficient was

$$a_P = a_W + a_E + a_S + a_N + a_F + a_B + (F_e - F_w) + (F_n - F_s) + \left(F_b - F_f\right)$$

and a_W, a_E, a_S, a_N, a_F and a_B were the TVD neighbor coefficients [176].

The deferred correction source term was given by

$$S_u^{DC} = \frac{1}{2}F_e[(1-\alpha_e)\psi(r_e^-) - \alpha_e\psi(r_e^+)](\phi_E - \phi_P) + \frac{1}{2}F_w[-(1-\alpha_w)\psi(r_w^-) + \alpha_w\psi(r_w^+)](\phi_P - \phi_W) + \frac{1}{2}F_n[(1-\alpha_n)\psi(r_n^-) - \alpha_n\psi(r_n^+)](\phi_N - \phi_P) + \frac{1}{2}F_s[-(1-\alpha_s)\psi(r_s^-) + \alpha_s\psi(r_s^+)](\phi_P - \phi_S) + \frac{1}{2}F_b[(1-\alpha_b)\psi(r_b^-) - \alpha_b\psi(r_b^+)](\phi_B - \phi_P) + \frac{1}{2}F_f\left[-\left(1-\alpha_f\right)\psi\left(r_f^-\right) + \alpha_b\psi(r_b^+)\right](\phi_P - \phi_B) \quad (5\text{-}43)$$

where r_e^+, r_e^-, r_w^+, r_w^-, r_n^+, r_n^-, r_s^+, r_s^-, r_b^+, r_b^-, r_f^+, and r_f^- were defined the same to ref. [176].

The thermal boundaries were treated using the additional source term method. A grid system with uniformly structured hexahedron grids 200×90×90 in the *x*, *y*, and *z* directions was utilized. The false time step was 0.0001 s to make sure CFL<1.0 for all the grids. The iterative procedure continued until the residuals of all the governing equations were less than 10^{-5} for each time step. The solution was assumed to be converged when $\left|\frac{\phi_N - \phi_{N-1}}{\phi_N}\right| < 10^{-3}$. The block correction method [177] and the alternating direction implicit (ADI) method [176, 177] was employed to accelerate the convergence.

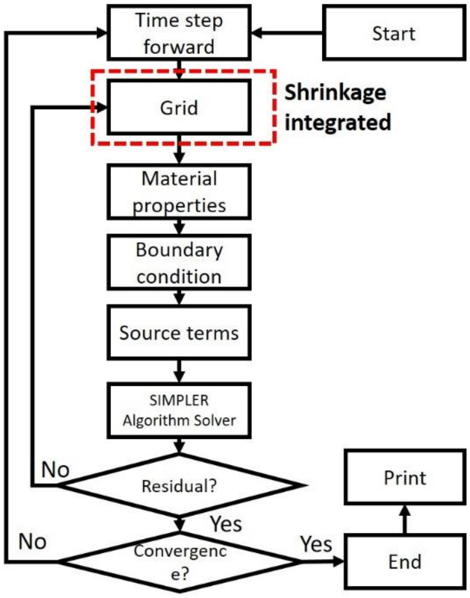

Figure 5.6. The numerical scheme for SLM simulation

5.4.6 Material properties and input parameters

The Mg_2Si powders were selected as the thermoelectric materials for SLM simulation. Some Si nanoparticles were added into the Mg_2Si powders to enhance both the thermoelectric performance and the mechanical properties of the sintered material. The thermal conductivity of the Mg_2Si documented in ref. [178] was used. Other physical properties of Mg_2Si, including the thermal capacity and the thermal expansion coefficient, were cited from ref. [179]. In this thesis, the additive material (Si particles) was assumed weighted 10% of the total mass. The physical properties of the Si documented in ref. [180] were used for this simulation. The material physical properties and SLM conditions used for the simulation were listed in Table 5.1 as follows.

Table 5.1. The physical properties of the Mg_2Si powders and SLM operation conditions

Scanning speed	$u_b = 0.01 - 0.2\ m \cdot s^{-1}$
Specific heat	$c_p = 67.87\ J \cdot kg^{-1} \cdot K^{-1}$
Bulk material thermal conductivity	$k_p = 7.0\ W \cdot m^{-1} \cdot K^{-1}$
Liquid thermal conductivity	$k_l = 5.0\ W \cdot m^{-1} \cdot K^{-1}$
Gas thermal conductivity	$k_g = 0.024\ W \cdot m^{-1} \cdot K^{-1}$
Initial powder thermal conductivity	$k_{eff} = 0.534\ W \cdot m^{-1} \cdot K^{-1}$, Eq. (5-12)
Porosity	$\varepsilon = 0.2$
Density	$\rho = 1990\ kg \cdot m^{-3}$
Liquid viscosity	$\mu_l = 5.0 \times 10^{-3}\ kg \cdot m^{-1} \cdot s^{-1}$
Solid viscosity	$\mu_s = 1.0 \times 10^{4}\ kg \cdot m^{-1} \cdot s^{-1}$
Specific diffusion coefficient	$D = 4.8 \times 10^{-9}\ m^2 \cdot s^{-1}$
Latent heat	$L = 4.5 \times 10^{5}\ J \cdot kg^{-1}$
Permeability coefficient	$K_0 = 2.0 \times 10^{6}\ kg \cdot m^{-3} \cdot s^{-1}$
Thermal expansion coefficient	$\beta_T = 1.1 \times 10^{-5}\ K^{-1}$
Melting point of pure material	$T_M = 1375\ K$
Equilibrium partition ratio	$k = 0.8$
Ambient temperature	$T_a = 298.15\ K$
Convective heat transfer coefficient	$h_c = 10.0\ W \cdot m^{-2} \cdot K^{-1}$
Laser diameter	$R = 0.003\ m$
Laser intensity	$Q = 10 \sim 100\ W$
Boltzmann constant	$\sigma_b = 5.67 \times 10^{-8}\ W \cdot m^{-2} \cdot K^{-4}$
Change rate of surface tension	$\partial\sigma/\partial T = -10^{-5}\ kg \cdot s^{-2} \cdot K$
Laser intensity	$q_0 = 1.8 \times 10^{4}\ W \cdot m^{-2}$

5.4.7 Results and discussion

Verification of the code

Before the simulation of the multi-component powders, this code was used to simulate the SLM fabrication of the nonporous 6063 aluminum sheet with dimensions of

229×152×3.2 mm^3. In an experiment documented in ref. [181], a continuous-wave CO_2 laser with a power of 1.3 kW and a travel speed of 4.23 mm/s was used to process the nonporous aluminum sheet. The diameter of the laser beam was measured to be 0.6 mm. The heat flux distribution of the beam was Gaussian. The power absorbed by the work piece was measured calorimetrically [182]. The measurement showed that about 86% of energy irradiated by the laser beam was lost via laser reflection, thermal radiation, and heat convection. In the simulation, the physical properties of the nonporous 6063 aluminum sheet and the boundary conditions were the same to the ref. [181], as shown in Table 5.2. The simulation result was compared with the simulation result presented in ref. [168, 181] and experimental result in ref. [182]. It showed that the simulated and measured fusion boundaries were in good agreement with each other (Figure 5.7).

Table 5.2. The physical properties of nonporous 6063 aluminum powders and melted aluminum [175]

Thermal expansion coefficient	$\beta_T = 1.0 \times 10^{-4}\ K^{-1}$
Change rate of surface tension	$\partial\sigma/\partial T = -0.35 \times 10^{-3}\ kg \cdot s^{-2} \cdot K$
Melting temperature	$T_M = 927.55\ K$
Solidification temperature	$T_s = 888.75\ K$
Ambient temperature	$T_a = 298.15\ K$
Latent heat	$L = 3.95 \times 10^5\ J \cdot kg^{-1}$
Density	$\rho = 2700\ kg \cdot m^{-3}$
Thermal capacity	$c_s = c_L = 1066\ J \cdot kg^{-1} \cdot K^{-1}$
Powder thermal conductivity	$k_s = 209\ W \cdot m^{-1} \cdot K^{-1}$
Liquid thermal conductivity	$k_L = 108\ W \cdot m^{-1} \cdot K^{-1}$
Liquid viscosity	$\mu_L = 1.0 \times 10^{-3}\ kg \cdot m^{-1} \cdot s^{-1}$
Solid viscosity	$\mu_s = 1.0 \times 10^5\ kg \cdot m^{-1} \cdot s^{-1}$

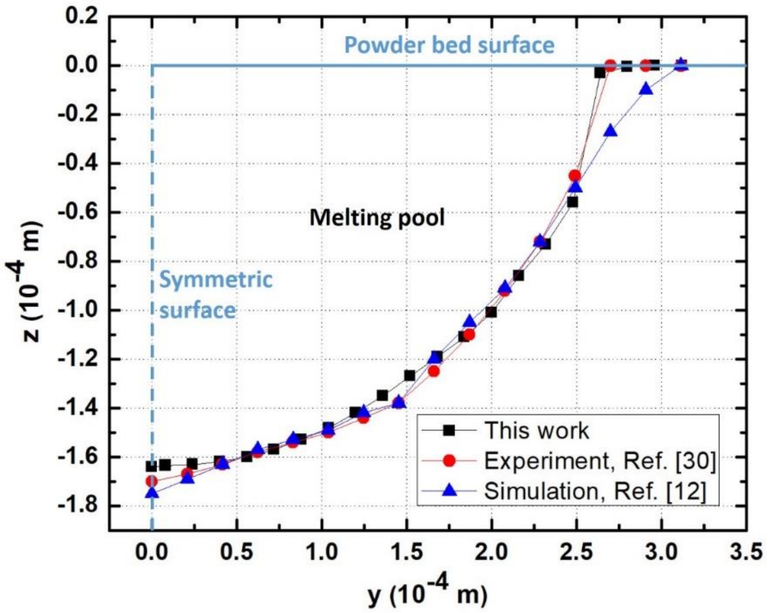

Figure 5.7. The comparison of the simulated and measured fusion boundaries for SLM of the 6063 aluminum sheet.

Shrinkage in the powder bed

The validated code was then used to simulate the SLM of Mg_2Si powders with Si nanoparticles mixed as the additive material. Figure 7 showed the shrinkage of the powder bed during the SLM process with different laser power inputs and scanning speeds. It was observed that the surface of the melting pool was not flat anymore. The maximum shrinkage depth was about 0.06 mm with a power input of 18.75 W. With the input power increased, the shrinkage region became broader and deeper. The scanning speed also affected the shrinkage of the powder bed. The higher scanning speed tended to uniform the temperature and thus led to more extensive and shallow shrinkage on the powder bed. Due to the shrinkage phenomenon, it was a challenge to control the contact quality between two layers of fabricated substrates. To reduce the shrinkage of the powder bed, the porosity of the powder bed should be as low as possible. Meanwhile, appropriate laser power should be selected, as too small energy input cannot melt the powder while too large energy input resulted in significant powder shrinkage and substantial deposited layer overlap. Finally, the scanning speed should be adjusted according to the laser energy input. For high power laser, the scanning speed should be higher so as to alleviate the potential evaporation and oxidation caused by the high temperature. The laser power input and the scanning speed should be calibrated synchronously to achieve optimal performance.

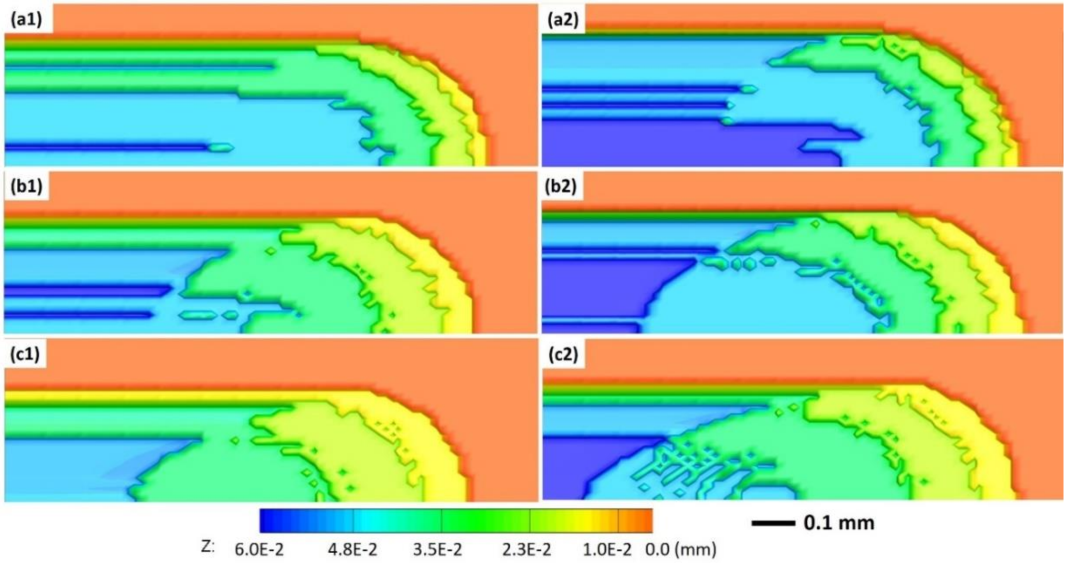

Figure 5.8. The shrinkages of the powder bed during the SLM process. P=18.75 W, R=0.3 mm, (a1) V= 0.02m/s; (b1) V= 0.04 m/s; (c1) V= 0.06 m/s; P=25 W, R=0.3 mm, (a2) V= 0.02 m/s; (b2) V= 0.04 m/s; (c2) V= 0.06 m/s.

Temperature profile

Shown in Figure 8 were the temperature profiles on the upper surface of the powder bed during the SLM process. A high-temperature spot was caused by the laser heating of the powder bed. As the laser beam moving from the left side to the right side, a high-temperature tail was left behind the laser. The highest temperature happened near the center of the laser on the surface of the powder bed with a peak temperature of ranges 2100-2500 K for different cases. With the laser input energy increasing, the high-temperature region expanded gradually. Since the peak temperature of the heating surface was much higher than the melting temperature, undesired evaporation and oxidation might happen during the SLM process. The input power of the laser beam should be carefully controlled to avoid such a situation. The laser scanning speed could be another factor that significantly affected the temperature distribution within the melting pool. The higher the scanning speed, the more extended high-temperature wake was observed. For the same laser energy input, the higher scanning speed resulted in lower peak temperature. By calibrating the scanning speed and the laser power, one could find the best processing parameters for specific material fabrication.

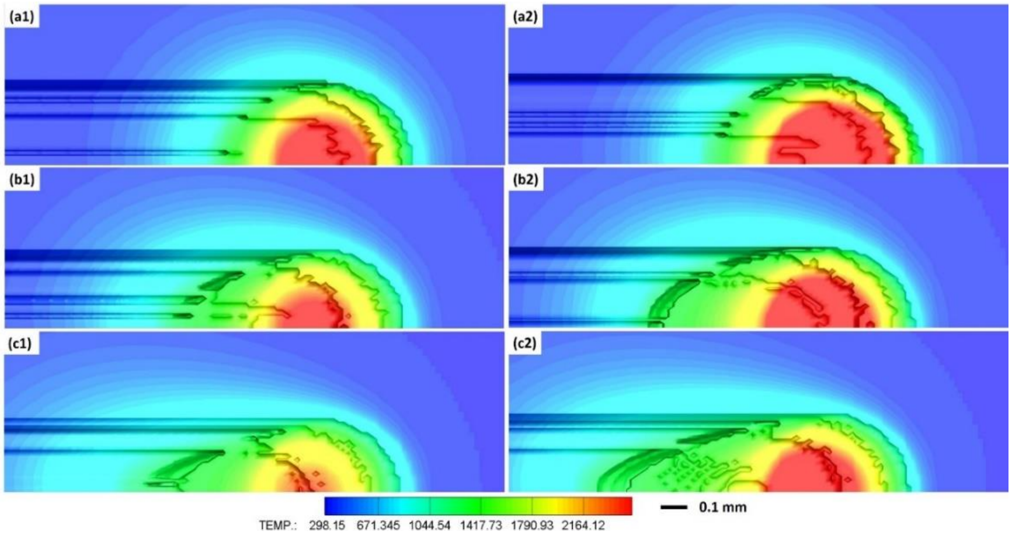

Figure 5.9. The temperature profiles during the SLM process. P=18.75 W, R=0.3 mm, (a1) V= 0.02m/s; (b1) V= 0.04 m/s; (c1) V= 0.06 m/s; P=25 W, R=0.3 mm, (a2) V= 0.02 m/s; (b2) V= 0.04 m/s; (c2) V= 0.06 m/s.

Melting pool size

The melting pool size played a vitally important role for the SLM fabrication. Tthe pool fluid dynamics in the melting pool could significantly affected the quality of the products. The size of the melting pool was directly correlated with the temperature profile. Shown in Figure 9 was the melting pool sizes for different simulation cases. The red region in the figure was the fully melted, and the green region were the powders, the blue region was partially melted. It was observed that the higher energy input generated the larger the melting pool. The shape of the melting pool changed accordingly with the scanning speed. The high scanning speed led to a narrow and long melting pool in the powder bed. The melting pool was not symmetrical on the front surface as the laser beam was moving from the left to the right. The un-symmetricity was more evident for the cases with the higher laser scanning speed. The melting pool size could significantly influence the heat and mass transfer process. The surface tension force and buoyancy force, which drove the fluid circulation in the melting pool, primarily depended on the size of the melting pool. A large melting pool size should induce strong heat and mass convection, which would accelerate the nanoparticle aggregation in the melting pool. Nanoparticles aggregation was undesired to achieve uniform physical properties and high thermoelectric performance in the final products. However, if the melting pool size was too small, the powders could not fully be melted and the density of the final product would be too small to achieve good electrical conductivity, which was essential for good thermoelectric performance. The process parameters should be carefully selected to maintain an appropriate melting pool size to made tradeoff.

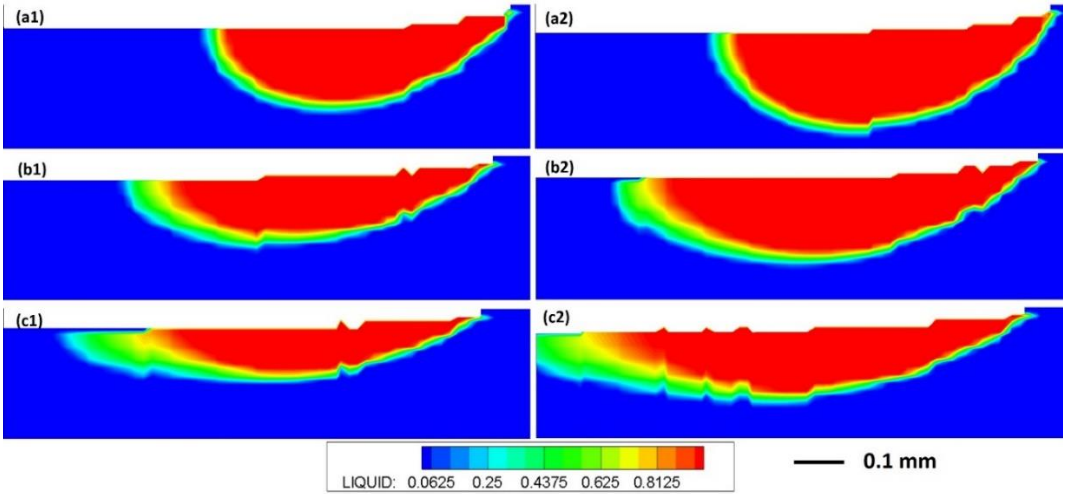

Figure 5.10. The melting pool size during the SLM process. P=18.75 W, R=0.3 mm, (a1) V= 0.02m/s; (b1) V= 0.04 m/s; (c1) V= 0.06 m/s; P=25 W, R=0.3 mm, (a2) V= 0.02 m/s; (b2) V= 0.04 m/s; (c2) V= 0.06 m/s.

Velocity profile

During the melting process, the temperature gradient on the free surface of the melting pool resulted in unbalanced surface tension along with the liquid-gas interface. Meanwhile, the density variation of the liquid generated a buoyance force in the melting pool. The two forces drove the fluid to circulate in the melting pool. The peak velocity in the melting pool was in the order of 10-4 mm/s. Though the flow velocity was very small, it would accelerate nanoparticle aggregation in the sintered material, which was undesired for thermoelectric material fabrication. Shown in Figure 10 was the circulation pattern within the melting pool. It was observed that the surface tension force tended to pull the flow from the center to the edge of the melting pool, while the buoyancy force tended to drove the flow from the bottom to the top surface of the melting pool. The combined effect of these two forces created a flow circulation in the melting pool, where the flow ran up in the center and down on the edge of the melting pool. The circulation pattern at the front face was nonsymmetrical because the laser beam moved from right to the left over the powder bed. The high-temperature region on the left side of the laser beam was more extended and uniform because the heat flux absorbed by the powders diffused deeper to the powder bed. The unsymmetrical temperature distribution led to an unsymmetrical flow pattern in the melting pool. The left flow circulation was larger than the right half, and the difference became more significant for cases with larger scanning speed. The circulation pattern illustrated in Figure 10was consistent with the experimental and simulation results documented in the literature. It was also found that the circulation and convection within the molting pool became stronger with the higher power input. The convection process accelerated the mass transport processes during the fabrication. Its impact on the nanoparticle aggregation should be carefully monitored and controlled during the process.

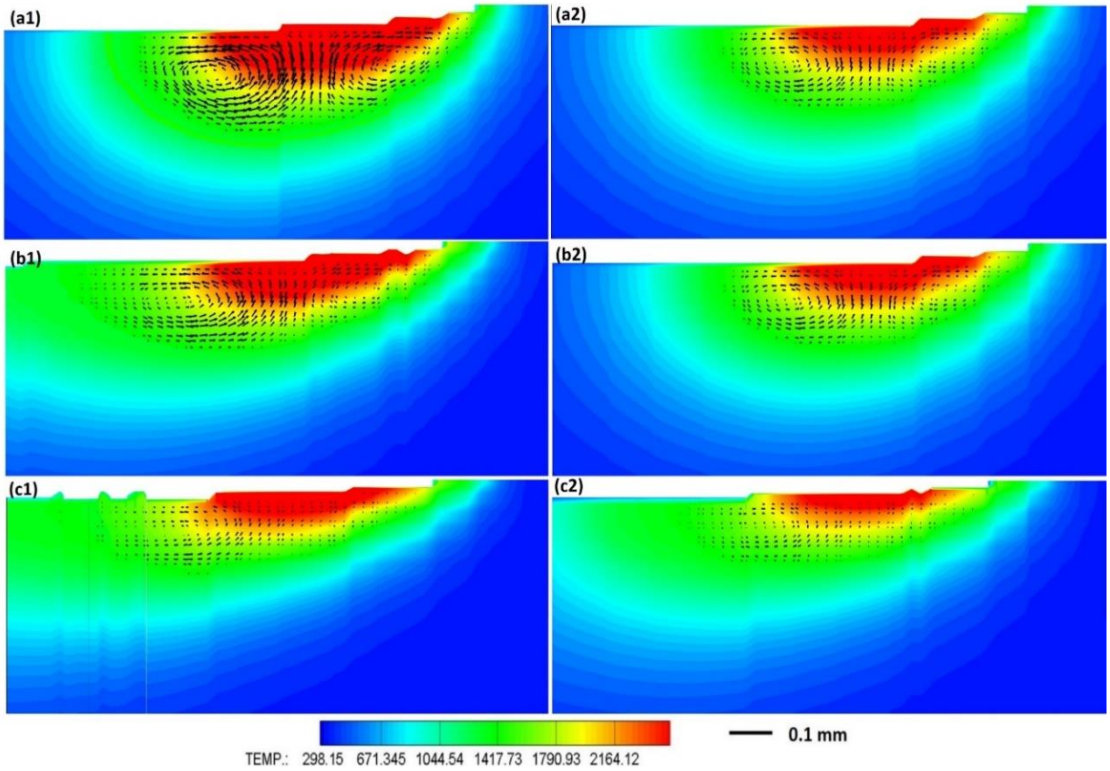

Figure 5.11. The velocity vector in the melting pool. P=18.75 W, R=0.3 mm, (a1) V= 0.02m/s; (b1) V= 0.04 m/s; (c1) V= 0.06 m/s; P=25 W, R=0.3 mm, (a2) V= 0.02 m/s; (b2) V= 0.04 m/s; (c2) V= 0.06 m/s.

Nano-particle concentration

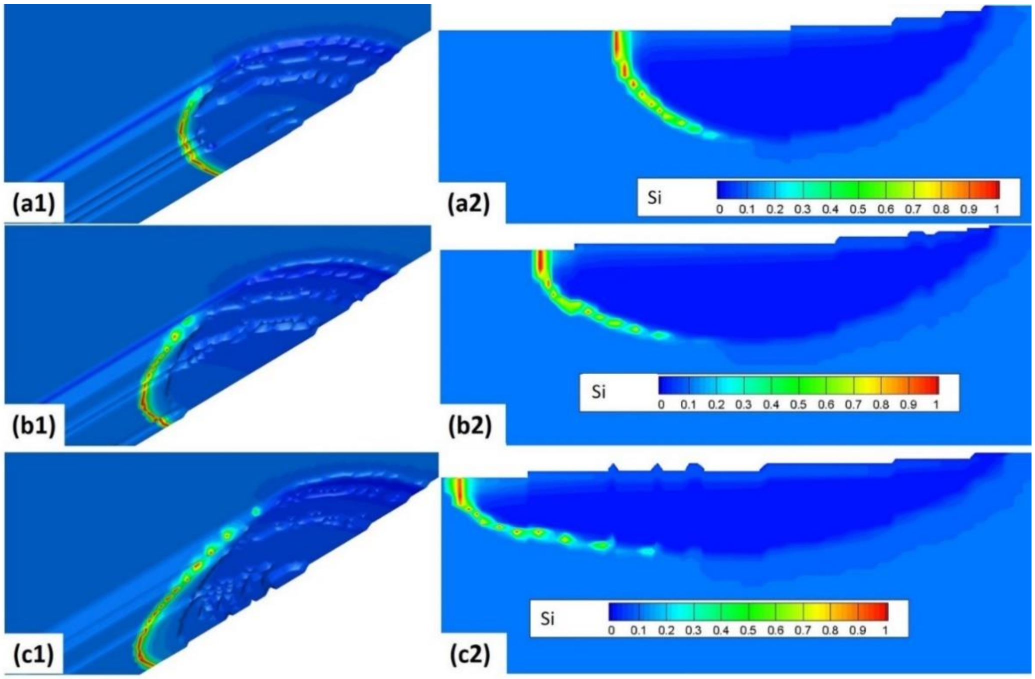

Figure 5.12. The Si nanoparticles concentration ratio distribution near the melting pool. P=18.75 W, R=0.3 mm, (a1) V= 0.02m/s; (b1) V= 0.04 m/s; (c1) V= 0.06 m/s; P=25 W, R=0.3 mm, (a2) V= 0.02 m/s; (b2) V= 0.04 m/s; (c2) V= 0.06 m/s.

The Si nanoparticles were through be able to enhance the ZT value of the Mg_2Si by reducing the thermal conductivity and enhance the electrical conductivity. The mixture ratio between the nanoparticles and the Mg_2Si powders were optimized before the SLM fabrication. Though the Si nanoparticles were uniformly mixed with the Mg_2Si powders, the nanoparticle distribution in the sintered material was non-uniform any more. As shown in Figure 11, the nanoparticles aggregated on the boundary of the melting pool. The nanoparticle concentration near the melting pool relatively small This phenomenon happened because the solubility of the nanoparticles in the solid and liquid was different. The aggregation of the nanoparticles had a negative influence over the thermoelectric performance of the final products. The material composition ratio deviated from the optimum value. Even a small change in the composition ratio would significantly reduce the ZT value of the sintered thermoelectric material. During the SLM fabrication of the thermoelectric material, the process parameters should be carefully selected to suppress the aggregation of the nanoparticles. A potential way to combat this phenomenon was increasing the scanning speed to shorten the residence time for material diffusion and convection. Other ways included reducing the input power to suppress the material diffusion and convection rates in the melting pool.

5.5 Summary for the chapter

In this thesis, a comprehensive 3D model was developed to simulate the convection-diffusion process during the SLM fabrication of thermoelectric powders (Mg_2Si) embedded with nanoparticles (Si). This model provided detailed information about the shrinkage of the powder bed, the shape of the melting pool, the temperature and velocity profiles, and the nanoparticles concentration ratio in the powder bed during the SLM fabrication. The code was validated by examining a case reported in the literature before it was used for the thermoelectric material simulation.

1) Because of the porosity in the thermoelectric powder bed, a shrinkage region was observed during the SLM fabrication. The shrinkage depth and coverage area were larger for cases with larger power input. The scanning speed helped to uniform the temperature profiles. The high scanning speed resulted in a long but shallow shrinkage region on the powder bed.
2) Both the energy input and the scanning speed had significant impacts on the melting pool. The energy input affected the size of the melting pool, while the scanning speed had more influence on the shape of the melting pool. The un-symmetricity of the melting pool was caused by the laser scanning speed direction.
3) The simulation results showed that the flow circulation induced by the surface tension and buoyancy force within the melting pool matched well with literature. The aggregation of the nanoparticles at the boundary of the melting pool should deteriorate the performance of the sintered thermoelectric material.

Section 6.3 of the chapter were adapted from a paper, "Yongjia Wu, Jackson Klein, Hanchen Zhou, Lei Zuo. Thermal and fluid analysis of dry cask storage containers over multiple years of service. Annals of Nuclear Energy, 2018, 112, 132-142." Part of Section 6.4 and 6.5 of the chapter were adapted from a paper, "Yongjia Wu, Jackson Klein, Hanchen Zhou, Lei Zuo. Energy harvesting for wireless communications in the nuclear environment. Annals of Nuclear Energy, 126 (2019): 376-388." Part of Section 6.4 and 6.5 of the chapter were adapted from a paper, "Yongjia Wu, Jackson Klein, Hanchen Zhou, Lei Zuo. Energy harvesting for nuclear waste sensing and monitoring. 2018 IDETC/CIE. Quebec. Canada."

Chapter 6. Thermoelectric Energy Harvesting for Through-Wall Wireless Communication in the Nuclear Environment

6.1 Chapter introduction

Monitoring the conditions inside enclosed metal vessels as found in spent fuel canisters and nuclear reactor pressure vessels were crucial to ensuring safe, dry cask storage and reactor operation. In this chapter, two energy harvesters, a gamma radiation energy harvester, and an existing-temperature gradient energy harvester, were designed to power wireless through-wall communication and in-situ monitoring of interior conditions in nuclear canisters.

As the first step, a detailed three-dimensional thermal and fluid analysis of a vertical dry storage cask with a canister containing 32 high-burnup pressurized water reactor (PWR) spent fuel assemblies for storage of 50 years was carried out using a CFD simulation. The input decay heat value was calculated based on a Westinghouse 17 × 17 PWR fuel assembly using the well-validated package ORIGAMI imbedded in SCALE, with a total heat load of 38.44 kW for year 5 and 10.67 kW for year 55. The temperature-dependent and anisotropic thermal properties of the fuel assemblies, filling gas within the canister, and air covering the canister were considered to preserve high accuracy. The peak temperature of 621.4 K occurred in the upper part of the fuel assemblies for year 5 case. And it decreased to 423.0 K after 50-years' service. The simulation results shed light on the temperature and flow environment within the canister for an operational time of 50 years.

The performance of the two energy harvesters over 50 years of service was evaluated, and a scaled experiment was performed to validate the designs. The gamma radiation energy harvester was found to have an energy output of 17.8 mW during the first year of canister storage. However, its power output decreases to less than 1.0 mW after 50-years storage. The thermal energy harvester was proved to be more practical with a simulated power output of 93.9 mW and an experimental output of 46.3 mW even after 50-years storage in the canister. The radiation shielding design for the energy harvesters was demonstrated at the end of the chapter.

6.2 Energy harvesting for nuclear waste monitoring

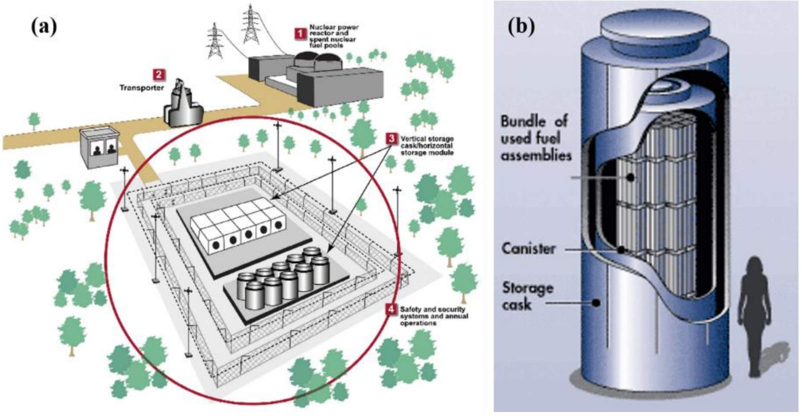

Figure 6.1. Depiction of dry cask storage where (a) nuclear waste storage at the at sites where it is generated [183] is shown along with (b) a cutaway of the dry storage canister [184].

In the nuclear industry, nuclear fuel rods were first stored in pools of water (wet storage) to remove heat from the assemblies and shield from gamma and neutron radiation left over from the production of radioactive nuclides in power generation. After five years or so, this fuel was then separated and stored in dry storage canisters for 30-60 years (Figure 6.1). After that, the fuel with low decay heat would be transported to a final disposal site for long term storage. In the U.S. alone, there were 1,500 loaded dry casks in 2010, and the number had been increasing by 200 each year. Since 2011, the close of the permanent nuclear waste disposal site in the Yucca Mountains, Nevada has brought dry storage and nuclear waste to the forefront of consciousness in the USA. Dry cask storage in the future might extend for up to one hundred years, which would bring large changes to the design of existing canisters.

Because of their lengthy use, monitoring of conditions within dry casks was of critical importance, as the temperature of the fuel and humidity within the cask could play a key role in the health of the system, and overall longevity of the storage containers. Thermal analysis of spent nuclear fuel had been identified as high priority by the DOE Nuclear Energy Division since potential failure mechanisms to the fuel and canisters were dependent on temperature. This offered a unique problem. As monitoring the cask internals could be very difficult, or indeed impossible due to a real potential for harm from radiation leakage, and containment rupture. To address this issue, energy harvesting for wireless communication of conditions within canisters had been studied. Wireless communication of data from inside the cask would remove the need for human inspection, and energy harvesting could potentially allow for sensors to run indefinitely. Such a system would be able to report, in a self-powered way, information of the fuel and environment within the canister, without the need for operators.

6.3 Thermal and fluid dynamic analysis of the dry cask system

To address this, a detailed thermal environment analysis in the canister was necessary to guide the placement of a thermoelectric energy harvester. This dissertation was primarily concerned with a simulation of the thermal performance of a vertical HI-STORM-100 dry storage cask with a MPC-32 canister containing 32 high-burnup (45 GWd/MTU) PWR spent fuel assemblies (Westinghouse PWR 17x17) for storage of 50 years. To better improve the accuracy of the simulation result and guide the future canister design, the present thesis introduced an improved model for thermal-fluid dynamic simulations of an MPC-32 dry cask. Built on approaches well validated in previous 3D CFD studies, some new approximations were adopted to improve the accuracy of the simulation, making it closer to real dry cask systems. First, temperature-dependent and anisotropic thermal properties of the fuel assemblies, filling gas, and air were introduced in order to preserve accuracy while overcoming drawbacks associated with traditional estimations. Second, in some of the previous literature, the filling gas was assumed to be steady, and only conduction was considered, which might cause the overestimation of the overall temperature within the canister. In this work, both the convective flows inside and outside the MPC were considered, which could significantly accelerate the heat transfer process. In addition to this, after examining the Reynolds number within the air gap, it was found to be in the transitional region. Thus turbulence modeling was also considered in this work. Last but not the least, the input decay heat value was not taken as randomly assigned value, as had been done extensively in the CFD analyses in the literature, but calculated based on a Westinghouse 17x17 fuel assembly using the well-validated package ORIGAMI imbedded in SCALE. The thermal analysis made in this work was used to guide the design a self-powered ultrasonic wireless monitoring system for the canister which could sense and monitor temperature, pressure, and moisture for the first 50-years life of this cask, and this analysis was given on the potential for energy harvesting within the dry cask. Ultimately, this work addressed some issues in the CFD modeling of the canister and provided comprehensive thermal-fluid dynamic data to guide both future canister designs and thermal energy harvesting for wireless sensors within MPCs.

6.3.1 SCALE decay heat calculation

ORIGAMI, a part of the SCALE Code System from ORNL, was widely used in the nuclear industry to calculate the isotopes present after various conditions were applied to a type of nuclear fuel. The software could accurately perform isotopic depletion and decay heat calculations for a wide range of fuel assemblies. In this work, the software was used to calculate the decay heat and nuclide makeup for the fuel under consideration from the time it left the reactor, to 50 years in dry cask storage (55 years since removal). In this way, the decay heat in the CFD analysis can be tailored to the specific fuel and time frame desired for simulation.

The fuel employed for the simulation here was a Westinghouse 17x17 assembly, with a total cask MTU of 15 spread over the 32 assemblies, an enrichment weight percentage of U235 of 4%, a burnup of 45 GWd/MTU, three runs per fuel assembly, and average power of 40 MW/MTU. This fuel configuration approximated an average assembly being removed from a reactor, as typical fuel now had a U235 enrichment between 3 and 5%, and was used up to, and in the future past, 45 GWd/MTU [185]. Using this average fuel allowed one to get a typical decay heat magnitude and trend. A more accurate representation of an actual fuel assembly could be made by inputting the data taken from a reactor history if desired. However as this data was highly specific to the reactor and fuel assembly, a general route was taken to show the process and to show the characteristics of an average set of fuel.

ORIGAMI offered an “Express form” [186] which could be used to quickly perform decay calculations on typical assembly types given a limited knowledge of the fuel and reactor. A more rigorous analysis could be done if actual data from a reactor was retrieved, and the results were desired. The calculations for decay heat were taken using this express form, and the parameters listed above. It was assumed the power reactor contained 90 MTU and the fuel was evenly distributed among 193 fuel assemblies. Based on this, the watts per assembly could be determined [187]. The total power of the MPC-32 along with the associated gamma and neutron intensities at various years throughout the lifetime of the cask, starting from 5 years after removal from the reactor, at the start of dry storage, and finishing with 55 years, at the 50-years mark for dry storage, were illustrated in Table 6.1.

Table 6.1. Decay heat, gamma intensity, and neutron intensity from the 15 MTUs of spent fuel for 50 years of dry cask storage.

Year (Since removal)	Decay Heat (kW)	Gamma Intensity (#/s)	Neutron Intensity (#/s)
5	38.44	2.64×10^{17}	1.02×10^{10}
10	24.52	1.47×10^{17}	8.4×10^{9}
15	21.07	1.20×10^{17}	7.0×10^{9}
20	19.00	1.04×10^{17}	5.9×10^{9}
25	17.31	9.2×10^{16}	4.9×10^{9}
30	15.85	8.2×10^{16}	4.1×10^{9}
35	14.56	7.3×10^{16}	3.4×10^{9}
40	13.42	6.5×10^{16}	2.9×10^{9}
45	12.40	5.8×10^{16}	2.4×10^{9}
50	11.49	5.1×10^{16}	2.0×10^{9}
55	10.67	4.6×10^{16}	1.7×10^{9}

The decay heat generated within the dry cask storage was highly dependent on the fuel makeup, and its operation within the reactor. As shown in table 6.1, it also depended on how long the fuel has been stored. This process of calculating the decay heat could be used to get a very precise approximation of the heat generated when placed into dry cask storage. The total decay heat was then assigned to each fuel assembly according to a ratio of X ($X = 9/11$ in this thesis) described below.

6.3.2 Conceptual principles

As mentioned above, typical dry casks [188], as depicted in Figure 6.2, are made up of a thick concrete overpack, and an internal MPC which can hold a variety of different fuels and assemblies inside the metal basket, ranging from 24 to 62 assemblies. The carbon steel basket and wall of the MPC, and the concrete overpack are meant to contain the radiation while removing heat from the fuel in order to ensure it does not reach a criticality point. This work focused on a specific canister, an MPC-32 canister made by Holtec International [188]. The concrete overpack (HI-STORM 100) was made to house the MPC and had inner channels to allow air to flow between the concrete and MPC, cooling the canister by taking advantage of the buoyancy force. Inside the MPC, a steel basket was used to hold the assemblies. The canister was also backfilled with helium to 3.3 atm in order to aid in the conduction and convection of heat away from assemblies, and give an inert gas environment. Decay heat generated by the spent fuel was transferred through the containment wall of the MPC to cooling air flow. Natural circulation drove the cooling air flow through an annular path between the MPC and the concrete overpack and carries the heat to the environment. The dimension of the canister and overpack were shown in table 6.2. To simplify the simulation, the support structures and some small components were neglected.

Table 6.2. The main dimensions of the Holtec HI-STORM 100 overpack and MPC-32 canister

HI-STORM 100 overpack (m)		
Concrete	Height	6.09
	Radius outer	1.68

	Radius inner	0.98
Inlet vent	Height	0.25
	Width	0.38
Outlet vent	Height	0.15
	Width	0.64
Pedestal	Height	0.64
	Radius	0.89
MPC-32 canister (m)		
Shell	Height outer	4.85
	Height inner	4.50
	Radius outer	0.89
	Thickness	0.013
Basket	Thickness	0.0096
	Basket Cell inner	0.224×0.224×3.66
Lid	Thickness	0.29
Westinghouse 17×17 fuel assembly (m)		
Fuel	Fuel Cell	0.214×0.214
	Active length	0.366

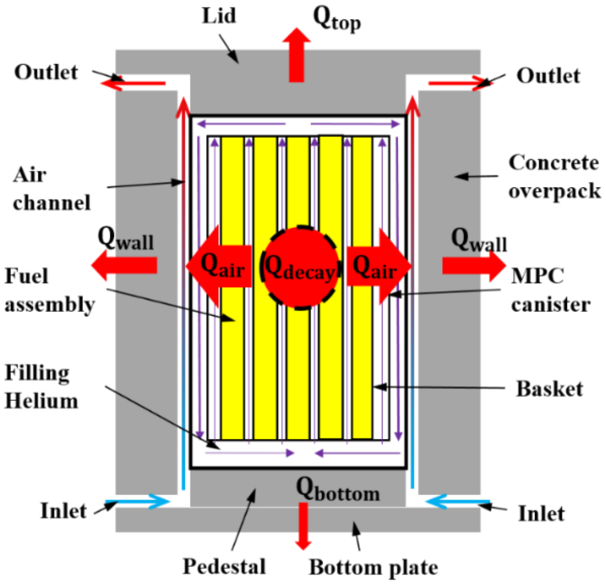

Figure 6.2. Model of the Holtec International dry cask canister.

6.3.3 Mathematical model

Reynolds and Grashof numbers were widely used to judge the flow regime for buoyancy force driven flow. According to ref. [189], the approximated fully developed velocity profile in the air channel between the MPC and the concrete overpack can be described as

$$\mathrm{v} = \frac{g\beta D^2 (T_0 - T_\infty)}{8\nu}\left[1 - \left(\frac{x}{D/2}\right)^2\right] \tag{6-1}$$

where β is the expansion coefficient, D is the characteristic length (width of the air channel), T_0 is the wall temperature, and T_∞ is the environmental temperature. A rough calculation of the Reynolds number showed that, in this region around the MPC, the Reynolds number was higher than 3,000 based on the channel hydraulic diameter and maximum air velocity in the annulus, which was clearly above the critical Reynolds number of 2,300 for internal flows. Thus we judged that the air flow was in a transitional range between the laminar and turbulent regimes. This was different from Zigh et al. [190] who mentioned that the air flow could be a laminar flow based on Grashof number, another criterion proposed by Sparrow and Azevedo [191]. On the other hand, the helium flow inside the canister was predicted to be in the laminar regime based on the Reynolds and Grashof numbers. Here, the temperature increase of the air flow was less than 70 K, thus $\beta(T - T_0) \ll 1$, so Boussinesq approximation could be used to calculate the buoyancy force without significant derivation.

The Reynolds time-averaged *k-ε* turbulence model with standard wall functions and transitional SST *k-ω* were used to model turbulence in the air channel and canister. The *k-ε* turbulence model with standard wall functions can predict the fluid behavior of fully developed turbulence flows with fairly high accuracy, as have been well validated by the industrial community in the past 30 years. On the other hand, the transitional SST *k-ω* is the most general turbulence model. The transitional SST *k-ω* model initially attracted attention because it does not require wall-damping functions for low Reynolds number applications. By introducing blending functions, this model combines the good near-wall behavior of the *k–ω* model with the robustness of the *k–ε* model in the far field in a numerically stable way. The governing equations [176] of the transitional SST k-ω model are prescribed by

Continuity equation

$$\frac{\partial(\rho)}{\partial t}+\frac{\partial(\rho u_j)}{\partial x_j}=0 \tag{6-2}$$

Momentum equations

$$\frac{\partial(\rho u_i)}{\partial t}+\frac{\partial(\rho u_i u_j)}{\partial x_j}=\rho g\beta(T-T_\infty)-\frac{\partial p}{\partial x_i}+\frac{\partial \tau_{ij}}{\partial x_j}+\frac{\partial}{\partial x_j}\left(\eta\frac{\partial u_i}{\partial x_j}\right) \tag{6-3}$$

where $\tau_{ij}=-\rho\overline{u_i'u_j'}=2\mu_t S_{ij}$, S_{ij} is the mean rate of the strain tensor.

Energy equation

$$\frac{\partial(\rho c_p T)}{\partial t}+\frac{\partial(\rho c_p u_j T)}{\partial x_j}=\frac{\partial}{\partial x_j}\left(\lambda\frac{\partial T}{\partial x_j}\right)-\tau_{ij}\frac{\partial u_i}{\partial x_j}+\beta T\left(\frac{\partial p}{\partial x_j}+u_j\frac{\partial p}{\partial x_j}\right)+S_i \tag{6-4}$$

The k equation

$$\frac{\partial(\rho k)}{\partial t}+\frac{\partial(\rho k u_j)}{\partial x_j}=\frac{\partial\left(\left(\mu+\frac{\mu_t}{\sigma_k}\right)\frac{\partial k}{\partial x_i}\right)}{\partial x_j}+\left(\tau_{ij}\cdot S_{ij}-\frac{2}{3}\rho k\frac{\partial u_i}{\partial x_j}\delta_{ij}\right)-\beta^*\rho k\omega \tag{6-5}$$

The ω equation

$$\begin{aligned}\frac{\partial(\rho\omega)}{\partial t}+\frac{\partial(\rho\omega u_j)}{\partial x_j}=\frac{\partial\left(\left(\mu+\frac{\mu_t}{\sigma_\omega}\right)\frac{\partial \omega}{\partial x_i}\right)}{\partial x_j}+\gamma_2\left(2\rho S_{ij}\cdot S_{ij}-\frac{2}{3}\rho\omega\frac{\partial u_i}{\partial x_j}\delta_{ij}\right)-\beta_2\rho\omega^2+\\ 2\frac{\rho}{\sigma_{\omega,2}\omega}\frac{\partial k}{\partial x_k}\frac{\partial \omega}{\partial x_k}\end{aligned} \tag{6-6}$$

where the σ_k, β^*, $\sigma_{\omega,2}$, γ_2 and β_2 are revised constants, with the corresponding values 2.0, 0.009, 1.17, 0.44, and 0.083, respectively. μ_t and σ_ω are related to the blending functions to make the equations suitable for both the low and high Reynolds numbers flow regions.

The Discrete Ordinates (DO) Radiation Model was used to model the thermal radiation in the cask. This model was selected because it spanned the entire range of optical thicknesses, and allowed for problems to be solved with surface-to-surface radiation. Four angular discretization steps were used in each direction of the spherical coordinates system to ensure reasonable accuracy.

The CFD analysis of the cask storage system was carried out using the ANSYS/FLUENT 14.0 package. A 90-degree section of the MPC–32 spent fuel dry storage system, shown in Figure 6.3, was employed for the simulation. Two grid systems with 1,814,658 and 4,442,080 hexahedral grids were used. The dimensionless distance (y+)

between the wall and the cell center of the near wall grid for the first mesh was around 20. To better improve the performance of the transitional *k*-*ω* SST model at the near wall viscosity-affected region, the grids near the canister wall was refined to let y+~1(with grids number increases to 4,482,080). The grid quality was well checked to ensure better convergence. The simulation on the year 5 case found no significant difference in the outlet air volume flow rate for these two grid systems. Thus, the grid system with 4,442,080/4,482,080 hexahedral nodes was used to do the case by case calculations. The SIMPLE algorithm was used to solve the Navier–Stokes equations in a segregated manner. A body-force-weighted scheme was used for the pressure discretization, as the buoyancy force acted as the driving force. The discretization method used for all the other parameters was the second-order upwind method. The iteration continued until the residuals were less than 10^{-3} for the mass, momentum, and turbulence equations, and 10^{-6} for the *k*, *ω*, and *ε* energy equations. A second criterion to check the convergence of the iteration was to monitor the volumetric flow rate of the air flow at the vent outlet. When the fluctuation was less than 1.0%, the iteration could be regarded as converged.

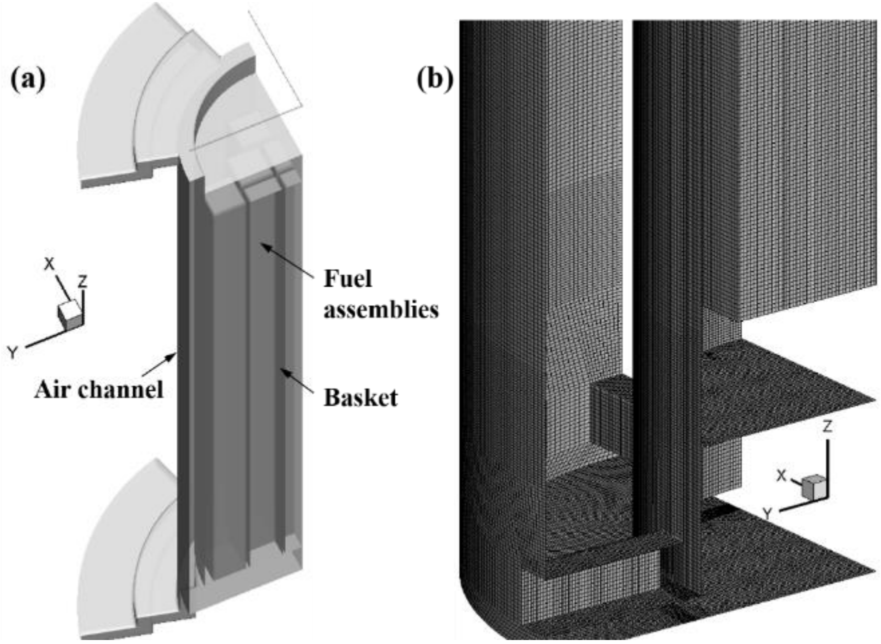

Figure 6.3. Holtec International dry cask canister: (a) Internal structure of the dry cask system; (b) the grid system.

6.3.4 Decay heat in the fuel assembly

In some previous literature, the heat load, was assumed to be uniformly distributed in the fuel assembly. In the real case, the heat load varied in both the radial and axial directions. The heat load distribution in the fuel assembly was known to be a key element in determining the real temperature profiles within the canister [188, 192]. Generally, the fuel assembly positions in the MPC basket honeycomb (Figure 6.4(a)) could be grouped in two regions: the inner one (orange), with 16 cells, and the outer one (yellow), with a total of 16 cells. The fuel assemblies in the same region were assumed to have the same load heat. To better simulate the real system, a more precise heat load function could be fit. The relation between the actual heat load (Q) and the designed one (Q_{des}) was a function of X [192],

$$\mathrm{Q(X)} = 2\frac{Q_{des}}{1+X^{0.23}/X^{0.1}} \tag{6-7}$$

where X was the ratio between inner and outer heat loads of fuel assemblies. For our case, the total heat load between the outer and inner fuel assembly were set to be 9/11.

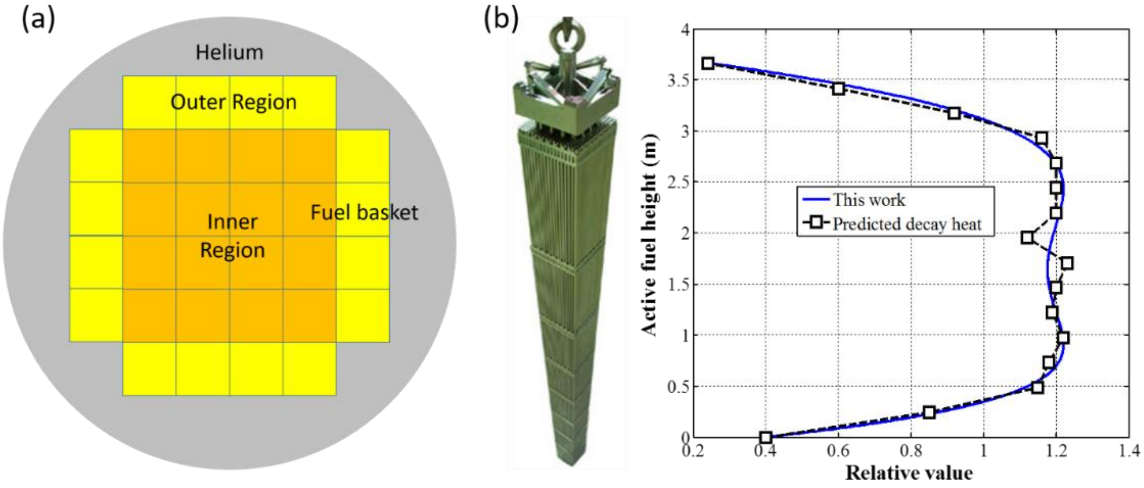

Figure 6.4. The load heat distribution in the fuel assembly: (a) Load heat profile in the radial direction; (b) Load heat profile in the axial direction of the fuel assembly [193].

According to Turner [194], the load heat for in a single fuel assembly was non-uniform shown in Figure 6.4(b). The cross-section edge was very much smaller than the length of the fuel assembly. Thus it was reasonable to assume a uniform heat generation rate on the cross-section. However, a peaking factor profile for the heat generation rate along the axial length of the fuel assembly was adopted to improve the simulation accuracy.

$$q_{load} = 1.1A \cdot (0.0237 \cdot Z^5 - 0.3287 \cdot Z^4 + 1.5058 \cdot Z^3 - 2.9965 \cdot Z^2 + 2.6204 \cdot Z + 0.3927) \qquad (6\text{-}8)$$

where the A was adapted according to each case to ensure the total load heat was equal to the total assigned heat load calculated from ORIGAMI. Numerical implementation of the distributed load heat was achieved by using the User Defined Functions (UDFs) embedded in FLUENT.

6.3.5 Material Properties and Boundary Conditions

The thermal properties of the materials, including the density, thermal conductivity, heat capacity, viscosity, thermal expansion coefficient, and surface emissivity, were obtained from the literature [190, 195]. Among all these properties, special attention should be paid to the thermal conductivity of the air and the fuel assembly. As the air took away more than 80% of the total decay heat, a small change in the air properties could introduce significant influence on the temperature profile in the fuel assembly.

6.3.5.1 The fuel assembly

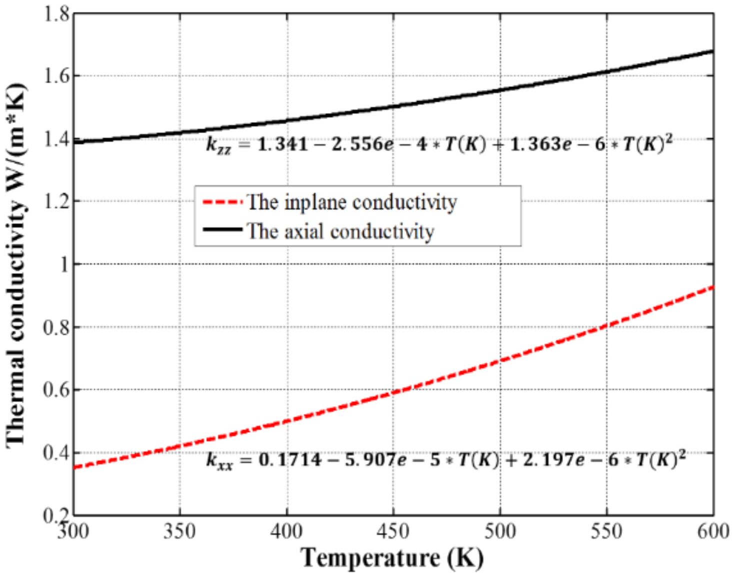

Figure 6.5. The in-plane thermal conductivity and the axial conductivity of the fuel region with a filling gas of helium.

In these simulations, the thermal conductivities were assumed to be constant for each of the solid components, except for the fuel assembly. The physical properties of canister/cask components were obtained from the Safety Analysis Report for the HI-STORM 100 Cask System [188].

The spent nuclear fuel generated heat as a result of continuing isotope decay resulting in gamma and neutron generation. All heat generated within the fuel rods would be rejected into the environment through the parallel heat transfer process combining the conductivity and convective heat transfer of the filling gas (helium), and thermal radiation. It was computationally cost expensive to model the details of every fuel rod in the stored fuel assemblies. In a fuel assembly, the fuel rods were arranged neatly, making it accurate and economic to characterize the anisotropic conduction media using an effective thermal conductivity method. A 2D model of a Westinghouse 17 × 17 Standard PWR spent fuel assembly was constructed to determine the planar effective thermal conductivity (k_{eff}) of the spent fuel assembly by Mittal et al. [195], following the k_{eff} methodology described in the TRW report [196] by Bahney and Lotz. The in-plane thermal conductivity and the axial conductivity of the fuel region with a filling gas of helium were illustrated in Figure 6.5. It should be noted that this method was accurate enough to catch the main characterization of the thermal and flow information, but might lost some accuracy to predict the peak temperature within the system.

6.3.5.2 The helium and air properties

The helium gas was used to fill the MPC, enhancing the convective and conductive heat transfer between the basket and the canister shell. In these simulations, the pressure was set to be 3.3 atm with corresponding gas properties taken from the literature [197]. The ambient pressure outside the cask was assumed to be 1.0 atm. The thermal conductivity of the air was temperature dependent in this simulation since the air flow played a key role in the heat dissipation. With the temperature increasing from 294.15 K to 364.15 K, the thermal conductivity of the air increased by nearly 20%, which might significantly influence the final result.

Table 6.3. Thermal physical properties of the helium and air

Helium	
Thermal conductivity (W/(m·K))	0.0383+4.1713e-4·T -1.0193e-7·T^2
Density (kg/m^3)	0.4875
Viscosity (kg/(s·m)	1.84e-5
Expansion coefficient (1/K)	0.002
Air	
Thermal conductivity (W/(m·K))	-5.22e-5+9.78e-5·T-3.39e-8·T^2
Density (kg/m^3)	1.00
Viscosity (kg/(s·m)	1.79e-05
Expansion coefficient (1/K)	0.00283

6.3.5.3 Boundary conditions

The boundary conditions below in Table 6.4 used in the CFD model were the same as used in refs. [190, 198]. These coefficients were calculated based on free convection correlation in still air for vertical and horizontal surfaces. At the bottom surface of the cask, the equivalent resistance of heat conduction to underlying soil was used to prescribe an equivalent heat transfer coefficient. The emissivity of all the internal surfaces was set to be 1.0 for simplification.

Table 6.4. Boundary conditions for the CFD simulation

Parameters	Value
Ambient temperature (K)	294.15 K
Inlet pressure (atm)	1.0
Outlet pressure (atm)	1.0
Heat transfer coefficient on the top and at the side of the dry cask (W/(m^2·K))	5.0
Heat transfer coefficient on the bottom surface (W/(m^2·K))	0.17
Soil temperature	288.15 K
Pressure in the canister (atm)	3.0
Vertical cross-sections	Symmetric

6.3.5.4 The thermal and hydro environment in the dry cask system

The thermal-fluid dynamic performance of the HI-STORM 100 cask and MCP-32 canister system had been explored under steady state conditions. The temperature and velocity profiles within the system were of primary concern in the development of a TEG energy harvester to power the wireless sensors, and thus were outlined below.

Figure 6.6 below showed the temperature contours for the vertical storage cask with a helium-filled (3 atm) canister and a stainless steel basket holding 32 spent fuel assemblies with a total heat load of 38.44 kW for year 5 (beginning of dry cask storage), and 10.67 kW for year 55 (50 years of dry cask storage) in Figure 6.7. The peak temperature of 621.4 K occurred in the upper part of the fuel assemblies for at year 5.

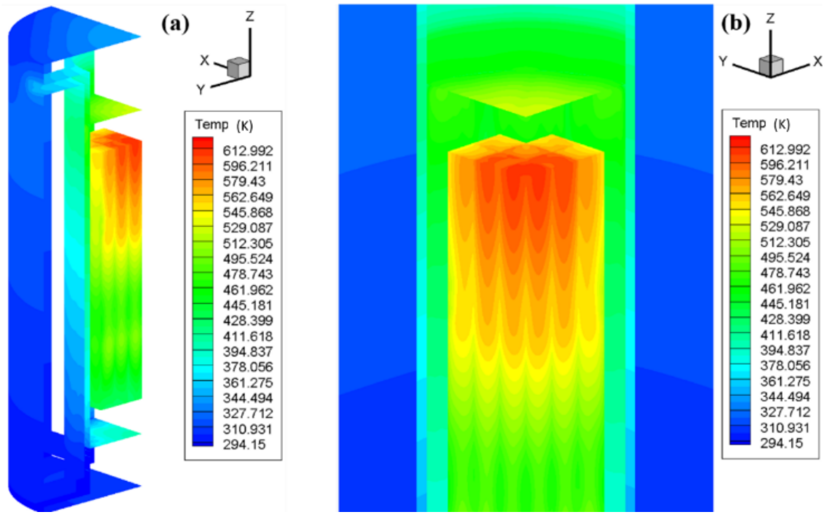

Figure 6.6. The temperature profiles in the canister at years five after the fuel removed from the reactor using the transitional SST k-ω turbulence model.

When comparing these results with other works which assumed that the helium gas was steady and only conductive heat transfer was considered, the peak temperature point in this work shifted significantly to a higher position within the fuel assemblies. This could be reasoned by a helium cycling phenomenon caused by the buoyancy force generated within the canister. On the one hand, the helium filling the gap between the basket and the fuel assembly was heated through the convective and conductive heat transfer process. On the other hand, the helium outside the basket was cooled down by the relative cold MPC wall. The buoyancy force aroused by the variation of the helium density drove the natural circulation flow within the canister, which enhanced the thermal performance of the canister. This phenomenon was more obvious for the cases with younger spent fuels, due to the more intensified helium circulation. This cooling process was also reflected in the relatively low temperature at the surface of the fuel assemblies. As expected, the overall temperature of the dry cask system decreased gradually with time. After 50-years operation, the peak temperature was about 436.0 K, far below the temperature safety margin.

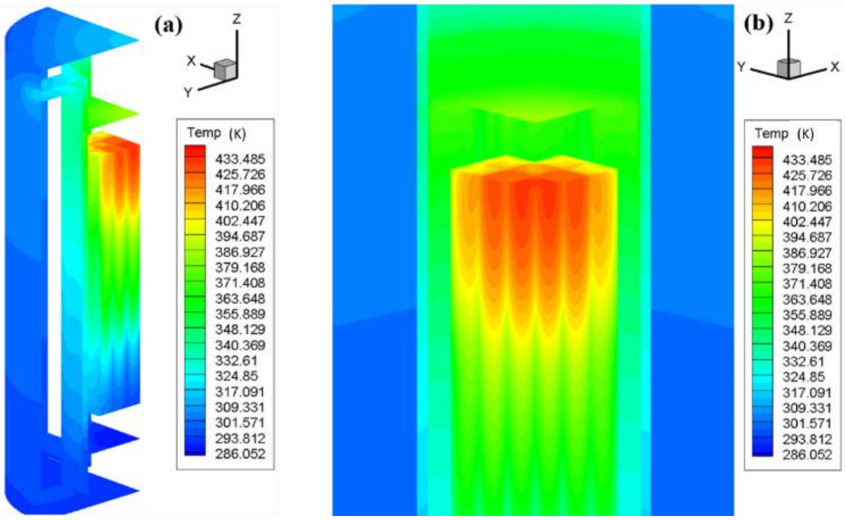

Figure 6.7. The temperature profiles in the canister at years 55 after the fuel removed from the reactor using the transitional SST k-ω turbulence model.

The thermal environmental information was extracted from the CFD simulation results to guide an energy harvester design. It was possible to install a TEG energy harvester above the fuel assembly, or near the vertical wall of the canister. Figure 6.8 below gave the radial temperature profile at Z=3.19 m at the center (axially) of the cask. It was found that both the k-ε and transitional SST k-ω model could reasonably predict the temperature field, as the temperature profiles obtained by these two models were similar to each other. Actually, to power a 1.0 W sensing and data transmission for 3 seconds every 5 minutes, ten mW of continuous power from an energy harvester was enough. For the year 5 case, the temperature drop near to the canister wall was as high as 70 K, which was more than enough for high-performance TEG to harvest enough energy for sensor network powering. However, for the year 55 case, the temperature drop was only about 13 K. To generate enough energy, like 10 mW estimated, the TEG energy harvester should be carefully designed to meet the goal.

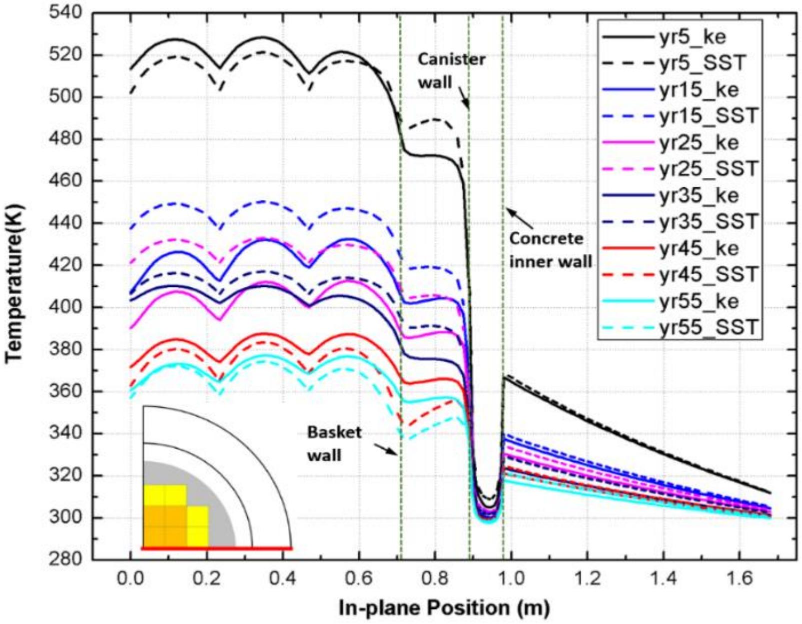

Figure 6.8. The radial temperature profile at Z=3.19 m at the symmetry surface

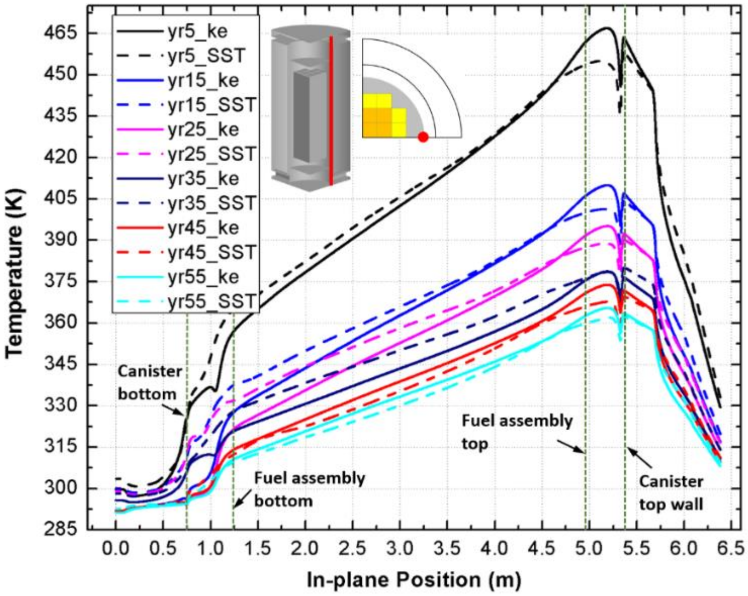

Figure 6.9. The temperature profile along the outer surface of the canister.

Another position might show promise for the TEG energy harvester installation was space somewhere above the fuel assembly. Thus the thermal profile of the canister was also taken axially along the MPC wall, as shown below in Figure 6.9. Because of the thermal radiation heat exchanged between the top surface of the fuel assembly and the top wall of the canister, there was a temperature jump at the canister surface, where the wall temperature was slightly higher than the helium gas near the wall. At year 5, the temperature difference near the canister wall was about 20 K, which reduced to ~5 K at year 55. Thus it would be challenging to install a successful energy harvester at this location.

Because of the air channel and the thick concrete wall, the temperature outside the canister was relatively low, as was presented below in Figure 6.10. A rough calculation found that less than 20% of the total heat was dissipated into the environment through the outer wall of the dry cask. The concrete outer surface temperature increased with the height, appropriately considering the heat distribution in the fuel and the air flow along the inner surface of the overpack. At the top end of the concrete surface, somewhere near the outlet of the air channel, the temperature reached the peak value. Considering the temperature difference between the wall and ambient (295.15 K) was more than 20 K even for the year 55 case, it was possible to build an independent TEG energy harvester to power smart sensors for concrete structural health monitoring.

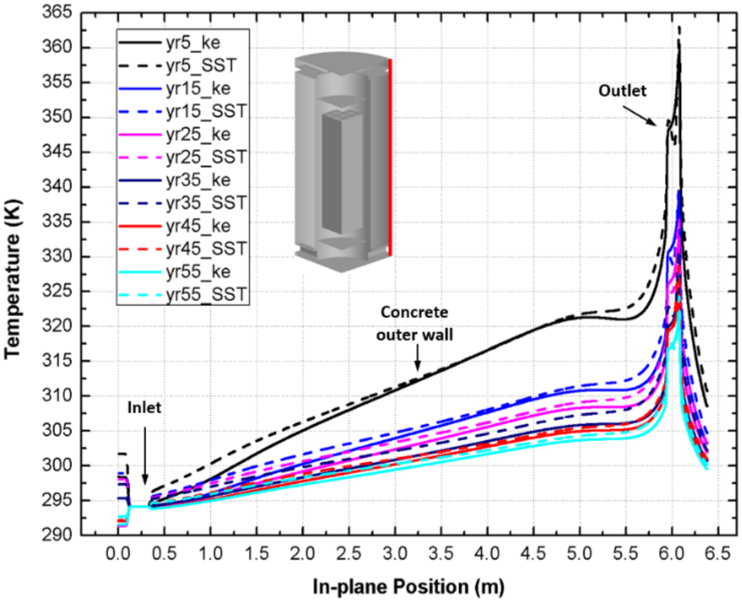

Figure 6.10. The temperature profile along the outer surface of the canister.

The flow regions within the dry cask system could be divided into two regions, with their thermal boundary coupled at the canister wall, as shown below in Figures 6.11 and 6.14. Inside the canister, there was a flow circulation driven by the buoyancy forces caused by the temperature difference between the core of the fuel assembly and the canister wall. Outside the canister, another flow was aroused by the stack effect cooling down the canister wall effectively. The CFD analysis found that the peak speed of the flow within the canister occurred near the canister wall, with another sub-peak near the basket wall. For the year 5 case, the flow speed was as high as 0.3 m/s near the MCP wall. After 55-years storage, the flow speed was still as high as 0.15 m/s. A TEG energy harvester might take advantage of the low-speed flow to enhance its performance.

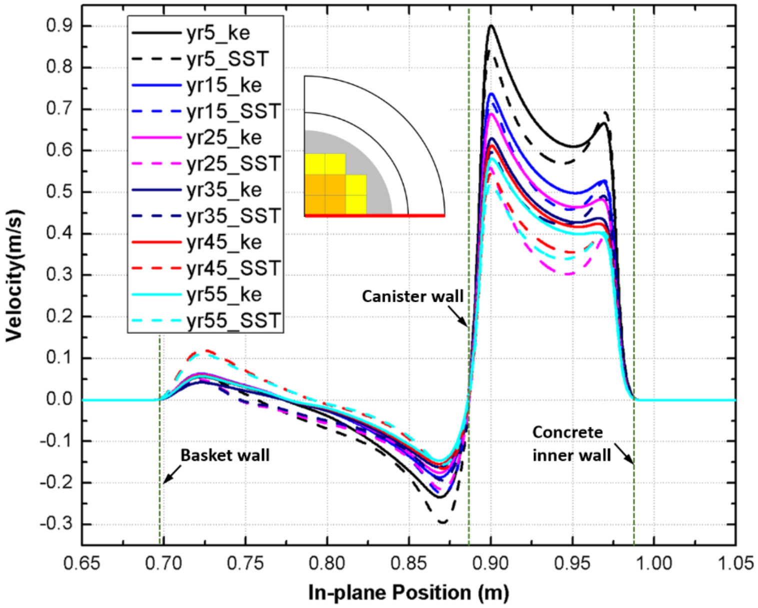

Figure 6.11. The radial flow velocity profile at Z=3.19 m in the symmetry surface

Outside the MPC within the air channels, we could identify two buoyancy driven natural convections near to the walls characterized as the two relative maxima in Figure 6.11. Importantly, the two velocity profiles driven by these two natural convection sections did not converge, which implied the flow here at the height of Z=3.19 m, the center of the cask, was still not fully developed. This showed that the *k-ε* model was less valid for turbulence modeling in the dry cask system.

The average flow temperature and volumetric flow rate within the air channel were illustrated in Figure 6.12 and could be seen to decrease gradually over time. The average temperature of the hot air was about 352 K at the beginning of dry cask storage and decreased to 319 K after 50-years operation. At the same time, the flow volume rate decreased from 0.102 (×4) m^3/s to 0.065 (×4) m^3/s. The thermal energy dissipated through the air channel could be calculated by $q = \dot{m}c_p\Delta T$. Thus, based on the simulation result, more than 80% of the total decay heat was rejected into the environment through the air convection process.

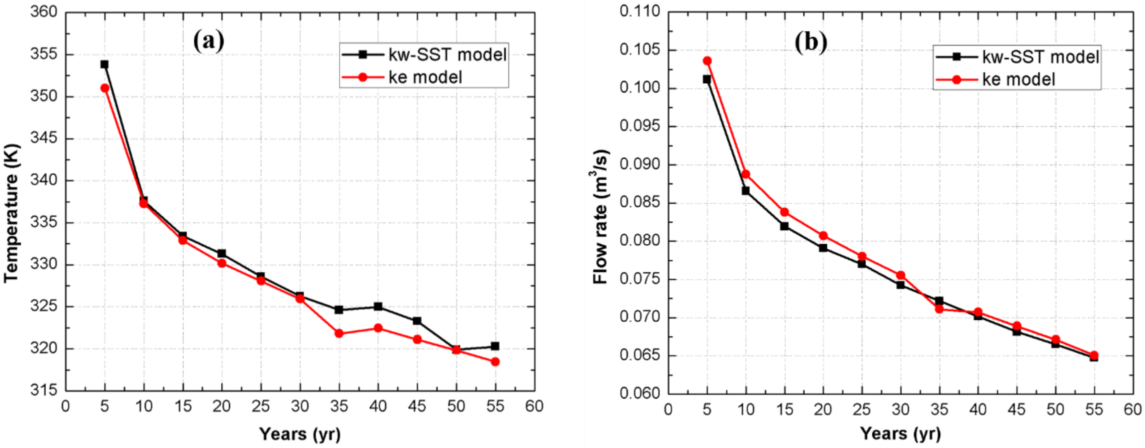

Figure 6.12. (a) The flow temperature at the outlet of the air channel; (b) The flow rate at the outlet of the air channel.

To validate the accuracy of the fluid model, the simulation result was compared with the experimental data documented in ref. [199]. In their report the total decay heat was 25.2 KW, a value close to year 10 in this scenario, and the ambient temperature is 293.15 K. The calculated temperatures along the vertical wall of the MPC at the symmetric surface are plotted in Figure 6.13 along with the data measured by Waldrop and Kessler [199] at Diablo Canyon and the simulation results obtained by Li and Liu [198]. Temperature measurements were performed at Diablo Canyon with thermocouples inserted from one of the air exit vents at the top of the cask. The simulation results agreed well with each other, while both of them deviated from the experimental result, especially at the top end of the MPC wall. This should be caused by the turbulence model we selected over predicting the convective heat transfer at the boundaries. Other minor reasons could include the neglect of some details of the cask's geometry and deviation in the boundary conditions. Overall, the simulation results were acceptable and provide some insights for a thermoelectric energy harvester design.

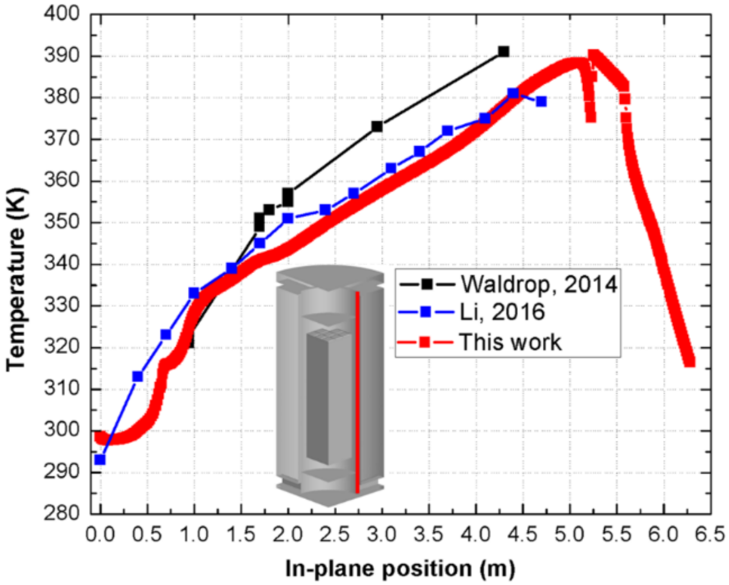

Figure 6.13. The temperature profile along the outer surface of the canister.

6.3.6 Discussion about the CFD simulation results

This chapter studied the thermal-fluid behavior of a HI-STORM 100 spent fuel dry cask with a MCP-32 canister. The decay heat of the fuel was calculated from the time it entered the dry cask (5 years since removal from the reactor), to 50 years in dry cask storage (55 years since removal) in intervals of 5 years using ORIGAMI. The decay heat for each specific 5-year increment was used as the input for the CFD analysis of the spent fuel cask. Some conclusions could be drawn from the results presented above:

1) In this simulation, based on some old methods and conditions well validated in previous research, several improvements were made to improve the accuracy of the final results. Specifically, the decay heat was obtained from an ORIGAMI simulation of a common fuel assembly. This heat load was non-uniformly distributed in the fuel to better fit the real situation. Temperature-dependent thermal properties of the air in the air channel and helium in nuclear canister were adopted along with convective heat transfer laws.

To simplify the simulation, an effective thermal conductivity method was employed to simulate the anisotropic thermal conductivity of the fuel assembly.

2) The flow in the canister was in the laminar region while the flow in the air channel was in the transitional regime. Thus, the transitional SST k-ω model was more valid than the k-ε model combined with wall functions to simulate the turbulence within the air channel. Both models, however, agreed well in comparing results for both the temperature and air flow velocity at the outlet of the airflow gap in the overpack.
3) The peak temperature in each fuel assembly occurred higher in the assembly than previously assumed due to a helium gas convective cycle in the MPC driven by the buoyancy force, and had a lower value than previous calculations. This natural convection process of the helium enhanced the heat transfer inside the fuel assemblies and lowered the peak temperature within the system. The air flow through the air channel appeared to take away more than 80% of the total decay heat.
4) The heat convection and conduction outside the MPC wall effectively reduced the wall temperature, creating an ideal place for TEG placement. There was at least 30 K temperature difference available for energy harvesting, which was more than enough for a TEG energy harvester to extract tens of mW energy for the powering of a wireless sensor.

There are still several ways to improve the accuracy of the simulation results including: (1) All the thermal properties should have temperature dependent values; (2) The natural convection coefficients of the concrete walls depend on the environmental temperature, thus more accurate boundary conditions are desired; (3) The grid number can be improved to get more details of the thermal-flow information within the system, which of course requires a higher computational cost; (4) The low Reynolds number k-ε model will be a better turbulence model to simulate the flow in the air channel, especially for the case with relatively low decay heat, while the laminar flow option is better to simulate the filling gas flow within the canister; (5) The emissivity of the various walls should be less than 1. Finally, an energy harvester should be designed which can effectively use the environment to self-power a wireless sensor node within the dry canister.

6.4 Energy harvester design to harvest gamma radiation energy

6.4.1 Problem formulation

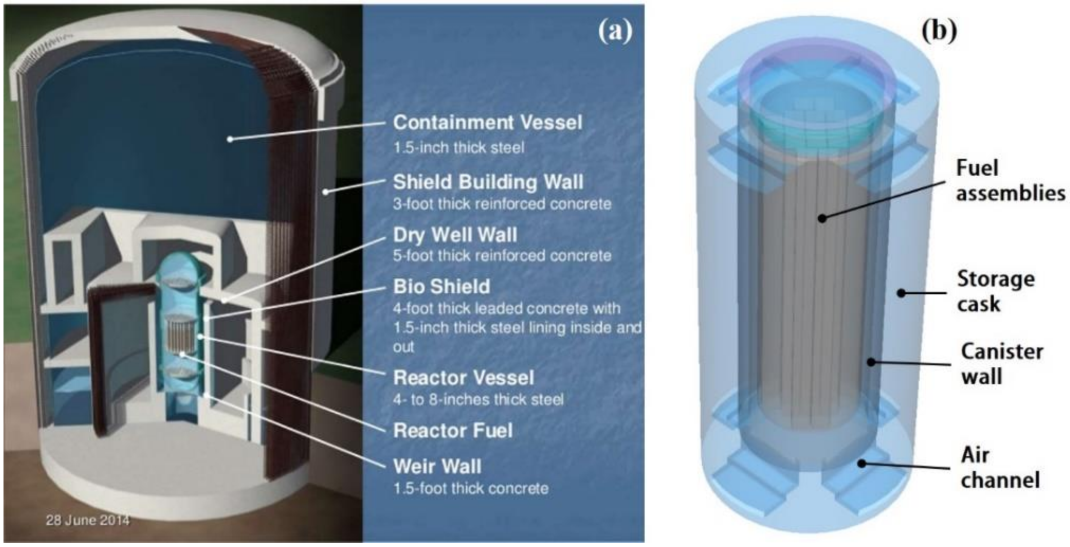

Figure 6.14. (a) The enclosed metal wall and thick concrete protection in nuclear reactors [200] and (b) spent fuel stored in the dry casks.

In the nuclear industry, many vital components, such as nuclear reactor pressure vessels (RPV) and spent fuel storage canisters (Figure 6.14), were entirely enclosed by metal and surrounded by thick concrete walls. The reason was to manage the potentially harmful radiation, preventing release to the environment. Taking dry cask storage as an example, typically one-third of the nuclear fuel elements in the reactors were replaced every 18 months, and the U.S. Nuclear Regulatory Commission estimated that 70,000 metric tons of uranium (MTU) was contained in spent fuel [201]. In the U.S. alone, there were ~2,100 loaded dry casks, and the number increased by 200 each year. Because radioisotopes resulted from the fission of uranium dioxide (UO^2) in nuclear waste, enough decay heat continued to be produced in spent fuel rods to require them to spend a minimum of one year, and more typically 5 to 10 years, in a spent fuel pool of water, before being further processed [202]. The spent nuclear fuel assemblies then would be stored inside (and transported with) containers called canisters surrounded by concrete and steel walls. The canisters were usually lined with leak-tight one-inch thick stainless steel cylinders, providing the front line of protection with a service life of 50 years or longer. Due to the longtime storage, monitoring temperature, pressure, radiation, humidity, structural health, etc. within these enclosed vessels was crucial to ensure the safety of fuel containment. Because of the potentially volatile nature of the spent fuel, wiring through holes in the vessel walls was undesirable and largely unfeasible in most nuclear environments. This offered a unique problem to harvest energy from the nuclear environment to power the wireless sensors for the canister monitoring.

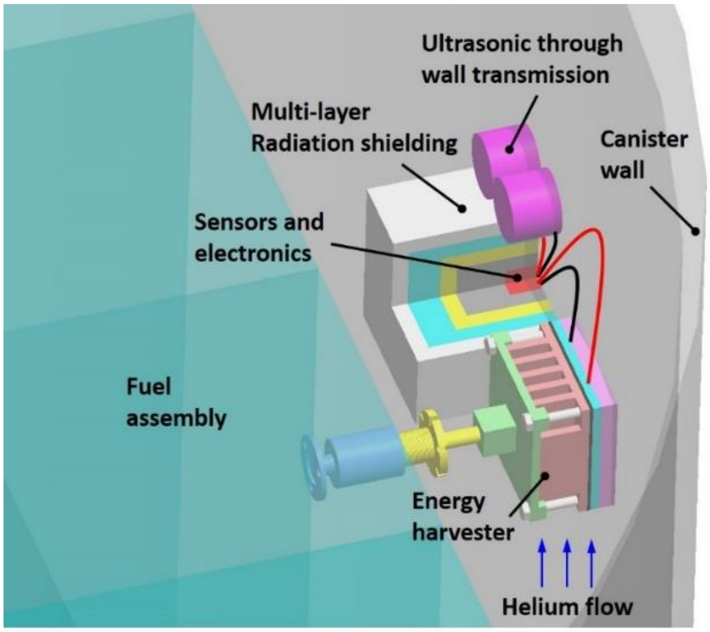

Figure 6.15. Energy harvesting for sensing and communicating system powering

Energy harvesting and wireless communication (Figure 6.15) provided a promising opportunity to revolutionize nuclear sensors and instrumentations and to benefit reactor design and fuel cycle facilities by reducing the cost of power, wiring, and signal transmission or eliminating battery replacement. More importantly, when a severe accident or massive loss of grid power happened, the energy harvester could still provide self-sustainable power to monitor the critical parameters of the nuclear power plant or fuel cycle facilities. Clayton et al. [203] gave a comprehensive review of the existing energy sources within the nuclear environment and various energy conversion technologies available for wireless sensor powering. They compared the energy densities of different technologies and pointed out the technology gaps that need to be filled with a workable energy solution being found. Chen et al. [204] presented an on-pipe thermoelectric energy harvester prototype, which could be easily installed on the pipe system to sense the temperature and pressure in the nuclear power plant. The prototype had a maximum open circuit voltage output of 8.06±0.007 V and a maximum power output of 2.25±0.13 W at a source temperature of 246 °C using two thermoelectric modules. Tewolde et al. [205] built a thermoelectric powered sensing and actuating devices for normal and off-normal conditions in Small Modular Reactors (SMRs). Zhang et al. [206] developed an efficient and reliable TEGs based on high-efficiency nanostructured bulk materials to power WSNs for nuclear application. Carstens et al. [207] described an interesting work using thermoelectric generators to power wireless sensors to monitor spent nuclear fuel stored in a horizontal dry storage container (DSC). The TEG energy harvester was installed in the air channel outside the canister, with the hot end attached to the canister wall and cold side connected to a heat sink. However, the heat flux on the canister wall was assumed to be uniform to calculate the temperature profile within the thermoelectric energy harvester, which might weaken the accuracy of the result. There was still no work done to harvest energy for sensor powering in the thick metal-enclosed canister.

6.4.2 Energy demand for sensing and communicating system powering

Table 6.5 below demonstrated the most popular wireless communication technologies, among which ultrasound-based communication provided excellent penetration capacity and reasonable data communication rate. 10 mW continuous energy harvesting was enough to power a 1.0 W sensing and data transmission system for 3 seconds every 5 minutes.

Table 6.5. The comparison between different through wall wireless communication technologies

Communication technologies	Ultrasound	EMAT	Inductive
Mechanism	Ultrasound	Ultrasound	Magnetic
Media	Any	Any	Large skin depth
Power (Est.)	~1 watt	~2 watt	~1 watt
Bitrate (Max)	5M bps	1M bps	1000 bps

6.4.3 Energy sources available

The typical sources for energy harvesting include mechanical vibration, solar light, electromagnetic wave, flow motion, and thermal heat. Inside the enclosed vessels, such as spent fuel storage canisters or reactor vessels, the mechanical vibration was too small, solar light and electromagnetic energy were not available. However, spent nuclear fuel emits alpha, beta, neutron and gamma rays as radioactive decay, which provided abundant energy sources for energy harvesting.

In the canister, the alpha particle flux was very small and could be easily absorbed by materials. The beta particles, rare in the nuclear-spent fuel, were high-energy (~1 MeV) high-speed electrons emitted from the beta decay with the medium penetrating power. The neutron and gamma rays were the two main radiation particles within the canister. The gamma rays were extremely high-frequency photons with energy 100 keV-1 MeV and very high penetration capability. Most of the radiation energy was emitted as gamma rays. Another important radiation particle in the spent fuel was the neutron rays (averaged ~1.5 MeV). However, the decay heat from neutron deposition was several orders lower than that from gamma because its flux was much smaller than that of the gamma ray. The decay heat generated within the dry cask storage was highly dependent on the fuel makeup and its operation within the reactor. According to the simulation result using SCALE, the decay heat in a MPC-32 canister was as high as 38.44 kW after 5-years storage in the pool (first-year storage in the canister) and decreased to 10.67 kW after another 50-years storage [208].

Because of the decay heat generated by the gamma and neutron rays' deposition, the peak temperature within the canister could be as high as 620 K. To accelerate the dissipation rate of the decay heat into the ambient, the canister was backfilled by the helium gas with a pressure of 3.3 atm in MPC-32. The concrete overpack was made to house the MPC (multi-purpose canister) and had inner channels to allow air to flow between the concrete and MPC, cooling the canister by taking advantage of buoyancy force. The strong convective heat transfer process inside and outside the MPC created a large temperature drop near the canister wall, making it an ideal place for thermoelectric energy harvesting. Our previous calculation found that the temperature drop near the canister wall could be as high as 70 K when it was initially restored in the canister. The temperature difference decreased to 15 K when it was stored in the canister for another 50 years (Figure 6.16).

The flow within the dry cask system could be divided into two regions, with their thermal boundaries coupled at the canister wall as shown below in Figure 6.16. Inside the canister, there was a flow circulation driven by the buoyancy forces caused by the temperature difference between the core of the fuel assembly and the canister wall. Outside the canister, another flow was driven by the stack effect caused by the temperature difference between the canister wall and ambient air. The peak flow velocity (downward) within the canister occurs near the canister wall, with another sub-peak (upward) near the basket wall. For the year 5 case, the peak flow velocity was as high as 0.24 m/s near the MCP wall. After 50-years storage in the canister, the flow velocity was still as high as 0.15 m/s. A small turbine could be introduced to harvest the flow kinetic energy to power sensors within the canister.

In this section, a strategy to harvest the gamma and thermal energy to power the through-wall wireless communication system to sense and monitor the critical parameters in the canister are demonstrated. This energy harvester should supply minimum energy of 10 mW to the electronics for the first 50-years of storage within the canister. Other potential energy conversion technologies for the canister energy harvesting included betavoltaics for gamma-ray energy harvesting, thermo-photovoltaic for thermal radiation energy harvesting, and small turbine generator for flow kinetic energy harvesting, which will not be discussed here.

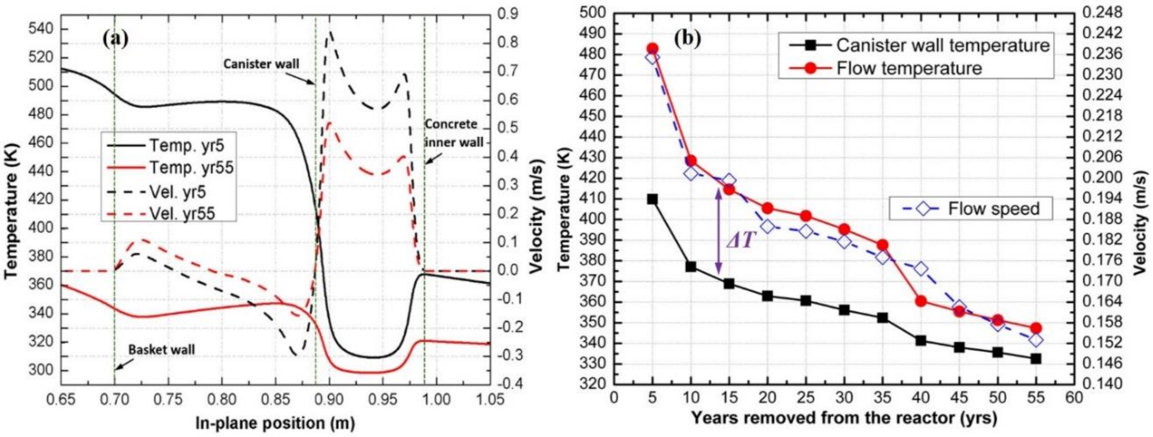

Figure 6.16. (a) The temperature and flow velocity profiles near the canister wall for years 5 and 55 (50 years of storage in the canister) [208]; (b) The temperature and flow velocity (4 cm away from the canister wall) variations with time.

6.4.4 Gamma heat deposited in the tungsten plate

The gamma radiation was the main radiation source in the spent fuel matrix. Taking advantage of gamma rays radiated from the spent fuel by converting their energy into the thermal movement of tungsten atoms, we could generate electricity via a thermoelectric module using the temperature gradient between the tungsten plate and the relatively cold wall of the canisters.

In SCALE software developed by ORNL, the time dependence of nuclide concentrations within the canister was calculated by [209]

$$\frac{dN_i}{dt} = \sum_{j=1}^{n} \gamma_{ji}\sigma_{f,j}N_j\Phi + \sigma_{c,i-1}N_{i-1}\Phi + \lambda_i'N_i' - \sigma_{f,i}N_i\Phi - \sigma_{c,i}N_i\Phi - \lambda_i N_i \tag{7-9}$$

where $\sum_{j=1}^{n} \gamma_{ji}\sigma_{f,j}N_j\Phi$ was the yielding rate of nuclide N_i due to fission of all the nuclides N_j. $\sigma_{c,i-1}N_{i-1}\Phi$ was the rate of transmutation into N_i due to radiative neutron capture by nuclide N_{i-1}. $\lambda_i'N_i'$ was the rate of formation of N_i due to the radioactive decay of nuclides N_i' . $\sigma_{f,i}N_i\Phi$ was the destruction rate of nuclide N_i due to fission. $\sigma_{c,i}N_i\Phi$ was the destruction rate of N_i due to all forms of neutron absorption other than fission. $\lambda_i N_i$ was the radioactive decay rate of N_i. Knowing the decay rate of the different nuclides, the emission rates of the gamma and neutron could be accurately predicted.

It was well known that all materials would be heated up to a certain degree when placed in ionizing radiation, such as gamma radiation, depending on their material properties. Generally, those with higher densities and thus higher atomic cross sections for scattering had better absorption ability for gamma rays. Tungsten had been selected as the material for gamma heating because of its high material density, 19.25 g/cm^3, and high thermal conductivity, ~170 W/(mK) at 175 °C, making it an ideal candidate to not only absorb maximum gamma radiation, but also transfer the deposited heat to TEGs placed on its surface. In this thesis, ORIGAMI embedded in SCALE [208] was first used to calculate the decay heat, gamma and neutron spectrums, and material list after certain-years storage. This information was then used to build a simulation in MCNP6, a Monte Carlo based particle transport simulation which took into account the tungsten plate (20×20×2 cm^3), dry cask geometry, and material make-up, providing the material heating in the tungsten for various years [210]. The gamma heating inside material was calculated using

$$\dot{Q} = \sum_{i=1}^{n} \varphi_i E_i \mu_i \tag{7-10}$$

where φ_i was the flux for each energy group, E_i was the average energy of each group, and μ_i was the mass energy absorption coefficient for each energy group.

The simulation was run on a quarter model to save the computational resources, with a tungsten plate placed on the top and another on the side of the fuel assembly, as depicted in Figure 6.17. A method called geometry splitting was adopted to accelerate convergence. The simulation was stopped until all statistical checks were well passed by the MCNP6 software (See Appendix A) and statistical uncertainty was less than 5% [210].

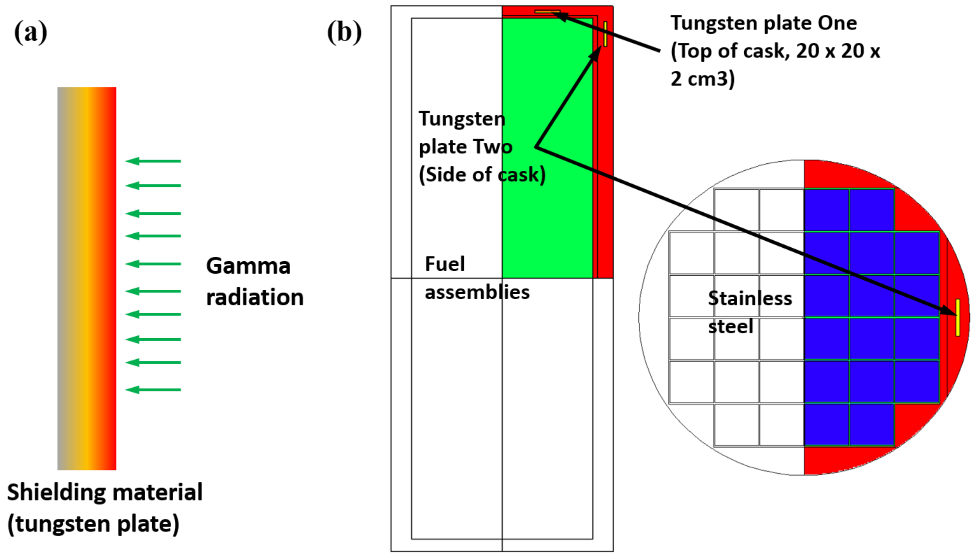

Figure 6.17. Gamma heating calculation: (a) gamma radiation deposited in tungsten; (b) a quarter model for gamma heating calculation using MNCP6.

The heating simulation was done for a total of 11 cases, every five years from year 5 (start of dry storage) to year 55 (50 years of dry storage) to see the heating effect trend throughout the life of the energy harvester. Shown below in Figure 6.18 were the results for energy generation due to gamma radiation in the tungsten slabs both at the top of the fuel assembly basket and to the side. Approximately 2.0 W was generated in the tungsten slab above the fuel assemblies, and 1.25 W was generated in the slab beside the assemblies in the first year of dry cask storage. This heat generation dropped quickly in the next five years, and eventually, at 50 years in dry storage, there were 200 and 300 mW generated in the side and top slabs, respectively. The neutron particles emitted from the fuel matrix was seven orders lower than the gamma radiation. The deposited heat from neutron heating was calculated to be only about 1.0 microwatt for the year 5 case [208, 210], which should be even lower for other cases. Thus the neutron heating effect was neglected in the following thermal analysis.

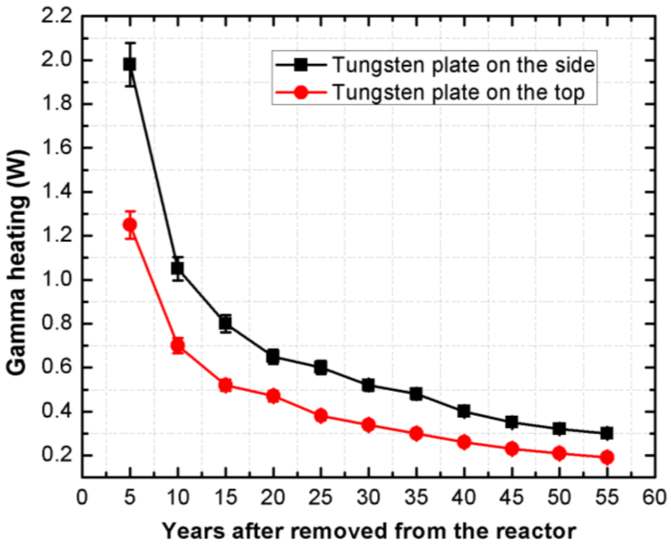

Figure 6.18 Energy deposited in the tungsten plates at the top and side of the MPC canister for 50 years of dry cask storage.

6.4.5 The design of the gamma-heating energy harvester

In this section, a concept design that took advantage of the gamma radiation within the canister by heating a tungsten plate was demonstrated. As mentioned in the section above, the maximum gamma deposited heat in tungsten of 20 × 20 × 2 cm^3 was only about 2.0 W on the top tungsten for the first year of storage in the dry cask. To utilize this small amount of energy effectively, the temperature difference created by the gamma heating should be as large as possible. First, the tungsten should be isolated very well to prevent heat leakage from the hot side of TEGs. Second, the thermal resistance of the TEGs should be large enough to create a high-temperature difference within the module. However, since the tungsten plate had large cross-sectional area and the spreading thermal resistance within the tungsten plate was considerable, it was not easy to effectively isolate the hot side of the energy harvester from the helium environment. What's worse, most of the commercial thermoelectric modules were for high heat flux applications. Their energy conversion efficiencies were pretty small when applied in this situation. Noticing these, we built a gamma heating energy harvester, as depicted in Figure 6.19, which could effectively use the gamma heating in the tungsten plate.

In this design, the tungsten plate was adapted to the wall of the basket and isolated from the helium gas by high-temperature plastic with very low thermal conductivity. As any material added before the tungsten would cause significant scattering of the gamma particles and result in a reduction in material heating, porous thermal isolation material with extremely low thermal conductivity, such as fiberglass, was good choice to isolate the tungsten plate. To create a high-temperature difference and use the deposited heat effectively, the TEG modules should be stacked thermally in series. The optimum number of the TEGs varied with the thermal isolation condition and the working temperature range of the thermoelectric material. In this design, two HZ-2 TEG (with 196 thermo-elements, Hi-Z Technology, Inc.[211]) modules made of Bi_2Te_3 were used to show the concept. To sink the heat and ensure a large temperature drop within the TEGs, the cold end of the second TEG was connected to the cooler canister wall via a backward threaded copper rod. By rotating the threaded rod, the canister wall adaptor would tighten against the canister wall. In this way, the TEGs were thermally connected to the canister wall without the need to mount to the canister. The overall size of the TEG energy harvester was about 30 × 30 × 18 cm^3.

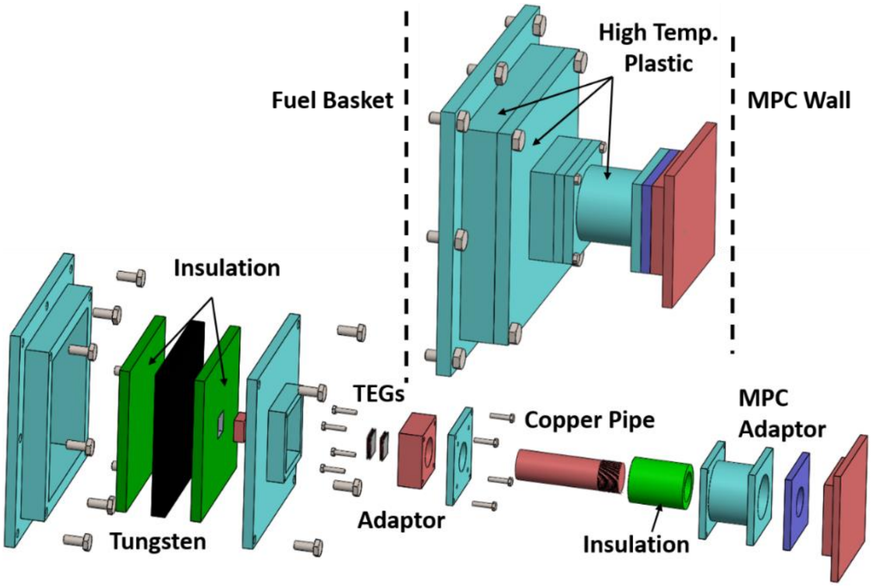

Figure 6.19. Gamma heating energy harvester design

A COMSOL simulation was performed on this harvester to estimate the expected voltage output for the first year of dry storage (year 5 case). The steady-state thermoelectric governing equation for 3-D model embedded in the COMSOL was given by

$$\rho c_p \vec{\boldsymbol{u}} \cdot \nabla T = \nabla \cdot \left(k \nabla T - P \cdot \vec{\boldsymbol{J}}\right) + Q \tag{7-11}$$

where ρ was the density, c_p was the thermal capacity, $\vec{\boldsymbol{u}}$ was velocity vector (zero for our case), k was the thermal conductivity, P was the Peltier coefficient, $\vec{\boldsymbol{J}}$ was the current flux vector, and Q was the source term caused by the Joule heat. This model took account of Peltier effect, Thomson effect, and Joule heat. The material properties used for thermodynamic analysis were demonstrated in Table 6.6, among which the properties of thermoelectric materials were cited from the datasheet. The iteration in the simulation stopped when the residuals of the governing equations are less than 10^{-6}. The tungsten plate, surrounded by the thermal isolation material, provided an energy source term of 2.0 W, obtained from the MNCP6 simulation. The adaptor surface connected to the cooler canister wall was set to be 410 K, a result of the CFD simulation. In the simulation, assuming the rest of the system was insulated well, a temperature difference of about 18 K was created in the TEG modules, with a corresponding open circuit voltage output of 0.378 V generated in each module (Figure 6.20). Using the reported value of 4 Ω for the internal electrical resistance in the datasheet [211], the power output with a matched load resistor was thus 17.8 mW, a bit higher than the necessary 10 mW as announced in the section above.

Table 6.6. Material properties

Material	Electrical resistivity (Ω·m)	Thermal conductivity (W/(m·K))	Seebeck coefficient (V/K)
Bi_2Te_3 n-type	$1.49 \times 10^{-10} T^2 - 8.66 \times 10^{-8} T + 2.30 \times 10^{-5}$	$-9.52 \times 10^{-6} T^2 + 7.33 \times 10^{-3} T - 0.153$	$-1.12 \times 10^{-9} T^2 + 1.04 \times 10^{-6} T - 5.15 \times 10^{-5}$
Bi_2Te_3 p-type	$-6.0 \times 10^{-12} T^2 + 6.29 \times 10^{-8} T - 8.79 \times 10^{-6}$	$-1.76 \times 10^{-6} T^2 + 1.39 \times 10^{-2} T - 1.517$	$-3.01 \times 10^{-9} T^2 + 2.387 \times 10^{-6} T - 2.53 \times 10^{-4}$
Copper	6.0×10^{-8}	400	0
Plastic	N/A	0.2	N/A

Tungsten plate	N/A	175	N/A
Thermal isolation	N/A	0.04	N/A
Ceramic covering	N/A	35	N/A

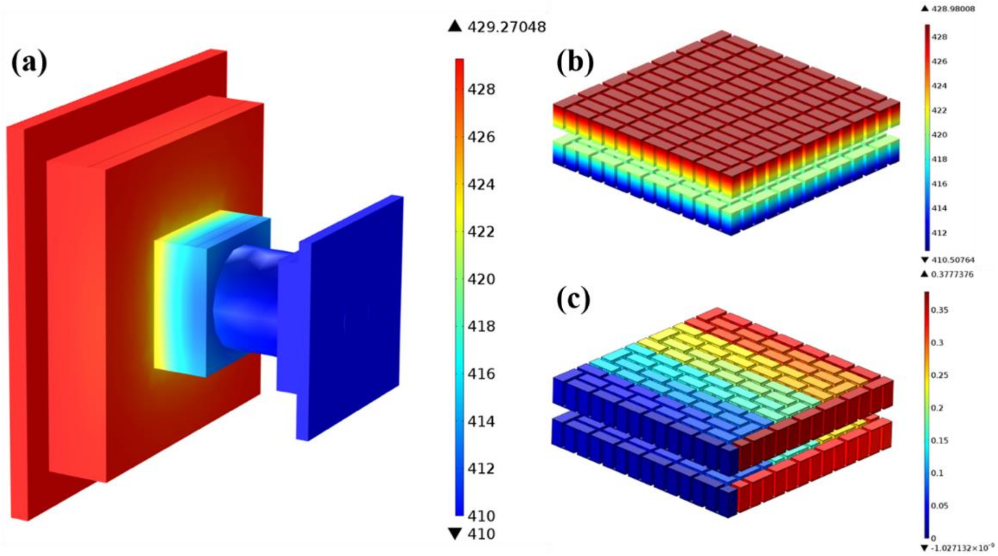

Figure 6.20. The performance of the gamma heating energy harvester: (a) temperature contour of the energy harvester; (b) temperature profile of the TEGs; (c) electrical potential profile of the TEGs

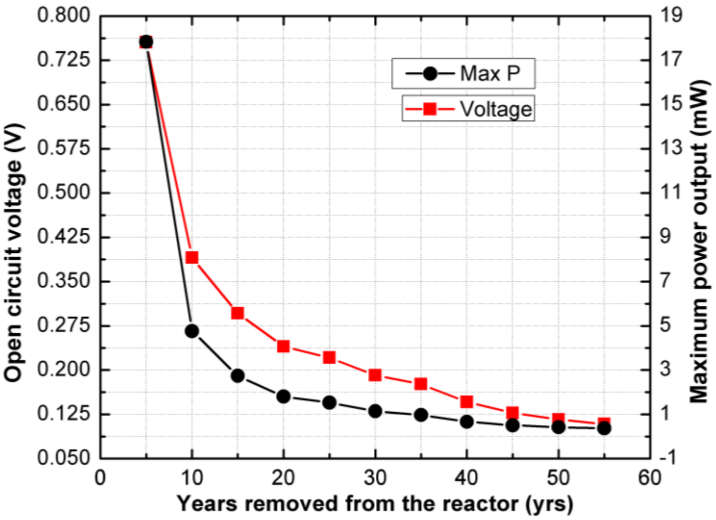

Figure 6.21. The voltage and power output of the gamma heating energy harvester during 50-years operation

However, because of the huge tungsten plate size and a large volume of thermal isolation material, the final energy harvester was heavy and cumbersome. The tungsten alone had a weight of 26 kg and a size of 20 × 20 × 2 cm^3, making it difficult to be installed and isolated. Also, the thermal isolation material would scatter some gamma rays before it deposited in the tungsten, the gamma heating effect was overestimated in the simulation. Meanwhile, the result presented here was for year 5 case when the gamma heating was highest among all the cases. With times going on, the voltage output and power output of the energy harvester reduced quickly as a result of a significant decrease in gamma deposited heat, as shown in Figure 6.21. For the year 55 case, the energy harvester can provide less than 1.0 mW energy, which was far less than 10 mW, a goal we targeted. Considering that at least 10 mW was necessary for the electronics involved in through wall transmission for over 50 years, it was evident that harvesting gamma radiation did not offer a complete solution. However, in the circumstances with higher gamma and neutron radiation fluxes, such as the main containment vessel in the nuclear power plant, gamma heating combined with thermoelectric energy harvester might generate enough energy for sensor powering.

6.5 Energy harvester design for harvesting existing temperature gradient

6.5.1 The design of the temperature-gradient energy harvester

Considering the power output of the gamma radiation energy harvester could hardly meet the power demand (~10 mW) for the wireless communication system, in this section, a more applicable energy harvester to harvest the existing temperature gradient existing near the canister wall was designed. As illustrated in Figure 6.16, the temperature difference near the canister wall was significantly high for thermoelectric energy harvesting. After 50 years of storage in the dry cask, the temperature difference near the canister wall was still as high as 15 K. As the efficiency and power output of the thermoelectric module increase rapidly with temperature difference, it was safe to conclude that, the energy harvester can generate more than enough energy for sensor powering if it could harvest 10 mW averaged power for the year 55 case. Based on this, in this thesis, we designed a simple, compact, and reliable energy harvester which could meet the energy demand for 55-years sensing of the canister, as depicted in Figure 6.22.

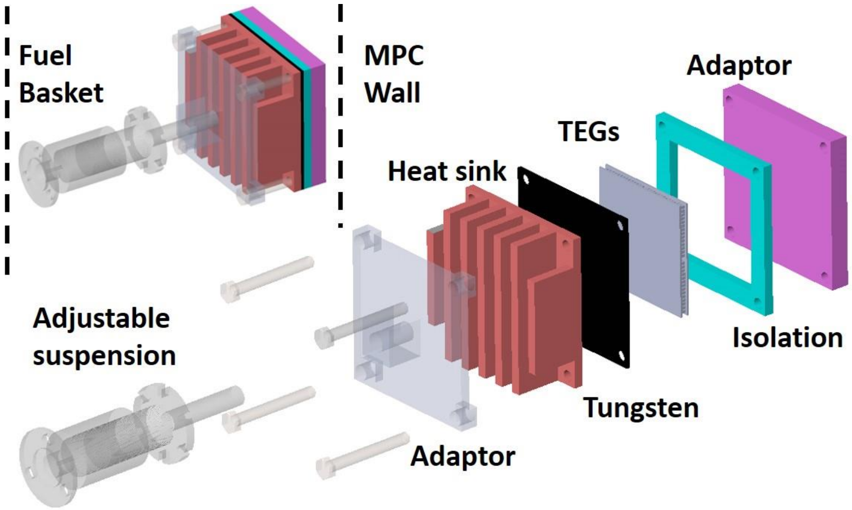

Figure 6.22. Thermal energy harvester design

As seen in Figure 6.16, there was a persistent convective flow close to both the basket and canister walls. Here a copper heat sink was designed to improve the convective heat transfer at the hot side of the Bi_2Te_3 TEGs. To be noted that, in this design, there was a tradeoff between the power output, directly correlated to the number of TEG modules, and the overall size of the energy harvester. Thus four TEG1-1263-4.3 modules (256 thermo-elements, TECTEG MFR. [212]) of size $3 \times 3 \times 0.4\ cm^3$ were attached to the back of the heat sink. A copper adaptor was mounted to the back of the TEGs to thermally attach them to the cooler canister wall. To make the best use of the space while constraining the device to be relatively small, the following dimensions were used: the fin array base had a length and width of 8 cm to accommodate the four TEGs, the height of each of the fins was 2.5 cm in order to penetrate the flow, and their thickness was constrained to be 5 mm according to the fin optimization result in the following section. The cold side adaptor was curved to fit the contour of the MPC wall and was thin enough such that the entire package had a height of 6 cm. Finally, it was thought that mounting to the MPC wall was undesirable, considering the potential for containment rupture. Thus a mounting rod was positioned, free to rotate, off the end of the finned array, which was screwed into and out of a base attached to the basket wall. In this way, the harvester could be “clamped” to the MPC canister wall, without the need for mounting to the canister itself, making the design modular, and easy to install. Thin sheets of pliable graphite were placed between the adaptor and the canister wall to aid in thermal conduction. The overall size of the TEG energy harvester was about 8 × 8 × 6 cm^3, making it compact and easy to install in the canister.

6.5.2 Fin number optimization

To achieve the best performance, the finned array (Figure 6.23) of the heat sink was optimized based on the flow condition along the canister wall. The dimensions of the baseplate and fin height were taken to be constant, and the fin spacing was varied to optimize the number of fins on the array. The convective heat transfer over the fins was a forced convective flow, and in light of this, optimization was performed accordingly as outlined below [210].

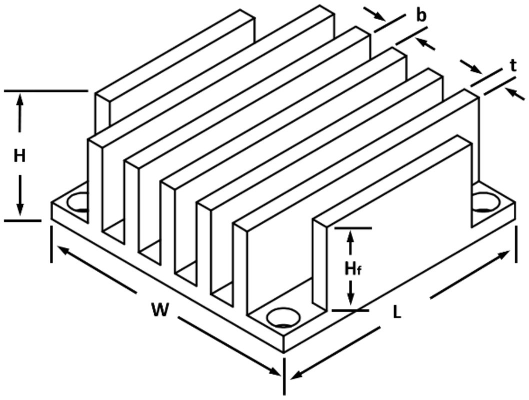

Figure 6.23. The geometry configuration of a heat sink

Bejan and Sciubba [213] presented a neat method to optimize the fin arrays in a forced convective flow to achieve the best heat transfer performance. In the thesis, they gave two approximations to predict the forced convective heat transfer rate for narrow and wide fin arrays,

$$\frac{Q_{nc}}{\Delta T} = C_P \left(\frac{\rho W H_f}{1+\frac{t}{b}}\right)\left(\frac{b^2}{12\mu}\right)\left(\frac{P}{L}\right) \tag{6-12}$$

$$\frac{Q_{wc}}{\Delta T} = 1.208 \left(\frac{k W H_f}{1+\frac{t}{b}}\right)\left(\frac{PrLP}{\rho \nu^2 b^2}\right)^{\frac{1}{3}} \tag{6-13}$$

where the parameters were illustrated in Figure 6.23. The pressure drop P in Eqs. (6-12) and (6-13) was given below in Eq. (6-14). It was first theorized by Bejan [213], and then well outlined and condensed in an online publication by Simons [214].

$$P = \left(K_c + \frac{4\,F_{app}L}{D_H} + K_e\right)\left(\frac{\rho\,U_{inf}}{2}\right) \tag{6-14}$$

And F_{app} was given by the following formula, again from Simons [214],

$$F_{app} = \frac{\sqrt{\frac{11.8336}{L_{st}} + (f\,Re_D)^2}}{Re_D} \tag{6-15}$$

where Re_D is the Reynolds number based on the hydraulic diameter ($D_H = 2b$), $L_{st} = \frac{L}{D_H\,Re_D}$, and f is a polynomial function based on dimensions of the finned structure, and can be found approximated by Simons [214].

Bejan claimed that an approximate solution to the optimum fin number was given by the intersection of the above two heat transfer rates. Here the fin number was calculated using the given fin thickness of 5 mm and assuming the fins fill the base surface. As can be seen, the two approximations for the heat transfer rate were plotted for varying fin number and flow velocity. Evidentially, according to this analysis, the crossing point and thus the approximate optimal fin number was between 7 and 8 (Figure 6.24) and did not vary significantly with decreasing flow velocity.

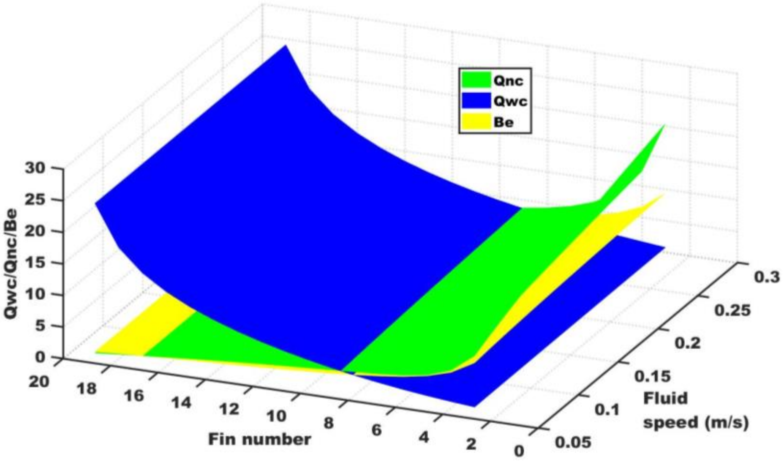

Figure 6.24. Optimization of fin number for a finned surface placed in the convective helium flow near the MPC wall.

To further address the issue, Bejan and Sciubba [213] also presented a numerical analysis to verify this approximation. They concluded that, for optimally spaced finned arrays, the following parameter should be close to 3.0 for flows with a Prandtl number below 0.72 ($Pr = 0.67$ for helium).

$$\delta = \left(\frac{S_f}{L_{hs}}\right)\left(\frac{P\,{L_{hs}}^2}{\alpha\,\mu}\right)^{\frac{1}{4}} \tag{6-16}$$

Assuming the Bejan Parameter was equal to 3.0, a simple calculation found that 7 or 8 fins gave the optimal heat transfer rate for this flow, confirmation of the result in this section above (Figure 6.24). Thus seven fins were chosen in this design.

6.5.3 Simulate the heat transfer performance of the high-pressure helium using hydraulic mineral oil

In the canister, to enhance the thermal dissipation rate, the canister was backfilled by helium with a pressure of 3.3 atm in MPC-32, whose properties were documented in [215] and listed in Table 6.7. However, it was hardly to duplicate the helium environment in the lab, as the high helium pressure made the experiment dangerous and helium leakage might happen. The most common fluids in the lab include air, water, and hydraulic mineral oil. Using these fluids to represent helium might achieve the same average convective coefficient as helium by carefully adjusting the flow velocity.

Table 6.7. The thermal properties of different fluids

Fluids	Helium (3.3 atm at 340 K)	Water (1 atm at 340 K)	Air (1 atm at 340 K)	Hydraulic mineral oil (1 atm at 340 K)
μ (N· s/m^2)	2.22e-5	3.69e-4	2.18e-5	1.47e-2
k (W/(m·K))	0.2129	0.67	0.032	0.162
Cp (J/(kg·K))	5195	4092	1010	1670
Pr number	0.67	2.26	0.68	151.6
ρ (Kg/m^3)	0.4121	973.46	1.0	865

The Reynolds number of the helium flow within the fin channel was given by

$$Re_D = \frac{2\rho ub}{\mu} \ll 2300\ (u = 0.15\,m/s\ \ for\ year\ 55\ case) \tag{6-17}$$

For laminar flow over an isothermal plate, the hydronic boundary layer thickness was

$$\delta_x = \frac{5.0}{\sqrt{u_\infty/vx}} = \frac{5.0x}{\sqrt{Re_x}} \tag{6-18}$$

In the laminar region, the thickness of the thermal boundary layer was related to the hydronic boundary layer through

$$\frac{\delta_x}{\delta_t} = Pr^{1/3} \tag{6-19}$$

If there were no interactions between the boundary layers on the different channel surfaces, at the outlet of the fin channel, the boundary layer thickness $\delta_L = 27\ mm$, with the corresponding thermal boundary layer thickness $\delta_t = 31\ mm$. Since $\delta_L >> \frac{b}{2} = 3.25 mm$ and $\delta_t \gg \frac{b}{2} = 3.25mm$, the flow in the channel should have been fully developed before it left the channel, as illustrated in Figure 6.25.

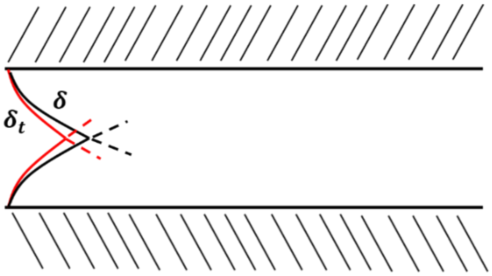

Figure 6.25. Flow pattern in the fin channel

Muzychka and Yovanovich [216] gave a comprehensive formula to calculate the heat transfer coefficient for laminar forced convective flow in the combined entry region of the non-circular duct. This formula combined the formula to calculate the Nusselt number at the entrance region and formula to predict the Nusselt number for fully developed flow. By introducing some geometry correction for the flow channel, the general model was pronounced to have the ability to evaluate the heat transfer performance for simultaneously developing flow in a duct of arbitrary cross-sectional shape. A comprehensive examination of this model found that the error of this model was less than 10.0% for low Reynolds number flow with $0.1 < Pr < \infty$.

$$Nu_{\sqrt{A}} = \left[\left(\frac{C_4 f(Pr)}{\sqrt{z^*}}\right)^m + \left(\left\{C_2 C_3 \left(\frac{fRe_{\sqrt{A}}}{z^*}\right)^{1/3}\right\}^5 + \left\{C_1 \left(\frac{fRe_{\sqrt{A}}}{8\sqrt{\pi}\epsilon^{\gamma}}\right)\right\}^5\right)^{m/5}\right]^{1/m} \tag{6-20}$$

The apparent friction factor ($f_{app}Re_{\sqrt{A}}$) in the entrance region was given by the following formula,

$$f_{app}Re_{\sqrt{A}} = \left[\left(\frac{12}{\sqrt{\epsilon}(1+\epsilon)\left[1-\frac{192\epsilon}{\pi^5}tanh\left(\frac{\pi}{2\epsilon}\right)\right]}\right)^2 + \left(\frac{3.44}{\sqrt{z^+}}\right)^2\right]^{1/2} \tag{6-21}$$

where

$m = 2.27 + 1.65Pr^{1/3}$,

$z^{+} = \frac{z}{L}/Re_L$,

$L = \sqrt{A}$, and

$z^{*} = z/LRe_L Pr$.

In this case, the boundary condition could be taken as a uniform wall temperature condition (UWT). The suggested values for the coefficients in Eq. (6-21) are presented in Table 6.8.

Table 6.8. The coefficients for Eq. (6-21) [216]

Boundary condition	
UWT	$C_1 = 3.24, C_3 = 0.409$, and $f(Pr) = \frac{0.564}{\left[1+\left(1.664Pr^{1/6}\right)^{9/2}\right]^{2/9}}$
Nusselt Number	
Local	$C_2 = 1, C_4 = 1, \gamma = 0.1$
Average	$C_2 = 1.5, C_4 = 2, \gamma = 0.1$

Using this model, we obtained the local and average heat transfer coefficients for air, helium, water, and hydraulic mineral oil, as shown in Figure 6.26. According to the CFD results, the helium flow went over the heat sink with a fluid velocity of 0.15 m/s for year 55 case, with an averaged corresponding heat transfer coefficient of 143.37 W/(m·K). A careful observation of Figure 6.26 found that the hydraulic mineral oil could achieve the same averaged heat transfer coefficient of the helium gas by adjusting the inlet flow velocity to 1.43 cm/s.

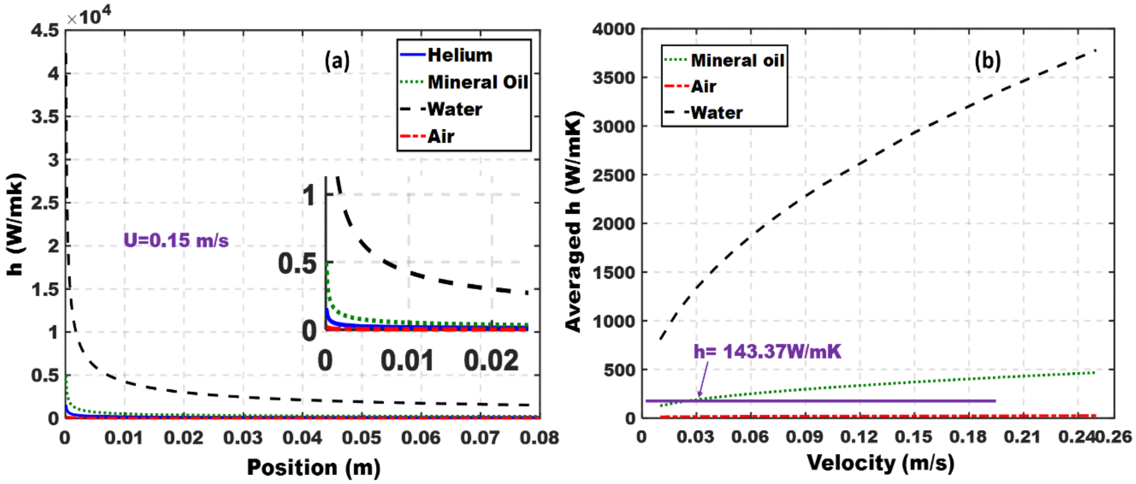

Figure 6.26. Heat transfer performance of different fluids: (a) local heat transfer coefficients when $u = 0.15\ m/s$ and (b) averaged heat transfer coefficients varying with the flow velocity.

6.5.4 Simulation results

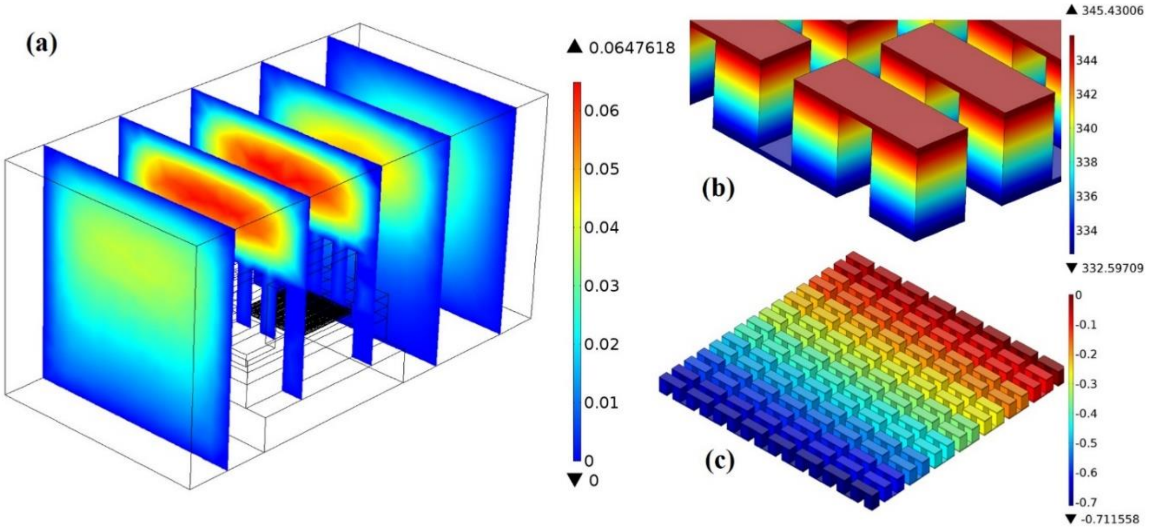

Figure 6.27. Simulation of the performance of the thermal energy harvester in hydraulic mineral oil at $u = 0.0143\ m/s$ for year 55 case: (a) Fluid velocity contours; (b) Temperature profile in TEG; and (c) Electrical potential profile in TEG.

Known from the analysis above, it was convenient to use hydraulic mineral oil to simulate the convective heat transfer performance of helium gas in the canister. Before the experimental verification, a multi-physics simulation was performed to estimate the voltage and power output of the thermal energy harvester. The thermal properties of all the components listed in Table 6.6 and 6.7 were used in the simulation. To save some computational resource, only part of the flow region was calculated by appropriately allocating the inlet and outlet. Since the hydraulic mineral oil flow has high viscosity thus low Reynolds number (~12), it did not lose much accuracy to put the inlet 10 cm ahead and the outlet 20 cm back from the energy harvester. The inlet flow was assumed to be uniform with an average velocity of 1.43 cm/s as computed in the above section. The inlet flow temperature and the temperature of the cooling block was set according to the CFD results demonstrated in Figure 6.27. No thermal and electrical contact resistances were considered in the computations. The multi-physics simulations with heat transfer, thermoelectric, and laminar flow physics models coupled, were done in three grid systems, namely normal (2.05 million), fine (3.26 million), and finer tetrahedral meshes (5.58 million) with their parameters optimized according to the energy harvester geometry. The results found that the relative difference between the voltages generated by the three grid systems were less than 1%. The results of the fine grid system were presented in the dissertation.

Demonstrated in Figure 6.27 was the performance of the thermal energy harvester in hydraulic mineral oil using the finer meshes at $u = 0.0143\ m/s$ for year 55 case. The temperature drop within the thermo-element was about 12.8 K, which was very high considering the total temperature difference was 15 K near the canister wall. The open circuit voltage generated was about 0.712 V for a single TEG. There were four TEGs assembled thermally in parallel. Thus the total voltage output of the energy harvester was 2.848 V. Considering the internal resistance of the TEG module was 5.4 Ω, the maximum power output of the energy harvester was about 93.9 mW, which was more than enough for electronics powering. The results for the different simulation cases were presented in table 6.9.

Table 6.9. The simulation results for different year cases

Cases	Oil temp. (K)	Cooling block temp. (K)	Flow velocity (cm/s)	Temp. drop in TEG (K)	Open circuit voltage (V)	Max. power output (mW)
Year 55	347.15	332.15	1.43	12.8	0.712	93.9
Year 50	351.15	335.15	1.50	13.7	0.757	106.1
Year 45	355.15	338.15	1.52	14.5	0.801	118.8

6.5.5 Experiment to test the energy harvester

For the year 5 case, the temperature of the flow near the canister wall was as high as 490 K and decreased to 332 K for year 55 case. Four the commercial TEG1-1263-4.3 modules, which could work continuously below 523 K, were connected thermally in parallel and electrically in series to supply power for the 50-years operation of the electronics. As outlined in the above section, the temperature gradient harvestable near the canister wall decreased with time. Thus the energy harvester could meet our energy demand if it could generate enough electricity for the year 55 case. In the experiment, we verified the performance of the energy harvester by testing its performance for the year 45, 50, and 55 cases to make sure that the energy harvester could supply enough energy during the 55-years operation.

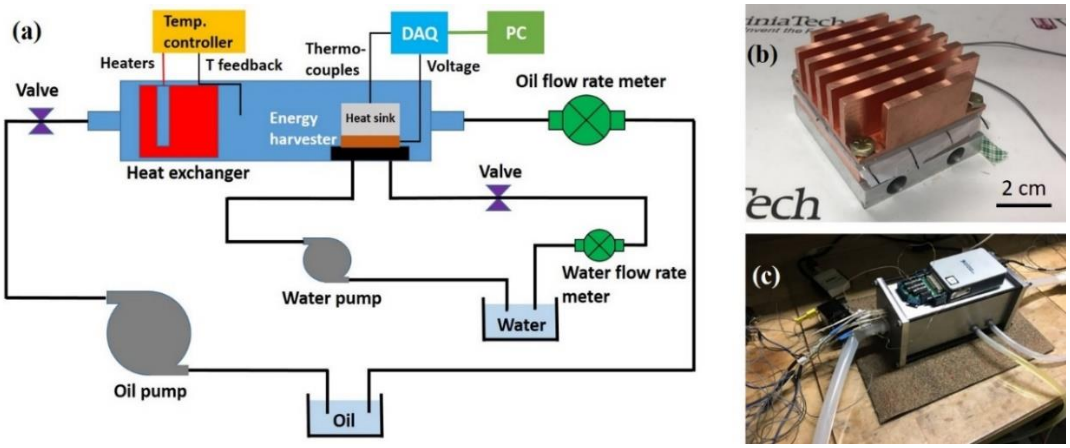

Figure 6.28. The performance test of the energy harvester: (a) The overall experimental setup in the lab, (b) The energy harvester, and (c) the oil channel to simulate the helium environment.

As can be seen in Figure 6.28, the hydraulic oil circulation loop was used to simulate the helium environment in the canister. The water circulation loop was utilized to control the temperature of the cooling block, which was used to simulate the temperature on the canister wall. The flow rates of the two circulations were controlled by two ball valves and measured by two flow rate meters, respectively. The oil flow was heated up by two 250 W, and two 500 W cartridge heaters (OMEGA Engineering) inserted into a heat exchanger, with their heating rates controlled by a temperature controller (CN7800, OMEGA Engineering). A flow filter was put 10 cm in front of the energy harvester to uniform the flow velocity. It was assumed the un-uniformity of the oil flow should be dumped in this short distance because of its high viscosity. Three K-type thermocouples (±0.45 K over 293.15 K) were used to measure the hot- and cold- end temperatures of the TEG modules and the temperature of the oil flow. Two data acquisitions (DAQs), NI TB-9214 (± 0.45 K) and NI USB 6008 (± 7.7 mV), were used to collect the temperature and voltage readings separately. The data was then automatically stored in a PC via LabVIEW every 5 seconds. The experiment was carried out in a room with a large space, and the room temperature was constant at 22.5 °C.

The COMSOL multi-physics simulation gave very promising results to achieve 10 mW energy harvesting taking advantage of the existing temperature difference near the canister wall. An experiment was done in this section to verify the simulation results. The experiment was divided into three periods, with each period lasting for 8 minutes. As shown in Figure 6.29(a), in the first time period, to simulate the year 55 case, the hydraulic mineral oil was heated up to 347.15 K (74 °C) and the cooling system was preserved to 332.15 K (59 °C), the same as the input value for the simulation. In the second and third periods, the oil flow velocity, the temperatures of the hydraulic mineral oil, and the cooling block were adjusted to the values corresponding to different year cases, as demonstrated in Table 6.9.

As shown in Figure 6.29(b), the open-circuit voltage output changed accordingly with the temperature difference between the hot and cold ends of the TEG module. The voltage outputs of a single TEG module were about 0.50, 0.55, and 0.60 V for the year 55, 50, and 55 cases. In this design, four TEG modules were connected thermally in parallel and electrically in series. The total voltage output of the energy harvester were about 2.0, 2.2, and 2.4 V, respectively. The matched load electrical resistance of the TEGs were 7.7x4 ohms. The corresponding maximum power outputs of the TEG energy harvester were about 46.3, 56.1, and 66.7 mW, which were more than 10 mW what we need for electronics powering. The performance of the thermal TEG energy harvester was poorer than the simulation result. This could be reasoned as follows. First, the thermal contact resistances were considerable in the energy harvester assembly. Second, the thermal properties of all the material were temperature dependent, especially for the hydraulic mineral oil. Third, though feedback controllers were used to control the temperatures of the oil and the cooling block, the temperature fluctuation during the experiment caused significant derivation in the temperature difference and voltage output.

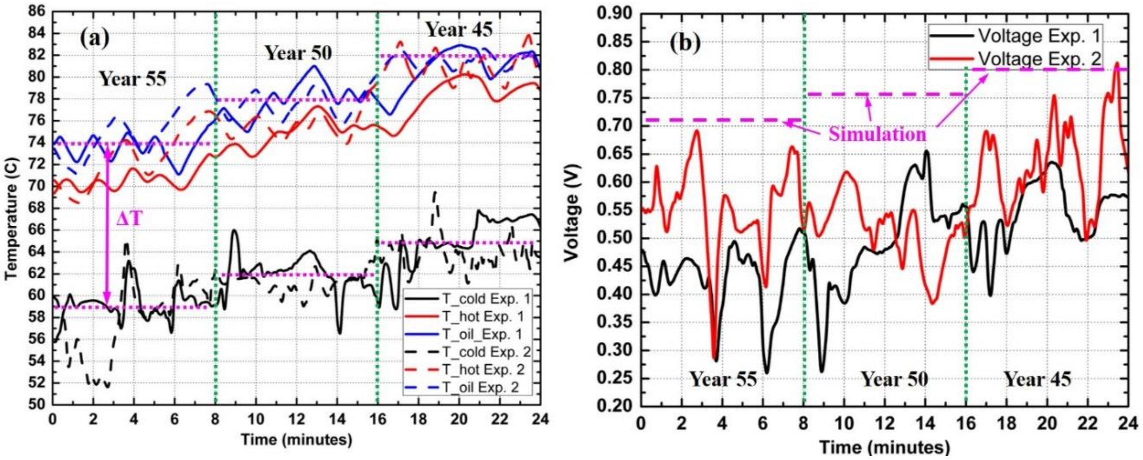

Figure 6.29. The experimental results for the thermal energy harvester in hydraulic mineral oil: (a) The hot- and cold- end temperatures of TEG, and flow temperature, (b) The open circuit voltage output.

Table 6.10. Summary of the experimental results

Cases	Temp. drop in TEG (K)	Open circuit voltage (V)	Power output (mW)
Year 55	12.8	0.50	46.3
Year 50	13.7	0.55	56.1
Year 45	14.5	0.60	66.7

*Averaged over each time slots.

Table 6.11. The electrical resistivity uncertainty sources

#	Source	Typical values
1	Thermocouple tip radius	0.25 mm
2	Thermal couple (K type)	0.45 K
3	Statistical variation	Calculated
4	Caliper uncertainty	±5.0 mm
5	Wire discrepancy	Small
6	DAQ voltage uncertainty	50 ppm
7	Flow rate uncertainty	5.0%

The uncertainty of the temperature measurement was 0.45 K (Table 6.11). Then the uncertainty of the temperature difference in the TEG could be calculated by

$$dT = \sqrt{(dT_1)^2 + (dT_2)^2} = 0.9\ K \tag{6-22}$$

The uncertain error of the voltage measurement was 7.7 mV. The error propagated to the power output by the voltage measurement was given by

$$dP = \sqrt{\left(\frac{\partial P}{\partial V}\right)^2 dV^2} = \frac{2V_{output}R_L}{(R_0+R_L)^2}dV = 4.06 \sim 12.9\ mW \tag{6-23}$$

The uncertainty of the measured data was much smaller than the fluctuation caused by the feedback controller.

6.6 The impacts of gamma radiation on the performance of the thermoelectric material

The thermoelectric material used for energy harvesting in the nuclear environment should be able to survive the radiation environment for long term application. In the canister, the primary radiation source is the gamma and neutron rays. Also, the gamma radiation dosage was more than six orders higher than the neutron dosage. It was critical to conduct a gamma radiation test on the thermoelectric materials to find the potential effects of the gamma radiation on its thermoelectric performance.

To examine the performance of the Bi_2Te_3 working in the nuclear environment, gamma exposure experiments were performed in a radiation test chamber provided by Westinghouse Electric Company in Pittsburgh.

6.6.1 Potential effects caused by the gamma radiation

The gamma-ray photons interact with materials in various ways depending on their energy. The photoelectric effect, the Compton Effect, and electron-positron pair production are the three effects which might happen when materials exposed to the gamma radiation environment [217]. Photoelectric effect dominates when the energy of a gamma-ray photon is low. In this process, the interaction between a gamma photon and an atom leads to the ejection of an electron from the atom where the energy of the gamma photon transfers to the electron entirely. The Campton effect and pair production happen for photons with higher energy. In the Campton effect, the photon transfers a portion of its energy to the electron, causing the ejection of an electron and an incident gamma ray with larger wavelength. In pair production, a gamma photon penetrates to the nucleus of an atom and forms an electron-positron pair. The high energy free electron generated during the ionizing damage spans to the forbidden gap and create electron-hole pair, which leads to the increment in electrical conductivity of the material [217].

6.6.2 The radiation experiment setup

In the experiment, a Bi_2Te_3 samples from TECTEG MFR., and a small Bi_2Te_3 based TEG module (TEG2-126LDT from TECTEG MFR., 8×8×8 cm^3) were tested. In the test, a cylindrical Co-60 gamma radiation source with a diameter of ~5cm was placed on a lifting jack plate was used.

The thermoelectric materials samples were put in appropriate distances to the gamma source by the research staff in the Westinghouse Company at Pittsburgh. Sample #1 received a total gamma irradiation dosage of 124 MRads in two weeks (Figure 6.30).

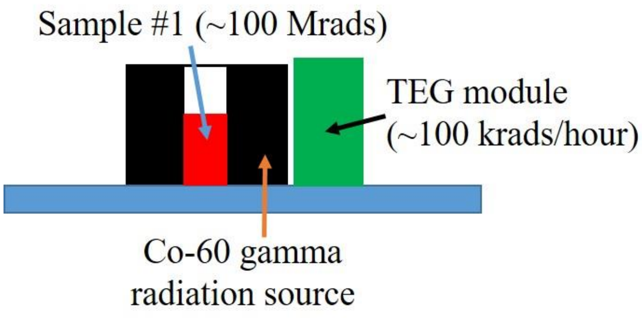

Figure 6.30. Thermoelectric material radiation test setup

In a typical canister, the radiation dosage is about 40 krads/hour. In the experiment, the TEG module was put as close as possible to the gamma source where the gamma radiation flux was about 100 krads/hour, the highest value that was achievable using the radiation source. The TEG module was heated periodically by a 1.5 inch long 200W cartridge heater controlled by a heat controller. The open circuit voltage of the TEG modules and the temperatures of the source and the ambient environment were measured and recorded every 10 seconds. The source temperature was controlled to oscillate between ~25 °C and ~ 60 °C.

All the components designed to be exposed to gamma radiation were set up in the radiation chamber with necessary sensors and cables connected to a laptop outside the radiation chamber. The performance of the system before and after irradiation was compared to identify the impact of gamma radiation on the TEG device.

6.6.3 The impacts of gamma radiation on the thermoelectric materials

As noted above, throughout the radiation experiment, the voltage output of the TEG module, as well as the important temperature readings, were recorded. As shown in Figure 6.31 (a), the temperature profiles for the no radiation test and the gamma radiation test were slightly different because the thermal mass was small and the temperature controller had limited accuracy. The voltage output of the TEG module varied accordingly with the source temperature. It was noted that there was no significant voltage output difference between the two tests. The gamma radiation's impact on the performance of the TEG module was minimal.

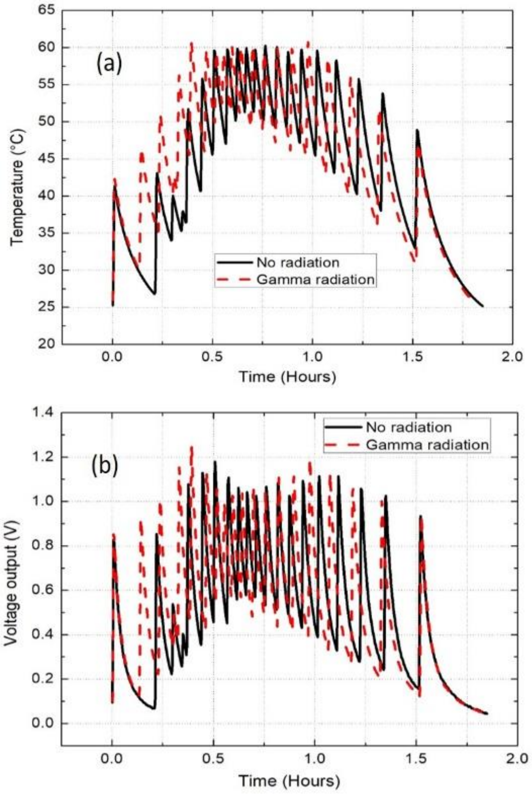

Figure 6.31. (a) Temperature profile of the source; (b) The open circuit voltage output of the TEG module.

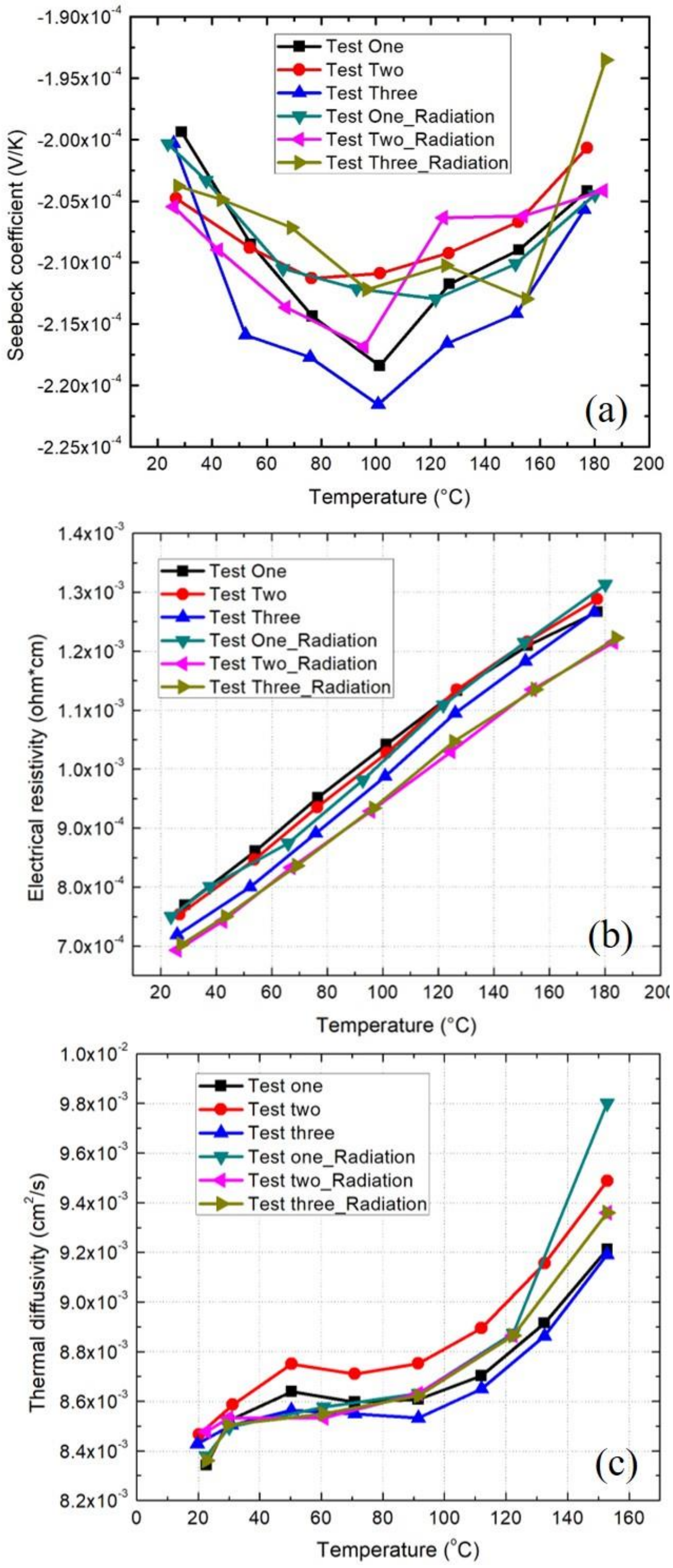

Figure 6.32. The comparison of (a) Seebeck coefficient, (b) electrical resistivity, and (c) thermal diffusivity of the Bi_2Te_3 sample before and after gamma radiation

To examine the influence of the accumulated gamma radiation on the n-type Bi_2Te_3 thermoelectric material, the Seebeck coefficient, electrical conductivity, and thermal conductivity before and after the gamma radiation test were compared. The accumulated gamma radiation dosage was 124 Mrads for this sample. Three independent measurements of the thermoelectric material sample were done before and after the radiation test, respectively. As shown in Figure 6.32(a), the absolute value of the Seebeck coefficient increased and then decreased with the temperature, reaching a peak value around 100 °C. The electrical resistivity of Bi_2Te_3 increased linearly with the temperature at this temperature range. The thermal diffusivity of the materials increased slowly at the relatively low-temperature range and then increased sharply at the high-temperature end. No significant changes were observed for the Seebeck coefficient, electrical resistivity, and thermal diffusivity after the radiation test. It can be concluded that the impacts of gamma radiation on the Seebeck coefficient, electrical resistivity, and thermal diffusivity were minimal.

6.6.4 Uncertainty analysis of the measurements

The Bi_2Te_3 sample and a Bi_2Te_3-based TEG were sent to Westinghouse for the radiation test. Before the radiation test, the thermoelectric properties of samples were measured by the ZEM-3 system and the TC-1200H system in our lab. The working principles of these two machines were documented in Chapter One.

The measurements of the Seebeck coefficient and electrical conductivity

The ZEM-3 instrument from Advanced Riko, Inc. was designed for simultaneous measurement of Seebeck coefficient and electric conductivity for the evaluation of thermoelectric characteristics of a wide range of materials, including semiconductor, metal, and ceramics. The equipment using the static dc method to measure the Seebeck coefficient and the four-terminal method to measure the electric resistance.

The electrical resistivity was calculated by $\rho = \frac{\Delta V \cdot A}{I \cdot \Delta L}$. The uncertainties of each parameter for the measuring system was shown in Table 6.12. The uncertainty can be calculated from a Taylor Series expansion around the nominal measurement value.

$$d\rho = \sqrt{\left(\frac{\Delta V}{I\cdot\Delta L}\right)^2 (dA)^2 + \left(\frac{A}{I\cdot\Delta L}\right)^2 (d\Delta V)^2 + \left(-\frac{\Delta V\cdot A}{I^2\cdot\Delta L}\right)^2 dI^2 + \left(-\frac{\Delta V\cdot A}{I\cdot(\Delta L)^2}\right)^2 (d\Delta L)^2} \qquad (6\text{-}24)$$

The uncertainties for the electrical resistivity were less than 8.1% in these measurements.

The Seebeck coefficient was calculated by $\alpha = -\Delta E/\Delta T$. The uncertaintiy of each parameters for the measure system was shown in Table 6.13. The uncertainty of the Seebeck coefficient was given by

$$d\alpha = \sqrt{\left(-\frac{1}{\Delta T}\right)^2 (d\Delta E)^2 + \left(\frac{\Delta E}{(\Delta T)^2}\right)^2 (d\Delta T)^2} \qquad (6\text{-}25)$$

Based on these, the estimated uncertainties for the Seebeck coefficient should be less than 6.7% in the measurements.

Table 6.12. The electrical resistivity uncertainty sources [218]

#	Source	Typical values
1	Thermocouple tip radius	0.25 mm
2	Thermocouple separation length	±0.1 mm
3	Sample uniformity	±0.1 mm/0.1 cm
4	Statistical variation	Calculated
5	Caliper uncertainty	±0.1 mm
6	Wire discrepancy	Small
7	DAQ voltage uncertainty	50 ppm
8	DAQ current uncertainty	0.2%
9	The temperature uniformity	0.1 K

Table 6.13. The Seebeck coefficient measurement uncertainty sources [218]

#	Source	Typical values
1	Cold-finger effect	10,000W/(m^2K)
2	Wire Seebeck variation	±5 %
3	Absolute temperature	±2.0 C
4	Statistical variation	Calculated
5	Wire discrepancy	Small
6	DAQ voltage uncertainty	50 ppm
7	DAQ temperature uncertainty	50 ppm
8	Thermal couple uncertainty (R type)	50 ppm
9	The temperature uniformity	0.1 K

Shown in Figure 6.33 was the temperature distribution in a thermo-element with a size of 4×4×20 mm^3. Because of the radiation heat exchange with the experiment, the temperature distribution along the length of the thermo-element is nonlinear because of the radiation heat loss. But it does not influence the measurements. The temperature uniformity on the cross-section has a small impact on the measures. However, the non-uniformity is very small, less than 0.1 K for this case.

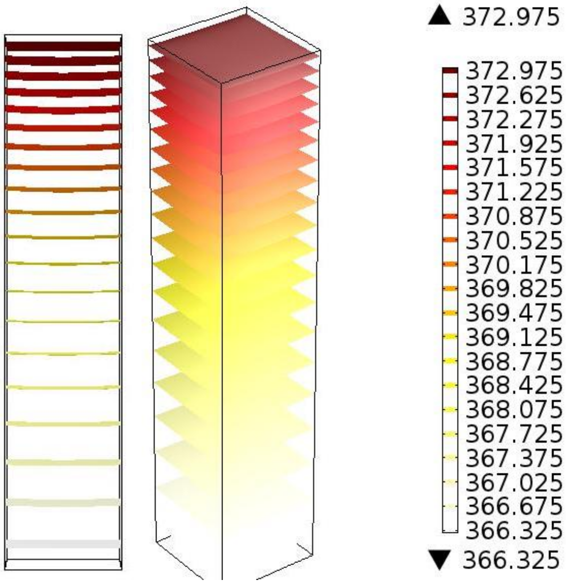

Figure 6.33. The temperature uniformity on each cross-section of the thermo-element when radiation emissivity is 0.8.

The measurement of thermal diffusivity

The TC-1200H system was designed to measure thermal diffusivity, specific heat, and thermal conductivity. According to the user manual, the measurements of thermal diffusivity and specific heat were claimed to have accuracies of ±5.0% and ±7.0%, respectively. The repeatability was claimed to be ±5.0% and ±7.0% for thermal diffusivity and specific heat, respectively. Here the TC-1200H system was used to measure the thermal diffusivity only.

The thermal diffusivity was calculated by $\alpha_{diff} = 1.37\frac{L^2}{\pi^2 t_{1/2}}$. Here $t_{1/2}$ represented the time required for the temperature on the back side of the sample to reach 1/2 of the maximum value after the sample surface was irradiated with an instantaneous heat source.

All that was necessary was to measure the thickness of the sample and the $t_{1/2}$. The factors that might introduce the error in the results includes:

1. The thermal radiation and conduction loss to the environment should be small.
2. The laser heating time should be sufficiently short.
3. The sample should be irradiated uniformly.
4. The diameter of the sample should be much larger than its thickness.

6.7 Radiation and thermal shielding for the electronics and energy harvesters

6.7.1 Radiation shielding material

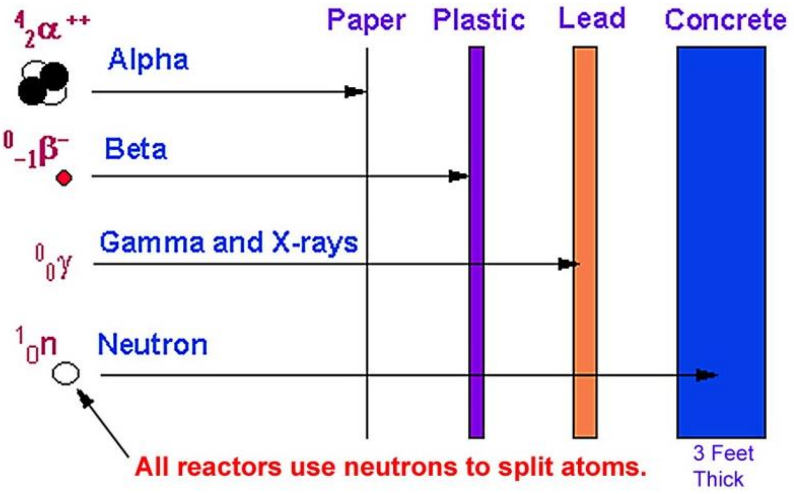

Figure 6.34. The penetration ability for different radiation particles [219].

Spent nuclear fuel emits alpha, beta, neutron, and gamma rays as radioactive decay providing abundant energy sources. The alpha particles are the nucleus of a helium-4 atom with a charge +2 and in the velocity of 5.0% the speed of light. They can be easily absorbed by materials (even a piece of paper) and don’t travel far from the spent fuel assembly. The beta particles are high-energy (~1MeV) high-speed electrons emitted from the beta decay with the medium penetrating power. The gamma rays are electromagnetic radiation of extremely high-frequency photon of wavelength ~1ppm of the visible light. The gamma photons have energy 100keV-1MeV and very high penetration capability. Neutron radiation is generated during the nuclear fission or nuclear fusion. According to the energy of the neutron particles, the neutron particles can be divided into three categories: cold, thermal, and fast neutrons. The two main radiation particles in the spent fuel are the gamma (γ) and thermal neutron (n) rays. According to Figure 6.34, the γ radiation dose is much higher than the neutron radiation dose.

Gamma rays are better absorbed by materials with high atomic numbers and high density, although neither effect is important compared to the total mass per area in the path of the gamma ray. For this reason, a lead shield is only modestly better (20–30% better) as a gamma shield than an equal mass of another shielding material, such as aluminum, concrete, water or soil. Lead's major advantage is not in lower weight, but rather its compactness due to its higher density. Also, it is found that the higher the energy of the gamma rays, the thicker the shielding made from the same shielding material is required.

Traditional neutron shielding methods rely on the use of specific, individual, material isotopes being placed between the source of neutrons and the area in which lower radiation levels are desired. The more effective shielding designs usually feature thermal neutron absorbers, which are materials that can readily remove lower energy neutrons through an atomic absorption interaction. Common elements used as "thermal absorbers" are cadmium (Cd-113) and boron (B-10). Considering that neutron radiation typically includes neutrons of varying energy levels, methods relying on thermal absorption also require the use of materials intended to moderate or slow down, faster neutrons. It is well known that materials with lower atomic masses are considered highly effective at this moderation process and used as the primary means to slow down the fast neutrons, as neutron energy loss via elastic scattering increases with decreasing atomic mass of the target nuclei. In most case, to effective shield neutrons with varying energy, it is desired to have multi-layer shielding materials functioned as moderation and absorption. This also leads to the observation that if a single material could effectively perform both functions, neutron shield design could potentially be simplified significantly.

To shielding both the neutron and gamma in the canister, the composite, tungsten boron carbide, and referred to as W-B_4C within this work, was studied. The idea to include the tungsten in this composite stemmed from the fact that tungsten was a commonly used material in gamma radiation shielding due to its high density. Therefore, using tungsten as the matrix and boron carbide as the filling material potentially yielded a composite, which was effective at shielding both neutron and gamma rays. Tungsten was chosen over other commonly used lead materials because it was not toxic and can be easily mixed with other materials to form composites.

The mass fraction of an element within a compound can be calculated by

$$w_i = \frac{M_i * n_i}{\sum_{i=1}^{n} M_i * n_i} \tag{6-26}$$

where M_i is the atomic mass of the element and n_i was the number of atoms of that element per molecule for a compound containing n elements.

The averaged density of that compound can then be estimated through the summation of the weighted elemental densities, ρ_i, via equation below.

$$\rho_{avg} = \sum_{i=1}^{n} w_i \rho_i \tag{6-27}$$

The parameters in the Eqs. (6-26) and (6-27) are shown below in Table 6.14.

Table 6.14. Constituent Element Weight Percentages and Theoretical Densities of the W-B$_4$C Composite Materials

W-B$_4$C	
Element	wt. %
W	77
B-10	4
B-11	14
C	5
Density (g/cm^3)	15.34

6.7.2 Gamma and neutron shielding in the canister

The radiation source for the MCNP6 simulation was obtained from the SCALE calculation results, in which the energy spectrum and materials compositions were given from year 5 to year 55. The spent fuel was uniformly assigned to the fuel assemblies, as shown in Figure 6.35. The shielding box, with a dimension of 20 x 20 cm^2, was fixed at the side of the fuel assemblies. The electronics were attached to the right side of the shielding material, assuming that most of the gamma and neutron rays came from the left side of the shielding box. The gamma and neutron fluxes were simulated at the electronics, as the tungsten plate was varied in thickness from 0.0 cm to 6.0 cm.

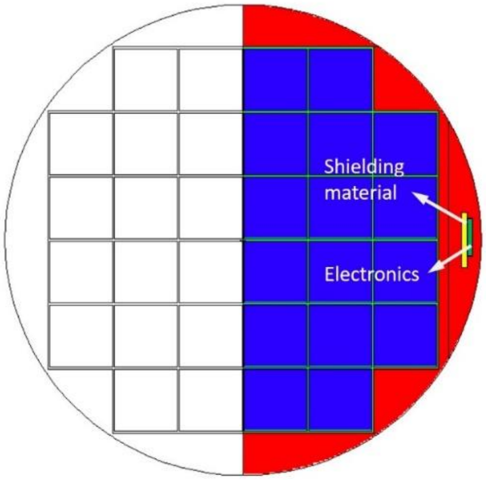

Figure 6.35. MNCP6 model to test the radiation shielding performance.

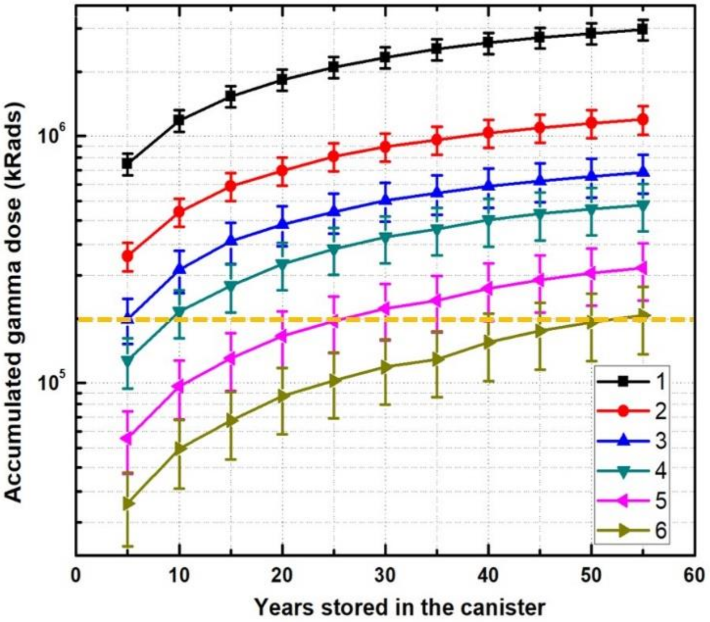

Figure 6.36. The accumulated gamma dose in the electronics vs time.

The gamma threshold for the electronics was estimated based on our test on a DC-DC converter that was built in our lab for the radiation environment application [23]. The gamma threshold varied depending on the specific circuits used in the DC-DC converter, which was not discussed here. According to our test in Westinghouse Company at Pittsburg, the accumulated gamma radiation dose was 94.4 kRads when the commercial DC-DC convector lost function [23]. As observed in Figure 6.36, the thicker the shielding material was, the smaller was the accumulated gamma dose in the electronics. According to the calculation in the MCNP 6, when the thickness of the shielding block was 6.0 cm, the cumulated radiation dose in the electronics was still as high as 2.0×10^5 kRads. To ensure 50-years safe operation in the canister, electronics with higher radiation-harden capacity should be developed, and a thicker shielding block should be developed. The neutron flux in the canister was seven order lower than the gamma flux. Though the energy of the neutron particles had higher averaged energy (~2.2 MeV), the accumulated neutron dose penetrating the shielding material was still six order lower than the gamma dose. Thus the neutron effect on the electronics was minor.

6.7.3 The thermal and radiation block design for the electronics

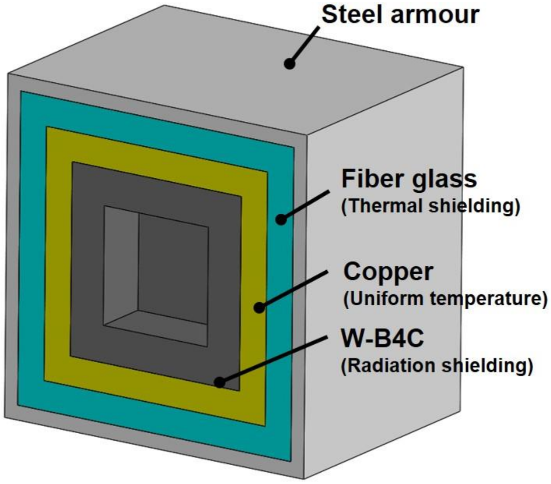

Figure 6.37. Radiation and thermal shielding block

Table 6.15. The thermal conductivity and thickness of each layer

Materials	**Thermal conductivity (**W/(m*K))	**Thickness (**mm**)**
Steel	50.2	2
Silica	1.4	5
Fiberglass	0.04	10
Copper	400	10
W-B4C	141.5 (Weight averaged)	25

According to the CFD simulation, the temperature within the canister could be another challenge for electronics. For year 5 case, the helium gas temperature near the canister wall was as high as 480 K, while the wall temperature was about 410 K. To ensure that the temperature of the electronics was less than 423 K (150 °C). The thermal and radiation shielding layers were integrated to protect the electronics, as shown in Figure 6.37. The outside layer was the steel armor, which was used for shielding block protection. The second layer was fiberglass. This layer was used for thermal shielding. The third layer was the copper layer, which was used to uniform the temperature. And the inner layer was W-B_4C, which was used for radiation shielding. The thickness of each layer was presented in Table 6.15. The W-B_4C layer had a thickness of 25 mm, which met the requirement for the gamma radiation shielding.

The temperature distribution in the shielding materials was illustrated in Figure 6.38. The temperature of the wall attached to the canister wall was set to be 410 K. And the five other walls exposed to the hot helium flow was assumed to have a convective heat coefficient of 143.37 W/(m·K), which was estimated from the CFD simulation in section 6.1. The thermal conductivity of each shielding material was listed in Table 6.2. A numerical analysis in the COMSOL found that the shielding block design can meet the requirement for the thermal shielding, as the temperature at inner surfaces was less than 423 K, a safe margin we targeted.

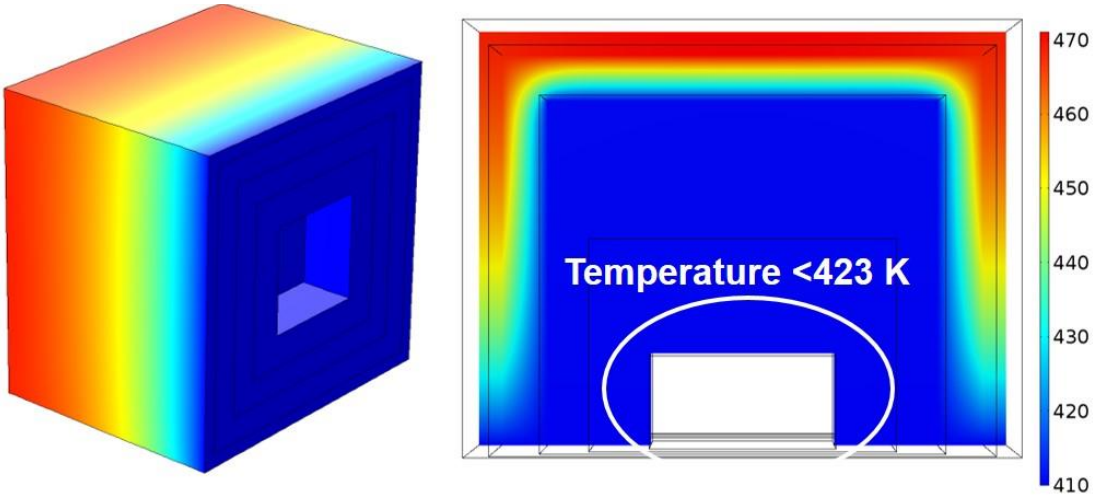

Figure 6.38. Temperature contours in the thermal and radiation shielding block.

6.7.4 Summary for the chapter

In this chapter, two energy harvesters for a self-powered wireless through-wall sensing and communicating system in nuclear canisters were designed, simulated, and tested. The first energy harvester was a novel conceptual design for gamma radiation energy harvesting. In addition to this, a more practical thermal energy harvester was designed to pull energy from the helium flow in canisters by taking advantage of the existing temperature difference near the canister wall. Also, we discussed the radiation and thermal shielding requirements for the electronics in the canister. The shielding strategy using one composition for both the neutron and gamma rays were proposed. The shielding performance of the W-B_4C was examined using the MCNP6 code. The key conclusions were presented as follows.

1) In the canister, there were abundant gamma rays. When a tungsten plate (20 × 20 × 2 cm^3) placed on the side of the canister, a deposited heat of 2.0 W could be achieved in the first-year of dry cask storage. However, gamma based deposited heat decreased to about 0.3 W after 50-years storage, making it increasingly difficult to harvest the gamma deposited energy.
2) A conceptual gamma radiation energy harvester was designed to show the potential using gamma heating effect to power electronics within the canister. Assuming the system was well isolated, and located close to the stored fuel, the energy harvester, utilizing two TEG modules connected thermally in series and electrically in parallel, gave an ideal voltage output of 0.756 V and a corresponding power output of 17.8 mW in the first year of dry cask storage. Throughout the life of cask storage, the simulated energy output dropped below 10 mW after 5-years storage, which was the desired threshold to power the electronics used in through wall communication. This was largely due to the exponentially decreasing heat energy deposited in the tungsten. Additionally, to provide enough power, this design was burdensome with a large tungsten plate, providing a practical problem considering the difficulty of thermal isolation and installation.
3) A second energy harvester was conceptualized and tested which utilized the existing temperature gradient in the canister. The heat sink of the energy harvester was optimized according to the flow condition in the canister. Four TEG modules were

connected thermally in parallel and electrically in series to harvest enough energy for sensor and communication system powering. The power output of the energy harvester could be easily scaled by adding more TEG modules at the cost of system size. The thermal energy harvester was simple and compact (8 × 8 × 6 cm), thus can be easily installed. To verify the result in the lab, hydraulic mineral oil was used to simulate the thermal performance of the helium gas in the canister after a careful thermal analysis.

4) A multi-physics simulation showed that the thermal energy harvester could supply an open circuit voltage of 2.848 V and energy of 93.9 mW even after 50-years of canister storage, which was more than enough to power the communications electronics. However, the experimental results showed that the open circuit voltage and power output of the energy harvester were about 2.0 V and 46.3 mW, respectively, with the same thermal boundary conditions. The difference between the simulation and experimental results could be reasoned by the relatively large thermal resistance at the contact layer and temperature fluctuation during the experiment.
5) A gamma radiation test was done to explore the potential impacts on the thermoelectric performance of the Bi_2Te_3 materials. It was found the TEG module can work normally under a gamma radiation dosage of 100 krad/h. No significant thermoelectric property changes were observed after the gamma radiation test.
6) The W-B_4C was identified as the shielding material for both gamma and neutron shielding, where tungsten element in the composition was used for the gamma shielding and the boron element was used for the neutron shielding.
7) When the thickness of the shielding block was 6.0 cm, the cumulated radiation dose in the electronics was still as high as 2.0×10^5 kRads, which was much higher than the threshold of the commercial electronics. To ensure 50-years safe operation in the canister, there was an urgent demand to develop electronics with higher radiation-harden capacity. Thermal analysis on the radiation-shielding block found that it could also meet the thermal shielding requirements for the electronics.

The uncertainties of the measured parameters were discussed in the chapter.

Parts of the chapter were adapted from a paper, "Yongjia Wu, Haifeng Zhang, Lei Zuo. Thermoelectric energy harvesting for the gas turbine sensing and monitoring system. Energy Conversion and Management, 157 (2018): 215-223."

Chapter 7. Thermoelectric Energy Harvesting for the Gas Turbine Sensing and Monitoring System

7.1 Chapter introduction

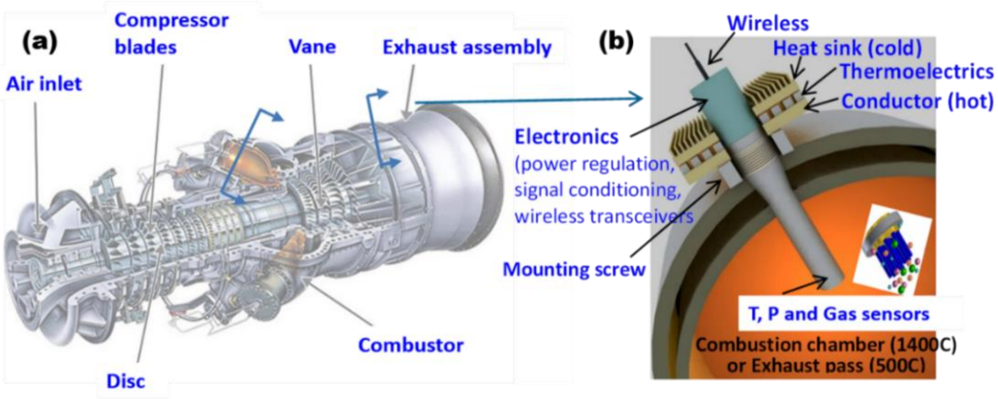

Figure 7.1. The concept of using TEG to power the sensing and monitoring system in the gas turbine: (a) a typical gas turbine used for power generation; (b) self-powered temperature, pressure, and gas sensors embedded in the gas turbine.

The gas turbine is a key component in a modern power plant, aircraft, and ship (Figure 7.1(a)). The increasing complexity of gas turbine has led to the desired need to introducing the reliable, smart, and automated prognostic and health monitoring systems. To provide such capability, hundreds of sensors of varying types are embedded in the engine to collect various physical parameters, such as pressure, temperature, vibration, and gas chemical compositions associated with engine operation (Figure 7.1(b)). Then, the data are transmitted to a central data processing unit, where the data are stored and processed. In the traditional wired sensing and monitoring system, cables of thousands of meters long are used to power the sensors and the auxiliary electronic devices. However, exposed to the harsh environment with high temperature and large vibrations, the expensive, long, and heavy cables make the overall system unreliable. To solve these problems, there was a need to develop an energy-independent wireless system. The system, taking advantage of the energy source in the sensor environment, can supply reliable, stable, and independent electric power for the sensing and monitoring systems. In this section, we developed a thermoelectric energy harvester to harvest the thermal energy from the gas turbine surface for the autonomous sensor nodes in the gas turbine, providing continuous, real-time, and reliable operation parameter sensing and monitoring for the data center (Figure 7.1(b)).

7.2 Sensors working in the gas turbine

To address this issue, there are several practical problems should be solved before it can be integrated into the existing system. For a modern gas turbine, the temperature in the combustion chamber can be as high as 1200 °C, which is a great challenge for the blade and chamber. To prolong the lifecycle of the system, a high-efficiency, and sophisticated cooling system design [46] combined with the thermal barrier coatings technology [47] is adopted in the industrial gas-turbine engines. Before entering the combustion chamber, the air coming out from the compressor at a temperature nearly 300 °C flows through the cooling channels covering the combustion chamber, at the same time preheated by the combustion chamber wall. Unlike the common situation, the extreme working conditions, such as high temperature (> 300 °C), bring about extra complication to the energy harvester design. Meanwhile, the gas turbine for power generation is covered by a thick thermal isolation material layer to prevent heat leakage and sustain high efficiency. To efficiently use the temperature difference between the gas turbine surface and the ambient environment, the thermal network should be carefully designed. Meanwhile, to minimize the impact of sensing and monitoring system on the performance of the gas turbine, the energy harvester should be compact and shall not involve the active cooling system. There is also a lack of experimental study of an energy harvester using segmented TEG to harvest thermal energy for the autonomous sensor nodes.

For a sensor node working in transmission mode, the general energy consumption is about 50 mW [27]. In this section, we built and tested a segmented TEG energy harvester prototype with the hot end temperature reaching up to 325 °C for the gas turbine sensor system. The TEG energy harvester developed here could harvest ~0.92 W energy, which was more than enough for the sensor node and auxiliary electronics. A numerical model, with Peltier heat, Thomson heat, Joule heat, gap heat leakage, and ceramic covering thermal resistance considered, was built to analyze the performance of the segmented TEG accurately. This design had reasonable energy output, and it was easy to be installed on site.

7.3 Thermoelectric energy harvester design

7.3.1 Experimental setup

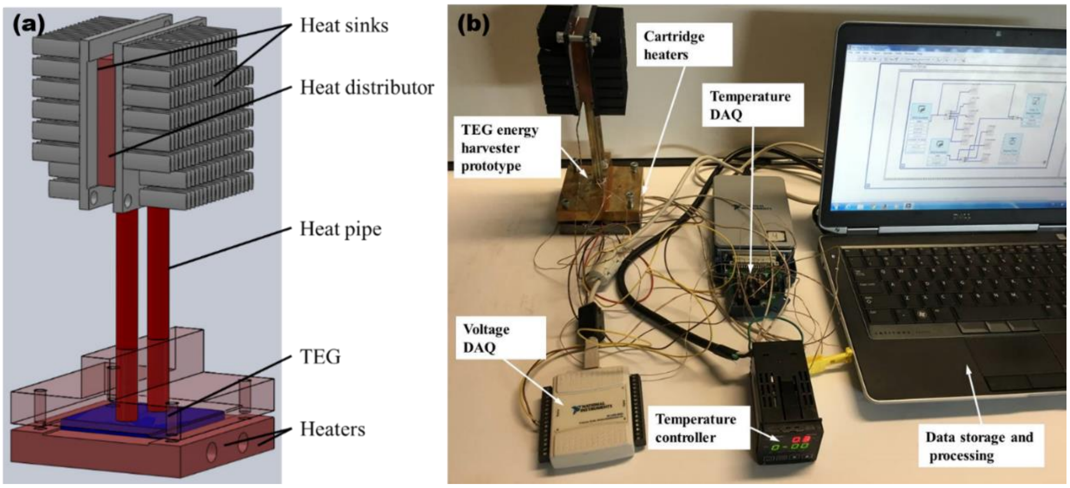

Figure 7.2 (a) TEG energy harvester prototype; (b) Experimental setup

The experimental setup of the energy harvester to supply power to the gas turbine sensing and monitoring system was presented in Figure 7.2. The temperature of the gas turbine surface was as high as 300 °C. The TEG used here was a commercial Bi_2Te_3–PbTe hybrid thermoelectric power module (56mm × 56mm) from TECTEG MFR. [220], which was optimized for hot side temperatures in the 250-370 °C range. Generally, the body of the gas turbine was covered with a thick thermal isolation layer to improve energy conversion efficiency. As the TEG module was embedded in the thermal isolation material, two heat pipes with a maximum operating temperature of 200 °C were employed to penetrate the thermal isolation material and dissipate heat from the cold side of the TEG module. The diameter and length of the heat pipe were 10 mm and 152.4 mm, respectively. Ref. [204] announced that, compared with an aluminum rod, heat pipe significantly improved the performance of the TEG module. To implement the device on the gas turbine, it was not practical to use an extra device to cool the cold end of the device. Cooling water or fans would make the device burdensome and unreliable, so only natural convection was used here. Two compact and high efficient heat sinks made by ALPHA Company were selected and installed symmetrically at the cold end of the heat pipe. Two 200 W cartridge heater (CIR-20252, OMEGA Engineering) and a temperature controller (CN7800, OMEGA Engineering) were used to control the source temperature during the experiment. Four K-type thermocouples (± 0.45 K above 273.15 K) were used to measure the hot & cold side temperatures of the TEG module and the temperature of the heat sink base. Two data acquisitions (DAQs) from National Instruments Inc., NI TB-9214 (± 0.45 K) and NI USB 6008 (± 7.7 mV), were used to collect the temperature and voltage readings separately. The experiment was carried out in a room with a large space, and the room temperature was constant at 22.5 °C.

7.3.2 A numerical model for the energy harvester

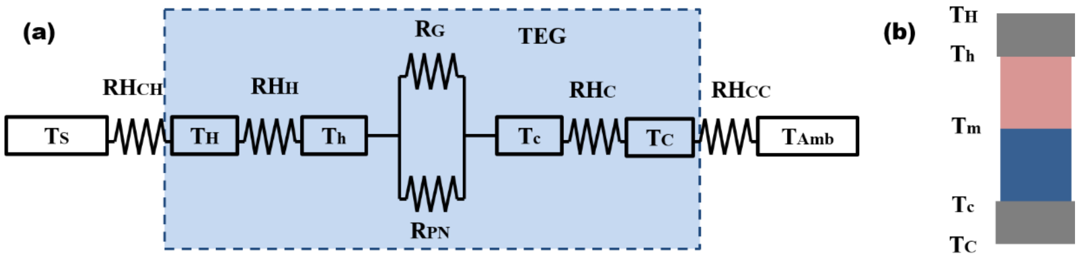

Figure 7.3. (a) Thermal network in the energy harvester; (b) Segmented thermo-element.

Figure 7.3(a) showed the thermal network of the TEG energy harvester prototype. To the best of our knowledge, there are no analytical models which can accurately give the thermal resistance of the heat pipe. Also, the intricate geometry structure of the heat sink introduced extra complexity in the calculation of the convective heat transfer coefficient. Though there were some empirical equations, they could only be applied to a specific condition and predict the order of the thermal resistance. In this section, we separated the thermal analysis into several parts, where the TEG module was emphatically studied, while the performance information of heat sink and heat pipe were cited from the datasheet of the products. The model presented here could predict the performance of the segmented TEG module, with Peltier heat, Thomson heat, Joule heat, gap heat leakage, and ceramic covering thermal resistance fully discussed. In the calculation, the properties of the materials were temperature dependent.

The thermal resistance of the thermoelectric materials was temperature dependent. The overall thermal resistance of the P, N-type thermo-element segments were given by

$$RH_{P1} = \frac{1}{A_{P1}}\int_0^{L_{P1}} \frac{1}{k_{P1}} dx,\ RH_{P2} = \frac{1}{A_{P2}}\int_0^{L_{P2}} \frac{1}{k_{P2}} dx,$$

$$RH_{N1} = \frac{1}{A_{N1}}\int_0^{L_{N1}} \frac{1}{k_{N1}} dx,\ RH_{N2} = \frac{1}{A_{N2}}\int_0^{L_{N2}} \frac{1}{k_{N2}} dx \qquad (7\text{-}1)$$

Similarly, the thermal resistances of ceramic covering at the hot and cold ends of the segmented TEG were

$$RH_H = \frac{L_H}{k_H A_H},\ RH_C = \frac{L_C}{k_C A_C} \qquad (7\text{-}2)$$

The gap between the thermo-elements was filled with thermal isolation material, such as air. The energy loss through radiation could be significant in a high-temperature environment. The thermal resistance of the air filling gap was calculated by

$$RH_G = 1/[\frac{k_G A_G}{L_G} + \varepsilon\sigma A_G F_{hc}(T_h^2 + T_c^2)(T_h + T_c)] \qquad (7\text{-}3)$$

While a segmented TEG had a high efficiency than a single-material-made TEG, the complex geometry caused some new issues, including compatibility problem [221], thermal expansion mismatch, and contact resistance at the interfaces. For our case, the thermal and electrical contact resistance at the interfaces between different material layers were negligible when compared with the resistance of the bulk TEG material.

For a thermo-element, the relationships between the cross-section areas were given by

$$A_P = A_{P1} = A_{P2},\ A_N = A_{N1} = A_{N2},\ A_H = A_C = A_P + A_N + A_G \qquad (7\text{-}4)$$

The lengths of the P and N-type thermo-elements were the same,

$$L = L_{P1} + L_{P2} = L_{N1} + L_{N2} \qquad (7\text{-}5)$$

The Fourier heat going through the air gap without passing the thermo-element was

$$q_G = \frac{T_h - T_c}{RH_G} \qquad (7\text{-}6)$$

Similarly, the thermal energy entering/leaving the module could be obtained by

$$q_H = \frac{T_H - T_h}{RH_H},\ q_C = \frac{T_c - T_C}{RH_C} \qquad (7\text{-}7)$$

The heat fluxes entering the hot end and leaving the cold end of the thermo-elements were

$$q_h = q_{Nh} + q_{Ph} = \left(\alpha_{P1}^{h} - \alpha_{N1}^{h}\right)T_h I - k_{N1}^{T_h} A_{N1} \left.\frac{dT_{N1}}{dx}\right|_{x=L} - k_{P1}^{T_h} A_{P1} \left.\frac{dT_{P1}}{dx}\right|_{x=L}$$

$$q_c = q_{Nc} + q_{Pc} = (\alpha_{P2}^{c} - \alpha_{N2}^{c})T_c I - k_{P2}^{T_c} A_{P2} \frac{dT_{P2}}{dx}\bigg|_{x=0} - k_{N2}^{T_c} A_{N2} \frac{dT_{N2}}{dx}\bigg|_{x=0} \tag{7-8}$$

where the first term was the Peltier heat and the last two terms were Fourier heat through P- and N-type thermo-elements.

The open circuit voltage of the device caused by the Seebeck effect was

$$V = N\left\{\int_{T_c}^{T_{m1}} \alpha_{P2} dT + \int_{T_{m1}}^{T_h} \alpha_{P1} dT - \int_{T_c}^{T_{m2}} \alpha_{N1} dT - \int_{T_{m2}}^{T_h} \alpha_{N2} dT\right\} \tag{7-9}$$

The electrical resistance of the TEG module was the sum of thermal resistance of all the thermo-elements, thus

$$R_M = N\left[\frac{1}{A_{P2}}\int_0^{L_{P2}} \rho_{P2}\, dx + \frac{1}{A_{P1}}\int_{L_{P2}}^{L} \rho_{P1}\, dx + \frac{1}{A_{N2}}\int_0^{L_{N2}} \rho_{N2}\, dx + \frac{1}{A_{N1}}\int_{L_{N2}}^{L} \rho_{N1}\, dx\right] \tag{7-10}$$

When a load resistance connected, the loop current through the thermo-elements was described as

$$I = \frac{V}{R} = \frac{V}{R_L + R_M} \tag{7-11}$$

And the corresponding power output of the module was

$$P = I^2 R_L = \frac{R_L}{(R_L + R_M)^2} V^2 \tag{7-12}$$

Combing Eqs. (8-8), (8-10) and (8-12) gave the efficiency of the TEG module

$$\eta = \frac{P}{q_h} = \frac{\left[N\left(\sum_1^n \int_0^{L_{Pn}}\left(\alpha_P \frac{dT}{dx}\right)dx - \sum_1^n \int_0^{L_{Nn}}\left(\alpha_N \frac{dT}{dx}\right)dx\right)\right]^2 R_L}{\left\{R_L + N\left[\sum_0^n \int_0^{L_{Pn}}\left(\frac{\rho_P}{A_P}\right)dx + \sum_0^n \int_0^{L_{Nn}}\left(\frac{\rho_N}{A_N}\right)dx\right]\right\}^2 \left[(\alpha_{P1}^{h} - \alpha_{N1}^{h})T_h I - k_{N1}^{h} A_{N1} \frac{dT_{N1}}{dx}\Big|_{x=L} - k_{P1}^{h} A_{P1} \frac{dT_{P1}}{dx}\Big|_{x=L}\right]} \tag{7-13}$$

An energy balance was achieved at the hot and cold ends of the thermo-elements, the heat flux going through the module came from the air gap and thermo-elements,

$$\begin{aligned} q_H &= q_h + q_G \\ q_C &= q_c + q_G \end{aligned} \tag{7-14}$$

where the heat fluxes going through the thermo-elements were given as

$$\begin{aligned} q_h &= q_{Nh} + q_{Ph} \\ q_c &= q_{Nc} + q_{Pc} \end{aligned} \tag{7-15}$$

Substituting Eqs. (7-6) and (7-7) into Eq. (7-14) gave the relationship between the source temperatures (T_H and T_C) and the temperature at the cold and hot ends of the thermo-elements(T_h and T_c),

$$\frac{T_H - T_h}{RH_H} = q_h + \frac{\Delta T}{RH_G} \frac{T_c - T_C}{RH_C} = q_c + \frac{\Delta T}{RH_G} \tag{7-16}$$

Substituting Eq. (7-15) into Eq. (7-16), the cold and hot end temperatures of the thermo-elements were rewritten as

$$T_c = (q_{Pc} + q_{Nc})RH_C + \frac{RH_C}{RH_G}\Delta T + T_C \tag{7-17}$$

$$T_h = -(q_{Ph} + q_{Nh})RH_H - \frac{RH_C}{RH_G}\Delta T + T_H \tag{7-18}$$

The thermodynamic governing equation in the thermo-element was given by Domenicali [222],

$$\frac{\partial}{\partial x}\left(k\frac{\partial T}{\partial x}\right) + \rho J^2 - JT\frac{\partial \alpha}{\partial x} = 0 \tag{7-19}$$

Similar to Eq. (7-8), the heat flux at the cross-section of the thermo-element was the sum of Peltier heat and Fourier heat

$$q = J\alpha T - k\frac{\partial T}{\partial x} \tag{7-20}$$

Eq. (8-20) could be rearranged as

$$\frac{\partial T}{\partial x} = \frac{1}{k}[J\alpha T - q] \tag{7-21}$$

For this case, $\frac{\partial J}{\partial x} = 0$. Differentiating Eq. (7-20) on both sides gave

$$\frac{\partial q}{\partial x} = JT\frac{\partial \alpha}{\partial x} + J\alpha\frac{\partial T}{\partial x} - \frac{\partial}{\partial x}\left(k\frac{\partial T}{\partial x}\right) \tag{7-22}$$

Substituting Eqs. (7-19) and (7-20) into Eq. (7-22), we arrived

$$\frac{\partial q}{\partial x} = \rho J^2\left[1 - \frac{\alpha^2}{\rho k}T\right] - \frac{J\alpha q}{k} \tag{7-23}$$

Discretizing Eqs. (7-21) and (7-23), the temperature and heat flux profiles along the thermo-elements could be explicitly calculated by

$$T_i = T_{i-1} + \frac{(JT_{i-1}\alpha_{i-1} - q_{i-1})}{k_{i-1}}\Delta x_i \tag{7-24}$$

$$q_i = q_{i-1} + \left[\rho_{i-1}J^2\left(1 - \frac{\alpha_{i-1}^2 T_{i-1}}{\rho_{i-1}k_{i-1}}\right) - \frac{J\alpha_{i-1}}{k_{i-1}}q_{i-1}\right]\Delta x_i \tag{7-25}$$

In the calculation, the temperatures at the hot (T_h) and cold (T_c) ends of thermo-elements were unknown. The two temperatures were correlated with the temperatures at the hot (T_H) and cold (T_C) ends of the TEG module through Eq. (7-18), which were measured by the thermocouples. According to the datasheet provided by the TECTEG MFR. corporation, the properties of the P, N-type thermoelectric materials (Figure 7.4) were highly temperature dependent [223]. Thus Thomson Effect cannot be neglected in this case. An iterative scheme was carried out to calculate the temperature profiles and other parameters of the TEG module, with the procedures presented in Figure 7.5. The iteration continued until the relative difference of the voltage output between two iterations was less than 0.1%.

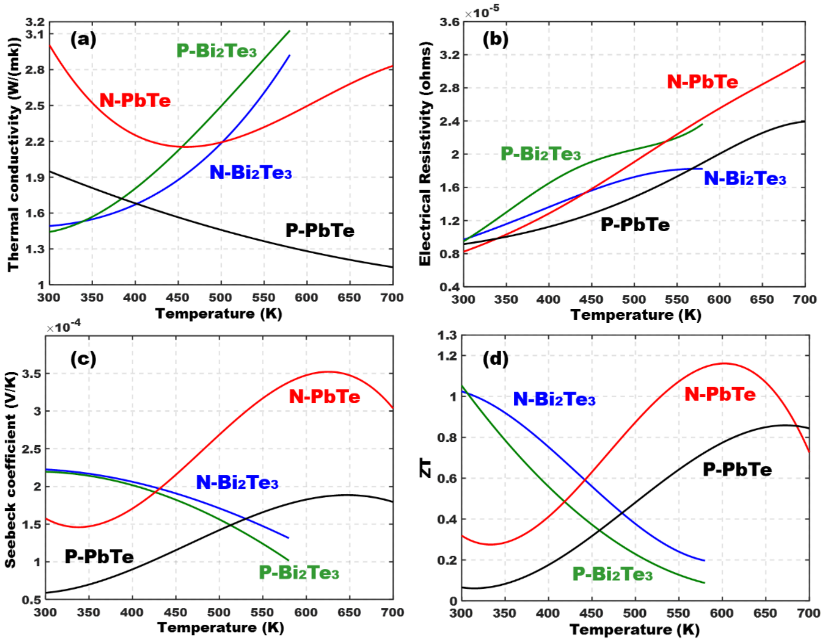

Figure 7.4. Properties of the P, N-type thermoelectric materials varying with temperature [223]: (a)Thermal conductivity; (b) Electrical resistivity; (c) Seebeck coefficient; (d) ZT.

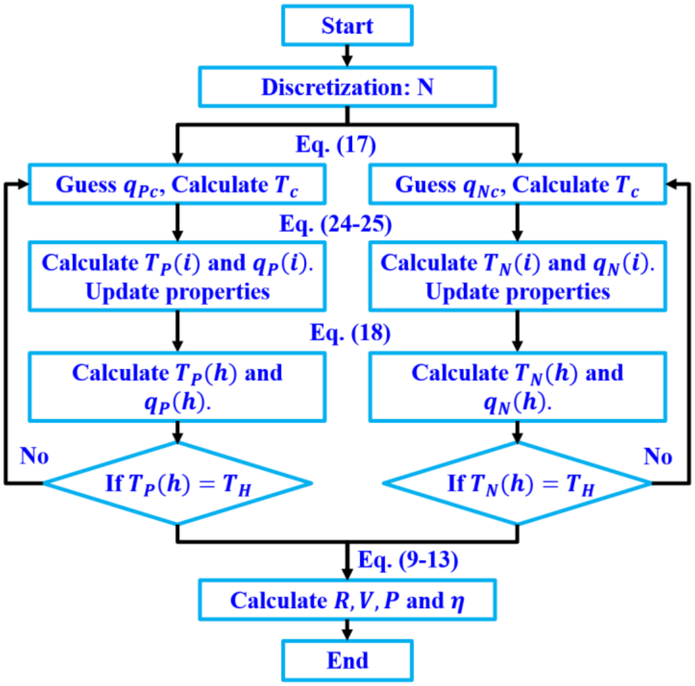

Figure 7.5. The iteration scheme for the TEG model

7.4 The Performance of the thermoelectric energy harvester

The voltage output of a TEG module was positively correlated with the temperature difference. To harvest enough energy for the wireless sensor nodes, a high-temperature drop within the TEG module was desired. Figure 7.6(a) showed the voltage output of the prototype for different load resistances with the source temperature increasing from 20 to 325 °C. Limited by the temperature restriction of the heat pipe, the hot side temperature was heated up to a maximum value of 350 °C, with a peak open circuit voltage output of 2.4 V. An even higher open circuit voltage output could be expected with a higher source temperature. The collected data fluctuated slightly with source temperature, which could be reasoned by the hysteresis effect caused by the thermal mass of the system. As depicted in Figure 7.6, the numerical result matched very well with the experimental result, showing that the model we developed in the section above could predict the voltage output of the system very well within the whole operating temperature range. As shown in Figure 7.6(a), the voltage output of the module did not linearly increase with the source temperature, which could be explained as follows. First, the thermal resistance of the heat pipe and the heat sink varied with the temperature. Thus the temperature drop in the TEG module was not linearly correlated with the source temperature. Second, the properties of the thermoelectric materials were temperature dependent. Thus the voltage output of the module did not linearly increase with the temperature difference.

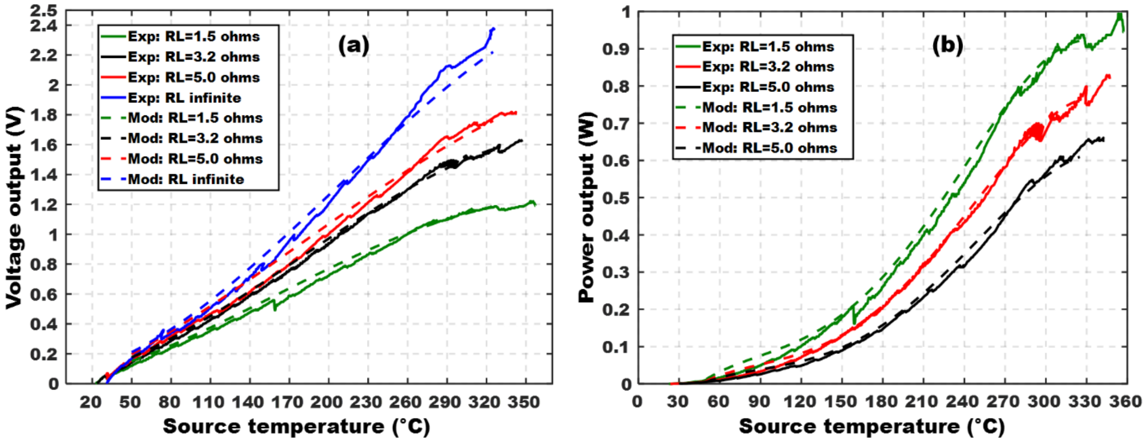

Figure 7.6. The comparison of the experimental and modeling results: (a) Voltage output and (b) Power output of the thermoelectric energy harvester prototype.

The most important parameter to judge the performance of the TEG energy harvester was the power output at the optimum load resistance. As shown in Figure 7.6(b), the power output of the TEG module increased significantly with the source temperature. With a load resistance of 1.5 Ω and a source temperature of 325 °C, the prototype could harvest about 0.92 W electrical energy for the sensor nodes embedded in the gas turbine. Different sensor nodes had different requirements for the voltage and power supply. As reported in [224], for a typical sensor node working in the transmission mode, the energy consumption was about 49.3 mW. As the working condition of the gas turbine might change during the operation process, the power output of the TEG module changed accordingly. Besides, the working voltages of the sensors were different. To provide stable and continuous power and voltage supply for the sensing and monitoring system, integrated energy management circuits with low energy consumption should be designed. The total power requirement for the electrical management circuit and wireless communication components was less than 1.0 W [204]. The prototype presented above can supply more than enough power for the sensors and auxiliary electronics.

The uncertainty of the measured temperature (dT) and voltage (dV) were 0.45 K and 7.7 mV, respectively. The error propagated to the power output was given by

$$dP = \sqrt{\left(\frac{\partial P}{\partial V}\right)^2 dV^2} = 2\left(\frac{V_{output}}{R_L}\right) dV = 12.32\ mW \tag{7-26}$$

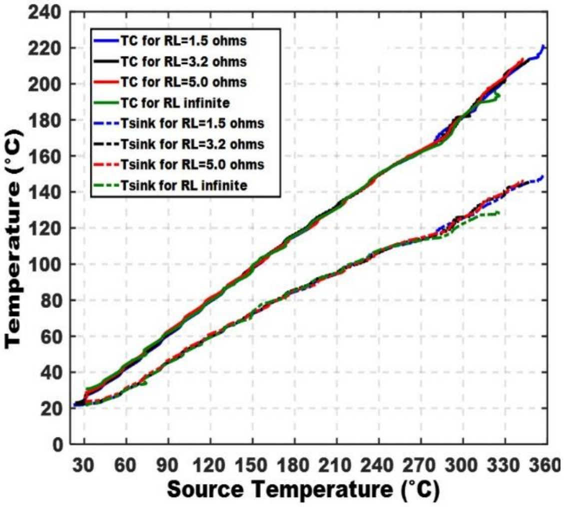

Figure 7.7. T_C and T_{sink} change versus the source temperature

As shown in Figure 7.7, the cold side temperature of the TEG module and the temperature of the heat sink base increased with the source temperature. For different load resistances, the experimental results were highly repeatable, because the amount of energy converted into electricity was relatively small. When the hot side temperature was 325 °C, the temperature drop in the TEG module was about 42 °C, while the temperature drops in the heat pipe and the heat sink were as high as 75 and 120 °C, respectively.

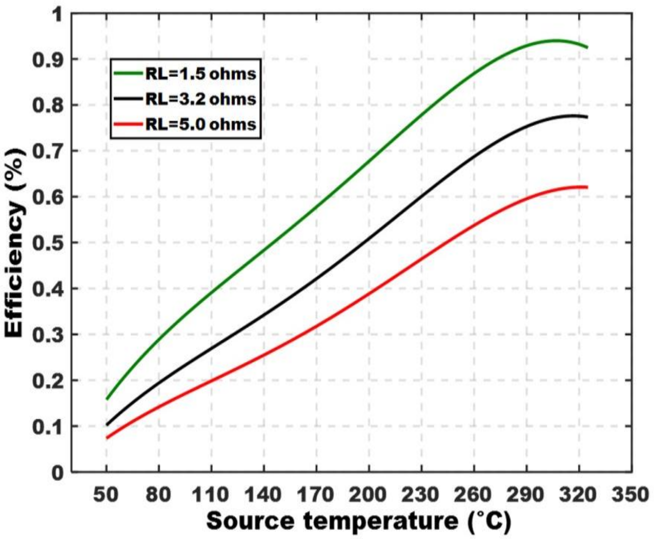

Figure 7.8. The efficiency of the TEG module

The peak efficiency of the TEG module was determined by ZT value and temperature drop in the thermo-elements. We calculated the efficiency of the TEG module based on the modeling results with different load resistance (Figure 7.8). With a load resistance of 1.5 Ω, the efficiency increased with source temperature and reached a peak value of 0.94%, which was relatively low for a segmented TEG. This low efficiency was reasoned as follows. First, natural convection was less efficient than other cooling methods. Thus the thermal resistance of the heat sink was relatively high. Second, several thermal contact layers existed in the prototype, further increasing the thermal resistance of the thermal network. Though the source temperature was high (325 °C), the temperature drop within the thermo-element was relatively small (~45 °C), which was validated by the calculated temperature profile presented in Figure 7.7. There was still some room further improving the performance of the energy harvester through optimization of the thermal network. The convenient ways to increase the power output and efficiency included adopting heat sink and heat pipe with better performance and using forced convection. However, these methods improved the performance of the energy harvester at the cost of system geometry size and reliability. Improving contact quality was a more practical way to improve system performance.

In the TEG module, as a small proportion of thermal energy was converted into electricity and properties of the materials varied with temperature, the temperature in the TEG module was not linearly distributed along the thermo-element length, as presented in Figure 7.9(a). With load resistance changing from infinite to 1.5 Ω, the nonlinearity of the temperature profile increased, because a larger proportion of thermal energy was converted into electricity. This phenomenon was more obviously observed in the N-type thermo-element. Note that, even when the source temperature was the same, the hot and code side temperatures of the thermo-elements would vary with the load resistance. The energy conversion process was illustrated clearly in Fig. 7.9(b), as the heat fluxes, decreased along with the thermal elements. According to the energy conservation law, the “disappeared” thermal energy was converted to electrical energy. An insight observation of the thermal fluxes along the thermo-element found that PbTe segment had higher conversion efficiency than Bi_2Te_3 at this operating temperature range. P-type thermo-element had very low efficiency, as the compatibility factors of P-type PbTe and Bi_2Te_3 did not match well in this temperature range. Segmented TEG module with the optimized design was desired to enhance the energy conversion efficiency.

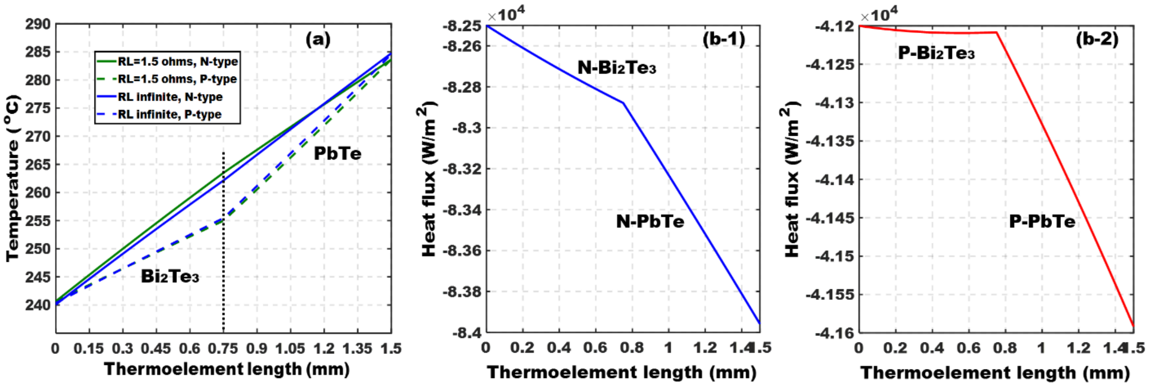

Figure 7.9 (a) The calculated temperature profiles in the thermo-elements; (b) Heat fluxes through the thermo-elements with RL=1.5 Ω.

7.5 Summary for the chapter

In this section, a compact and reliable segmented TEG energy harvester was designed to power wireless sensor nodes in the gas turbine, providing continuous data for the sensing and monitoring system. A detailed analysis of the TEG energy system found that:

1) With the hot side of the TEG heated up to 325 °C, the module had a peak open circuit voltage output of 2.4 V and a power output of ~0.92 W, which was more than enough to power quite a few wireless sensors in the gas turbine.
2) An accurate model to analyze a segmented TEG module was developed, with Peltier heat, Thomson heat, Joule heat, gap heat leakage, and ceramic covering thermal resistance were considered. The resistance of the TEG module almost doubled with the source temperature changing from 50 °C to 325 °C. Meanwhile, the radiation heat leakage increased significantly with the increase in source temperature.
3) The temperature distribution along the thermo-element was nonlinear, as the properties of the thermoelectric materials were temperature dependent and the energy conversion process existed in the thermoelectric materials. The energy conversion process was observed clearly by noticing the decrease of heat flux along the thermo-element length.
4) The energy conversion efficiency of the prototype was about 0.94% with a source temperature of 325 °C and a load resistance of 1.5 Ω. As only natural convection was used to cool the heat sink, the thermal resistance of the heat sink was high, making the efficiency of the TEG relatively low. There was a tradeoff between higher energy output and smaller energy harvester size.

Chapter 8. Conclusion and Future work

8.1 Conclusions

The dissertation focused on developing high-performance thermoelectric energy harvester to power sensor nodes working in an environment where the cable system was precluded. The following conclusions can be drawn from the work accomplished in the dissertation.

1) After a detailed review of the recent advance in thermoelectrics, it was suggested that nano-structured bulk materials integrated with the functionally-graded-material conceptual design were the most promising way for the development of the next-generation high-performance thermoelectric generator or cooler.
2) A general model was established to analyze the impacts of the Thomson effect, contact resistance, and heat leakage on the performance of a TEG module. The Thomson effect could significantly influence the performance of the device if the temperature drop in the thermo-element was large. Also, it was found that the thermal contact resistance dramatically reduced the energy conversion efficiency of the device when the internal resistance of the TEG was comparable to the contact resistance. The model could be easily adapted for other thermoelectric energy harvesting systems.
3) A high-temperature difference was desired for the high energy conversion efficiency of the TEG. To further enlarge the temperature difference, a high-performance microchannel heat sink was designed to cool the cold end of the TEG. The fluidic oscillators array enhanced the heat transfer performance of the heat sink by creating sweeping jets in the fluid channel. To improve accuracy, large eddy simulation (LES) was conducted to do the numerical simulation with very fine grids and extremely low numerical residuals. To partially validate the numerical results, the LES result was compared with conventional RANS turbulence models. This was the first time using LES to analyze the fluidic oscillator. The LES analysis of the fluidic oscillator found that the sweeping jets cooled the heating wall more uniformly and increased the averaged Nu by 3.0-8.0%.
4) Material compatibility mismatch had been the primary limitation to further enhance the energy conversion efficiency of segmented TEG. This issued was first time solved

by a novel method proposed in this dissertation. The thermo-element was divided into many segments mathematically. By calibrating the thickness and height of each segments, the thermoelectric materials achieved their high energy conversion efficiency at each segment. The model was solved numerically using a spreadsheet method with a relative error of 1.0%. Theoretically, this method made the most of the existing thermoelectric materials with high ZT values. The optimized TEG module achieved an unprecedented efficiency of 23.72% at a temperature difference of 800 K.

5) The fabricate the novel design proposed above, a novel integrated design and manufacturing of the nanostructured TEG by the one-step strategy using selective laser melting based additive manufacturing was proposed. Graded doping can be easily achieved using additive manufacturing. To analyze the impact of the processing parameters on the performance of the thermoelectric materials, a comprehensive model was built to simulate the SLM processing of multi-component thermoelectric powders based on the conservation equations. The model was solved using the SLM code developed in our lab. The most advanced CFD schemes were used to accelerate the convergence. The model was not perfect because a lot of assumptions were introduced for simplification. The physical error cannot be judged because some terms in the governing equations should be improved and modified in future work. The model was partially validated by comparing the simulation result of Aluminum powders with a reported experimental result in the literature, which matched each other very well. The numerical iteration stopped when the relative difference between two iterations was less than 0.1%, and numerical residuals were less than 10^{-5} for each equation. It was observed that the temperature distribution within the melting pool was highly non-equilibrium. The shrinkage of the powder bed and the flow circulation within the melting pool could influence the performance of the thermoelectric materials.

6) Monitoring the temperature and pressure within the dry cask system was very important to ensure the safe storage of the nuclear-spent fuel. Penetration was not allowed on the canister wall because of the potential nuclear leakage. In this dissertation, a numerical model was built to analyze the heat and mass transfer within the dry cask system for nuclear storage. This was done as the first step for a TEG

energy harvester design in the dry cask system. The results were validated by comparing simulation results using different turbulence models. Two energy harvesters were designed to harvest the energy sources within the canister for the self-powered sensors. The first energy harvester was a conceptual design to show the possibility of using gamma heating effect for energy harvesting. This was the first time that the gamma heating was calculated and used for energy harvesting. The gramma heating calculation was done using the MCNP code based on Monte Carlo method provided by ORNL. The uncertainties of the Monte Carlo simulations were less than 5.0%. The energy conversion of the TEG was calculated in COMSOL. The iteration stopped when the residuals were less than 10^{-6} for all the governing equations. The second design took advantage of the existing temperature gradient near the canister wall for thermoelectric energy harvesting. To protect the device from the canister wall, radiation shielding block was designed for both gamma and neutron shielding. The gamma radiation simulation was also conducted with MCNP, the error for each simulation was presented in the dissertation. It was found that a shielding block of 6 cm can reduce the accumulated gamma dosage to 200 Mrads for 50 years storage. There was an urgent need to develop better radiation-harden electronics for wireless communication in the nuclear environment. The gamma radiation impact on the thermoelectric properties of the thermoelectric materials were also measured. The uncertainties of the measured data were also discussed.

7) A compact thermoelectric energy harvester was designed, modeled, and experimentally test for the powering of the autonomous sensor nodes in the gas turbine. A high-performance segmented TEG was used in the energy harvester design to achieve higher energy conversion efficiency. It was showed that the energy harvester can supply power for dozens of sensors nodes working on the gas turbine. The uncertainties of the measurements were also documented.

8.2 Future work

There are still a lot of things can be done to improve the work presented in this dissertation. I summarized the future work as follows:

1) The model to simulate the selective laser sintering of the thermoelectric powders can be further improved by considering the phase diagram in the simulation. Also, the temperature dependent properties of the materials should be considered for better accuracy. The code used for the selective laser melting of thermoelectric powders was only verified by simulating the aluminum powders. More materials should be examined before they could be used as a general model for SLM simulation.
2) The experiment using mineral oil to simulate the helium environment in the canister was not fully validated. The performance of the energy harvester should be further verified by experimenting using the helium gas in the nuclear environment.
3) In the dissertation, a high-performance microchannel heat sink using fluidic oscillator arrays to cool the cold end of the TEG was demonstrated. The sweeping jet generated by the fluidic oscillator generates strong vortex near the impingement wall, which can help to enhance the convective heat transfer, accelerate bubble separation, and alleviate the dry out phenomenon. The extremely high heat fluxes (>1 kW/cm^2) in modern devices, such as GaN-based HEMT radar electronics and MW semiconductor lasers, have been the main obstacle to exploring the device performance limits. Fluidic oscillator arrays are extremely suitable for the hot spot cooling. The sweeping jet generated by the fluidic oscillator generates strong vortex near the impingement wall, which can help to enhance the convective heat transfer, accelerate bubble separation, and alleviate the dry out phenomenon. In the future study, researchers can develop novel heat-removal solutions (Figure 8.1) to combine the novel heat sink design with the fundamental study of boiling and condensation, surface chemistry, micro/nanofabrication, and multi-phase transport in variable-permeability porous media.

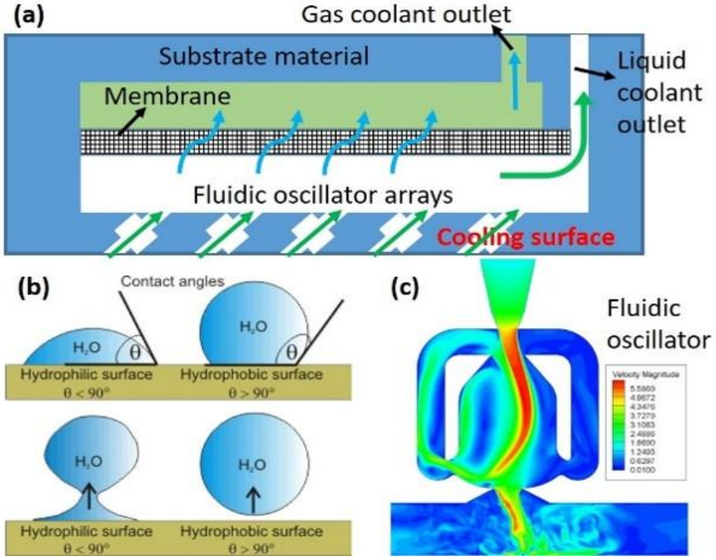

Figure 8.1. (a) A high performance heat sink design; (b) membrane surface chemistry; (c) fluidic oscillator.

4) Reduce the lattice thermal conductivity of the thermoelectric material is the most straightforward way to enhance ZT. Boltzmann equation that built on the reciprocal space rely on the relax time approximation and the dispersion relationship between the wave-vectors and frequency to evaluate the lattice thermal conductivity. However, in real situation, the relax time is highly frequency dependent, and could be hard to implemented for quantitative analysis. Molecular dynamic simulation is a method built on the real space. The macroscopic properties of the material can be calculated using the trajectories of all the particles based on the statistical mechanics principle. The only required inputs are an atomic structure and an appropriate interatomic potential. The physical properties can be extract from the information of the particle evolution using the statistical mechanics, particular the linear response theory. For thermal conductivity calculation, there are two main methods, including equilibrium method (EMD, also called Green-Kubo method) and non-equilibrium method (NEMD, also called direct method). The model built in Chapter Five can help to analyze the impact of processing parameters on the final product. However, it cannot predict the changes in the material properties. MD simulation, in turn, can be used to calculate the thermal conductivity of bulk Mg2Si material with Si nanoparticles added as doping material (Figure 8.2).

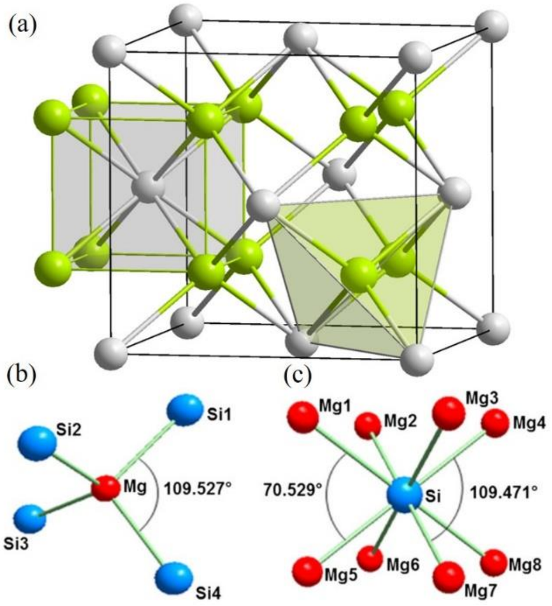

Figure 8.2. The atomic structure of Mg_2Si

5) Turbulence models were very important for the numerical heat and mass transfer. In this dissertation, several turbulence models, including the Reynolds-averaged turbulence models and the large eddy simulation models were used to model the thermal and fluid environments. How to relate the Reynolds /SGS stress to the resolved scales in an accurate way if there is some correlation between these scales is the key issue for the turbulence modeling. Most of the turbulence model was developed based on the Boussinesq approximation, in which the turbulence/SGS stresses was related to the mean/resolved flow to close the system of equations. The treatment can be inaccurate and sometimes fail to predict the behavior of the turbulence flow. Big data might a useful way to establish a general model to simulate the turbulence if the sample number is large enough (Figure 8.3). Thought we do not know the physical meaning of the final results. However, if the model works, then it is a good model. History tells us, we might obtain the result firstly and explain later.

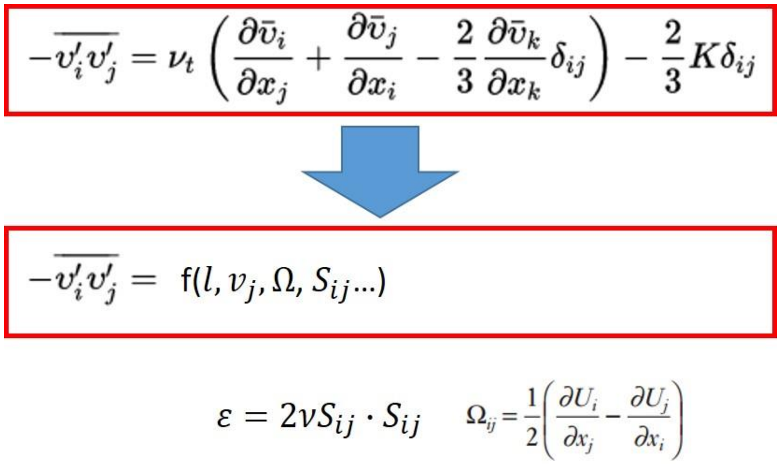

$$-\overline{v_i'v_j'} = \nu_t\left(\frac{\partial\bar{v}_i}{\partial x_j}+\frac{\partial\bar{v}_j}{\partial x_i}-\frac{2}{3}\frac{\partial\bar{v}_k}{\partial x_k}\delta_{ij}\right)-\frac{2}{3}K\delta_{ij}$$

$$-\overline{v_i'v_j'} = \mathrm{f}(l, v_j, \Omega, S_{ij}\ldots)$$

$$\varepsilon = 2\nu S_{ij}\cdot S_{ij} \qquad \Omega_{ij}=\frac{1}{2}\left(\frac{\partial U_i}{\partial x_j}-\frac{\partial U_j}{\partial x_i}\right)$$

Figure 8.3. Big data analysis to find a general turbulence model by related the Reynolds/SGS stress to multiple parameters of the mean/resolved flows.

References

[1] M.S. El-Genk, H.H. Saber, T. Caillat, Efficient segmented thermoelectric unicouples for space power applications, Energ Convers Manage, 44(11) (2003) 1755-1772.

[2] J.P. Longtin, L. Zuo, D. Hwang, G.S. Fu, M. Tewolde, Y.K. Chen, S. Sampath, Fabrication of Thermoelectric Devices Using Thermal Spray: Application to Vehicle Exhaust Systems, J Therm Spray Techn, 22(5) (2013) 577-587.

[3] Z.T. Tian, S. Lee, G. Chen, Heat Transfer in Thermoelectric Materials and Devices, J Heat Trans-T Asme, 135(6) (2013).

[4] T.C. Harman, M.P. Walsh, B.E. Laforge, G.W. Turner, Nanostructured thermoelectric materials, J Electron Mater, 34(5) (2005) L19-L22.

[5] R. Venkatasubramanian, E. Siivola, T. Colpitts, B. O'Quinn, Thin-film thermoelectric devices with high room-temperature figures of merit, Nature, 413(6856) (2001) 597-602.

[6] G.D. Mahan, J.O. Sofo, The best thermoelectric, P Natl Acad Sci USA, 93(15) (1996) 7436-7439.

[7] C.B. Vining, An inconvenient truth about thermoelectrics, Nat Mater, 8(2) (2009) 83-85.

[8] O.o.N. Energy, Powering Curiosity: Multi-Mission Radioisotope Thermoelectric Generators, in, 2008.

[9] T.E. Hammel, R. Bennett, R.K. Sievers, S. Keyser, W. Otting, L. Gard, Multi mission radioisotope thermoelectric generator (MMRTG) performance data and application to life modeling, in: 11th International Energy Conversion Engineering Conference, 2013, pp. 3925.

[10] D. Woerner, A Progress Report on the eMMRTG, J Electron Mater, 45(3) (2016) 1278-1283.

[11] P. Patel, Powering your car with waste heat, Retrieved from MIT technology review, (2011).

[12] B. Orr, A. Akbarzadeh, M. Mochizuki, R. Singh, A review of car waste heat recovery systems utilising thermoelectric generators and heat pipes, Appl Therm Eng, 101 (2016) 490-495.

[13] S. Yadav, P. Sharma, P. Yamasani, S. Minaev, S. Kumar, A prototype micro-thermoelectric power generator for micro-electromechanical systems, Appl Phys Lett, 104(12) (2014).

[14] G.J. Snyder, E.S. Toberer, Complex thermoelectric materials, Nat Mater, 7(2) (2008) 105-114.

[15] M. Kishi, H. Nemoto, T. Hamao, M. Yamamoto, S. Sudou, M. Mandai, S. Yamamoto, Micro thermoelectric modules and their application to wristwatches as an energy source, in: Thermoelectrics, 1999. Eighteenth International Conference on, IEEE, 1999, pp. 301-307.

[16] S.J. Kim, J.H. We, B.J. Cho, A wearable thermoelectric generator fabricated on a glass fabric, Energ Environ Sci, 7(6) (2014) 1959-1965.

[17] V. Leonov, T. Torfs, P. Fiorini, C. Van Hoof, Thermoelectric converters of human warmth for self-powered wireless sensor nodes, IEEE Sensors Journal, 7(5) (2007) 650-657.

[18] I. Chowdhury, R. Prasher, K. Lofgreen, G. Chrysler, S. Narasimhan, R. Mahajan, D. Koester, R. Alley, R. Venkatasubramanian, On-chip cooling by superlattice-based thin-film thermoelectrics, Nat Nanotechnol, 4(4) (2009) 235-238.

[19] J.A. Lee, A.E. Aliev, J.S. Bykova, M.J. de Andrade, D. Kim, H.J. Sim, X. Lepro, A.A. Zakhidov, J.B. Lee, G.M. Spinks, S. Roth, S.J. Kim, R.H. Baughman, Woven-Yarn Thermoelectric Textiles, Adv Mater, 28(25) (2016) 5038-5044.

[20] D. Surie, O. Laguionie, T. Pederson, Wireless Sensor Networking of Everyday Objects in a Smart Home Environment, Issnip 2008: Proceedings of the 2008 International Conference on Intelligent Sensors, Sensor Networks, and Information Processing, (2008) 189-194.

[21] S. Hussain, S. Schaffner, D. Moseychuck, Applications of Wireless Sensor Networks and RFID in a Smart Home Environment, 2009 7th Annual Communication Networks and Services Research Conference, (2009) 153-157.

[22] I.F. Akyildiz, W. Su, Y. Sankarasubramaniam, E. Cayirci, Wireless sensor networks: a survey, Computer networks, 38(4) (2002) 393-422.

[23] J. Chen, J. Klein, Y.J. Wu, S.X. Xing, R. Flammang, M. Heibel, L. Zuo, A Thermoelectric Energy Harvesting System for Powering Wireless Sensors in Nuclear Power Plants, Ieee T Nucl Sci, 63(5) (2016) 2738-2746.
[24] S. Priya, D.J. Inman, Energy harvesting technologies, Springer, New York ; London, 2009.
[25] Z.A. Eu, H.P. Tan, W.K.G. Seah, Design and performance analysis of MAC schemes for Wireless Sensor Networks Powered by Ambient Energy Harvesting, Ad Hoc Netw, 9(3) (2011) 300-323.
[26] S. Ulukus, A. Yener, E. Erkip, O. Simeone, M. Zorzi, P. Grover, K.B. Huang, Energy Harvesting Wireless Communications: A Review of Recent Advances, Ieee J Sel Area Comm, 33(3) (2015) 360-381.
[27] J.A. Paradiso, T. Starner, Energy scavenging for mobile and wireless electronics, Ieee Pervas Comput, 4(1) (2005) 18-27.
[28] C.J. Eiting, V. Krishnamoorthy, S. Rodgers, T. George, J.D. Robertson, J. Brockman, Demonstration of a radiation resistant, high efficiency SiC betavoltaic, Appl Phys Lett, 88(6) (2006).
[29] C. Knight, J. Davidson, S. Behrens, Energy Options for Wireless Sensor Nodes, Sensors-Basel, 8(12) (2008) 8037-8066.
[30] S. Chalasani, J.M. Conrad, A survey of energy harvesting sources for embedded systems, Proceedings Ieee Southeastcon 2008, Vols 1 and 2, (2008) 442-447.
[31] M. Tewolde, C.C. Lin, H. Tao, H. Chen, G. Fu, D. Liu, T. Zhang, D. Benjamin, L. Zuo, D. Hwang, Sensors for small modular reactors powered by thermoelectric generators, in: ASME 2014 Small Modular Reactors Symposium, American Society of Mechanical Engineers, 2014, pp. V001T002A007-V001T002A007.
[32] J. Corelli, R. Frost, The effects of reactor irradiation on the thermoelectric properties of lead and bismuth tellurides, Knolls Atomic Power Lab., Schenectady, NY, 1960.
[33] G. Kilp, P. Mitchell, Radiation effects on thermoelectric materials, Westinghouse Electric Corp. Atomic Power Dept., Pittsburgh, 1961.
[34] A.A. Alothman, M.Y. Zakaria, M.R. Hajj, S.F. Masri, Use of thermoelectric generator for water flow metering, Appl Phys Lett, 109(3) (2016).
[35] A. Luque, S. Hegedus, Handbook of photovoltaic science and engineering, 2nd ed., Wiley, Chichester, West Sussex, U.K. ; Hoboken, N.J., 2010.
[36] M.A. Green, K. Emery, Y. Hishikawa, W. Warta, E.D. Dunlop, Solar cell efficiency tables (Version 45), Prog Photovoltaics, 23(1) (2015) 1-9.
[37] W.-Q. Wu, Y.-F. Xu, C.-Y. Su, D.-B. Kuang, Ultra-long anatase TiO 2 nanowire arrays with multi-layered configuration on FTO glass for high-efficiency dye-sensitized solar cells, Energy & Environmental Science, 7(2) (2014) 644-649.
[38] L. Zuo, B. Scully, J. Shestani, Y. Zhou, Design and characterization of an electromagnetic energy harvester for vehicle suspensions, Smart Mater Struct, 19(4) (2010).
[39] S.P. Beeby, M.J. Tudor, N.M. White, Energy harvesting vibration sources for microsystems applications, Meas Sci Technol, 17(12) (2006) R175-R195.
[40] W.L. Zhou, L. Zuo, A Self-Powered Piezoelectric Vibration Control System With Switch Precharged Inductor (SPCI) Method, Ieee-Asme T Mech, 20(2) (2015) 773-781.
[41] D. Siegert, M. Peigney, Study of Energy Harvesting from Traffic-Induced Bridge Vibrations, 11th World Congress on Computational Mechanics; 5th European Conference on Computational Mechanics; 6th European Conference on Computational Fluid Dynamics, Vols Ii - Iv, (2014) 643-654.
[42] T. MFR., PbTe/TAGS 400-600 C high efficiency (up to 12%) TEG modules, in, 2017.
[43] T. Fujisaka, H. Sui, R.O. Suzuki, Design and Numerical Evaluation of Cascade-Type Thermoelectric Modules, J Electron Mater, 42(7) (2013) 1688-1696.
[44] M.G.L. Roes, J.L. Duarte, M.A.M. Hendrix, E.A. Lomonova, Acoustic Energy Transfer: A Review, Ieee T Ind Electron, 60(1) (2013) 242-248.

[45] H.J. Visser, R.J.M. Vullers, RF Energy Harvesting and Transport for Wireless Sensor Network Applications: Principles and Requirements, P Ieee, 101(6) (2013) 1410-1423.

[46] A.J. Minnich, M.S. Dresselhaus, Z.F. Ren, G. Chen, Bulk nanostructured thermoelectric materials: current research and future prospects, Energ Environ Sci, 2(5) (2009) 466-479.

[47] D.M. Rowe, Thermoelectrics handbook: macro to nano, CRC press, 2005.

[48] G.J. Tan, L.D. Zhao, M.G. Kanatzidis, Rationally Designing High-Performance Bulk Thermoelectric Materials, Chem Rev, 116(19) (2016) 12123-12149.

[49] L.D. Hicks, M.S. Dresselhaus, Effect of Quantum-Well Structures on the Thermoelectric Figure of Merit, Phys Rev B, 47(19) (1993) 12727-12731.

[50] L.D. Hicks, M.S. Dresselhaus, Thermoelectric Figure of Merit of a One-Dimensional Conductor, Phys Rev B, 47(24) (1993) 16631-16634.

[51] M.S. Dresselhaus, G. Chen, M.Y. Tang, R. Yang, H. Lee, D. Wang, Z. Ren, J.P. Fleurial, P. Gogna, New directions for low-dimensional thermoelectric materials, Adv Mater, 19(8) (2007) 1043-1053.

[52] M.G. Kanatzidis, Nanostructured thermoelectrics: the new paradigm?, Chemistry of materials, 22(3) (2009) 648-659.

[53] J. Zhou, W. Feng, Y. Zhang, Y. Yao, Engineering Topological Surface States and Giant Rashba Spin Splitting in BiTeI/Bi2Te3 Heterostructures, Scientific reports, (2014).

[54] S.-H. Baek, K.-C. Kim, J.-S. Kim, Free-electron Creation at the 60° Twin Boundary in Bi2Te3, in: APS March Meeting Abstracts, 2017.

[55] H. Goldsmid, R. Douglas, The use of semiconductors in thermoelectric refrigeration, British Journal of Applied Physics, 5(11) (1954) 386.

[56] H.J. Goldsmid, Bismuth Telluride and Its Alloys as Materials for Thermoelectric Generation, Materials, 7(4) (2014) 2577-2592.

[57] T. Schroder, T. Rosenthal, N. Giesbrecht, M. Nentwig, S. Maier, H. Wang, G.J. Snyder, O. Oeckler, Nanostructures in Te/Sb/Ge/Ag (TAGS) Thermoelectric Materials Induced by Phase Transitions Associated with Vacancy Ordering, Inorg Chem, 53(14) (2014) 7722-7729.

[58] E.M. Levin, S.L. Bud'ko, K. Schmidt-Rohr, Enhancement of Thermopower of TAGS-85 High-Performance Thermoelectric Material by Doping with the Rare Earth Dy, Adv Funct Mater, 22(13) (2012) 2766-2774.

[59] T. Zhu, H. Gao, Y. Chen, X. Zhao, Ioffe–Regel limit and lattice thermal conductivity reduction of high performance (AgSbTe 2) 15 (GeTe) 85 thermoelectric materials, Journal of Materials Chemistry A, 2(9) (2014) 3251-3256.

[60] G.A. Slack, The thermal conductivity of nonmetallic crystals, in: Solid state physics, Elsevier, 1979, pp. 1-71.

[61] W. Jeitschko, D. Braun, LaFe4P12 with filled CoAs3-type structure and isotypic lanthanoid–transition metal polyphosphides, Acta Crystallographica Section B: Structural Crystallography and Crystal Chemistry, 33(11) (1977) 3401-3406.

[62] G. Nolas, D. Morelli, T.M. Tritt, Skutterudites: A phonon-glass-electron crystal approach to advanced thermoelectric energy conversion applications, Annual Review of Materials Science, 29(1) (1999) 89-116.

[63] C. Uher, Skutterudites: Prospective novel thermoelectrics, in: Semiconductors and semimetals, Elsevier, 2001, pp. 139-253.

[64] D. Wee, B. Kozinsky, N. Marzari, M. Fornari, Effects of filling in CoSb3: Local structure, band gap, and phonons from first principles, Phys Rev B, 81(4) (2010).

[65] Oysteinp, Skutterudite-structure-large, in, 2005.

[66] M. Rull-Bravo, A. Moure, J.F. Fernandez, M. Martin-Gonzalez, Skutterudites as thermoelectric materials: revisited, Rsc Adv, 5(52) (2015) 41653-41667.

[67] N. Farahi, S. Prabhudev, G.A. Botton, J.R. Salvador, H. Kleinke, Nano-and microstructure engineering: an effective method for creating high efficiency magnesium silicide based thermoelectrics, ACS applied materials & interfaces, 8(50) (2016) 34431-34437.

[68] J. Li, J.P. Longtin, S. Tankiewicz, A. Gouldstone, S. Sampath, Interdigital capacitive strain gauges fabricated by direct-write thermal spray and ultrafast laser micromachining, Sensors and Actuators A: Physical, 133(1) (2007) 1-8.

[69] T. Yi, S. Chen, S. Li, H. Yang, S. Bux, Z. Bian, N.A. Katcho, A. Shakouri, N. Mingo, J.-P. Fleurial, Synthesis and characterization of Mg 2 Si/Si nanocomposites prepared from MgH 2 and silicon, and their thermoelectric properties, Journal of Materials Chemistry, 22(47) (2012) 24805-24813.

[70] I. Laboratory, Mg2Si-Research on thermoelectronics, in, 2015.

[71] M. Christensen, A.B. Abrahamsen, N.B. Christensen, F. Juranyi, N.H. Andersen, K. Lefmann, J. Andreasson, C.R.H. Bahl, B.B. Iversen, Avoided crossing of rattler modes in thermoelectric materials, Nat Mater, 7(10) (2008) 811-815.

[72] G. Chen, M.S. Dresselhaus, G. Dresselhaus, J.P. Fleurial, T. Caillat, Recent developments in thermoelectric materials, Int Mater Rev, 48(1) (2003) 45-66.

[73] G.S. Nolas, J.L. Cohn, G.A. Slack, S.B. Schujman, Semiconducting Ge clathrates: Promising candidates for thermoelectric applications, Appl Phys Lett, 73(2) (1998) 178-180.

[74] P.F. Qiu, J. Yang, X.Y. Huang, X.H. Chen, L.D. Chen, Effect of antisite defects on band structure and thermoelectric performance of ZrNiSn half-Heusler alloys, Appl Phys Lett, 96(15) (2010).

[75] L.D. Zhao, S.H. Lo, Y.S. Zhang, H. Sun, G.J. Tan, C. Uher, C. Wolverton, V.P. Dravid, M.G. Kanatzidis, Ultralow thermal conductivity and high thermoelectric figure of merit in SnSe crystals, Nature, 508(7496) (2014) 373-+.

[76] Y.Z. Pei, A. LaLonde, S. Iwanaga, G.J. Snyder, High thermoelectric figure of merit in heavy hole dominated PbTe, Energ Environ Sci, 4(6) (2011) 2085-2089.

[77] J.P. Heremans, V. Jovovic, E.S. Toberer, A. Saramat, K. Kurosaki, A. Charoenphakdee, S. Yamanaka, G.J. Snyder, Enhancement of thermoelectric efficiency in PbTe by distortion of the electronic density of states, Science, 321(5888) (2008) 554-557.

[78] K. Biswas, J.Q. He, I.D. Blum, C.I. Wu, T.P. Hogan, D.N. Seidman, V.P. Dravid, M.G. Kanatzidis, High-performance bulk thermoelectrics with all-scale hierarchical architectures, Nature, 489(7416) (2012) 414-418.

[79] G. Fu, Integrated Design and Manufacturing of Thermoelectric Generator for Energy Harvesting, State University of New York at Stony Brook, Ann Arbor, 2015.

[80] A.Y. Cho, J. Arthur, Molecular beam epitaxy, Progress in solid state chemistry, 10 (1975) 157-191.

[81] W.P. McCray, MBE deserves a place in the history books, Nat Nanotechnol, 2(5) (2007) 259.

[82] T.C. Harman, D.L. Spears, M.P. Walsh, PbTe/Te superlattice structures with enhanced thermoelectric figures of merit, J Electron Mater, 28(1) (1999) L1-L4.

[83] M. Kondow, K. Uomi, K. Hosomi, T. Mozume, Gas-source molecular beam epitaxy of GaNxAs1-x using a N radical as the N source, Japanese journal of applied physics, 33(8A) (1994) L1056.

[84] V. Ottesen, A Molecular Beam Epitaxy reaction chamber concept drawing, in, 2011.

[85] A. El-Desouky, M. Carter, M. Mahmoudi, A. Elwany, S. LeBlanc, Influences of energy density on microstructure and consolidation of selective laser melted bismuth telluride thermoelectric powder, J Manuf Process, 25 (2017) 411-417.

[86] Y. Mao, Y.G. Yan, K.P. Wu, H.Y. Xie, Z.K. Xiu, J.H. Yang, Q.J. Zhang, C. Uher, X.F. Tang, Non-equilibrium synthesis and characterization of n-type Bi2Te2.7Se0.3 thermoelectric material prepared by rapid laser melting and solidification, Rsc Adv, 7(35) (2017) 21439-21445.

[87] Y.G. Yan, H.Q. Ke, J.H. Yang, C. Uher, X.F. Tang, Fabrication and Thermoelectric Properties of n-Type CoSb2.85Te0.15 Using Selective Laser Melting, Acs Applied Materials & Interfaces, 10(16) (2018) 13669-13674.

[88] J. Karthikeyan, Cold spray technology, Advanced materials & processes, 163(3) (2005) 33-35.

[89] 3-Omega, in, Heat lab, Georgia Tech, 2018.
[90] Van der Pauw method, in, Wikipedia, 2018.
[91] A. RIKO, Seebeck Coefficient / Electric Resistance Measurement System ZEM-3 series, in, 2018.
[92] G. Chen, Nanoscale energy transport and conversion: a parallel treatment of electrons, molecules, phonons, and photons, Oxford University Press, 2005.
[93] R. Ure Jr, Practical limits to the thermoelectric figure of merit—II, Energy conversion, 12(2) (1972) 45-52.
[94] E. Rittner, G. Neumark, Theoretical Bound on the Thermoelectric Figure of Merit of Two-Band Semiconductors, Journal of Applied Physics, 34(7) (1963) 2071-2077.
[95] R. Simon, Thermoelectric Figure of Merit of Two-Band Semiconductors, Journal of Applied Physics, 33(5) (1962) 1830-1841.
[96] A.F. Ioffe, Semiconductor thermoelements and thermoelectric cooling, (1957).
[97] J. Zhang, R. Liu, N. Cheng, Y. Zhang, J. Yang, C. Uher, X. Shi, L. Chen, W. Zhang, High-Performance Pseudocubic Thermoelectric Materials from Non-cubic Chalcopyrite Compounds, Adv Mater, 26(23) (2014) 3848-3853.
[98] Y.Z. Pei, X.Y. Shi, A. LaLonde, H. Wang, L.D. Chen, G.J. Snyder, Convergence of electronic bands for high performance bulk thermoelectrics, Nature, 473(7345) (2011) 66-69.
[99] D. Byeon, R. Sobota, K. Delime-Codrin, S. Choi, K. Hirata, M. Adachi, M. Kiyama, T. Matsuura, Y. Yamamoto, M. Matsunami, T. Takeuchi, Discovery of colossal Seebeck effect in metallic Cu2Se, Nat Commun, 10 (2019).
[100] C. Wu, Analysis of waste-heat thermoelectric power generators, Appl Therm Eng, 16(1) (1996) 63-69.
[101] M.J. Lampinen, Thermodynamic Analysis of Thermoelectric Generator, J Appl Phys, 69(8) (1991) 4318-4323.
[102] J.C. Chen, Z.J. Yan, L.Q. Wu, The influence of Thomson effect on the maximum power output and maximum efficiency of a thermoelectric generator, J Appl Phys, 79(11) (1996) 8823-8828.
[103] S.A. Omer, Solar Thermoelectric System for Small Scale Power Generation, Doctoral Thesis, Loughborough University 1997.
[104] M. Freunek, M. Muller, T. Ungan, W. Walker, L.M. Reindl, New Physical Model for Thermoelectric Generators, J Electron Mater, 38(7) (2009) 1214-1220.
[105] D.M. Rowe, Thermoelectric Handbook-Macro to Nano, Taylor & Francis Group, 2006.
[106] G. Min, D.M. Rowe, Improved model for calculating the coefficient of performance of a Peltier module, Energ Convers Manage, 41(2) (2000) 163-171.
[107] M.J. Huang, R.H. Yen, A.B. Wang, The influence of the Thomson effect on the performance of a thermoelectric cooler, Int J Heat Mass Tran, 48(2) (2005) 413-418.
[108] D.M. Rowe, Thermoelectrics handbook : macro to nano, CRC/Taylor & Francis, Boca Raton, 2006.
[109] I. Hi-Z Technology, HZ-2 Thermoelectric Module, in, 2014.
[110] S. Ekkad, Exhaust pipe with pin fins, in, 2015.
[111] L. Agricola, R. Prenter, R. Lundgreen, M. Hossain, A. Ameri, J. Gregory, J. Bons, Impinging Sweeping Jet Heat Transfer, in: 53rd AIAA/SAE/ASEE Joint Propulsion Conference, 2017, pp. 4974.
[112] C. Camci, F. Herr, Forced convection heat transfer enhancement using a self-oscillating impinging planar jet, J Heat Trans-T Asme, 124(4) (2002) 770-782.
[113] M.A. Hossain, L. Agricola, A. Ameri, J.W. Gregory, J.P. Bons, Effects of Curvature on the Performance of Sweeping Jet Impingement Heat Transfer, in: 2018 AIAA Aerospace Sciences Meeting, 2018, pp. 0243.

[114] M.A. Hossain, R. Prenter, R.K. Lundgreen, A. Ameri, J.W. Gregory, J.P. Bons, Experimental and Numerical Investigation of Sweeping Jet Film Cooling, Journal of Turbomachinery, 140(3) (2018) 031009.

[115] S. Raghu, Feedback-free fluidic oscillator and method, in, Google Patents, 2001.

[116] J. Gregory, M.N. Tomac, A review of fluidic oscillator development, in: 43rd AIAA Fluid Dynamics Conference, 2013, pp. 2474.

[117] J. Seo, C. Zhu, R. Mittal, Flow Physics and Frequency Scaling of Sweeping Jet Fluidic Oscillators, AIAA Journal, (2018) 1-12.

[118] R. Woszidlo, I. Wygnanski, Parameters governing separation control with sweeping jet actuators, in: 29th AIAA Applied Aerodynamics Conference, 2011, pp. 3172.

[119] M. Metka, J.W. Gregory, Drag Reduction on the 25-deg Ahmed Model Using Fluidic Oscillators, J Fluid Eng-T Asme, 137(5) (2015).

[120] H.S. Jeong, K.Y. Kim, Shape optimization of a feedback-channel fluidic oscillator, Eng Appl Comp Fluid, 12(1) (2017) 169-181.

[121] B.C. Bobusch, R. Woszidlo, J.M. Bergada, C.N. Nayeri, C.O. Paschereit, Experimental study of the internal flow structures inside a fluidic oscillator, Exp Fluids, 54(6) (2013).

[122] T. Choephel, J. Coder, M. Maughmer, Airfoil Boundary-Layer Flow Control Using Fluidic Oscillators, in: 30th AIAA Applied Aerodynamics Conference, 2012, pp. 2655.

[123] M. DeSalvo, E. Whalen, A. Glezer, High-lift enhancement using fluidic actuation, in: 48th AIAA Aerospace Sciences Meeting Including the New Horizons Forum and Aerospace Exposition, 2010, pp. 863.

[124] L.N. Cattafesta III, M. Sheplak, Actuators for active flow control, Annual Review of Fluid Mechanics, 43 (2011) 247-272.

[125] T. Park, K. Kara, D. Kim, Flow structure and heat transfer of a sweeping jet impinging on a flat wall, International Journal of Heat and Mass Transfer, 124 (2018) 920-928.

[126] M. Germano, U. Piomelli, P. Moin, W.H. Cabot, A dynamic subgrid-scale eddy viscosity model, Physics of Fluids A: Fluid Dynamics, 3(7) (1991) 1760-1765.

[127] F. Ostermann, R. Woszidlo, C. Nayeri, C.O. Paschereit, Experimental comparison between the flow field of two common fluidic oscillator designs, in: 53rd AIAA Aerospace Sciences Meeting, 2015, pp. 0781.

[128] G. Raman, S. Raghu, Cavity resonance suppression using miniature fluidic oscillators, Aiaa Journal, 42(12) (2004) 2608-2612.

[129] G. Raman, S. Packiarajan, G. Papadopoulos, C. Weissman, S. Raghu, Jet thrust vectoring using a miniature fluidic oscillator, Aeronaut J, 109(1093) (2005) 129-138.

[130] R. Seele, E. Graff, J. Lin, I. Wygnanski, Performance enhancement of a vertical tail model with sweeping jet actuators, in: 51st AIAA Aerospace Sciences Meeting including the New Horizons Forum and Aerospace Exposition, 2013, pp. 411.

[131] J.H. Seo, R. Mittal, Computational Modeling and Analysis of Sweeping Jet Fluidic Oscillators, in: 47th AIAA Fluid Dynamics Conference, 2017, pp. 3312.

[132] R. Woszidlo, T. Stumper, C. Nayeri, C.O. Paschereit, Experimental study on bluff body drag reduction with fluidic oscillators, in: 52nd Aerospace Sciences Meeting, 2014, pp. 0403.

[133] A. Fluent, Theory Guide and User's Guide, Ansys Inc, USA, (2015).

[134] F.R. Menter, M. Kuntz, R. Langtry, Ten years of industrial experience with the SST turbulence model, Turbulence, heat and mass transfer, 4(1) (2003) 625-632.

[135] D.K. Lilly, A proposed modification of the Germano subgrid-scale closure method, Physics of Fluids A: Fluid Dynamics, 4(3) (1992) 633-635.

[136] S.V. Garimella, R.A. Rice, Confined and submerged liquid jet impingement heat transfer, J Heat Trans-T Asme, 117(4) (1995) 871-877.

[137] H. Sun, C. Ma, W. Nakayama, Local characteristics of convective heat transfer from simulated microelectronic chips to impinging submerged round water jets, Journal of Electronic Packaging, 115(1) (1993) 71-77.

[138] C.Y. Li, S.V. Garimella, Prandtl-number effects and generalized correlations for confined and submerged jet impingement, Int J Heat Mass Tran, 44(18) (2001) 3471-3480.

[139] X.T. Trinh, M. Fenot, E. Dorignac, The effect of nozzle geometry on local convective heat transfer to unconfined impinging air jets, Exp Therm Fluid Sci, 70 (2016) 1-16.

[140] M.P. David, J.E. Steinbrenner, J. Miler, K.E. Goodson, Adiabatic and diabatic two-phase venting flow in a microchannel, Int J Multiphas Flow, 37(9) (2011) 1135-1146.

[141] E. Muller, C. Drasar, J. Schilz, W.A. Kaysser, Functionally graded materials for sensor and energy applications, Mat Sci Eng a-Struct, 362(1-2) (2003) 17-39.

[142] W.S. Liu, X. Yan, G. Chen, Z.F. Ren, Recent advances in thermoelectric nanocomposites, Nano Energy, 1(1) (2012) 42-56.

[143] G.J. Snyder, Application of the compatibility factor to the design of segmented and cascaded thermoelectric generators, Appl Phys Lett, 84(13) (2004) 2436-2438.

[144] X.A. Yan, B. Poudel, Y. Ma, W.S. Liu, G. Joshi, H. Wang, Y.C. Lan, D.Z. Wang, G. Chen, Z.F. Ren, Experimental Studies on Anisotropic Thermoelectric Properties and Structures of n-Type Bi2Te2.7Se0.3, Nano Lett, 10(9) (2010) 3373-3378.

[145] B.Y. Moizhes, Y. Shishkin, A. Petrov, L. Kolomoets, CHOICE OF OPTIMAL MODE OF OPERATION OF A CASCADE THERMOELECTRIC ELEMENT, SOVIET PHYSICS-TECHNICAL PHYSICS, 7(4) (1962) 336-&.

[146] G. Min, D.M. Rowe, Recent concepts in thermoelectric power generation, Xxi International Conference on Thermoelectrics, Proceedings Ict '02, (2002) 365-374.

[147] L.P. Hu, H.J. Wu, T.J. Zhu, C.G. Fu, J.Q. He, P.J. Ying, X.B. Zhao, Tuning Multiscale Microstructures to Enhance Thermoelectric Performance of n-Type Bismuth-Telluride-Based Solid Solutions, Adv Energy Mater, 5(17) (2015).

[148] Z.L. Tang, L.P. Hu, T.J. Zhu, X.H. Liu, X.B. Zhao, High performance n-type bismuth telluride based alloys for mid-temperature power generation, J Mater Chem C, 3(40) (2015) 10597-10603.

[149] A.T. Duong, V.Q. Nguyen, G. Duvjir, V.T. Duong, S. Kwon, J.Y. Song, J.K. Lee, J.E. Lee, S. Park, T. Min, J. Lee, J. Kim, S. Cho, Achieving ZT=2.2 with Bi-doped n-type SnSe single crystals, Nat Commun, 7 (2016).

[150] R. Basu, S. Bhattacharya, R. Bhatt, M. Roy, S. Ahmad, A. Singh, M. Navaneethan, Y. Hayakawa, D.K. Aswal, S.K. Gupta, Improved thermoelectric performance of hot pressed nanostructured n-type SiGe bulk alloys, J Mater Chem A, 2(19) (2014) 6922-6930.

[151] S. Il Kim, K.H. Lee, H.A. Mun, H.S. Kim, S.W. Hwang, J.W. Roh, D.J. Yang, W.H. Shin, X.S. Li, Y.H. Lee, G.J. Snyder, S.W. Kim, Dense dislocation arrays embedded in grain boundaries for high-performance bulk thermoelectrics, Science, 348(6230) (2015) 109-114.

[152] Y.Y. Li, D. Li, X.Y. Qin, X.H. Yang, Y.F. Liu, J. Zhang, Y.C. Dou, C.J. Song, H.X. Xin, Enhanced thermoelectric performance through carrier scattering at heterojunction potentials in BiSbTe based composites with Cu3SbSe4 nanoinclusions, J Mater Chem C, 3(27) (2015) 7045-7052.

[153] G.J. Tan, F.Y. Shi, S.Q. Hao, L.D. Zhao, H. Chi, X.M. Zhang, C. Uher, C. Wolverton, V.P. Dravid, M.G. Kanatzidis, Non-equilibrium processing leads to record high thermoelectric figure of merit in PbTe-SrTe, Nat Commun, 7 (2016).

[154] C.G. Fu, S.Q. Bai, Y.T. Liu, Y.S. Tang, L.D. Chen, X.B. Zhao, T.J. Zhu, Realizing high figure of merit in heavy-band p-type half-Heusler thermoelectric materials, Nat Commun, 6 (2015).

[155] G.J. Snyder, T.S. Ursell, Thermoelectric efficiency and compatibility, Phys Rev Lett, 91(14) (2003).

[156] R. Cohen, B. Abeles, Efficiency calculations of thermoelectric generators with temperature varying parameters, J Appl Phys, 34(6) (1963) 1687-1688.

[157] T.C. Harman, P.J. Taylor, M.P. Walsh, B.E. LaForge, Quantum dot superlattice thermoelectric materials and devices, Science, 297(5590) (2002) 2229-2232.

[158] V.L. Kuznetsov, L.A. Kuznetsova, A.E. Kaliazin, D.M. Rowe, High performance functionally graded and segmented Bi2Te3-based materials for thermoelectric power generation, J Mater Sci, 37(14) (2002) 2893-2897.

[159] B. Poudel, Q. Hao, Y. Ma, Y.C. Lan, A. Minnich, B. Yu, X.A. Yan, D.Z. Wang, A. Muto, D. Vashaee, X.Y. Chen, J.M. Liu, M.S. Dresselhaus, G. Chen, Z.F. Ren, High-thermoelectric performance of nanostructured bismuth antimony telluride bulk alloys, Science, 320(5876) (2008) 634-638.

[160] K. Nishio, T. Hirano, Improvement of the efficiency of thermoelectric energy conversion by utilizing potential barriers, Jpn J Appl Phys 1, 36(1a) (1997) 170-174.

[161] S.Y. Wang, J. Yang, T. Toll, J.H. Yang, W.Q. Zhang, X.F. Tang, Conductivity-limiting bipolar thermal conductivity in semiconductors, Sci Rep-Uk, 5 (2015).

[162] G. Chen, Nanoscale energy transport and conversion : a parallel treatment of electrons, molecules, phonons, and photons, Oxford University Press, Oxford ; New York, 2005.

[163] S. Bremen, W. Meiners, A. Diatlov, Selective laser melting, Laser Technik Journal, 9(2) (2012) 33-38.

[164] K. Zeng, D. Pal, B. Stucker, A review of thermal analysis methods in Laser Sintering and Selective Laser Melting, in: Proceedings of Solid Freeform Fabrication Symposium Austin, TX, 2012, pp. 796-814.

[165] I.A. Roberts, C.J. Wang, R. Esterlein, M. Stanford, D.J. Mynors, A three-dimensional finite element analysis of the temperature field during laser melting of metal powders in additive layer manufacturing, Int J Mach Tool Manu, 49(12-13) (2009) 916-923.

[166] V.R. Voller, A.D. Brent, C. Prakash, The Modeling of Heat, Mass and Solute Transport in Solidification Systems, Int J Heat Mass Tran, 32(9) (1989) 1719-1731.

[167] J.F. Li, L. Li, F.H. Stott, A three-dimensional numerical model for a convection-diffusion phase change process during laser melting of ceramic materials, Int J Heat Mass Tran, 47(25) (2004) 5523-5539.

[168] B. Xiao, Y.W. Zhang, Marangoni and buoyancy effects on direct metal laser sintering with a moving laser beam, Numer Heat Tr a-Appl, 51(8) (2007) 715-733.

[169] C. Korner, E. Attar, P. Heinl, Mesoscopic simulation of selective beam melting processes, J Mater Process Tech, 211(6) (2011) 978-987.

[170] S.A. Khairallah, A. Anderson, Mesoscopic simulation model of selective laser melting of stainless steel powder, J Mater Process Tech, 214(11) (2014) 2627-2636.

[171] Y.B. Bao, J. Meskas, Lattice boltzmann method for fluid simulations, Department of Mathematics, Courant Institute of Mathematical Sciences, New York University, (2011).

[172] P. Dutta, Y. Joshi, R. Janaswamy, Thermal Modeling of Gas Tungsten Arc-Welding Process with Nonaxisymmetric Boundary-Conditions, Numer Heat Tr a-Appl, 27(5) (1995) 499-518.

[173] G.R. Hadley, Thermal-Conductivity of Packed Metal Powders, Int J Heat Mass Tran, 29(6) (1986) 909-920.

[174] S.S. Sih, J.W. Barlow, The prediction of the emissivity and thermal conductivity of powder beds, Particul Sci Technol, 22(3) (2004) 291-304.

[175] B. Van Leer, Towards the ultimate conservative difference scheme. II. Monotonicity and conservation combined in a second-order scheme, Journal of computational physics, 14(4) (1974) 361-370.

[176] H.K. Versteeg, W. Malalasekera, An introduction to computational fluid dynamics: the finite volume method, Pearson Education, 2007.

[177] W. Tao, Numerical heat transfer (Second edition), Xi'an Jiaotong University Press, 2001.

[178] M. Akasaka, T. Iida, A. Matsumoto, K. Yamanaka, Y. Takanashi, T. Imai, N. Hamada, The thermoelectric properties of bulk crystalline n- and p-type Mg2Si prepared by the vertical Bridgman method, J Appl Phys, 104(1) (2008).

[179] B.H. Yu, D. Chen, Q.B. Tang, C.L. Wang, D.H. Shi, Structural, electronic, elastic and thermal properties of Mg2Si, J Phys Chem Solids, 71(5) (2010) 758-763.

[180] C. Glassbrenner, G.A. Slack, Thermal conductivity of silicon and germanium from 3 K to the melting point, Physical Review, 134(4A) (1964) A1058.
[181] S. Kou, Y. Wang, Three-dimensional convection in laser melted pools, Metallurgical transactions A, 17(12) (1986) 2265-2270.
[182] S. Kou, Y. Wang, Weld pool convection and its effect, Weld. J, 65(3) (1986) 63s-70s.
[183] U.S.G.A. Office, Disposal of High-Level Nuclear Waste, in, 2017.
[184] U.S.N.R. Commission, Typical Dry Cask Storage System, in, 2017.
[185] J. Bruno, R.C. Ewing, Spent nuclear fuel, Elements, 2(6) (2006) 343-349.
[186] M.L. Williams, S.E. Skutnik, I.C. Gauld, W.A. Wieselquist, R.A. Lefebvre, ORIGAMI: A code for computing assembly isotopic with origen in, 2015.
[187] T.A. Carstens, Thermoelectric Powered Wireless Sensors for Dry-Cask Storage, University of Wisconsin-Madison, 2013.
[188] H. International, Final Safety Analysis Report for the HI-STORM 100 Cask System, 2010.
[189] A. Bejan, Convection heat transfer, John wiley & sons, 2013.
[190] A. Zigh, J. Solis., Computational fluid dynamics best practice guidelines for dry cask applications, Office of U.S. Nuclear Regulatory Research, 2012.
[191] E.M. Sparrow, L.F.A. Azevedo, Vertical-Channel Natural-Convection Spanning between the Fully-Developed Limit and the Single-Plate Boundary-Layer Limit, Int J Heat Mass Tran, 28(10) (1985) 1847-1857.
[192] L.E. Herranz, J. Penalva, F. Feria, CFD analysis of a cask for spent fuel dry storage: Model fundamentals and sensitivity studies, Ann Nucl Energy, 76 (2015) 54-62.
[193] W.n. association, Nuclear Fuel and its Fabrication, (2017).
[194] S. Turner, An Uncertainty Analysis-Axial Burnup Distribution Effects, 1989.
[195] K. Mittal, Z. Han, J. Li, H. Tsai, Y. Liu, Temperature of Interest for the TN-32 Cask during Storage of High Burnup Fuel, in: INMM 55th Annual Meeting, Atlanta, Georgia, USA, 2014.
[196] R. Bahney, T. Lotz, Spent nuclear fuel effective thermal conductivity report, Prepared for the US DOE, Yucca Mountain Site Characterization Project Office by TRW Environmental Safety Systems, Inc., July, 11 (1996).
[197] J. Tallackson, Thermal transport properties of helium, helium--air mixtures, water, and tubing steel used in the CACHE program to compute HTGR auxiliary heat exchanger performance, Oak Ridge National Lab., Tenn.(USA), 1976.
[198] J. Li, Y.Y. Liu, Thermal modeling of a vertical dry storage cask for used nuclear fuel, Nucl Eng Des, 301 (2016) 74-88.
[199] K. Waldrop, J. Kessler, Update on in-service inspections of stainless steel dry storage canisters document ML14052A430 (slides), in, NEI-NRC Meeting on Spent Fuel Dry Storage Cask Material Degradation, 2014.
[200] T.N.I. Center, Nuclear Power Plants Built with Earthquakes in Mind, in, 2011.
[201] U.S.N.R. Commission, Spent Fuel Pools, in, 2017.
[202] J.H. Ko, J.H. Park, I.S. Jung, G.U. Lee, C.Y. Baeg, T.M. Kim, Shielding Analysis of Dual Purpose Casks for Spent Nuclear Fuel under Normal Storage Conditions, Nucl Eng Technol, 46(4) (2014) 547-556.
[203] D.A. Clayton, W.H. Andrews Jr, R. Lenarduzzi, Power harvesting practices and technology gaps for sensor networks, Oak Ridge National Laboratory (ORNL), 2012.
[204] J. Chen, L. Zuo, Y.J. Wu, J. Klein, Modeling, experiments and optimization of an on-pipe thermoelectric generator, Energ Convers Manage, 122 (2016) 298-309.
[205] M. Tewolde, C.C. Lin, H. Tao, H.F. Chen, G.S. Fu, D. Liu, T. Zhang, D. Benjamin, L. Zuo, D. Hwang, J. Longtin, Sensors for Small Modular Reactors Powered by Thermoelectric Generators, Proceedings of the Asme Small Modular Reactors Symposium, 2014, (2014).
[206] Y. Zhang, D. Butt, V. Agarwal, Nanostructured Bulk Thermoelectric Generator for Efficient Power Harvesting for Self-powered Sensor Networks, Idaho National Laboratory (INL), Idaho Falls, ID (United States), 2015.

[207] T.A. Carstens, M.L. Corradini, J.P. Blanchard, C.H. Liu, M. Li, N. Behdad, Z.Q. Ma, Thermoelectric Powered Wireless Sensors for Dry-Cask Storage, Ieee T Nucl Sci, 60(2) (2013) 1072-1079.
[208] Y. Wu, J. Klein, H. Zhou, L. Zuo, Thermal and fluid analysis of dry cask storage containers over multiple years of service, Annals of Nuclear Energy, 112 (2018) 132-142.
[209] T.A. Carstens, Thermoelectric Powered Wireless Sensors for Dry-Cask Storage, University of Wisconsin-Madison, 2013.
[210] J.A. Klein, Energy Harvesting Opportunities Throughout the Nuclear Power Cycle for Self-Powered Wireless Sensor Nodes, Virginia Tech, 2017.
[211] I. Hi-Z Technology, HZ-2 Thermoelectric Module, in, 2017.
[212] TECTEG, Specifications TEG Module TEG1-1263-4.3, in, 2018.
[213] A. Bejan, E. Sciubba, The Optimal Spacing of Parallel Plates Cooled by Forced-Convection, Int J Heat Mass Tran, 35(12) (1992) 3259-3264.
[214] R. Simons, Estimating Parallel Plate-fin Heat Sink Pressure Drop, in, 2003.
[215] H. Petersen, The properties of helium: density, specific heats, viscosity, and thermal conductivity at pressures from 1 to 100 bar and from room temperature to about 1800 K, 1970.
[216] Y.S. Muzychka, M.M. Yovanovich, Laminar forced convection heat transfer in the combined entry region of non-circular ducts, J Heat Trans-T Asme, 126(1) (2004) 54-61.
[217] H. Nikjoo, S. Uehara, D. Emfietzoglou, Interaction of radiation with matter, CRC press, 2012.
[218] J. Mackey, A. Sehirlioglu, F. Dynys, Detailed Uncertainty Analysis of the ZEM-3 Measurement System, 2014.
[219] B.W. Church, Penetrating Distances, in, 2015.
[220] T. MFR., Hybrid Thermoelectric Power Modules PbTe-BiTe, in, 2016.
[221] G.J. Snyder, T. Caillat, Using the compatibility factor to design high efficiency segmented thermoelectric generators, Thermoelectric Materials 2003-Research and Applications, 793 (2004) 37-42.
[222] C.A. Domenicali, Irreversible Thermodynamics of Thermoelectric Effects in Inhomogeneous, Anisotropic Media, Phys Rev, 92(4) (1953) 877-881.
[223] T. MFR., Thermoelectric Generator Power Bulk Materials BiTe, PbTe, in, 2016.
[224] D. Samson, M. Kluge, T. Becker, U. Schmid, Energy Harvesting for Autonomous Wireless Sensor Nodes in Aircraft, Procedia Engineer, 5 (2010) 1160-1163.

Appendix A

The following is the input file for the MCNP6 simulation. A quarter model of dry cask with basket and assemblies estimations was presented. This code was used for the simulation of the gamma-shielding performance of a W-B4C plate with a thickness of 0.5mm.

```
C **************CELL CARDS*************************
C
C
C *******Four sections of fuel assemblies*********
11 1 -2.4 -19 23 24 3 4 5 6 7 8 9 10 12 13 14 16 18
12 0      -19 -23 24 1 2 3 6 7 8 9 10 11 13 14 15 17
13 0      -19 -23 -24 1 2 3 6 7 8 9 10 11 13 14 15 17
14 0      -19 23 -24 3 4 5 6 7 8 9 10 12 13 14 16 18
C
C *******Four sections of the basket*********
21 2 -7.8 (-3:-4:-5:-6:-7:-8:-9:-10:-12:-13:-14) 23 24
22 0      (-1:-2:-3:-6:-7:-8:-9:-10:-11:-13:-14) -23 24
23 0      (-1:-2:-3:-6:-7:-8:-9:-10:-11:-13:-14) -23 -24
24 0      (-3:-4:-5:-6:-7:-8:-9:-10:-12:-13:-14) 23 -24
C
C ***************Electronic*********
3  6 -2.55 -20
C ********Tungsten at the medium height*********
4  3 -15.34 -21
C
C *******Helium filled MPC canister********
C *******Geometry split near tungsten***
511 4 -0.0004316 -22 23 24 -25 20 33 #11 #21 $Quadrant 1
512 4 -0.0004316 -22 23 24 25 21 #7 $Quadrant 1
C *******Rest of canister******
52 0      -22 -23 24 #12 #22 $Quadrant 2
53 0      -22 -23 -24 #13 #23 $Quadrant 3
54 0      -22 23 -24 #14 #24 $Quadrant 4
6  0      22
C
C ********** Copper Fins************
7  5 -8.92  -26:-27:-28:-29:-30:-31:-32
C ************Tungsten shielding at the right corner*******
8  3 -15.34  -33

C **************SURFACE CARDS************************
C
C
C *********Inner 16 basket sections****************
1 RPP -47 -46.29 -70.3225 70.3225 -216 216
```

```
2 RPP -23.6775 -22.9675 -70.3225 70.3225 -216 216
3 RPP -0.355 0.355 -70.3225 70.3225 -216 216
4 RPP 22.9675 23.6775 -70.3225 70.3225 -216 216
5 RPP 46.29 47 -70.3225 70.3225 -216 216
6 RPP -70.3225 70.3225 46.29 47 -216 216
7 RPP -70.3225 70.3225 22.9675 23.6775 -216 216
8 RPP -70.3225 70.3225 -0.355 0.355 -216 216
9 RPP -70.3225 70.3225 -23.6775 -22.9675 -216 216
10 RPP -70.3225 70.3225 -47 -46.29 -216 216
C
C ********Outer 16 basket sections***********
11 RPP -70.3225 -69.6125 -47 47 -216 216
12 RPP 69.6125 70.3225 -47 47 -216 216
13 RPP -47 47 69.6125 70.3225 -216 216
14 RPP -47 47 -70.3225 -69.6125 -216 216
15 RPP -70.3225 -47 -70.3225 -47 -216 216
16 RPP 47 70.3225 -70.3225 -47 -216 216
17 RPP -70.3225 -47 47 70.3225 -216 216
18 RPP 47 70.3225 47 70.3225 -216 216
C
C ************Bounding box for fuel assemblies******
19 RPP -70.3225 70.3225 -70.3225 70.3225 -216 216
C
C ***********Electronics************
20 RPP 72.51 73.51 -10 10 180 200
C
C ***********Tungsten at the middle height**********
21 RPP 81.5 81.7 -5 5 100 110
C
C ***********Copper Fins**************
26 RPP 81 81.5 -5 5 100 110
27 RPP 79 81 -3 -2.5 100 110
28 RPP 79 81 -1.9 -1.4 100 110
29 RPP 79 81 -0.8 -0.3 100 110
30 RPP 79 81 0.3 0.8 100 110
31 RPP 79 81 1.4 1.9 100 110
32 RPP 79 81 2.5 3 100 110
C
C **********Tungsten shielding***********
33 RPP 72 72.5 -10 10 180 200
C
C ***********Outer MPC*************
22 RCC 0 0 -226 0 0 452 85.7
C
C **********Geometry Split********
23 PX 0
```

```
24 PZ 0
25 RPP 0 77 -70.3225 70.3225 0 219

C **************DATA CARDS******************
C
C
PHYS:N
MODE N
C ********Increase importance towards tungsten*******
IMP:N 1 0 0 0 6 0 0 0 108 972 36 108 0 0 0 0 324 36
PRINT 10 30 110
C ********Start gammas in the fuel assemblies*****
SDEF PAR=P ERG=D101 X=D1 Y=D2 Z=D3 CEL=11
SI1 0 70.3225
SP1 0 1
SI2 -70.3225 70.3225
SP2 0 1
SI3 0 216
SP3 0 1
C ******Source information from ORIGAMI**********
SI101        H   1.0000E-04  1.0000E-03  1.0000E-02  5.0000E-02 &
 1.0000E-01  2.5000E-01  5.0000E-01  7.5000E-01 &
 1.0000E+00  1.2500E+00  1.5000E+00  2.0000E+00 &
 3.0000E+00  4.0000E+00  5.0000E+00  1.0000E+01 &
 1.5000E+01  2.0000E+01
SP101        D   1.1494E-05  3.6266E-04  3.7668E-03  7.3971E-03 &
 3.2048E-02  7.0478E-02  7.9582E-02  8.1630E-02 &
 7.9782E-02  7.5711E-02  1.3503E-01  1.9882E-01 &
 1.1567E-01  6.0678E-02  5.7821E-02  1.1939E-03 &
 1.7453E-05
C *********Tallies*********
C F2:P 20.2 21.6
C E2
*F1:N 20.2 33.2 21.1 33.1
C ************Fuel makup from ORIGAMI (can be different for different
cases)**********
m1 1001   -4.355408E-09 &
          1002   -9.121062E-10 &
          1003   -1.975469E-11 &
          2003   -2.630581E-06 &
          2004   -5.421321E-06 &
          3006   -6.370921E-17 &
          3007   -1.892944E-17 &
          4009   -9.533631E-13 &
          5010   -1.766030E-16 &
          5011   -1.149523E-14 &
```

```
 7014   -1.412623E-13 &
 7015   -1.491603E-10 &
 8016   -1.179071E-01 &
 8017   -4.797949E-05 &
 9019   -4.232378E-10 &
11023   -4.628435E-27 &
12024   -1.190626E-30 &
31069   -1.263104E-30 &
32070   -1.246774E-11 &
32072   -1.077385E-08 &
32073   -1.077385E-08 &
32074   -6.242219E-08 &
32076   -3.979030E-07 &
34074   -1.660692E-13 &
34076   -6.443369E-09 &
34077   -6.443369E-09 &
34078   -2.715752E-06 &
34079   -1.507817E-05 &
34080   -1.507817E-05 &
34082   -3.948947E-05 &
36078   -2.575044E-20 &
36080   -3.740784E-10 &
36082   -9.494312E-07 &
36083   -1.316513E-04 &
36084   -1.316513E-04 &
36085   -1.316513E-04 &
36086   -2.183715E-04 &
37085   -2.929610E-28 &
38084   -6.997705E-12 &
38086   -6.444682E-07 &
38087   -3.993019E-04 &
38088   -3.993019E-04 &
38089   -3.993019E-04 &
38090   -5.580075E-04 &
39089   -9.687560E-16 &
39090   -1.415454E-07 &
40090   -9.927497E-05 &
40091   -7.593844E-04 &
40092   -7.593844E-04 &
40093   -7.593844E-04 &
40094   -9.041800E-04 &
40095   -9.568958E-04 &
40096   -9.568958E-04 &
41093   -3.498447E-13 &
41094   -1.696714E-09 &
42092   -9.889854E-19 &
```

```
42094   -1.311628E-08 &
42095   -5.241635E-05 &
42096   -5.241635E-05 &
42097   -5.241635E-05 &
42098   -9.885171E-04 &
42099   -1.117070E-03 &
42100   -1.117070E-03 &
44096   -7.394696E-24 &
44098   -5.988122E-13 &
44099   -1.362599E-04 &
44100   -1.362599E-04 &
44101   -1.362599E-04 &
44102   -9.671796E-04 &
44103   -6.718947E-04 &
44104   -6.718947E-04 &
44105   -6.718947E-04 &
44106   -6.344942E-06 &
46102   -4.339369E-10 &
46104   -2.921744E-04 &
46105   -2.921744E-04 &
46106   -4.536411E-04 &
46107   -1.775236E-04 &
46108   -1.775236E-04 &
46110   -5.912154E-05 &
47107   -1.500695E-19 &
47109   -1.500695E-19 &
48106   -8.186924E-21 &
48108   -3.488214E-10 &
48110   -4.785621E-05 &
48111   -1.519079E-05 &
48112   -1.519079E-05 &
48113   -1.519079E-05 &
48114   -1.762833E-05 &
48116   -6.534397E-06 &
50112   -4.991676E-16 &
50113   -4.991676E-16 &
50114   -4.478895E-11 &
50115   -4.289553E-06 &
50116   -4.289553E-06 &
50117   -4.289553E-06 &
50118   -5.556338E-06 &
50119   -5.540319E-06 &
50120   -5.540319E-06 &
50122   -7.054003E-06 &
50123   -1.118552E-05 &
50124   -1.118552E-05 &
```

```
50125   -1.118552E-05 &
50126   -2.438974E-05 &
51123   -4.652802E-17 &
51124   -4.652802E-17 &
51125   -4.652802E-17 &
51126   -5.019043E-13 &
52120   -2.683680E-16 &
52122   -4.657733E-07 &
52123   -3.889990E-07 &
52124   -3.889990E-07 &
52125   -3.889990E-07 &
52126   -6.518539E-07 &
52128   -1.120086E-04 &
52130   -4.502813E-04 &
54123   -5.279747E-21 &
54124   -5.279747E-21 &
54126   -1.099213E-10 &
54128   -3.994521E-06 &
54129   -3.994521E-06 &
54130   -8.538114E-06 &
54131   -1.347018E-03 &
54132   -1.347018E-03 &
54133   -1.347018E-03 &
54134   -1.812647E-03 &
54135   -2.764296E-03 &
54136   -2.764296E-03 &
55134   -3.186458E-05 &
56132   -1.852292E-10 &
56133   -1.852292E-10 &
56134   -2.034402E-04 &
56135   -2.471027E-05 &
56136   -2.471027E-05 &
56137   -2.471027E-05 &
56138   -1.550695E-03 &
57138   -1.873955E-08 &
58138   -1.176403E-12 &
58139   -1.450809E-03 &
58140   -1.450809E-03 &
58141   -1.450809E-03 &
58142   -1.339309E-03 &
58143   -4.486092E-06 &
58144   -4.486092E-06 &
59143   -1.889624E-10 &
60142   -2.773771E-05 &
60143   -1.601617E-03 &
60144   -1.601617E-03 &
```

```
60145   -1.601617E-03 &
60146   -8.441732E-04 &
60147   -4.430108E-04 &
60148   -4.430108E-04 &
60150   -2.128465E-04 &
61147   -4.551073E-22 &
61148   -4.551073E-22 &
61149   -4.551073E-22 &
62144   -5.060132E-18 &
62147   -1.756044E-04 &
62148   -1.756044E-04 &
62149   -1.756044E-04 &
62150   -3.513770E-04 &
62151   -1.130855E-04 &
62152   -1.130855E-04 &
62153   -1.130855E-04 &
62154   -4.526513E-05 &
63151   -6.267408E-09 &
63152   -6.267408E-09 &
63153   -6.267408E-09 &
63154   -2.191385E-05 &
64152   -2.659694E-08 &
64153   -2.659694E-08 &
64154   -1.370931E-05 &
64155   -1.185241E-04 &
64156   -1.185241E-04 &
64157   -1.185241E-04 &
64158   -2.304546E-05 &
64160   -1.319381E-06 &
65159   -2.622721E-15 &
65160   -2.622721E-15 &
66156   -2.021751E-18 &
66158   -8.335729E-14 &
66160   -3.498372E-07 &
66161   -3.498372E-07 &
66162   -3.245143E-07 &
66163   -6.460763E-08 &
66164   -6.460763E-08 &
68162   -1.568371E-18 &
68164   -8.747034E-13 &
68166   -3.659291E-08 &
68167   -6.665866E-09 &
68168   -6.665866E-09 &
68170   -3.935182E-10 &
82204   -3.144781E-26 &
82206   -1.553099E-16 &
```

```
82207   -3.449489E-11 &
82208   -3.449489E-11 &
83209   -3.438145E-20 &
88223   -1.905210E-13 &
88224   -1.905210E-13 &
88225   -1.905210E-13 &
88226   -1.310809E-13 &
89227   -1.350356E-22 &
90227   -3.683982E-11 &
90228   -3.683982E-11 &
90229   -3.683982E-11 &
90230   -3.585824E-09 &
90232   -5.303128E-09 &
90233   -5.303128E-09 &
90234   -1.183516E-11 &
91231   -1.103038E-20 &
91232   -1.103038E-20 &
91233   -1.103038E-20 &
92232   -1.916255E-09 &
92233   -1.916255E-09 &
92234   -1.707719E-04 &
92235   -4.806143E-03 &
92236   -4.806143E-03 &
92237   -4.806143E-03 &
92238   -8.151303E-01 &
92239   -9.129853E-19 &
92240   -9.129853E-19 &
92241   -9.129853E-19 &
93235   -2.375195E-10 &
93236   -2.375195E-10 &
93237   -2.375195E-10 &
93238   -1.234802E-13 &
93239   -8.016386E-23 &
94236   -5.764925E-10 &
94237   -5.764925E-10 &
94238   -2.541312E-04 &
94239   -2.393469E-03 &
94240   -2.393469E-03 &
94241   -2.393469E-03 &
94242   -6.645746E-04 &
94243   -4.685856E-08 &
94244   -4.685856E-08 &
94246   -9.836826E-23 &
95242   -8.585440E-12 &
95243   -7.648419E-21 &
95244   -7.648419E-21 &
```

```
        96242   -9.980436E-09 &
        96243   -5.227338E-05 &
        96244   -5.227338E-05 &
        96245   -5.227338E-05 &
        96246   -5.250113E-07 &
        96247   -4.804188E-10 &
        96248   -4.804188E-10 &
        96249   -4.804188E-10 &
        96250   -1.552563E-16 &
        97249   -6.067406E-17 &
        97250   -6.447126E-23 &
        98249   -1.016952E-18 &
        98250   -2.046033E-12 &
        98251   -2.098859E-13 &
        98252   -2.098859E-13 &
        98254   -3.467606E-27 &
        99254   -1.337276E-19
C *********Stainless Steel Basket*********
M2 26056 -0.85 24052 -0.1 28058 -0.05
C **********Tungsten**********
M3 74000 -0.77 5010 -0.04 5011 -0.14 6012 -0.05
C ***********Helium Gas at 3.3 atm********
M4 2004 1 GAS=1
C ***********Copper Fins***********
M5 29000 1
C *************Thermal Isolation (Fiberglass)*******
M6 8016 -0.485868 14028 -0.257 20040 -0.143 13027 -0.052925 &
  5011 -0.031055 12024 -0.030152
C ***************Stop after: ************
CTME 150
```

Publications

Peer-reviewed journal papers

[1] **Yongjia Wu**, Shifeng Yu, Lei Zuo. Large eddy simulation analysis of the heat transfer enhancement using self-oscillating fluidic oscillators. *International Journal of Heat and Mass Transfer*, 131 (2019): 463-471.

[2] **Yongjia Wu**, Jackson Klein, Hanchen Zhou, Lei Zuo. Energy harvesting for wireless communications in the nuclear environment. *Annals of Nuclear Energy*, 126 (2019): 376-388.

[3] Shifeng Yu, **Yongjia Wu**, Shuyu Wang, Ming Lu, Lei Zuo. Thermodynamic analysis of a MEMS based differential scanning calorimeter. *Sensors & Actuators: A. Physical*, 2019.

[4] **Yongjia Wu**, Haifeng Zhang, Lei Zuo. Thermoelectric energy harvesting for the gas turbine sensing and monitoring system. *Energy Conversion and Management*, 157 (2018): 215-223.

[5] **Yongjia Wu**, Jihui Yang, Shikui Chen, Lei Zuo. Thermo-element geometry optimization for high thermoelectric efficiency. *Energy*, 147 (2018): 672-680.

[6] **Yongjia Wu**, Jackson Klein, Hanchen Zhou, Lei Zuo. Thermal and fluid analysis of dry cask storage containers over multiple years of service. *Annals of Nuclear Energy*, 2018, 112, 132-142.

[7] **Yongjia Wu**, Lei Zuo, Jie Chen, Jackson Klein. A model to analyze the device level performance of the thermoelectric generator, *Energy*, 115 (2016): 591-603.

[8] Jie Chen, Lei Zuo, **Yongjia Wu**, Jackson Klein. Modeling, experiments, and optimization of an on-pipe thermoelectric generator. *Energy Conversion and Management*, 122 (2016): 298-309.

[9] Jie Chen, Jackson Klein, **Yongjia Wu**, Lei Zuo. A Thermoelectric Energy Harvesting System for Powering Wireless Sensors in Nuclear Power Plants. *IEEE Transactions on Nuclear Science*, 63.5 (2016): 2738-2746.

[10] **Yongjia Wu**, Shifeng Yu, Kan Sun, Lei Zuo. Modeling the selective laser melting of thermoelectric powders. *Journal of Materials Processing Technology*. 2019. (Submitted)

[11] Shifeng Yu, **Yongjia Wu**, Shuyu Wang, Michael Siedler, Peter M. Ihnat, Dana I. Filoti, Ming Lu, Lei Zuo. A MEMS-based differential scanning calorimeter and its application to the thermal stability study of proteins, Sensors & Actuators: B. Chemical, 2019. (Submitted)

Peer-reviewed conference papers

[1] **Yongjia Wu**, Lei Zuo, Kan Sun. Modeling the selective laser melting of multi-component thermoelectric powders. *2018 IDETC/CIE*. Quebec. Canada.

[2] **Yongjia Wu**, Jackson Klein, Hanchen Zhou, Lei Zuo. Energy harvesting for nuclear waste sensing and monitoring. *2018 IDETC/CIE*. Quebec. Canada. (**ASME best paper award**)

[3] **Yongjia Wu**, Lei Zuo, Suresh Kaluvan, Haifeng Zhang, Nance Ericson, Kyle Reed, Roger Kisner. Self-powered Wireless Through-wall Data Communication for Nuclear Environments. *2019 11th NPIC/HIMT*. Orlando FL.

[4] Xiaoqiang Xu, **Yongjia Wu**, Lei Zuo, Shikui Chen. Multimaterial topology optimization of thermoelectric generators. *2019 IDETC/CIE*. Anaheim, CA.

Newsletter

[1] Lei Zuo, **Yongjia Wu,** Haifeng Zhang, Roger Kisner, Nance Ericson. Self-powered Wireless Through-wall Data Communication for Nuclear Environments. *Advanced sensor and instrument (DOE Nuclear Engineering NEET Program)*, 2018.